Bjørn Christian Abrahamsen

Sloshing induced tank-roof impact with entrapped air pocket

Bjørn Christian Abrahamsen

Doktoravhandling

Doctoral theses at NTNU, 2011:38

NTNU
Norges teknisk-naturvitenskapelige
universitet
Avhandling for graden
philosophiae doctor
IVT
Marin teknikk

NTNU
Det skapende universitet

NTNU
Det skapende universitet

NTNU

Bjørn Christian Abrahamsen

Sloshing induced tank-roof impact with entrapped air pocket

Thesis for the degree of Philosophiae Doctor

Trondheim, January 2011

Norwegian University of
Science and Technology
Faculty of Engineering Science and Technology
Department of Marine Technology

NTNU
Norwegian University of
Science and Technology

Abstract

During the impact between the free surface of a liquid and a solid structure, air might be entrapped. The air can then be compressed and radically affect the behaviour of the slamming event. The knowledge about the physical effects governing slamming with air entrapment is sparse compared to the knowledge about slamming without air entrapment. Uncertainty related to the governing physical mechanisms generates uncertainty related to scaling laws when model scale experiments are carried out.

In order to obtain new knowledge about the physical effects governing the air pocket impact, idealized studies of an entrapped air pocket was performed. This air pocket impact took place during sloshing inside a rectangular tank with water at a large filling ratio. The problem was studied both by dedicated experiments and mathematical methods. The time history of the pressure measured inside the air pocket resembles the free oscillations of an under-damped single degree of freedom mass-spring system. Hence, the pressure oscillations have a characteristic period and amplitude, where the amplitude generally shows decay.

Two mathematical models have been applied to describe this air pocket slamming event: The Mixed Eulerian-Lagrangian (MEL) method and the semi-analytical air pocket model (SAM). The MEL method, is an existing method often applied to free surface problems where the liquid can be modelled using potential flow theory assuming incompressible liquid. The MEL method is applied from the instant when the wave first touches the roof and during the air pocket impact. The initial conditions to the MEL method is obtained by a novel numerical method which we denote the boundary-element-finite-difference method (BEFDM). The second method used to model the air pocket impact was an existing semi-analytical air pocket model.

The comparison between the mathematical models and the experiments shows that these existing models can describe the period and maximum pressure of the oscillations. However, the overall decay trend seen in the experiments cannot be represented by the present models. Due to this deficiency of the mathematical models, different physical effects believed to cause decay were investigated. The probable sources of decay were (i) heat exchange between the air inside the air pocket and the surrounding tank wall and water, (ii) viscous boundary layers in the water at the tank walls, and (iii) air leakage to and from the air pocket. The effect of heat exchange to and from the air inside the air pocket and the surrounding water and tank walls was studied mathematically through a linear, one-dimensional, steady-state and constant pressure heat exchange model. Based on this it was found that the polytropic gas model used for the MEL and SAM methods fail to model the damping effect of heat exchange. In addition the heat exchange modifies the polytropic exponent and hence the stiffness properties of the air pocket oscillations. However, it was found that a good representation of the air pocket stiffness can be obtained by assuming adiabatic conditions for the air pockets studied in this work.

The effect of viscous boundary layers was investigated through a mathematical model assuming linear unsteady laminar boundary layers. The interaction between the flow field of the entering water and the flow field of the oscillating air pocket was neglected. Based on this model a lower bound of the damping ratio was estimated and it was seen that viscous

boundary layers contributes to the damping of the pressure oscillations.

Based on images taken of the air pocket during the experiments we concluded that air leakage was not present after the first pressure minimum, and could therefore not be the cause of the overall decay trend. To see the effect of air leakage on air pocket oscillations in general, differently sized holes in the tank roof were made and the effect of air leakage studied. Air leakage was seen to cause decay of the pressure oscillations. The damping due to air leakage can, depending on the leakage area, be the largest source of damping.

In order to scale these types of air pocket impacts a new scaling procedure is proposed. This is the pressure-amplitude and rise-time scaling procedure (PARTS). The method applies to the case when air pocket model experiments are performed by maintaining the same Froude number, applying geometric similarity and using atmospheric reference pressure for the model as for the prototype. The method is applicable for tank roof impact. However, the method may be generalized to the impact of breaking waves entrapping air pockets on vertical walls. Through an existing method by Lundgren only the pressure amplitude can be estimated. With the present method both the pressure amplitude and the rise time can be found. The rise time is an important parameter in dynamic structural analysis.

Acknowledgements

A PhD is a challenge in many ways, requiring endurance, patience, confidence and creativity. It has been a lot of work, a lot of learning, some hard times and some moments of achievement I will never forget. I would like to thank the people who helped me along the way:

Thanks to my excellent supervisor Professor Odd M. Faltinsen. It has been an honour to be your student. Thanks to Professor Torgeir Moan for giving my PhD work a head start by hiring me for research work during the summers of 2004 and 2005. Thanks to dr. Petter A. Berthelsen, dr. Vibeke S. Nørstebø, Mia Prsic, dr. Jørgen Hals, Anette Abrahamsen and Robin A. Svendsen for reading parts of this thesis and suggesting improvements. Thanks to dr. Trygve Kristiansen, dr. David Kristiansen, dr. Petter A. Berthelsen, Professor Marilena Greco, Arnt G. Fredriksen, dr. Andrea Califano for discussions regarding marine hydrodynamics and PhD life in general. Thanks to my good friends and flat mates Maxime Thys and Reza Firoozkoohi for all the interesting conversations, and cultural learnings. Thanks to dr. Olav Rognebakke for answering questions related to the sloshing experiments. Thanks to my good friends and training companions dr. Vibeke S. Nørstebø , dr. Øyvind Sandbakk and dr. Hagbart S. Alsos. Jeg vil også takke min mor Alma Irene, min far Bjørn og min søster Anette for støtten dere har gitt meg slik at dette arbeidet kunne gjennomføres.

To all of you: I would like to return the favour somehow.

Contents

Abbreviations:

AP	Air pocket.
BEFDM	Boundary-element-finite-difference method.
CA	Camera angle.
MEL	Mixed Eulerian-Lagrangian method.
PARTS	Pressure-amplitude and rise-time scaling procedure.
SDNM	Single-dominant nonlinear multimodal method.

Subscripts:

n	Component of gradient in the direction of the normal vector $\boldsymbol{n}$.
τ	Component of gradient in the direction of the tangential vector $\boldsymbol{\tau}$.
x	Derivative with respect to x-coordinate.
y	Derivative with respect to y-coordinate.

Greek symbols:

α	Modulus of decay.
β	Time stepping variable for the BEFDM.
γ	Ratio of specific heats.
ϵ	Displacement in the one-dimensional heat model.
ϵ_0	Amplitude of the displacement in the one-dimensional heat model.
ζ	Wave elevation.
θ	Relative temperature.
κ	The polytropic exponent of the gas compression.
λ	Ratio of characteristic lengths in the prototype and model.
ξ	Damping ratio of the gravity waves or the air pocket oscillations.
ϕ_{ap}	The velocity potential at the free surface inside the air pocket.
$\boldsymbol{\tau}$	Counter clockwise pointing tangential vector of the BEM boundary.
ρ	Density of the liquid.
ρ_g	Density of the gas.
ρ_{g0}	The density of the gas at ullage conditions.
σ	The velocity component normal to the free surface. $\sigma = \phi_n$.
$\bar{\phi}$	Velocity potential in the inertial coordinate system.
ϕ	Velocity potential for the liquid in the accelerated coordinate system.
ϕ_g	Velocity potential for the gas in the accelerated coordinate system.
$\bar{\phi}_g$	Velocity potential in the gas for an inertial coordinate system.
ω_0	Natural frequency of the air pocket pressure oscillations.
ω_1	First natural frequency of the sloshing motion.
Ω	Volume of the air pocket.
Ω_0	Volume of the air pocket at the time of closure.

Latin symbols:

a	x-coordinate describing the wetted section of the roof.
a_f	Horizontal acceleration of the tank.
A_L	Area of the hole in the tank roof where air is leaking.
b	Horizontal dimension of the air pocket.
Ca	Cavitation number.
c_0	Speed of sound.
c_p	Specific heat at constant pressure.
c_v	Specific heat at constant volume.
d	Diameter of the hole in the roof above the air pocket.
Dr	Density ratio of the fluids inside the tank $Dr = \rho_g/\rho$.
E	The complete elliptic integral of the second kind.
E_k	Amplitude of the kinetic energy of the air pocket oscillations.
Eu	The Euler number.
Fn	The Froude number.
H	Tank filling height.
h_0	Characteristic thickness of the air pocket.
h_1	The vertical distance from the mean free surface to the tank roof.
K	The complete elliptic integral of the first kind.
K_1	Thermal conductivity.
L	Tank length.
L_p	Characteristic length of the prototype.
L_m	Characteristic length of the model.
M	The Mach number.
$\boldsymbol{x}$	Position in tank fixed coordinate system.
r	The distance between two points P and Q.
$\boldsymbol{n}$	Inward pointing normal vector of the BEM boundary.
x_f	Horizontal displacement of the tank.
u_f	Horizontal velocity of the tank.
p	Dynamic pressure.
P	Maximum dynamic pressure of the pressure oscillations.
$\bar{p}$	Absolute pressure; $\bar{p} = p_0 + p$.
Pe	The Péclet number.
p_0	Ullage pressure.
p_v	Vapour pressure for the liquid.
p_{0p}	Initial absolute pressure inside the air pocket at closure.
Q_{in}, Q_{out}	Volume flux of air into and out of the air pocket.
R	Gas constant (value dependent on the specific gas).
Re	The Reynolds number.
s	Polygonal arc length along the boundary of the liquid domain.
S_{ap}	The free surface between the air pocket and the liquid.
s_c	Cubic spline arc length along the boundary of the liquid domain.
T	Rise time of the pressure.
t	Time.

t_{ap} Duration of the air pocket slamming event.

T_0 Ullage temperature.

T_{abs} Absolute temperature.

T_n Natural period of the pressure oscillations.

T_{ns} Natural period of the first mode of sloshing.

u Component of the tank relative velocity in the x-direction.

U Characteristic velocity of the physical problem.

u_g The horizontal gas velocity.

v Component of the tank relative velocity in the y-direction.

V Vertical velocity of the free surface before impact.

V_0 The vertical velocity of the free surface before air pocket impact.

V_1 Vertical acceleration of the free surface prior to impact.

We Weber number.

x Horizontal coordinate in the tank fixed coordinate system.

y Vertical coordinate in the tank fixed coordinate system.

z Coordinate normal to the $x - y$ plane.

Chapter 1

Introduction

An impact between a marine structure and a liquid is denoted slamming. Examples of slamming are when life boats are dropped into the water, when breaking waves hit sea walls, when high waves hit the superstructure of oil platforms and when the liquid hits the walls inside cargo tanks in ships. In these cases slamming effects need to be considered in structural design.

Roughly speaking slamming phenomena can be divided in two types. This is when gas is entrapped between the free surface and the structure during impact and when it is not. The entrapped gas, when present, adds complexity to the problem. The physical problem then contains two phases of fluid and compressibility of the gas often matters. This makes the problem harder to model mathematically than if no gas is entrapped. The fact that compressibility of the gas might be important, leads to extra challenges when experiments in model scale are performed because Froude number and geometrical similarity in model and prototype scale is no longer sufficient to obtain geometrical similar flows in model and full scale. Other non-dimensional numbers, like the Euler number, are also of importance. Furthermore, experiments of slamming including gas entrapment often show poor repeatability.

The present study considers a particular type of slamming event inside a rectangular tank, filled with water, during sloshing at high filling. This impact scenario is illustrated on the left side of figure 1.1. Here a rectangular tank filled with water and air is seen. The forced horizontal tank motion causes a wave which at a certain time instant hits the roof in such a way that air is entrapped between the free surface and the roof. As the wave entraps the air, the air is compressed and the entrapped air and surrounding water starts to oscillate. The pressure inside the air pocket is seen to oscillate in a way that resembles the solution of a freely oscillating, under-damped, one degree of freedom, mass-spring system. The spring is associated with the compressibility of the air and the mass is associated with the generalized added mass effect of the oscillating water. These oscillations have a characteristic period and amplitude, where the amplitude generally shows decay. In the following, this slamming event is referred to as the air pocket at the upper corner. The present study is relevant for other slamming scenarios including entrapped gas, as long as the gas follows the ideal gas law. Examples are breaking waves inside sloshing tanks at low filling levels or breaking waves at sea walls.
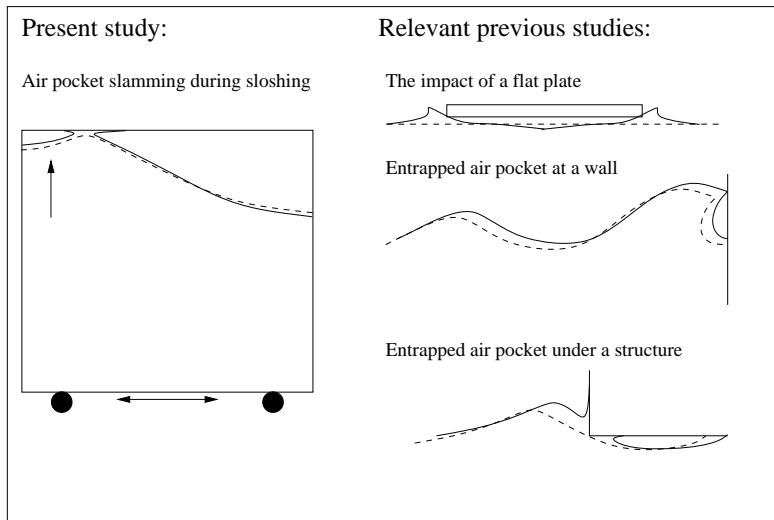
13

1.1   Previous work

Figure 1.1:   *Left:* The present study is a slamming event where air is entrapped at the roof-wall corner of a rectangular sloshing tank. *Right:* Relevant previous studies which have similarities to the present study.

Here previous work on slamming phenomena including entrapped air is reviewed. This includes the air pocket at the upper corner seen on the left in figure 1.1 and other relevant slamming events seen on the right in figure 1.1. The other relevant slamming events are the air pocket entrapped underneath a horizontal flat plate hitting a flat free surface, the entrapped air pocket between a breaking wave at a vertical wall and the entrapped air pocket under a marine structure. These different cases are discussed in the following in order to summarize the knowledge related to these phenomena, with special emphasis on experimental findings, mathematical modelling and scaling.

The air pocket at a wall is formed when a wave with plunging breaking entraps air as it approaches a wall. The air pocket is then compressed and can start to oscillate in a similar way as the air pocket at the upper tank corner. This type of air pocket impact is illustrated on the right side in figure 1.1. Entrapped air pockets at walls can for instance occur when a breaking wave entraps an air pocket at a sea wall or at a wall of a prismatic sloshing tank at low filling. The loads exerted on the tank walls are of concern for some types of tanks like for instance prismatic liquefied natural gas (LNG) tanks. This type of tanks has an insulating material attached to the inside of the tank walls. The purpose of this material is to keep the LNG cold. The insulating material can be damaged due to liquid motion.

The entrapped air pocket between a breaking wave and a wall has been studied extensively in the past. One of the first researchers investigating air pocket impacts on vertical walls was Bagnold [1], who investigated the problem both mathematically and experimentally. The experiments showed lack of repeatability. This is due to the inherent randomness of the
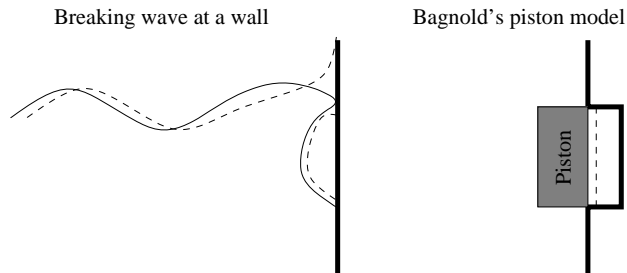
Figure 1.2: Bagnold assumed that water compressing an air pocket at a wall (left) behaves as a piston compressing an air pocket (right).

breaking wave process. This has later been seen to be a general challenge related to this type of experiments by for instance Hattori and Arami [2]. Bagnold also presented a mathematical model where the breaking wave entrapping an air pocket at a wall was assumed to behave as a rigid piston entrapping an air pocket. This model is illustrated in figure 1.2. The wave is assumed to arrive at the wall with a certain kinetic energy available to compress the air pocket. Bagnold represented the entering water as a rigid piston. This piston is then doing work to compress the air pocket, until its velocity is brought to zero at the time instant of maximum pressure. The model assumes an adiabatic compression of the air pocket, where the pressure inside the air pocket is assumed to be uniform.

The pressure time histories reported from experiments for air pocket impacts at walls generally show a similar type of oscillatory behaviour as the air pocket at the upper corner. More specifically, the pressure time history does to some extent resemble the free oscillations of a single degree of freedom, under-damped, mass-spring system. Hence, the pressure time history has a characteristic period and amplitude, where the amplitude generally show decay. Explanations for this decay has been suggested. Mitsuashu [3] explained the decay by air leaking from the air pocket during the oscillations. Here air leakage refers to air flowing into or out from the air pocket through an opening between the air pocket and the atmosphere during the time when the air pocket is oscillating. Later Lugni et al. [4] and [5] identified air leakage for an entrapped air pocket at a wall. The leakage was observed at the tip of the breaking wave after it had hit the wall. Lugni et al. did not quantify the air leakage. The breaking wave on a sea wall was modelled mathematically by Zhang et al. [6] assuming incompressible potential flow for the water. The pressure inside the air pocket was assumed uniform in space and an adiabatic pressure density relationship was assumed neglecting air leakage. The pressure time history resulting from their numerical model shows decay of the pressure time history although no leakage is modelled. This suggests that there might be other sources for the decay than air leakage.

A flat plate falling on a calm free surface is a simplified problem which is relevant for many fields in marine hydrodynamics. A relevant application is the impact between the bottom of a ship and the free surface. Verhagen [7] modelled the impact of a rigid flat plate onto a free surface both experimentally and numerically. Linear, incompressible potential flow theory was assumed for the water, while the escaping air during the time before the

plate hit the liquid was modelled as quasi-one-dimensional and compressible. After the plate hit the water, the air pressure was assumed uniform in space and the compression adiabatic. The comparison of the experiments and the mathematical model shows good agreement. The experimental results show that repeatability is reduced with increasing impact speed. Verhagen also reports a complicated two phase mixing phenomenon during the impact which causes leakage of air. Faltinsen and Timokha [8] report the drop test of elastic plates. Large scatter was seen for the maximum pressure measured for a given impact speed, however the maximum strain measured in the plate was more repeatable.

The entrapped air pocket at the upper corner, which is the type of air pocket studied in this work, has previously been studied experimentally by Allers and Rognebakke reported by Allers [9] and mathematically by Faltinsen and Timokha [8]. The experiments show an entrapped air pocket slamming event during sloshing. The entrapped air pocket was close to the corner of the tank. The air pocket was modelled by a semi-analytic model (SAM) using potential flow theory for the water flow. The model was able to reproduce nearly the same oscillation frequency, however the pressure amplitude was over predicted and the mathematical model was not able to predict the overall decay trend of the experimental pressure oscillations. However, the mathematical model showed decay of the pressure time history during the first period of oscillation. The source of this decay was nonlinear effects. The overall decay of the pressure time history from the experiments could not be reproduced. One reason for this was explained to be possible air leakage from the experimental air pocket. A leakage model was included in the mathematical (SAM) method and it was concluded that only a small circular hole could produce large decay of the pressure time history. A different type of air pocket which also shows decay is an air bubble in water. Devin [10] investigated the decay of spherical air bubbles in infinite water. He modelled the air pocket using linear theory and found that the decay of the air bubble oscillations was due to heat exchange, viscosity and acoustic effects.

When performing model test experiments of slamming events with entrapped air, there are uncertainty related to scaling laws. What are the non-dimensional numbers which should be similar for the model and the prototype? Many of the non-dimensional numbers which have been discussed in the literature in connection with air pocket slamming events are listed in table 1.1. In the first part of this discussion the emphasis is on model tests where the prototype contains air and water.

The Froude number $Fn = U/\sqrt{gL}$ should be maintained in model and full scale when gravity waves dominate the physical behaviour. Here U is a characteristic velocity, g is the acceleration due to gravity and L is a characteristic length of the physical problem. In the case of slamming including entrapped air other non-dimensional numbers are also important. A non-dimensional version of Bagnold's piston model shows that, in addition to the Froude number, the Euler number Eu and the polytropic index κ must be equal in model and full scale in order to obtain similar motions. The Euler number is defined as $Eu = p_0/(\rho U^2)$, where p_0 is the ullage pressure, ρ is the density of the liquid and U is a characteristic velocity of the entering wave. The polytropic index κ is equal to one if the air pocket undergoes an isothermal (constant temperature) process and equal to the ratio of specific heats $\gamma = c_p/c_v$ if the air pocket undergoes an adiabatic (no heat exchange) process. Here c_p is the specific

Non-dim. number	Formula
Froude number	$Fn = \frac{U}{\sqrt{gL}}$
Euler number	$Eu = \frac{p_0}{\rho U^2}$
Cavitation number	$Ca = \frac{p_0 - p_v}{\rho U^2}$
Density ratio	$Dr = \frac{\rho_{g0}}{\rho}$
Ratio of specific heats	$\gamma = \frac{c_p}{c_v}$
Péclet number	$Pe = \frac{\omega_0 L^2}{D_1}$
Mach number	$M = U/c_0$
Reynolds number	$Re = \frac{UL}{\nu}$
Weber number	$We = \frac{\rho U^2 L}{\Upsilon}$

Table 1.1: Non-dimensional numbers discussed in connection with air pocket slamming events. (L: characteristic length, g: acceleration of gravity, U: characteristic velocity, p_0: ullage pressure, p_v: vapour pressure, ρ: density of liquid, ρ_{g0}: density of gas, c_p: the specific heat at constant pressure, c_v: is the specific heat at constant volume, ω_0: natural frequency of the air pocket, D_1: thermal diffusion coefficient of air, c_0: speed of sound, ν: kinematic viscosity coefficient and Υ: surface tension coefficient)

heat at constant pressure and c_v is the specific heat at constant volume.

In the case when water and air at atmospheric conditions are used to model fresh/sea water and air at atmospheric conditions at full scale, by applying geometrical similarity and Froude scaling, Lundgren [11] established a scaling procedure for the maximum pressure of air pocket impacts based on Bagnold's piston model assuming adiabatic conditions for the air pocket. A limitation of this procedure is that it does not give any information about the temporal variation of the pressure, which from a dynamic structural point of view is important.

The importance of the Euler number is also shown by the work of Greco et al. [12] who investigated numerically the air pocket entrapped under a very large floating structure (VLFS). The impact scenario is shown in figure 1.1. The numerical model was a nonlinear boundary element method, where the water was modelled as incompressible using potential flow and the air pocket was modelled assuming uniform spatial pressure and adiabatic compression. They investigated scaling effects by varying the Euler number and compared their results with the scaling law obtained by linearising Bagnold's nonlinear piston model assuming adiabatic conditions for the air pocket. The time t_p and dynamic pressure p_p in the air pocket in full scale is then related to the model scale values t_m and p_m as $t_p = t_m\lambda$, and $p_p = p_m\sqrt{\lambda}$. Here λ is given as $\lambda = L_p/L_m$ where L_p is a characteristic length for the prototype and L_m is a characteristic length in model scale. The results from Greco et al. [12] show that this scaling procedure is inaccurate. Faltinsen and Timokha [8] solved for the air pocket impact in the upper corner using the semi-analytic method and compared the results with the scaling procedure by Lundgren [11] which was based on Bagnold's nonlinear piston model. They found that this scaling procedure was fairly accurate.

If the same Euler number is maintained in model and prototype lower ullage pressure is needed for the model than for the prototype. The ullage pressure in model scale must then be set to $p_0^m = p_0^p/\lambda$. Here p_0^m and p_0^p are the ullage pressure for the model and the prototype, respectively. Experiments varying the Euler number was carried out by Lugni et al. [4] and [5], for an entrapped air pocket at a wall inside a sloshing tank filled with water and air. The

ullage pressure p_0 was varied and it was found that the air pocket behaves differently when the ullage pressure p_0 is close to the vapour pressure p_v. This means that small cavitation number, defined by $Ca = (p_0 - p_v)/(\rho U^2)$, matters. Here p_v is the vapour pressure of the liquid. Further, Lugni et al. investigated the decay of the pressure time history. The decay calculated from the initial stage of the pressure oscillations, that is the decay calculated from the two first pressure peaks, showed much more decay than the later pressure oscillations. In addition the initial decay was seen to be more sensitive to the Euler and cavitation numbers than the decay observed later in the time series.

It should be noted that the density ratio was not kept constant when the ullage pressure was varied in Lugni's work. The reason for this is that reduced ullage pressure leads to reduced ullage density ρ_{g0} of the air. This will lead to a different density ratio $Dr = \rho_{g0}/\rho$, if air and water is used in model and prototype. Here ρ is the density of the liquid. Stive [13] then suggests to use a heavier gas in model than in prototype to obtain the same density ratio at a lower ullage pressure. Maillard and Brosset [14] investigated the importance of the density ratio on the pressure measured inside a sloshing tank. They concluded that the density ratio affects the way the air escapes the impact region, and that increasing density ratio increases the number of gas pocket impacts. This suggests that if the tank is evacuated in order to obtain the same Euler number, a heavier gas should be used in order to model slamming including air entrapment correctly.

Compressible effects are of concern when slamming is investigated. In a compressible flow the density is not constant. The air pocket type of slamming is often governed by uniform compression. Since the air pocket is uniformly compressed, the density of the air cannot be treated as constant. The work by Allers [9], also reported by Faltinsen and Timokha [8], shows that the pressure inside the air pocket is uniform in space. Hence, many mathematical models, like Bagnold [1], Zhang et al. [6], Greco et al. [12] and Faltinsen and Timokha [8] assume uniform pressure inside the air pocket. They also assume that the pressure and density inside the air pocket follow a polytropic gas model assuming adiabatic conditions. An assumption regarding the heat exchange between the gas and the liquid is required when using a polytropic gas model. In practice this leads to either an adiabatic or an isothermal assumption. This assumption significantly affects the results. The work by Devin [10] on the spherical air bubble shows that the polytropic exponent used in the polytropic gas model, is dependent on the ratio of specific heats and the Péclet number when linear theory is assumed. The Péclet number for the entrapped air pocket at the upper corner is defined as $Pe = \omega_0 L^2/D_1$ where ω_0 is the natural frequency of the air pocket oscillations, L is a characteristic length of the air pocket and D_1 is the thermal diffusion coefficient of air. The Péclet number shows the importance of convection compared to thermal diffusion. Devin's model also shows that the polytropic pressure-density model fails to model the damping of the air pocket oscillations due to heat exchange between air and water. Compressible effects are also important if the local flow speed is high compared to the sound speed. More specifically, if the Mach number which is defined as $M = U/c_0$, where U is the local fluid velocity and c_0 is the sound speed, is larger than 0.3 (White [15]) then fluid compressibility is important. Also compressible effects matter if there are time scales of the flow which trigger acoustic effects. Acoustic effects inside the air pocket can be disregarded if the frequency of oscillation

is significantly lower than the lowest natural frequency of the acoustic problem. Based on this argument, acoustic effects in the air pocket can often be neglected. For acoustic effects in the water, it should be specified if the slamming event contains a mix of water and air, because the speed of sound can be much smaller for a mix of water and air, than for pure water or pure air.

Viscosity is often neglected in slamming analysis, and hence the Reynold's number is not similar in model and full scale. The Reynolds number represents the effect of viscosity and is given as $Re = UL/\nu$, where ν is the kinematic viscosity coefficient of the fluid. Viscosity is often neglected in mathematical models of air pocket slamming, like for instance the reported works by Zhang et al. [6], Verhagen [7] and Greco et al. [12]. For the spherical air bubble investigated by Devin [10], viscosity was seen to influence the decay of the oscillations of the bubble. Viscous effects and their influence on the decay of the air pocket at the upper corner is investigated in chapter 5.

Surface tension effects are represented by the Weber number $We = \rho U^2 L/\Upsilon$, where Υ is the surface tension coefficient which depends on the two fluids. Surface tension can affect the shape of a free surface before it impacts a structure if it has large curvature. In the case of a breaking wave at a wall, Stive [13] recommends that the wave in model scale should exceed $H = 0.5[\mathrm{m}]$.

Fresh water is often used to model seawater at prototype scale. At a seawall the wave hits the wall periodically, which means that the water can be aerated due to previous impacts. Aeration refers to the many small air bubbles mixed with the water. These small bubbles behave differently for salt and freshwater which have implications on the validity of using fresh water and air to model salt water and air in full scale. Bullock et al. [16] studied the influence of aeration level on slamming pressures for air and fresh water and air and salt water. They found that the air bubbles formed in freshwater tend to be larger than air bubbles formed in seawater, and that they coalesce more easily. Larger bubbles rise faster to the free surface than small bubbles which leads to less aeration in freshwater than in seawater.

In the case of model tests of sloshing inside LNG tanks the scaling problem gets more involved. Until recently a mix of air and water at atmospheric conditions has been used to model the prototype tank containing boiling LNG, where the LNG coexists as both liquid and vapour. To investigate the effect of phase transition, Maillard and Brosset [14] used boiling water to model the liquid phase and water vapour to model the gas. They found that as the wave approached the roof and entrapped the vapour, the vapour was compressed and changed phase from vapour to liquid state. The resulting pressure time history does not show oscillations. However, there is large uncertainty related to how water in liquid and vapour state can model LNG. The role of condensation is a present research topic for the patent holders of the insulation systems used in prismatic LNG tanks.

In the present discussion the structure is assumed to be rigid. In reality the fluids and the structure might interact causing hydro-elastic effects. Further information about hydro-elastic effects is given by Faltinsen and Timokha [8].

1.2 Objectives

Allers [9], who investigated an air pocket at the upper corner of a sloshing tank during sloshing at high filling, found that the measured pressure showed low repeatability when the water had hit the roof multiple times. Bagnold [1] experimentally investigating the wave pressures also experienced repeatability problems. He reports: "It was considered that the most fruitful method of studying such a problem was likely to be the use of a model wave tank in which the characteristics of the wave causing the pressures could be maintained under close control." Since repeatable air pocket impacts are hard to create experimentally, the first objective of this work was:

Objective 1: To design experiments of idealized air pocket slamming events in the upper corner of a liquid filled tank during sloshing at high filling which are as repeatable as possible.

The air pocket impact at the upper corner was investigated mathematically in Faltinsen and Timokha [8] using the semi-analytic method (SAM). The SAM calculations showed that nonlinear effects related to the change of the air pocket geometry gave reduction of the amplitude of pressure during the first period of oscillation. The SAM calculations showed a natural frequency close to the frequency of the air pocket oscillations. However, two major deviations between the experiments and the SAM was identified. The method over predicted the maximum pressure, and the method could not reproduce the overall decay of the experimental pressure time history.

Objective 2: To investigate the entrapped air pocket impact through experiments and mathematical models and through this obtain new knowledge regarding the physical effects governing air pocket slamming events. More specifically, to try to explain the physical mechanism behind the decay of the air pocket oscillations often seen experimentally.

Model tests of slamming including entrapped air pockets, when air and water at atmospheric conditions are used to model full scale problems consisting of air and fresh or salt water at atmospheric conditions, only maintaining the same Froude number and geometric similarity, is problematic. This because Bagnold's mathematical model shows that the Euler number Eu is an important parameter. To find a scaling procedure when non-dimensional quantities governing the physical behaviour, is not maintained similar in model and full scale is ambitious. However, a lot of experiments are carried out at atmospheric conditions, and the consequences are uncertain, hence, even a crude scaling procedure can help removing uncertainty related to this practice. This leads to the third objective of the present work:

Objective 3: To investigate the scaling of air pocket impact events, and to describe the errors made by model experiments where the Euler number is different in model and prototype. The objective is also to investigate if there are other non-dimensional numbers which are important related to slamming including air pockets.

1.3   Scope

The phenomenon studied is characterized by a free surface entrapping an air pocket at a structure. Mathematical and experimental models are used to investigate one type of such entrapped air pockets. This type of impact is the entrapped air pocket in the upper corner of a sloshing tank at high filling. The fluids used in the study are water and air. The study is relevant for slamming problems including entrapped air, where the fluids in prototype scale is fresh/sea water and air. It is an ongoing research task to identify to what extent fresh water and air represents LNG in full scale (Maillard and Brosset [14]). One question related to this is the role of condensation. The present work does not contain new knowledge about the validity of using fresh water and air in model scale to represent LNG in full scale.

The problem is studied in two dimensions using numerical, semi-analytical and experimental methods. The water is modelled as incompressible, irrotational and inviscid, using potential flow theory. This means that compressible effects of the liquid are neglected. Numerous discretisation methods exist for potential flow. From the experiments the fine detail of closure is seen to be of importance and hence a numerical method which treats the free surface as sharp was preferred. In computational fluid dynamics (CFD) there is a family of methods called surface tracking methods which treats the free surface as sharp. One possible way to solve the Laplace equation maintaining a sharp free surface is the boundary element method (BEM). This method was chosen for solving the problem. The effect of surface tension is neglected all together in the mathematical modeling. No parts of this thesis include the effect of aerated water. Aeration is the phenomenon when many small air bubbles are mixed with the water and is often due to previous slamming events.

Although the present study is considering one special case of entrapped air pocket slamming events, the knowledge obtained in terms of experimental results, mathematical modelling and scaling effects are believed to be, to some extent, generalizable to other types of air pocket events. This includes the case of the horizontal flat plate falling onto a free surface, the breaking wave at a wall and the entrapped air pocket underneath a marine structure.

1.4   Outline of the thesis

The experimental set up and results are reported in chapter 2. Based on the experiments, the case studied is split in a sloshing stage an air escape stage, and an air pocket oscillation stage. The numerical model of the sloshing and air escape stage is derived, tested and applied to the sloshing and air escape stage in chapter 3. The numerical model of the oscillation stage is explained, tested and applied to one air pocket impact in chapter 4. After this the semi-analytic model by Faltinsen and Timokha [8] is extended to include the damping effect of heat exchange and viscous boundary layers in chapter 5. The different mathematical models are then compared with the experimental results in chapter 6. Finally a new scaling procedure, the pressure-amplitude and rise-time scaling procedure (PARTS), is proposed in chapter 7. Finally, conclusions and suggestions for future work are given in chapter 8 and 9.

1.5   Contributions of the thesis

A new excitation signal producing an entrapped air pocket at the upper corner of a rectangular tank at the first contact with the roof is derived based on the linear multimodal method. One of the air pocket slamming events produced, named air pocket 6, showed quite repeatable results. This air pocket was then chosen for comparison with mathematical models. The experiments are reported in chapter 2.

A new, fully nonlinear and incompressible two phase numerical model for sloshing, where the air is modelled as quasi-one-dimensional is proposed. The method applies a known discretisation method, the boundary element method (BEM) for the liquid, and the finite difference method (FDM) for the air but the present combination is new. This method is hence denoted the boundary-element-finite-difference method (BEFDM) and is presented in chapter 3.

The experimental results show that the air leakage into or out of the air pocket during the pressure oscillations leads to decay of the resulting pressure oscillations. Air leakage was observed by Lugni et al. [4] and [5] during the air pocket oscillations of an air pocket at a wall. The leakage was seen to take place through the breaking wave tip after it had hit the wall. In the present experiments the air pocket is fully closed, and the role of air leakage is investigated by drilling circular holes in the tank roof with different diameters. The role of air leakage was seen to be decay of the air pocket oscillations, and the decay increased with increasing diameter of the hole. However, when the hole in the roof was closed no leakage was present, but still all air pockets showed a general decay trend. This means that the overall decay of the presently studied air pockets is not due to air leakage. To find the reason for the decay Faltinsen and Timokha's SAM method [8] was extended to include the effect of heat exchange to and from the air pocket during the air pocket oscillation stage. The model shows that the heat exchange contributes considerably to the decay of the air pocket oscillations. Further, Faltinsen and Timokha's model is extended to investigate damping of the air pocket oscillations due to viscous boundary layers in the water. The method contains uncertainties but it is shown that viscous boundary layers also contribute to damping of the air pocket oscillations. These extensions of the SAM model can be found in chapter 5 and results are presented in chapter 5 and 6.

A new scaling procedure, the pressure-amplitude and rise-time scaling procedure (PARTS), for air pocket slamming events is proposed in the case when air and water at atmospheric conditions is present in both model and prototype. The method further assumes that the model and prototype are geometric and Froude similar. However, the Euler number is different since atmospheric pressure is the reference pressure in both scales. The method is based on the same assumptions as Lundgren's procedure. Lundgren's scaling procedure can however only estimate the peak pressure. The advantage of the present procedure is that information about the rise time of the pressure time history is obtained. This method is presented in chapter 7.

Chapter 2

Experimental investigation of idealized air pockets

Experiments were conducted in order to understand the physics of the air pocket impact during sloshing at high filling. Some questions about this type of impact were stated during the initiation of this work: Is it possible to create an experimental set up which creates repeatable air pocket slamming events? How can the decay of the pressure oscillations from such air pocket slamming events be explained? And what valid assumptions can be made when solving such an impact event mathematically? What are the effects of air leakage from the air pocket during the pressure oscillations? In this chapter the experiments are explained in detail starting with the experimental set up. Then the excitation signals used to create the air pocket impacts are described. After this, sections containing results and discussions of the observed physical phenomena are presented. These experiments motivate the assumptions used in the mathematical models in chapter 3 and 4. This model is later solved numerically and compared with the experimental results in chapter 6.

2.1 Experimental setup

One of the objectives of the experiments was to create as two-dimensional flow as possible. To obtain two-dimensional flow a slim tank was chosen. The interior length, height and width of the tank was L=1000[mm], H_{tot}=980[mm] and D=100[mm], respectively. These dimensions are seen in figure 2.1. The tank was made by 20[mm] thick acrylic plates and the filling level H was set to 85 % of the tank height (H=0.85H_{tot}). The tank was mounted on a steel frame and the frame was mounted on rollers running on steel rails as shown in the left picture in figure 2.2. The frame was moved horizontally by an excitation mechanism consisting of a ball screw attached to an electric engine. To measure the pressure inside the air pocket, four
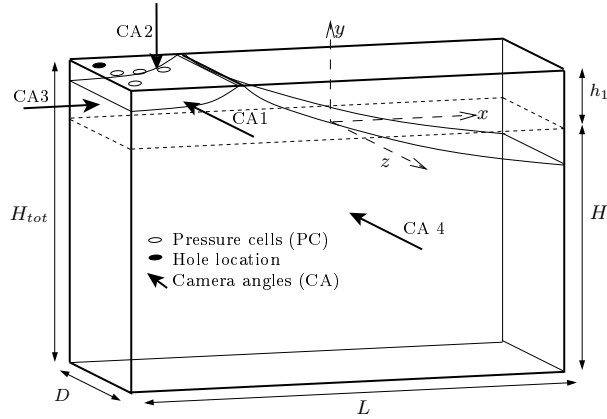

Figure 2.1: A drawing of the tank including notation for dimensions, camera views, location of the pressure sensors and definition of coordinate system. The tank was made of 20[mm] acrylic sheets with internal dimensions L=1000[mm], D=100[mm] and H_{tot}=980[mm].

pressure sensors were attached in the roof close to the corner. These pressure sensors can be seen on the right image in figure 2.2. The pressure sensors were absolute pressure sensors of the Kulite XTL-190 type with a measuring area of 2×2 [mm]. The numbering of the different pressure sensors and the locations of the pressure sensors relative to the tank walls are seen in figure 2.3. An accelerometer was mounted on the tank roof in order to capture possible deflections of the acrylic plate. The location of the tank roof accelerometer is shown on the right image in figure 2.3.

To see the evolution of the air pocket a high speed camera was used to film the air pocket from different angles (see figure 2.1). Camera angle CA 1, CA 2 and CA 3 focus on the air pocket from the front, the top and the side, while CA 4 views the global sloshing behaviour. A camera sample frequency of 1000 [Hz] was used for camera angle 1, 2 and 3 to capture the motion of the air pocket, which had a frequency between 50 and 200 [Hz]. The intention of camera angle 4 was to capture the overall water motion hence a camera frequency of 100 [Hz] was found sufficient. The trigger signal from the high speed camera was recorded in order to synchronise the pressure measurements and the images.
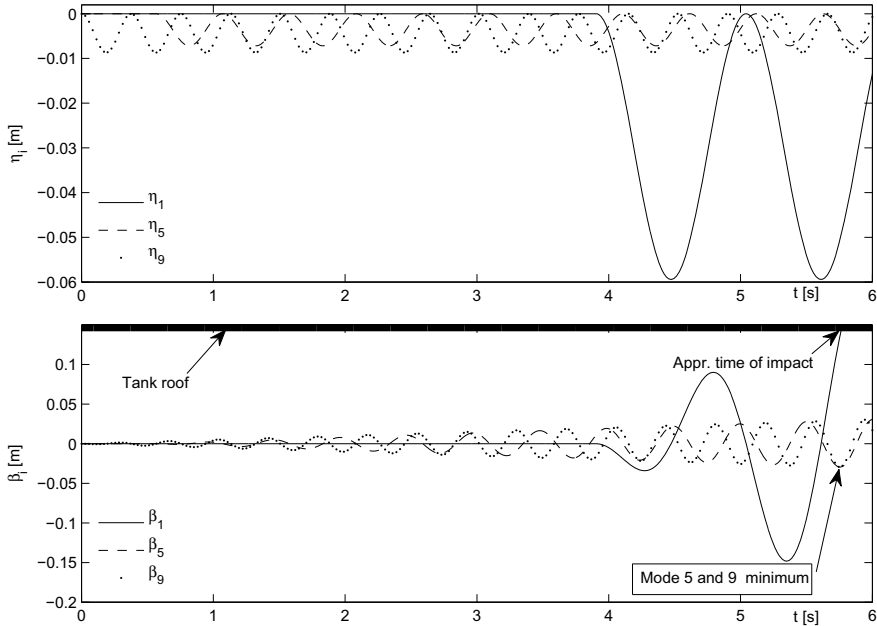
Figure 2.5: *Top:* An example of a set of excitation components $\eta_i(t)$. *Bottom:* The corresponding resonant modal amplitudes $\beta_i^i(t)$. The higher modes 5 and 9 are tuned to be minimum at the time instant when $\eta_1 = h_1$.

together with some higher mode like 5,7 or 9 by oscillating the tank with a frequency equal to the natural frequencies $\sigma_n, n = 1, 5, 7, 9$ of the wanted modes. The sway excitation signal $\eta(t)$ is written as a sum:

$$\eta(t) = \sum_{i=1}^{N} \eta_i(t). \tag{2.1}$$

Here each η_i is responsible of triggering mode number i in the resulting free surface elevation. η_i is written as:

$$\eta_i(t) = \begin{cases} \eta_{ai}\big[cos(\sigma_i\{t - t_{si}\}) - 1\big] & t \geq t_{si} \\ 0 & t < t_{si} \end{cases} \qquad \text{where:} \qquad \sigma_i = \sqrt{\frac{g\pi i}{L}\tanh\frac{H\pi i}{L}}. \tag{2.2}$$

Here η_{ai} is the amplitude and t_{si} is the start time of the excitation component $\eta_i(t)$. The start time t_{si} is used to tune the different components in time so that the resulting wave has an air pocket shape at the time of impact $t = t_0$. The resulting free surface elevation is written as

$$\zeta(x,t) = \sum_{n=1}^{\infty} \cos\left(\pi n\{x + L/2\}/L\right) \sum_{i=1}^{N} \beta_n^i(t). \tag{2.3}$$

Here β_n^i is the response due to excitation component $\eta_i(t)$. Using linearised boundary conditions and writing the velocity potential as a sum of the natural sloshing modes, the modal

amplitudes $\beta_n^i(t)$ due to $\eta_i(t)$ can according to Faltinsen and Timokha [8] be found by solving

$$\ddot{\beta}_n^i + \sigma_n^2 \beta_n^i = \sigma_i^2 P_m^i \cos\left(\sigma_i\{t - t_{si}\}\right) \qquad (2.4)$$

where

$$P_n^i = \eta_{ai} \left[\frac{2}{n\pi} \tanh\left(\frac{\pi n H}{L}\right) (\{-1\}^n - 1) \right].$$

An analytical solution to this equation can be found in Faltinsen and Timokha [8] (page 206). This solution, assuming that all $\beta_n^i(t = t_{si})$ and $\dot{\beta}_n^i(t = t_{si})$ are zero, is given as:

$$\beta_n^i(t) = \begin{cases} 0 & t < t_{si} \\[2mm] \dfrac{P_n^i \sigma_i}{\sigma_n^2 - \sigma_i^2}\left(\cos\left(\sigma_i\{t - t_{si}\}\right) - \cos\left(\sigma_n\{t - t_{si}\}\right)\right) & t \geq t_{si} \quad i \neq n \\[3mm] \frac{1}{2} P_i^i \sigma_i (t - t_{si}) \sin\left(\sigma_i\{t - t_{si}\}\right) & t \geq t_{si} \quad i = n. \end{cases} \qquad (2.5)$$

As the purpose of excitation component $\eta_i(t)$ is to trigger response in the corresponding mode $\beta_i(t)$, it means that the components of the solution corresponding to $i \neq n$ is unwanted noise and should be limited. Since the solution for $i = n$ increases linearly with time, it will after some time, dominate the response. By neglecting all terms $i \neq n$ the elevation on the left hand side in the tank ζ_{lhs} can be written as:

$$\zeta_{\mathrm{lhs}} = \sum_i^N \beta_i^i(t) \qquad (2.6)$$

Here $\beta_i^i(t)$ is given in equation 2.5. An example of an excitation signal using this theory can be seen in figure 2.5. The upper plot shows the three components of the excitation signal used. That is η_1, η_5 and η_9. The higher modes are excited prior to mode 1. At the lower plot the corresponding response in mode 1, 5 and 9 are shown. Mode 5 and 9 are tuned to be minimum at the instant when $\beta_1^1 = h_1$ by choosing appropriate start times t_{s1}, t_{s5} and t_{s9}.

Due to nonlinear effects and the interference by the unwanted components of the solution, β_n^i for $n \neq i$, some ad hoc adjustments of the theoretical excitation signal had to be made to create air pockets in the experiments. This tuning consisted of adjusting the start time of mode 1, that is t_{s1}. The experimentally adjusted excitation signal can be seen in figure 2.6, alongside with images showing the free surface inside the tank at five time instants. This air pocket is named air pocket 6 (AP6) and is one of six reported air pockets in this work. A close fit to the measured excitation in figure 2.6 is given by t_{s1}=3.820[s], t_{s5}=0.5652[s], t_{s9}=0.0[s], η_{a1}=0.0202[m], η_{a5}=0.00145[m] and η_{a9}=0.00077[m]. This analytical excitation signal is fitted to the measured position in the experiment and must be considered an approximation of the measured tank motion. By varying the excitation amplitude of the higher modes 5,7,9,11 the shape of the air pocket can be varied. Further, the impact velocity can be varied by adjusting the excitation amplitude of the first mode of sloshing. In the following section air pockets of different types are presented based on this variation.
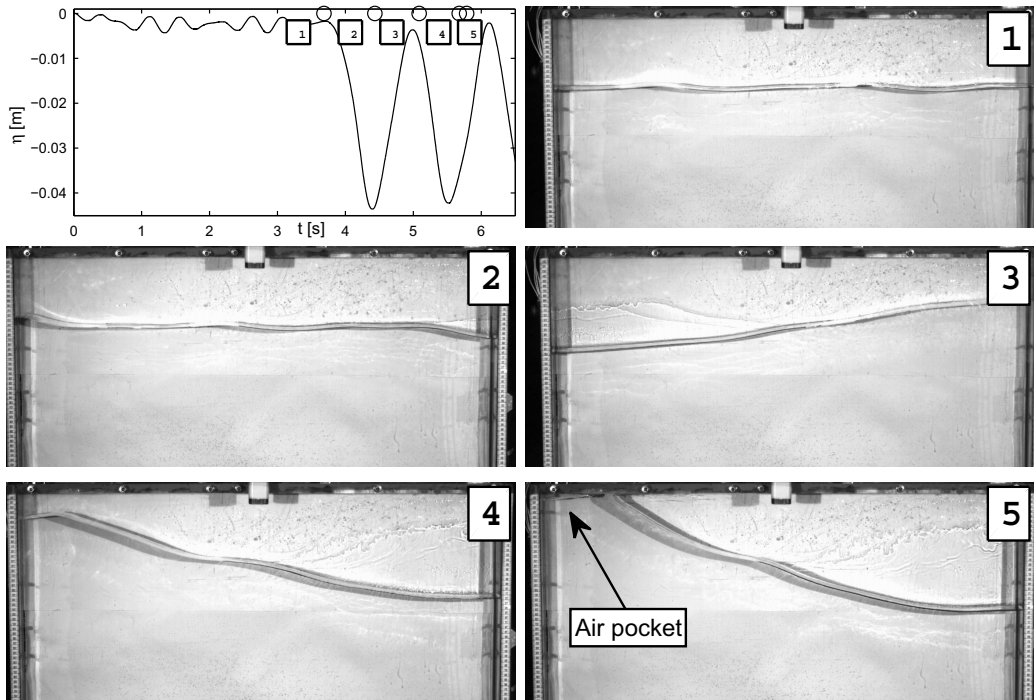
Figure 2.6: The measured forced sway motion $\eta(t)$ and pictures of the free surface flow for the run air pocket 6 run 24. The air pocket seen in image 5 is created at the first contact with the roof.

2.3   Overview of the different air pockets

Many different types of air pockets were produced by varying the excitation signal. Here six of these air pockets are discussed in detail. The shape of these air pockets are seen in figure 2.7. The images are taken just prior to the impact. A rough estimate of the initial volume and vertical velocity of the free surface are given in the images. These estimates are based on an analysis of the experimental images. The estimate of the vertical velocity is made when the peak of the free surface is 6[mm] from the roof. This velocity is estimated both at the free surface along the left wall and at the wave crest. The pressure inside the air pocket is plotted at the lower right corner of the images. The time instant of the image is seen as a circle (○) in the pressure plots.

    The repeatability of the pressure signal from the air pocket impacts are reported in figure 2.8. Each presented plot is an average of the indicated number of runs, for one pressure sensor inside the air pocket. The pressure curves from all the different runs were aligned so that the zero down crossing between the first pressure maximum and the first pressure minimum occurred at the same time instant. This means that the variability of when the pressure peak occurs in time after the start of the sloshing motion is neglected. The height of the

Figure 2.7: Images showing the different air pockets studied. The images show the air pocket from CA 1 just before impact. The pressure measurements show the pressure inside the air pocket. The time instants when the pictures are taken are indicated with circles (○). An estimate of the initial volume Ω_0 and vertical velocity at the left hand side wall V_1 and at the peak point V_2 are shown. The velocities are estimated when the peak point is approx. 6[mm] from the roof.
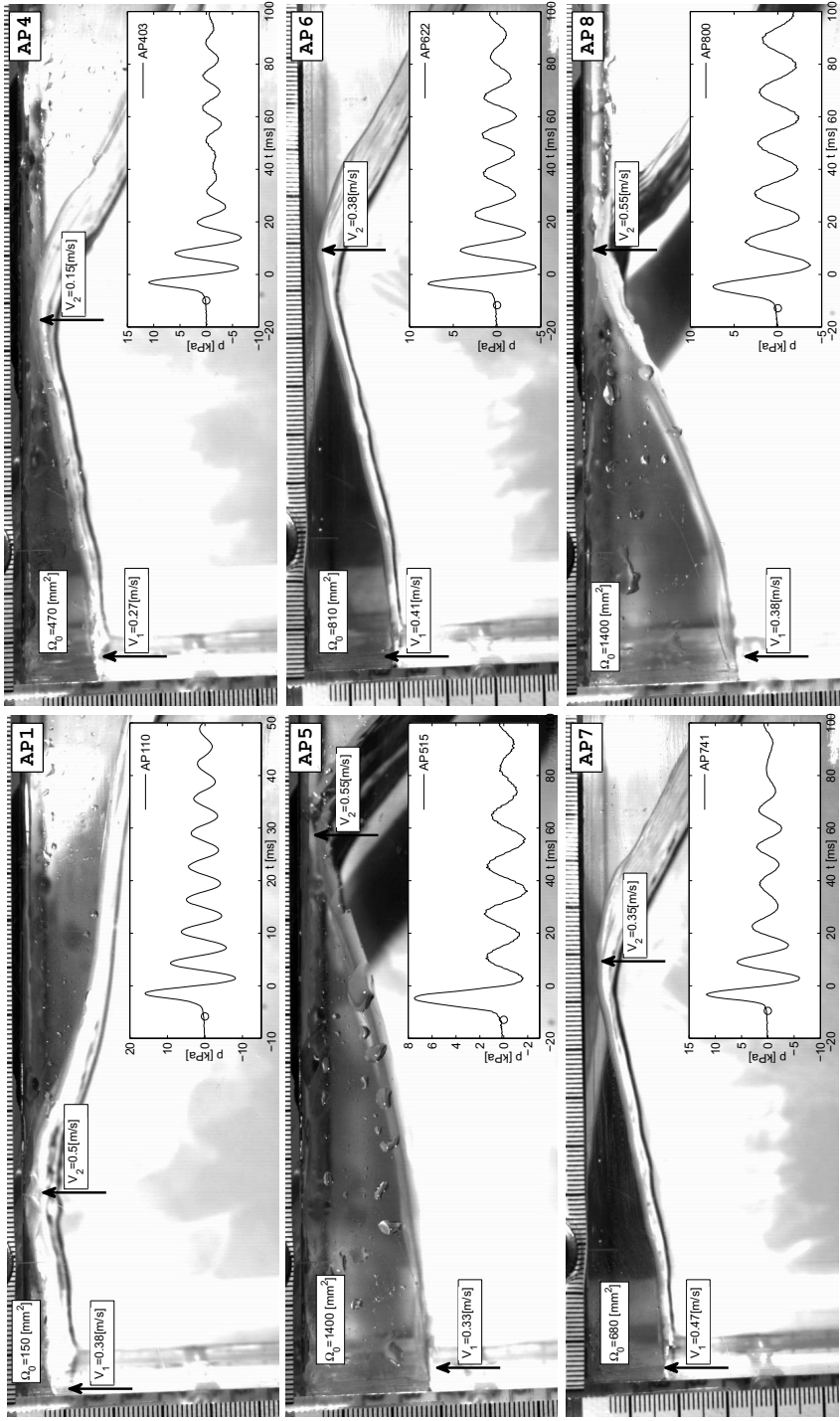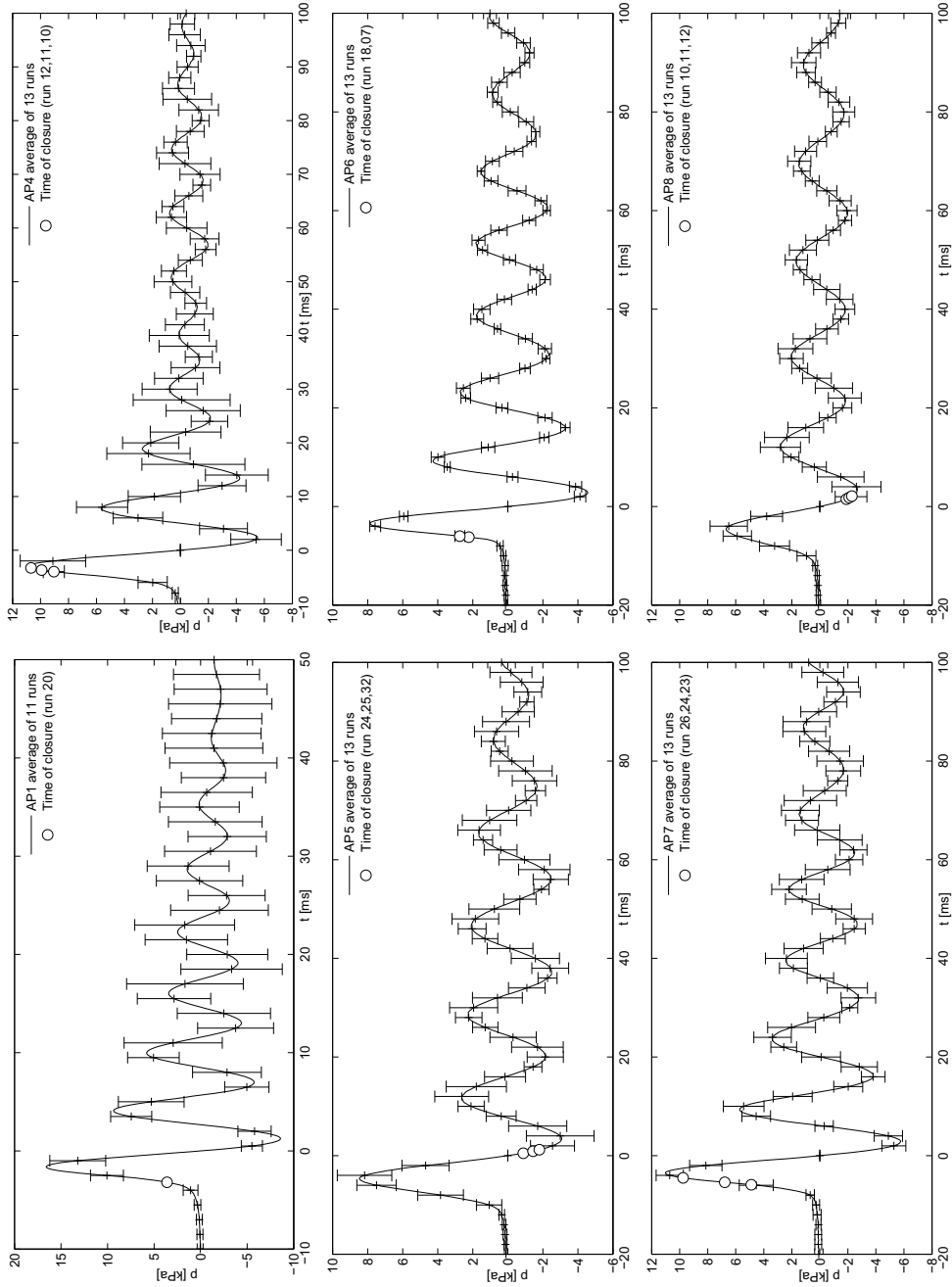
Figure 2.8: The average pressure time history for the number of runs indicated, including error bars showing a 95% confidence interval. The circles (∘) indicates the time instant when the air pocket is completely closed.
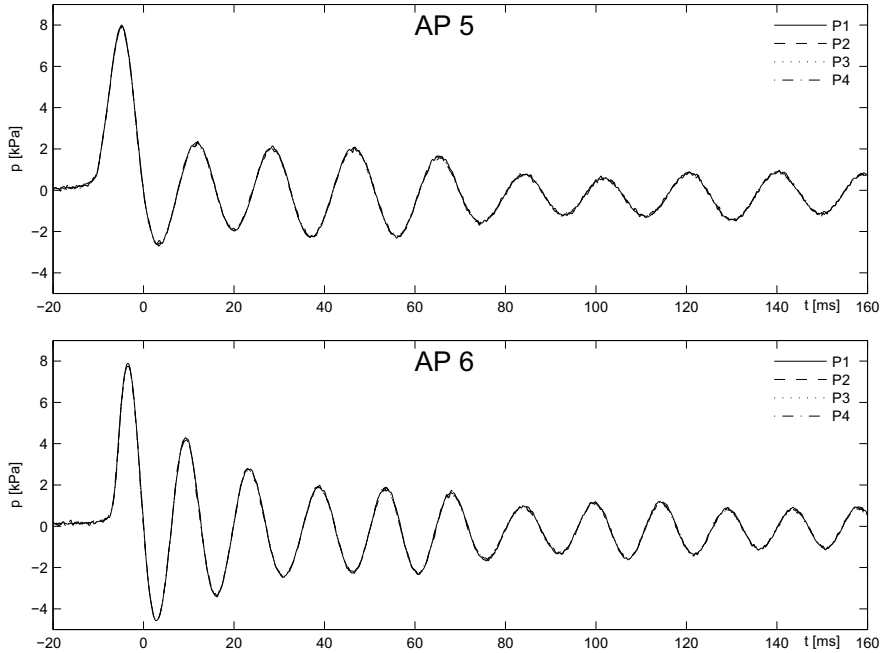
Figure 2.9: The pressure inside two different air pockets. The pressure is nearly spatially uniform for the sample frequency used. *Top:* All pressure sensors for air pocket 6 run 18. *Bottom:* All pressure sensors for air pocket 5 run 25.

error bars indicate the repeatability error using a 95% confidence interval. For comparison the repeatability of the horizontal tank displacement was investigated for air pocket 6. A total of 13 runs was filtered digitally using a bidirectional 2.nd order Butterworth low-pass filter at 10 [Hz] and the standard deviation at different points in time was calculated. The 95% confidence interval of the tank motion measurements at the different time instances was seen to be approximately 0.08 [mm]. The plots in figure 2.8 show the measurements from one pressure sensor since the pressure is nearly constant inside the air pockets. In figure 2.9 the pressure from all three pressure sensors inside the air pocket are plotted. The topmost plot shows air pocket 5 and the lowermost plot shows air pocket 6. The plots show that the pressure inside the air pocket is very close to spatially uniform for the sampling frequency used. In the following the measurements from pressure sensor P1 is reported for air pocket 1, while the measurements from pressure sensor P2 is reported for the other air pockets. Only the first part of the pressure time history is plotted in figure 2.8. This is because the period of the pressure time histories from the different runs deviate, which introduces a phase shift of the pressure time history of the individual runs. This means that the average pressure time history will contain more decay than the individual pressure time histories and is hence no longer a representative pressure time history for the corresponding air pocket impact event.
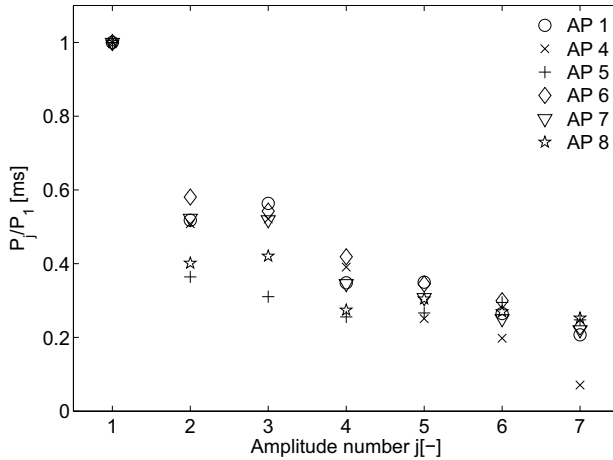
Figure 2.10: The dynamic pressure amplitudes P_j for the first three oscillations. The pressure shows large decay during the first half period for all air pockets. Even numbers of j are pressure minima while odd numbers of j are pressure maxima.

In addition, the error bars in the later stage of the slamming event will be much larger than in the beginning of the slamming event due to this phase shift. In the plots in figure 2.8 the circles ($\circ$) indicate the time when the air pockets are closed. These time instants are found by investigating the high speed camera images taken from above (CA 2) and identifying the time instant when the roof is continuously wetted across the thickness of the tank (z-direction).

The pressure measurements resemble the free oscillations of some sort of mass-spring system. This oscillatory behaviour is characterised by the amplitude and the period of the oscillations. The amplitudes of the pressure time history P_j for the first three periods are plotted in figure 2.10 as a function of the amplitude number j. Here j denotes the amplitude number where odd numbers of j denotes pressure peaks and even number of j denotes the amplitude of the pressure minima. In order to compare the decay of the different air pockets the pressure amplitudes P_j are made non-dimensional with respect to the first pressure peak P_1. The pressure amplitudes of all the air pockets show large decay during the time from the first pressure maximum to the first pressure minimum. The largest decay is seen for air pocket 5 and 8, the reason for this could be that these air pockets close at a later time instant than all the other air pockets and thereby cause air leakage damping (see figure 2.8). After the first pressure minimum $j = 2$, all air pockets show little or no decay at all from the first pressure minimum to the second pressure maximum. After the second pressure peak the air pockets behave in a less uniform fashion, but the trend is that the amplitudes of the pressure oscillations decay further after the second pressure peak and until the end of the slamming event.

To investigate the pressure time history at later times the averaged pressure time history cannot be used as explained previously. Here the pressure time history from one single run of each type of air pocket is presented. This is seen in figure 2.11 and 2.12. The left column of plots show the pressure time histories of the different type of air pockets. All the pressure time histories experience decay during the impact. The oscillations do, to some extent, resemble the free decay of a under-damped linear mass-spring system. If this
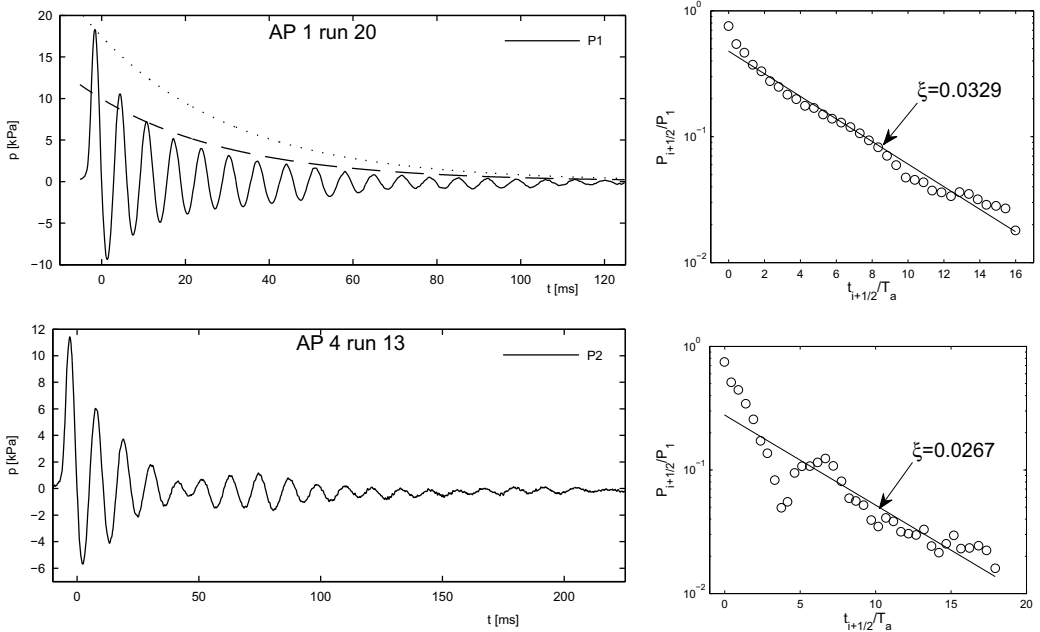
Figure 2.11: *Left:* Pressure time histories of air pocket 1 and 4. *Right:* The relative amplitude $P_{i+1/2}/P_1 = (P_i+P_{i+1})/(2P_1)$ plotted as a function of the the non-dimensional time $t_{i+1/2}/T_a = (t_i+t_{i+1})/(2T_a)$ in a log-linear plot.

air pocket behaves according to such a system, then the peaks would follow the formula $P_i = Ce^{-\alpha t_i/T_a}$. Here the damping ratio is $\xi = \alpha/(2\pi)$ and the parameter C is dependent of the initial conditions. The damping ratio can then be estimated from the pressure time history when the pressure amplitude is plotted on a log-linear plot. This is done in the right column of plots in figures 2.11 and 2.12. These plots show the average amplitude $P_{i+1/2} = (P_i + P_{i+1})/2$ made non-dimensional with respect to the first pressure amplitude P_1 as a function of time $t_{i+1/2} = (t_i + t_{i+1})/2$ made non-dimensional with respect to the average period T_a of the whole impact. The reason for using the average pressure amplitude $P_{i+1/2}$ is that the pressure oscillations does not accurately oscillate around zero. The damping ratio can be found by noting that $-\alpha$ is the slope of the straight line fitted to the peak values in the log-linear plot. The damping ratio only makes sense to the extent that the pressure time history really behaves comparable to the free decay of a linear mass-spring system with small linear damping relative to the critical damping. In this case the pressure amplitudes should form a straight line in the logarithmic plot. Air pocket 1 is the smallest air pocket studied and is the one which is closest to fulfilling this criteria. In the upper right plot of figure 2.11 the exponential function is fitted to the first and fifth pressure peak and shows to what extent the solution of the free oscillations of a linear under-damped mass-spring system really fits the experimental results for air pocket 1. The period of the pressure time history
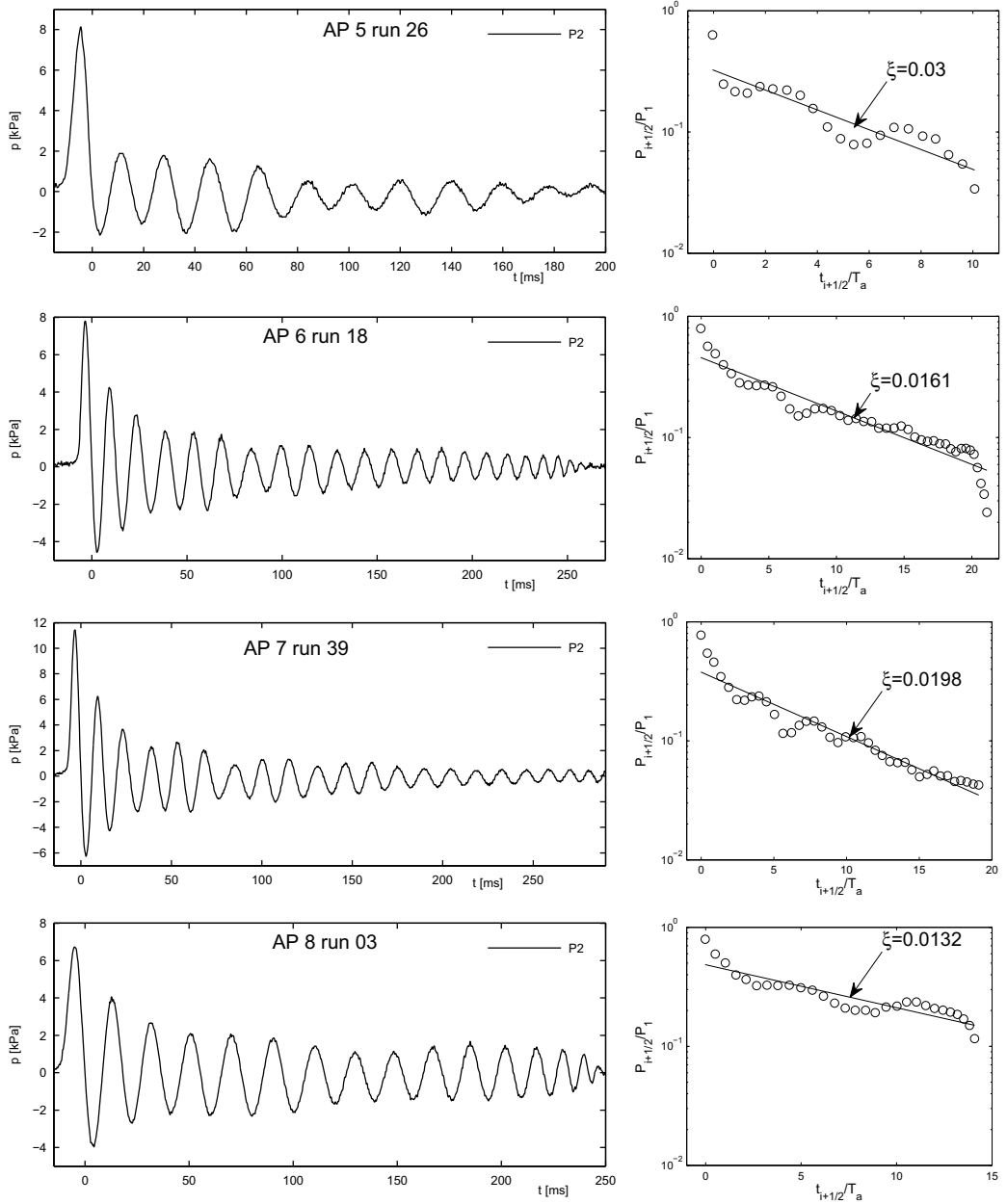
Figure 2.12: *Left:* Pressure time histories for air pocket 5, 6, 7 and 8. *Right:* The average relative amplitude $P_{i+1/2}/P_1 = (P_i + P_{i+1})/(2P_1)$ plotted as a function of the $t_{i+1/2}/T_a = (t_i + t_{i+1})/(2T_a)$ in a log-linear plot.
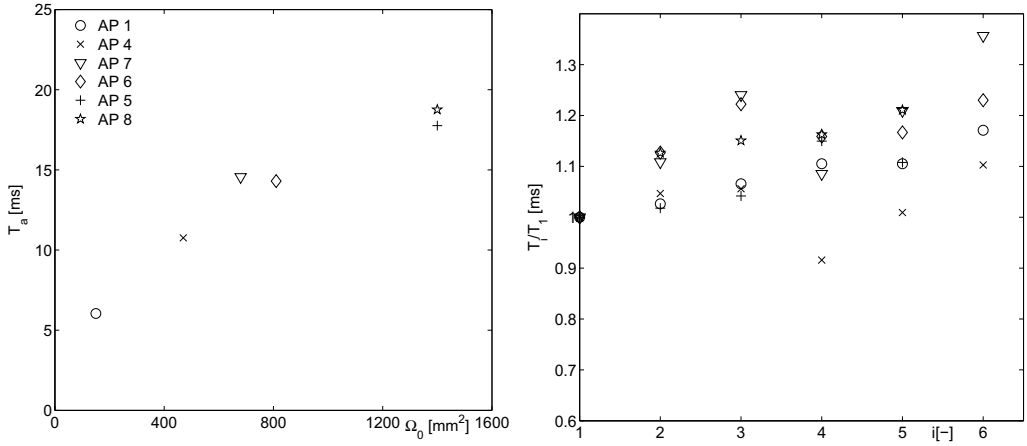
Figure 2.13: *Left:* Average period T_a of the first five pressure oscillations for all the air pockets as a function of initial air pocket volume Ω_0. *Right:* The variability of the period for the first 6 pressure oscillations.

was also investigated. The period of the signal T_i is defined as $T_i = t_{i+1} - t_i$. Here the time of the pressure peak i is denoted t_i. In this way the average of the five first periods is equal to $T_a = \frac{1}{5}\sum_{i=1}^{5} T_i$. This average period for all the air pockets is seen on the left plot of figure 2.13. It is seen that the average period of the oscillations increase with the initial volume of the air pocket. In the right plot in the same figure T_i is plotted as a function of the period number i. The period is generally seen to increase with time although a large scatter is observed.

2.4   The air pocket impact divided in stages

In the following the air pocket experiment is divided in stages based on the physics observed. The air pocket number 6 (AP6) is most repeatable and is therefore a good choice for comparison with mathematical models. Based on this, the following discussion mainly follows air pocket 6 through the different stages, while the other air pockets are commented if physical effects are observed which are not observed for air pocket 6. The first stage is called the sloshing stage. It is characterized by the build up of the different sloshing modes. In this stage the gas flow does not affect the liquid flow. Air escapes the air pocket region at increasing speed as the wave approaches the roof. This stage is therefore called the air escape stage. When the wave crest touches the roof, the gas flow is cut off, and the air inside the pocket is compressed and starts to oscillate. This stage is hence denoted the air pocket oscillation stage.
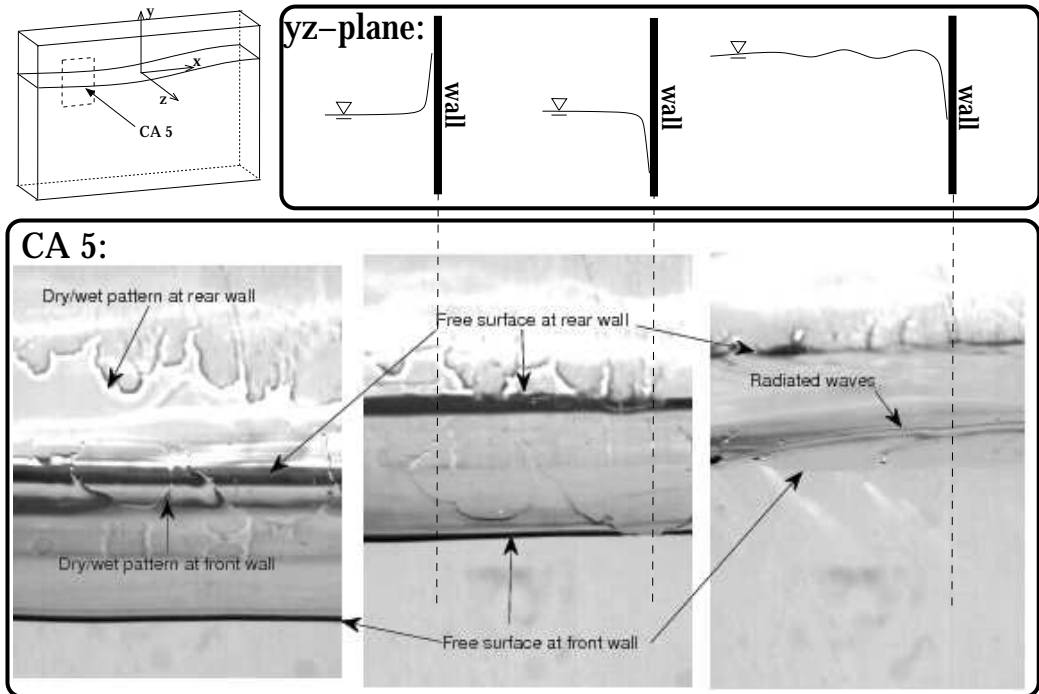
Figure 2.14: 3D capillary waves are triggered when the free surface crosses the random pattern which indicates the dry/wet intersection on the walls.

2.4.1   The sloshing stage

Pictures of air pocket 6 from the sloshing stage are seen in image 1-4 in figure 2.6. The wave seen in these images is subjected to some damping. One source of damping is viscous boundary layers. Keulegan [17] used linear potential flow theory to describe the wave motion outside the thin boundary layers while linear laminar viscous boundary layer theory was used close to the tank walls. By assuming that the damping was small, he found an analytical expression for the damping ratio of the first mode of sloshing. The damping ratio due to boundary layers is dependent on which natural mode which is considered. Here decay tests of the first natural sloshing mode is investigated. For the first mode, the "bulk" damping, that is the viscous energy dissipation outside the boundary layers, does not contribute significantly. However, it is of importance for higher modes.

Keulegan [17] also investigated experimentally the damping of the sloshing motion inside tanks made of both acrylic and glass. Inside the acrylic tank he observed that the free surface contained ripples generated by meniscus effects, these ripples was not seen inside a similar sized glass tank. The ripples in the acrylic tank was suggested to be generated because the water does not wet the acrylic tank material while it wets the glass material. More important the damping of the wave motions was seen to be bigger for the acrylic tank than the glass

tank. It should be noted that the damping of the wave in the glass tank corresponded well with the results from the mathematical model based on linear laminar boundary layers. Keulegan later added aerosol to the water in the acrylic tank to make the water wet the walls. Then the ripples was no longer generated and the acrylic tank showed the same level of damping as the glass tank. Keulegan then concluded that the larger damping experienced in the acrylic tank than the glass tank was due to ripples generated by meniscus effects. A mathematical model of the damping due to meniscus effects does to the author's knowledge not exist and the link between the ripples generated by meniscus effects and damping is solely based on Keulegan's observations. In the following pictures of the meniscus effect generating ripples in the present experiments are presented.
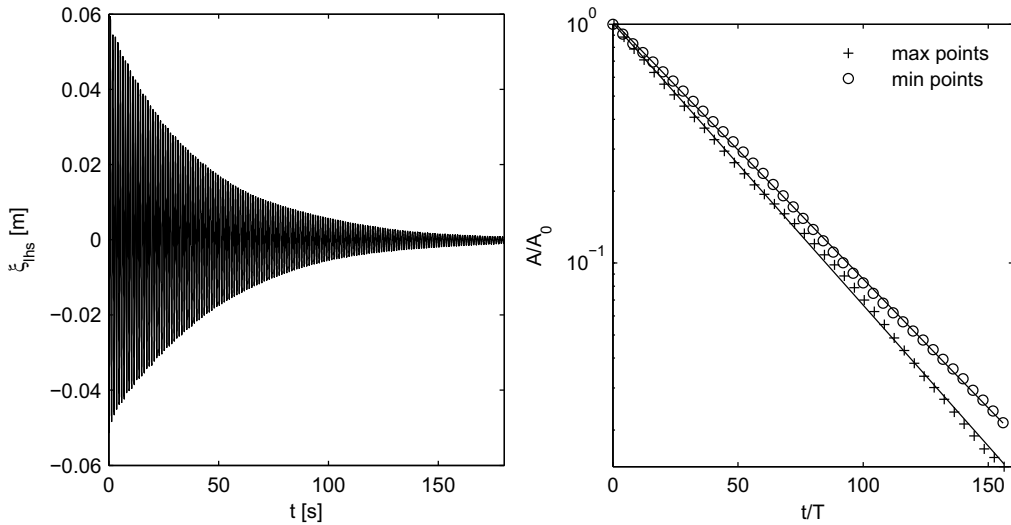

Figure 2.15: Decay test results for a standing wave in the tank. *Left:* Time history of the wave elevation on the left hand side of the tank. *Right:* Log-linear plot of the wave elevation amplitudes on the left hand side of the tank.

The meniscus effects generating ripples are connected to how the water wets the acrylic tank material. This is shown in the images in figure 2.14. These images are taken from camera angle 5 (CA 5), indicated in the upper left drawing in the figure. Above the images, qualitative drawings are made of the free surface close to the front wall of the tank in the $y - z$-plane. These drawings are taken from different cross sections indicated by the three dotted vertical lines in the images. At the left image the lines indicating the intersection between the free surface and the front and rear wall are indicated. Also the image shows the dry/wet pattern on the front and rear wall. These patterns were left on the wall as the wave moved down since the water wetting the walls does not fall down as fast as the wave moves down. The image sequence shows the free surface as it moves up, and crosses this dry/wet pattern. In the middle image two dotted lines are shown where two $y - z$-plane

drawings show the free surface close to the wall. At the right dotted line the free surface has crossed the dry/wet pattern while at the left it has not. In the area where the free surface has not crossed the dry/wet pattern the free surface bends upwards as indicated in the left $y - z$-plane drawing. As the free surface crosses the dry wet pattern the free surface flips downwards as indicated in the centre drawing of the $y - z$-plane. This causes the free surface to be almost invisible in the present experiments. At the right image the free surface has crossed the dry/wet pattern for the whole length of the pictured area, and three-dimensional surface tension waves are seen to travel generally in the z-direction, towards the centre of the tank.

Decay tests for the first natural sloshing mode were carried out to quantify the damping. The decay of the wave elevation at $x = -L/2$ denoted $\zeta_{\text{lhs}}(t)$, can be seen in the left plot in figure 2.15. The amplitudes of the elevation, denoted A, is plotted non-dimensionally in the logarithmic plot seen on the right hand side in figure 2.15. Assuming that the amplitudes follow the motion of a linear under-damped mass-spring system, then $A/A_0 = e^{-\alpha t/T_{ns}}$. Here α is denoted the modulus of decay and T_{ns} is the natural period of the first natural mode of sloshing. This means that the amplitudes should form a straight line in the logarithmic plot. The peaks and minima are plotted separately. Linear polynomials were fitted to the peaks and minima and they suggest a modulus of decay of $\alpha = 0.0272$ and $\alpha = 0.0249$, respectively. The corresponding damping ratio ξ of the first mode of sloshing is given as $\xi = \alpha/(2\pi)$. Keulegan [17] derived an analytical formulae for the modulus of decay due to linear laminar boundary layers. Inserting the dynamic viscosity $\nu = 1.01 \cdot 10^{-6} [\text{m}^2/\text{s}]$ this formula returns $\alpha = 0.0209$. In the numerical model of the sloshing and air-escape stages presented in chapter 3, the modulus of decay of the first mode of sloshing is used as input. The average of the estimates of α from the peaks and minima in the experiments is then used, that is $\alpha = 0.0261$.

2.4.2 The air escape stage

During the different runs the air pocket was filmed from different angles using one high speed camera. The images from the different camera angles are taken at slightly different times. Figure 2.16 shows images for air pocket 6 from the camera angles 1, 2 and 3 as illustrated in the upper left corner of the figure. These images originate from three separate runs. The pressure time histories from pressure sensor P2 of the three runs are plotted in the lower right corner of the figure. The location of pressure sensor P2 is shown in figure 2.3. The vertical bars in the pressure plot indicate the time instants when the different pictures were taken. In image number 1, FSF indicates the line where the free surface intersects the front wall. Similarly FSR indicates the line where the free surface intersects the rear wall. The first set of images of air pocket 6 shown in figure 2.16 are taken before the wave touches the roof. From the pressure measurements it is seen that the dynamic pressure inside the air pocket is nearly zero. In image 3 the air pocket is seen from the side. The continuous bright area is the opening where air escapes the air pocket. The variation of the thickness of the opening is due to a nearly symmetric capillary wave. This wave is seen to have wave length approximately equal to half the width of the tank, and amplitude of about $1-2[\text{mm}]$.
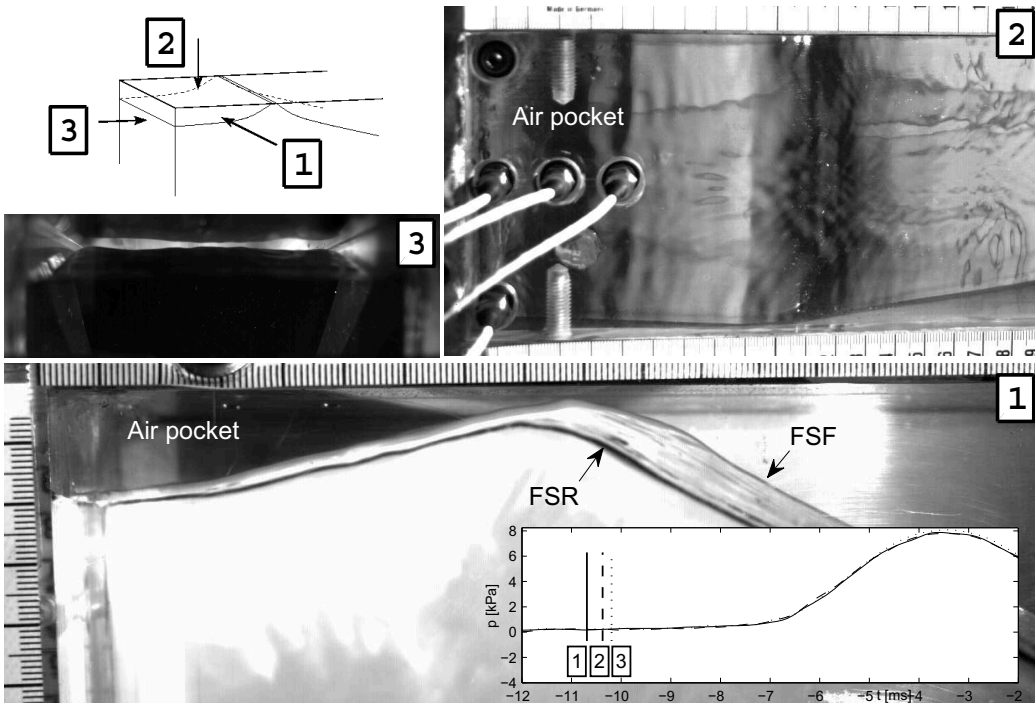
Figure 2.16:   Image sequence before the time instant when the water first touches the roof for air pocket 6. The images are taken during three different runs. Image 1, 2 and 3 are taken from camera angle 1, 2 and 3. FSF and FSR denote the intersection between free surface and the front and rear wall respectively.

From image 2 these waves are seen from the top. They are seen to be generally 3D. These waves cause the air pocket not to close instantly across the width of the tank. This leads to a period of time when the air pocket is partially open and closed along the width of the tank. The mechanism triggering this wave was explained in connection with the sloshing stage in section 2.4.1.

   The images of air pocket 6 in the figure 2.17 and 2.18 are taken during the time when the wave touches the roof for the first time. From the front view images in these two figures, the wave is seen to be more and more sharpened at the wave crest. The reason for this is believed to be that the rapidly escaping air starts to affect the liquid flow. The escaping air is modelled in section 3.6 assuming that the water is rigid and approaching the roof at constant speed. The results show that there is a negative dynamic pressure at the wave crest. This is believed to cause the sharpening of the wave crest seen in figure 2.18. At the sharpened wave crest the curvature of the free surface is large, this indicates surface tension effects. This suggests that a coupled gas/liquid model should be used to capture this effect. From the side view (image 3) in figure 2.17 the wave just touches the roof in the middle of the tank
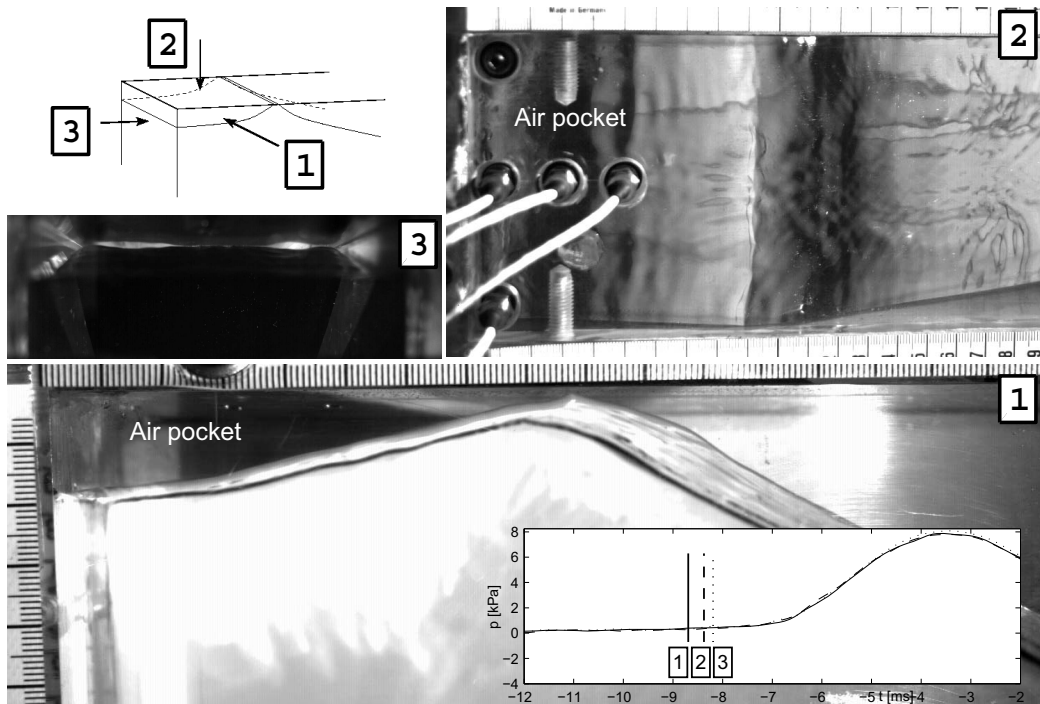
Figure 2.17: Image sequence towards the time instant when the water first touches the roof for air pocket 6. The first touch time instant is approximately the time instant of image nr. 3.

(around $z = 0$). This is the first touch time instant and the time is approximately equal to $t = -8.2$[ms]. In figure 2.18 the air pocket 6 is shown during the time when the air pocket is partly closed and partly open across the width of the tank. In image 2 the wet area of the roof is indicated. Air is seen to escape close to the $x - y$ parallel walls.

The images in figure 2.19 show the air pocket towards closure. In image 2 the tank roof is seen to be nearly continuously wetted across the thickness of the tank. The time of closure is defined as the time instant when the full width of the tank roof is continuously wetted. The time of closure for air pocket 6 is estimated to be around the time instant of image 3, that is $t = -6.2$[ms]. Air pocket 6 is seen to close just after the first contact with the roof. This is not a general result applicable to all the other air pockets. From figure 2.8 it is seen that the air pockets 5 and 8 close at a later time, just after the dynamic pressure is zero between the first pressure peak and the first pressure minimum. The three-dimensional leakage of air pocket 5 can be seen in figure 2.20. In image 1 of this figure two symmetrical wetted areas of the roof are seen. These areas expand throughout the time series, but air continues to leak out of the air pocket until image 7, where the roof is wetted continuously across the whole width of the tank. This air leakage is believed to affect the strong decay of the air pocket oscillation experienced for these two pockets during the time from the first
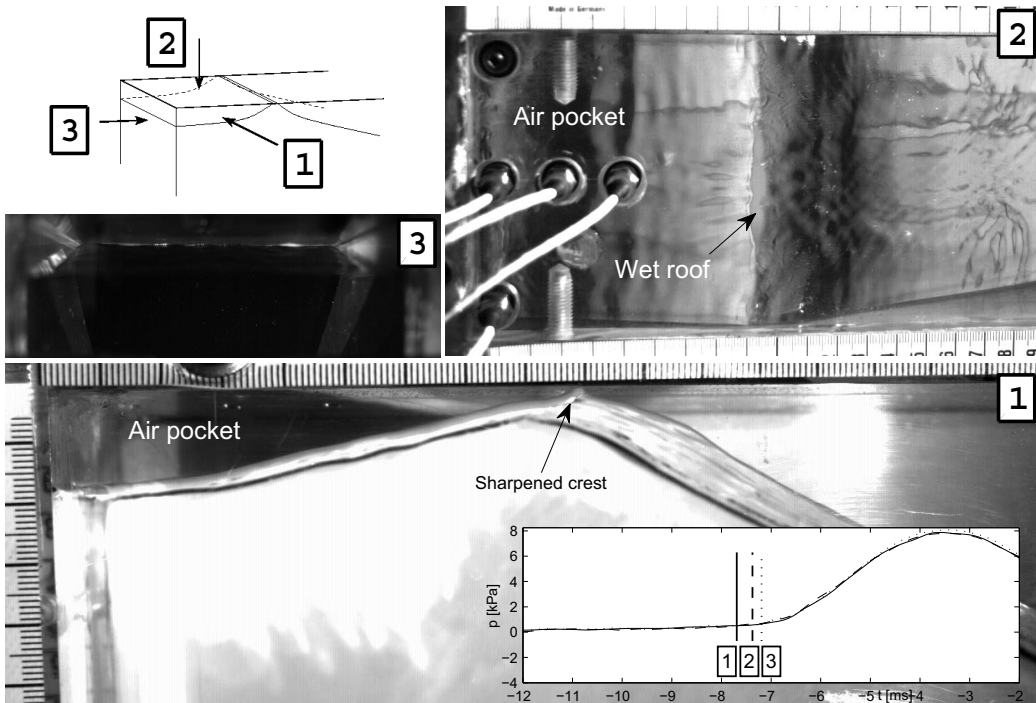
Figure 2.18:   Image sequence during the time when the air pocket 6 is partially closed. In image 2 the air can still exit the air pocket close to the walls.

pressure maximum to the first pressure minimum which was commented in connection with figure 2.10.

To investigate the role of air leakage on the pressure oscillations, air pocket 6 and 7 was punctured by opening a hole in the roof. Practically this was done by drilling holes in screws which were mounted in the hole in the roof of the tank seen in figure 2.2. The diameter of the hole d was varied as $d = 0, 1, 2$ and 4[mm]. The results for the air pocket 6 and 7 can be seen in figure 2.21. Here the zero diameter results are the mean of 13 runs, that is the same curve as in figure 2.8. The curves for $d > 0$ are the average pressure time history of three runs at each diameter. As seen from the figure, the effect of leakage is decay of the pressure peaks. This suggests that the leakage observed for air pocket 5 reduces the amplitude of the first pressure peak and the first pressure minimum.

From the presented images of air pocket 5 and 6 it is seen that the air pocket does not close instantaneously across the thickness of the tank. This means that the variation of the water and air flow in the z-direction is significant during this time period. The goal of the experiment was to produce 2D flow conditions to ease the mathematical modelling. It is seen that the time period of this 3D closure is about 2[ms] which is significant compared to the rise time of the pressure signal. Also the pressure inside the air pocket during closure changes
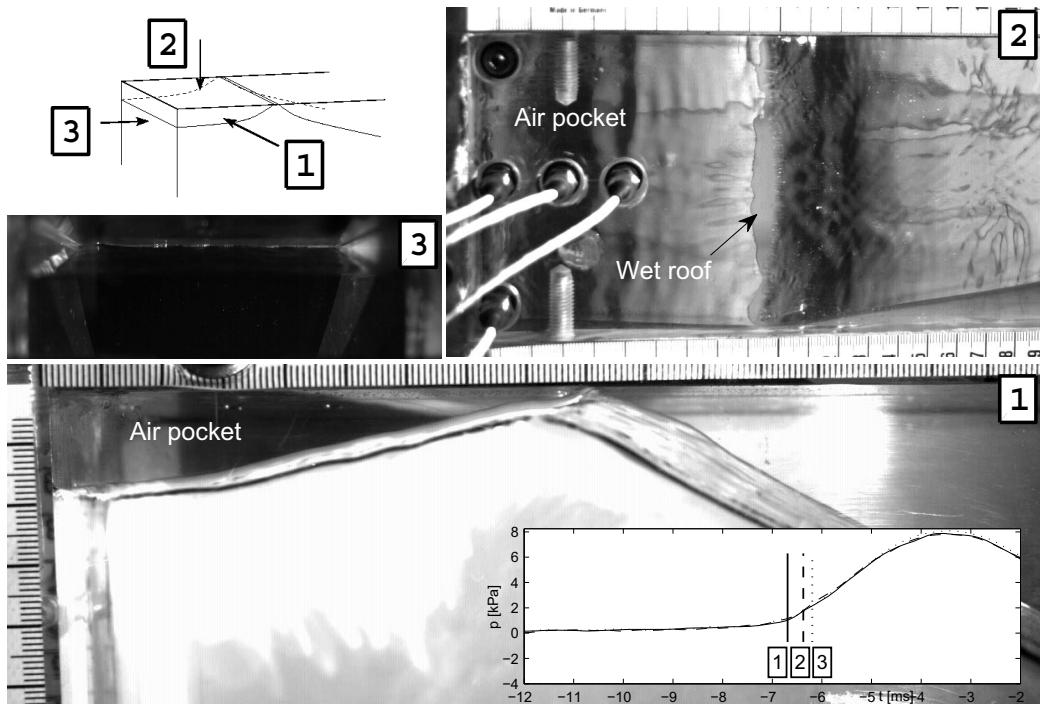
Figure 2.19: Image sequence of air pocket 6 towards the fully closed air pocket. The time of closure is approximately at the time of image nr. 3.

with 2[kPa] which is significant compared to the pressure amplitude which is 8[kPa]. Hence, this 3D closure, induced by the capillary waves and the escaping air, is believed to affect the later pressure oscillations. Since the effect of adding a hole in the air pocket caused damping, it is believed that the leakage due to 3D effects reduces the peak pressure P_1, compared to the ideal case when the air pocket closes instantly across the full width of the tank. The fact that leakage of air through holes causes damping of the air pocket oscillations will be illustrated by a mathematical model in chapter 5.

2.4.3 The air pocket oscillation stage

When the leakage area is reduced, the air cannot easily escape any more and the pressure inside the air pocket starts to increase until it reaches a peak value and starts to oscillate. This stage is called the air pocket oscillation stage. Images from the first part of this stage for air pocket 6 can be seen in figure 2.22. For air pocket 6 the free surface geometry near the wave crest was nearly symmetrical in the x-y plane before the wave touched the roof (see image 1 in figure 2.17). As the wave approached the roof the free surface was sharpened at the wave crest. Later this peak moved up towards the roof during the closure, but also moved to the right, that is in the direction of the escaping gas flow. In the middle of the
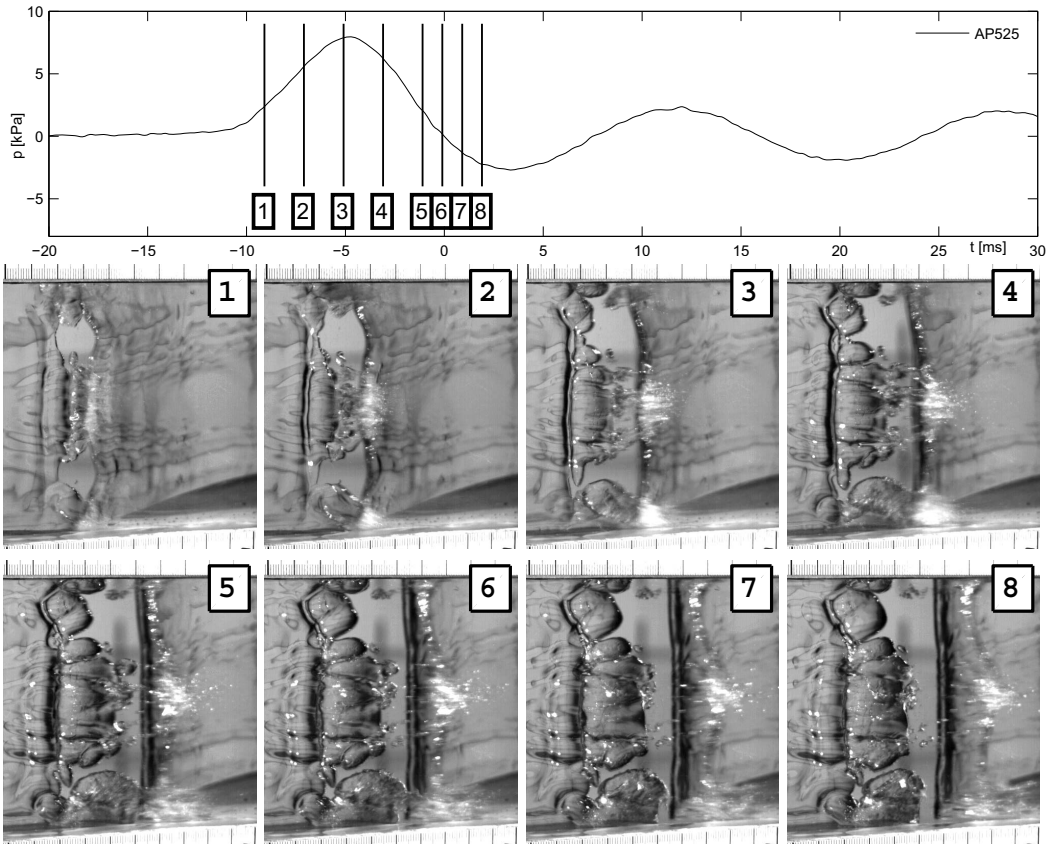
Figure 2.20: Closure of air pocket 5. *Top:* The pressure time history. *Bottom:* Images showing the 3D closure where the roof is partially wetted across the thickness of the tank.

right image 2 of figure 2.22 the wave crest has wetted the roof nearly continuously across the width of the tank. The geometry of the wetted area changes rapidly during the initial stage of the air pocket oscillation stage. From the right image column, the wetted length of the roof is increasing during this period.

In the figures 2.23 and 2.24 more images taken during the air pocket oscillation stage of air pocket 6 are seen. The images are taken close to the time of maximum and minimum pressure. From the right images the wetted length of the roof is seen to increase while moving leftwards throughout the image sequence. There is no signs of an inward water jet during the initial compression of the air pocket and until image 2 for the pressure oscillation stage while there is a right going jet, during this time period. However, the right image of time instant 3 shows a thin spray of water into the air pocket. This indicates that there is a jet towards the air pocket at this time instant. This jet is believed to be connected to the negative dynamic pressure inside the air pocket preceding this time instant. In the right image corresponding
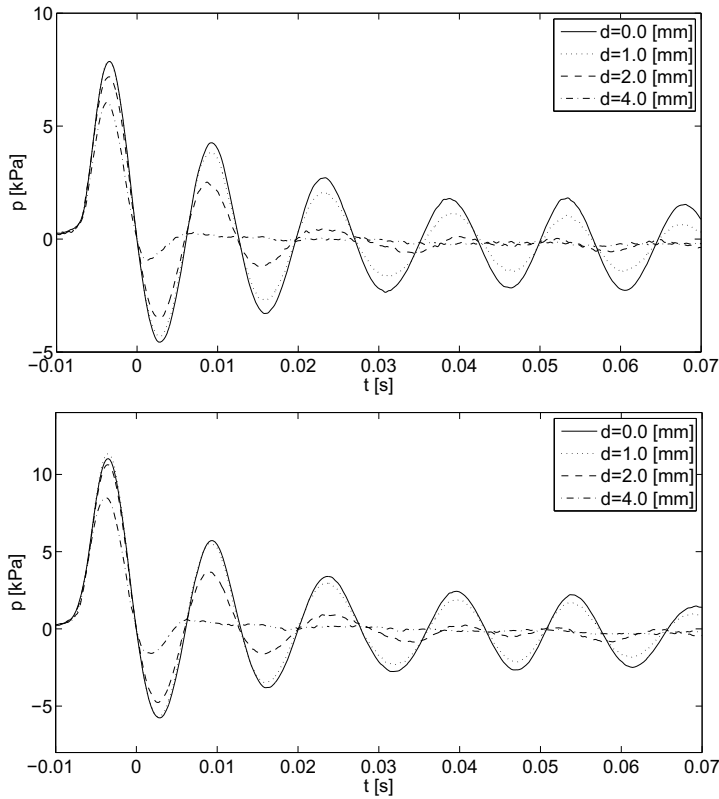
Figure 2.21: The pressure inside the air pocket for pressure sensor P2. Top: The effect of different holes for air pocket 6. Bottom: The effect of different holes for air pocket 7.

to the time instants 4, 5 and 6, a shadow shaped as a vertical bar is seen to the right of the wetted section. This shadow bar spans the whole width of the tank and is moving to the right. This shadow is a pulse of water coming out with the jet in the left image corresponding to time instant 4. This pulse of water is believed to be thrown out of the jet as a consequence of the pressure maximum preceeding this time instant, that is the time instant of image 3. In the same way a similar pulse is released in the jet at time instant 6 and is seen to travel to the right in the same way as the previous pulse. A view of the pulses released in the jet from camera angle 1 can be seen in figure 2.25.

At the end of the image sequence in figure 2.24, the right intersection line between the free surface and wetted area of the roof starts to reduce. This indicates that the velocity of the entering water has changed direction. This can be used to define the time instant when the air pocket goes from water entry to water exit. Water entry and exit is hence defined to be the time period of increase and decrease of the wetted tank roof surface, respectively. Images taken during the water exit stage is shown in figure 2.26 and 2.27. During the water

exit stage the right going jet stops and the wetted length of the roof is reduced. The right intersection line between the water and air on the roof forms a characteristic pattern. The flow is seen to be three-dimensional during water exit.

In appendix A an investigation of the possible fluid-structure interaction effect between the air pocket impact and the deflection of the roof is made. The measured response of the roof is seen to be too small to cause any important fluid-structure interaction effects.

2.5   Experimental findings

- A procedure for creating air pocket slamming events in the upper corner of a rectangular tank was derived using linear multimodal theory. The pressure time history from the experimental impacts show varying degree of repeatability. Air pocket 6 is seen to have good repeatability and is hence most appropriate for comparison with mathematical models. Some types of air pockets close just after the first contact with the roof, like air pocket 1 and 6, while other types of air pockets close at the time instant of maximum pressure, like air pocket 4, or just after the first zero down crossing, like air pocket 5 and air pocket 8. For these two air pockets the leakage took place through the wetted section of the roof. This means that the tank roof was not continously wet accross the thickness (z-direction). For all the air pockets interaction between the escaping air and the water was observed. For air pocket 6 this was seen as a sharpened wave crest just prior to closure of the air pocket. The closure of the air pocket 6 was also seen not to be instantanous across the thickness z-direction of the tank.

- All the investigated air pockets show large decay during the time from the first pressure maximum to the first pressure minimum. This is referred to as the initial decay. After the first period of oscillation the amplitude of the pressure time history behaves in a less uniform fashion, however a general decay trend is observed. This decay trend is to a varying degree exponential. The decay trend after the first period of oscillation is later referred to as the later decay.

- A separate set of experiments was carried out to investigate the role of air leakage into or out from the air pocket during the air pocket oscillation stage. This was done by varying the diameter of a circular hole in the tank roof. Air pocket 6 and 7 were used, which was seen to close before the first pressure peak. This means that air was only leaking through the hole in the roof during the air pocket oscillation stage. The air pocket oscillations show larger decay if air is allowed to leak into or out from the air pocket during the air pocket oscillations than if such leakage does not exist.

- Air leakage cannot explain the initial and later decay of the air pockets oscillations of air pocket 1, 5 and 6 because they are closed before the first pressure maximum. These air pockets show a large initial decay relative to the later decay. However, air leakage can explain the larger initial decay experienced for air pocket 5 and 8 compared to the closed air pockets 1, 5 and 6. This because air pocket 5 and 8 show air leakage almost until the first pressure minimum.
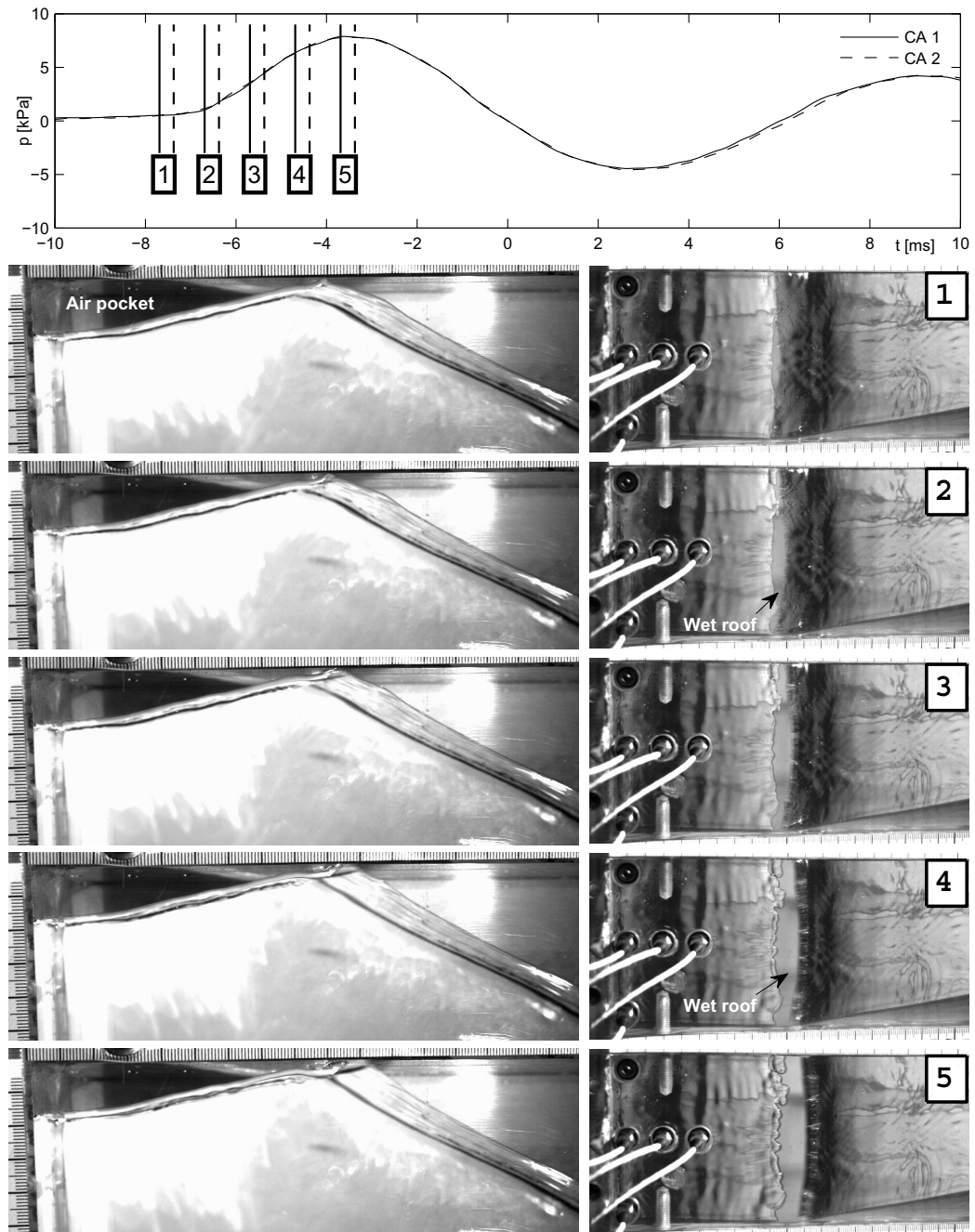
Figure 2.22: Image sequence during the initial compression of air pocket 6. The left column of images are pictures taken from the front of the air pocket (CA 1), while the right column are taken from above (CA 2).
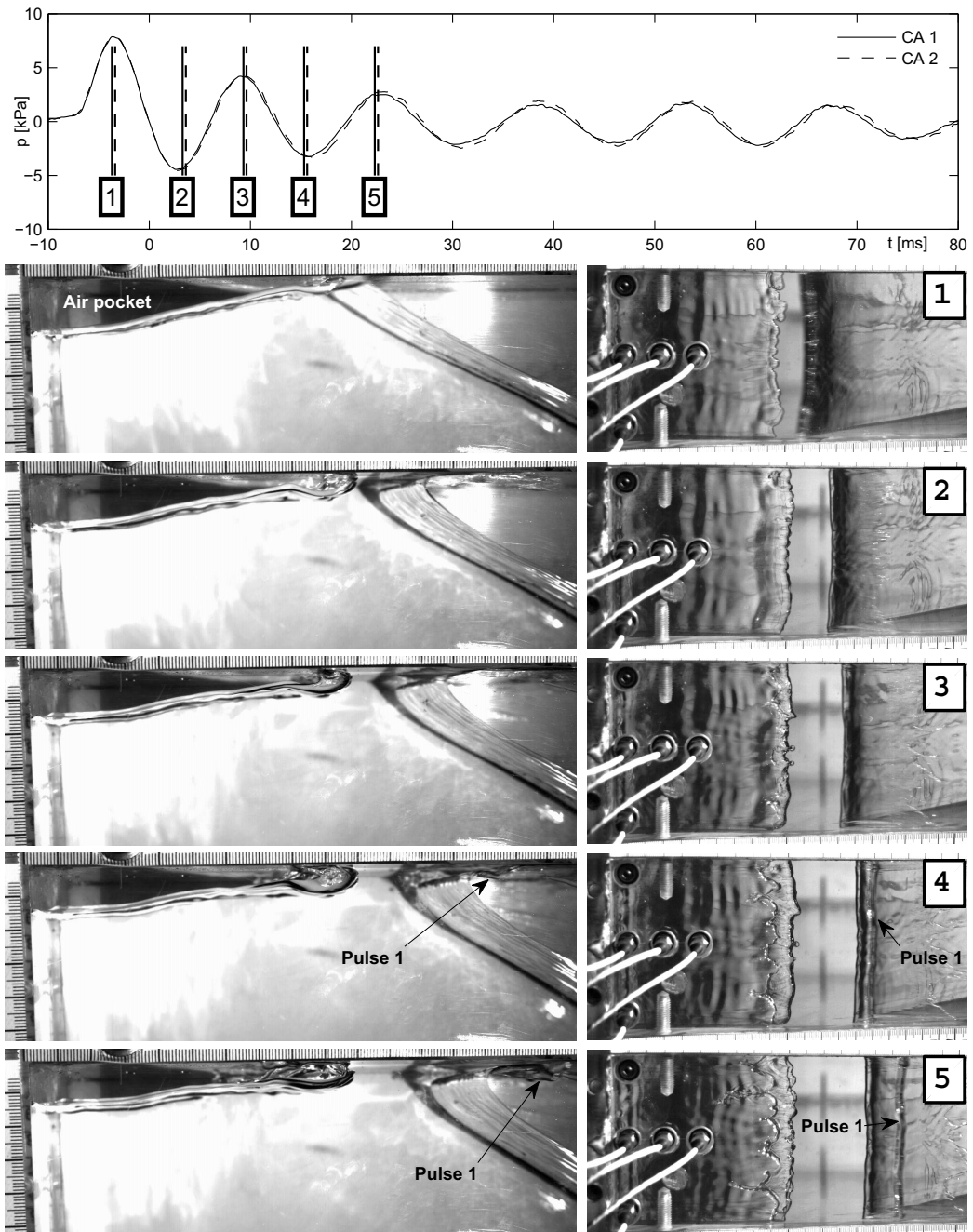
Figure 2.23: Images taken during the air pocket oscillation stage of air pocket 6. The left column of images are taken from the front of the air pocket (CA 1), while the right column are taken from above (CA 2).
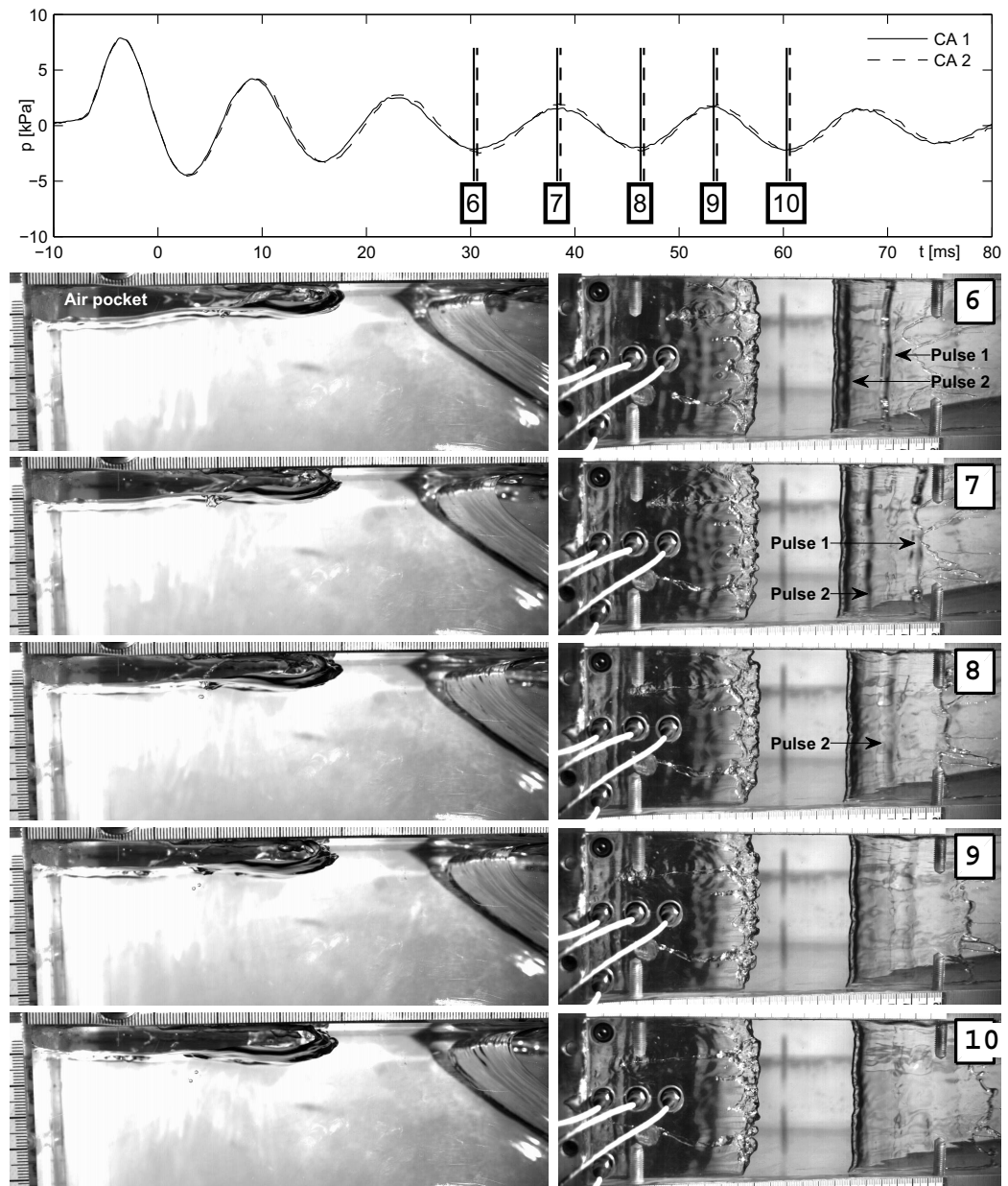
Figure 2.24: More images taken during the air pocket oscillation stage of air pocket 6. The left column of images are taken from the front of the air pocket (CA 1), while the right column are taken from above (CA 2).
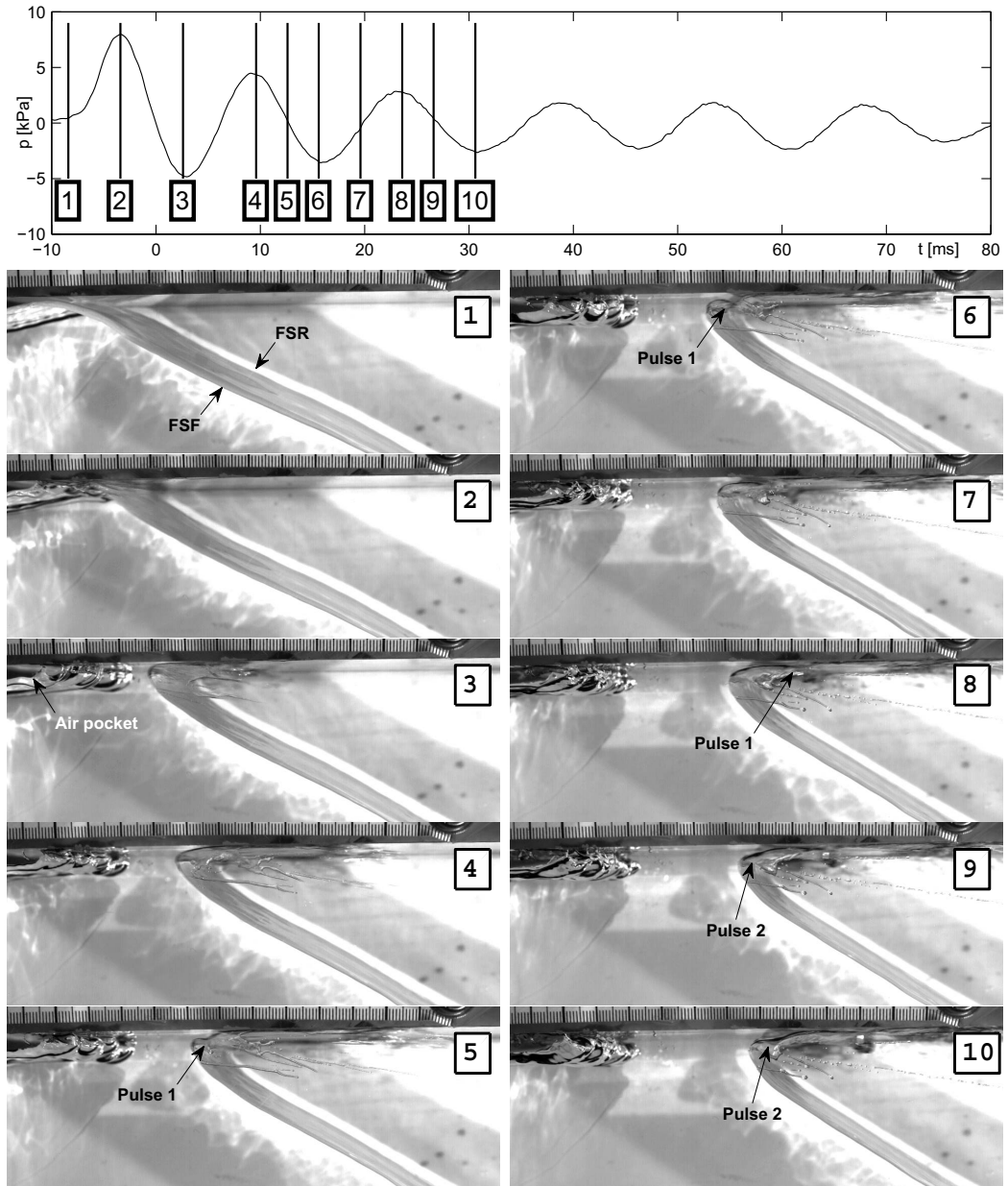
Figure 2.25: Images taken of the jet during the air pocket oscillation stage of air pocket 6. The images show the right going jet. The images are taken from the front of the air pocket (CA 1)

Figure 2.26: Images taken during water exit of the air pocket oscillation stage of air pocket 6. The left column of images are taken from the front of the air pocket (CA 1), while the right column are taken from above (CA 2).

Figure 2.27: Images taken during water exit of the air pocket oscillation stage of air pocket 6. The left column of images are taken from the front of the air pocket (CA 1), while the right column are taken from above (CA 2).

Chapter 3
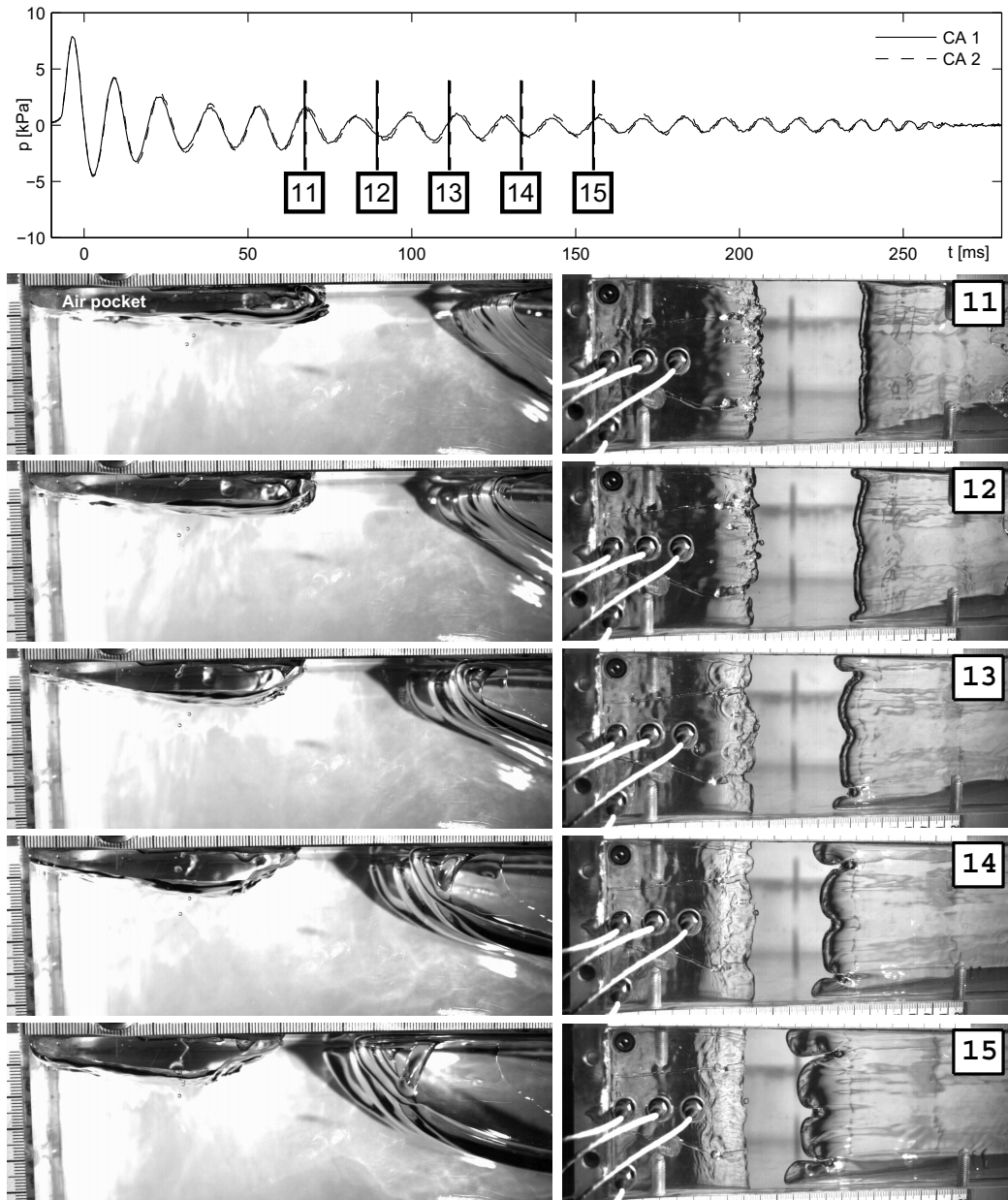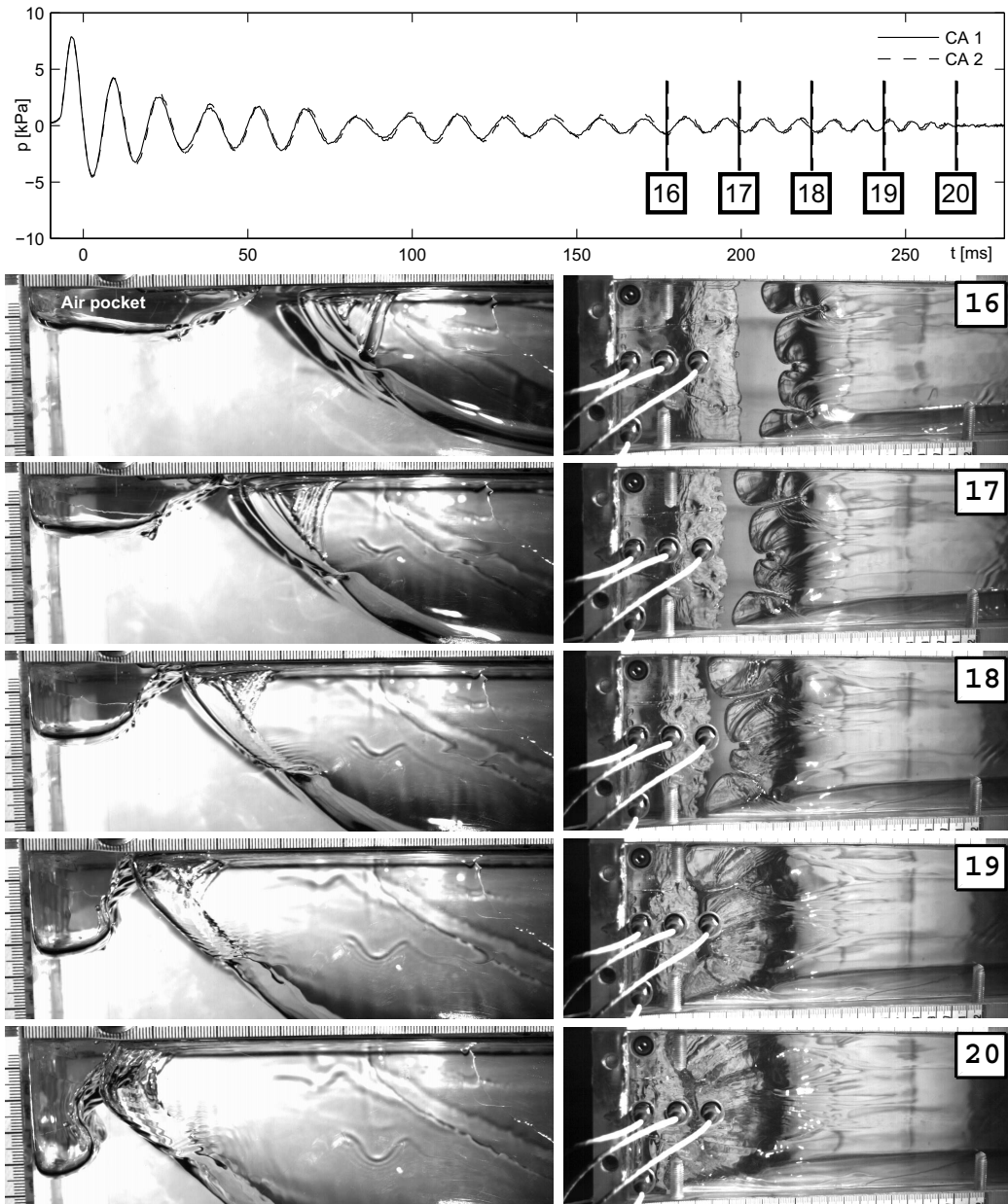
Numerical model of the sloshing and air-escape stages

In the previous chapter a subdivision of the air pocket impact event was made into a sloshing stage, an air-escape stage and an air pocket oscillation stage. In the sloshing stage the amplitude of the different modes are build up to create the air pocket impact. As the wave approaches the roof, air escapes the air pocket area at increasing speed. Hence, this stage is denoted the air-escape stage. Here a mathematical problem of the sloshing and air-escape stages is proposed and then a new numerical procedure is used to solve it. The new numerical method is denoted the boundary-element-finite-difference method. After this the new numerical procedure is compared with different types of test cases. The first being a linear standing wave inside a tank where an analytical solution exists. Then the method is compared with the single-dominant nonlinear multimodal method by Faltinsen and Timokha [8]. This to see the accuracy of the method in the nonlinear case. Finally a comparison with experiments is made for the same case.

3.1   Physical assumptions in the sloshing stage

In this section relevant physical assumptions for the sloshing stage is made based on the experiments presented in chapter 2. These assumptions are summarized in figure 3.1. The water is assumed incompressible as well as irrotational and inviscid, hence potential flow theory is valid. In the experiments damping of the sloshing waves was observed. This damping was due to viscous boundary layers and meniscus effects. The damping due to meniscus was seen to be of importance. Since the author is not aware of any mathematical model for this effect, a simplified approach is taken. In the present work the damping effect of viscosity and meniscus is included in the same way as Faltinsen [18] did. This is done by adding a Rayleigh damping term to the dynamic free surface condition and yields one parameter which can be fitted to an experimental decay test involving the lowest sloshing mode. The fact that the damping is sloshing mode dependent cannot be modelled by the described numerical procedure.

The meniscus effect was also seen to introduce three-dimensional effects in the experi-
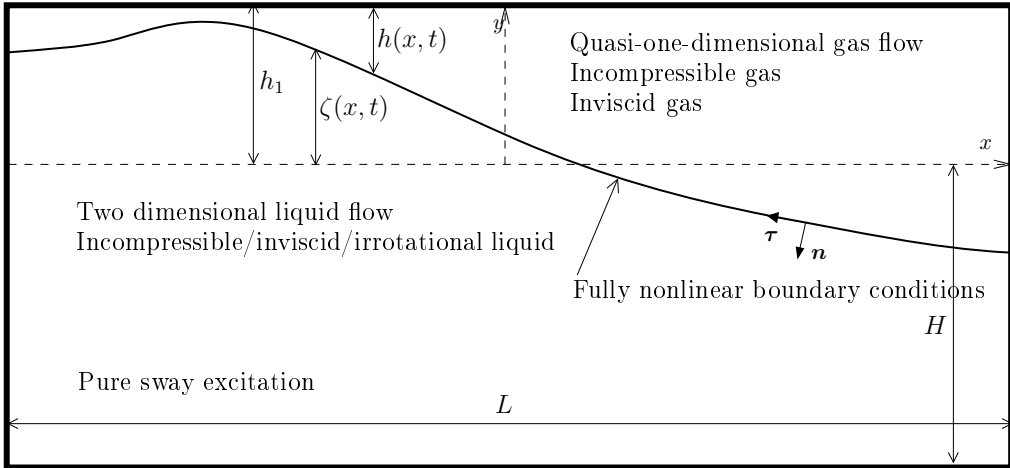
Figure 3.1:   The assumptions used for the boundary-element-finite-difference method which is used to model the sloshing and the air-escape stages. In addition, the definition of the wave elevation $\zeta(x,t)$ the cross sectional dimension of the air flow $h(x,t)$ and the distance from the mean free surface to the roof h_1 is defined.

ments. These effects are neglected and the numerical method is hence derived in two dimensions. In addition fully nonlinear boundary conditions will be used on the free surface. The free surface is assumed to be a single-valued function of the horizontal coordinate x and is identified by the elevation of the free surface $\zeta(x,t)$.

In the sloshing stage the air is not assumed to affect the water flow. However, as the wave approaches the roof, air escapes the region where impact is going to occur at increasing speed. The experiments show that the air starts to interact with the water when the minimum gap $h_{\min}$, defined as the vertical distance between the maximum wave elevation $\zeta_{\max}$ and the roof, is less than $3-4$[mm]. In comparison the maximum thickness of the air pocket is 18 [mm], while the initial length of the air pocket is 89 [mm]. The air flow is assumed to be mainly horizontal and can hence be modelled as quasi-one-dimensional. Quasi-one-dimensional means that the cross section of the air domain $h(x,t)$ in figure 3.1 is assumed to have small variation in the x-direction, and hence that the y-component of the velocity can be neglected. This assumption also means that the air velocity is constant over the cross section. Hence viscous and turbulent flow effects which generally produce variation of velocity over the cross section are neglected. The density of the air is assumed constant which means that the air flow in the sloshing stage is assumed incompressible. This means that compressible effects like shock and acoustic waves are not modelled. As the wave crest is $3-4$[mm] from the roof, the air speed increases rapidly and compressible effects might be of importance. This effect of compressibility is neglected in this section but is investigated further in section 3.6.

3.2 A mathematical problem for the sloshing stage

Based on the physical assumptions discussed in the previous section the mathematical boundary value problem in figure 3.2 is established. Here the derivation of the equations in this figure is presented in detail.

Figure 3.2: The mathematical problem for the boundary-element-finite-difference method (BEFDM) used to model the sloshing and the air-escape stages of air pocket 6.

3.2.1 The boundary integral equation for the water

The velocity in an irrotational flow can be written as the gradient of the potential function ϕ, that is $\boldsymbol{u} = \nabla\phi$. Mass conservation of an incompressible fluid then leads to Laplace equation, which can be solved by a distribution of sources, sinks and normal dipoles along the boundary of a closed domain. Then Laplace equation is not solved directly, but through a boundary integral equation which is given as:

$$\theta(\boldsymbol{x})\phi(\boldsymbol{x}) = \int_s \phi(\boldsymbol{\xi})\frac{\partial \log(r(\boldsymbol{\xi},\boldsymbol{x}))}{\partial n(\boldsymbol{\xi})} - \frac{\partial \phi(\boldsymbol{\xi})}{\partial n(\boldsymbol{\xi})}\log(r(\boldsymbol{\xi},\boldsymbol{x}))ds(\boldsymbol{\xi}). \qquad (3.1)$$

Here $\theta = -2\pi$ if the point $\boldsymbol{x}$ is in the interior of the domain. However, if the point $\boldsymbol{x}$ is on the boundary then θ is equal to the negative of the internal angle. $\boldsymbol{n}$ is the normal vector pointing into the water domain and $\boldsymbol{\tau}$ is the tangential vector pointing in the counterclockwise direction along the water boundary. s denotes the arc length coordinate which is increasing in the counter clockwise direction around the domain. Further, r is the distance between the field point $\boldsymbol{x} = (x, y)$ and the integration point $\boldsymbol{\xi} = (\xi, \eta)$. That is

$$r = \sqrt{(x-\xi)^2 + (y-\eta)^2}. \qquad (3.2)$$

Equation (3.1) ensures mass conservation in the water and is later solved numerically using the boundary element method (BEM).

3.2.2 The free surface conditions

The boundary conditions on the free surface listed in figure 3.2 is derived next. Since no overturning waves occur during the sloshing stage, the free surface can be represented by a single-valued function $\zeta(x,t)$. The kinematic free surface condition is seen as equation (3.4) in figure 3.2. This is obtained by noting that

$$\frac{D(\zeta - y)}{Dt} = \frac{\partial \zeta}{\partial t} + \frac{\partial \phi}{\partial x}\frac{\partial \zeta}{\partial x} - \frac{\partial \phi}{\partial y} = 0 \tag{3.3}$$

on the free surface. Here the notation $D()/Dt = \partial()/\partial t + \nabla\phi \cdot \nabla()$ has been used. The kinematic free surface condition is then given as:

$$\frac{\partial \zeta}{\partial t} = \frac{\partial \phi}{\partial y} - \frac{\partial \phi}{\partial x}\frac{\partial \zeta}{\partial x}. \tag{3.4}$$

This equation is used to step the nodes vertically during the time integration of the mathematical problem. The coordinate system defined in figure 3.2, is fixed to the tank and is hence an accelerated coordinate system. This does not affect the boundary integral equation (3.1) or the kinematic free surface condition, but it affects the dynamic free surface condition derived next. The dynamic free surface condition states that the pressure is equal on the two sides of the free surface. It is seen as equation (3.17) in figure 3.2. Since the coordinate system used follows the tank motion it means that it is an accelerated coordinate system. Newton's second law must be modified in order to be applied to an accelerated coordinate system. This means that also the Euler equations and Bernoulli's equation are different for an accelerated coordinate system. First Bernoulli's equation is written for a non-accelerating (inertial) coordinate system:

$$\bar{p} + \rho\frac{\partial \bar{\phi}}{\partial t} + \frac{\rho}{2}\nabla\bar{\phi} \cdot \nabla\bar{\phi} + \rho g y = C. \tag{3.5}$$

Here the coordinate system does not follow the tank motion and origo is on the still water level with y pointing upwards. $\nabla\bar{\phi}$ is the velocities in the inertial reference system and $\bar{p}$, ρ and g are the absolute pressure, the density of the water and the acceleration of gravity, respectively. In an accelerated system, the term $\partial\bar{\phi}/\partial t$ must be rewritten. All the other terms are not affected by acceleration of the coordinate system when angular motions of the coordinate system are neglected. The time derivative at a fixed point in a moving coordinate system is then written as a function of the time derivative in a non-accelerated coordinate system as follows:

$$\begin{aligned}
\frac{\partial \bar{\phi}}{\partial t}\bigg|_{\text{acc.}} &= \lim_{\Delta t \to 0}\left[\frac{\bar{\phi}(x, t+\Delta t) - \bar{\phi}(x,t)}{\Delta t}\right] \\
&= \lim_{\Delta t \to 0}\left[\frac{\bar{\phi}(x',t) + u_f\bar{\phi}_x\Delta t - \bar{\phi}(x,t)}{\Delta t}\right] \\
&= \frac{\partial \bar{\phi}}{\partial t}\bigg|_{\text{non acc.}} + u_f\frac{\partial \bar{\phi}}{\partial x}.
\end{aligned} \tag{3.6}$$

Here u_f is the velocity of the forced sway tank motion. It is convenient to operate with the velocities observed when moving with the tank, $\boldsymbol{u} = \nabla\phi$. The velocity potential for the relative velocity ϕ is related to the absolute velocity potential $\bar{\phi}$ as follows:

$$\bar{\phi} = u_f x + \phi. \tag{3.7}$$

Bernoulli's equation in the sway accelerated coordinate system using relative velocities $\nabla\phi$ then reads:

$$\rho\frac{\partial\phi}{\partial t} + x\rho a_f - \frac{\rho}{2}u_f^2 + \frac{\rho}{2}\nabla\phi\cdot\nabla\phi + \rho g y + \bar{p} = p_0. \tag{3.8}$$

Here the value of C in equation 3.5 is found by evaluating the equation at $y = 0$, without excitation or fluid motions, using the coordinate system defined in figure 3.2. Then the pressure inside the tank is equal to the ullage pressure p_0. The Bernoulli's equation is then rewritten to express the time rate of change of ϕ on the free surface, as one travels with the wave vertically. This is denoted $d\phi/dt$, and is given as

$$\frac{d\phi}{dt} = \frac{\partial\phi}{\partial t} + \frac{\partial\phi}{\partial x}\frac{\partial x}{\partial t} + \frac{\partial\phi}{\partial y}\frac{\partial y}{\partial t} = \frac{\partial\phi}{\partial t} + \frac{\partial\phi}{\partial y}\frac{\partial\zeta}{\partial t}. \tag{3.9}$$

Here $\partial x/\partial t$ is equal to zero since the free surface is followed in the vertical direction only. $\partial y/\partial t = \partial\zeta/\partial t$ expresses that the y-coordinate changes according to the wave elevation. By inserting the kinematic free surface condition equation (3.4) for $\partial\zeta/\partial t$ in equation (3.9) and inserting the result into Bernoulli's equation for $\partial\phi/\partial t$, the Bernoulli's equation on the free surface is written as:

$$\frac{d\phi}{dt} = -g\zeta - \mu\phi - a_f x + \frac{1}{2}u_f^2 - \frac{1}{2}\left(\frac{\partial\phi}{\partial x}\right)^2 + \frac{1}{2}\left(\frac{\partial\phi}{\partial y}\right)^2 - \frac{\partial\phi}{\partial y}\frac{\partial\phi}{\partial x}\frac{\partial\zeta}{\partial x} + \frac{p_0 - \bar{p}}{\rho}. \tag{3.10}$$

The term $-\mu\phi$ has been added to model the damping effect of viscous boundary layers and meniscus. Faltinsen [18] used a similar type of term to obtain steady state results for sloshing. The term can be fitted to experimental decay tests. Faltinsen linearised the free surface conditions and obtained the following relation between the modulus of decay α estimated from experiments and μ:

$$\mu = \frac{2\alpha}{T_n}. \tag{3.11}$$

Here T_n is the first natural frequency of the tank. Details of this derivation can be found in Faltinsen [18]. A boundary condition towards the rigid tank walls is also required. This is given as:

$$\frac{\partial\phi}{\partial n} = 0. \tag{3.12}$$

Here the notation $\partial()/\partial n = \boldsymbol{n}\cdot\nabla()$ is used. In equation (3.10) the pressure $\bar{p}$ is equal to the pressure in the air. At the rightmost point on the free surface ($x=L/2$) the pressure is set equal to the ullagem pressure. That is:

$$\bar{p} = p_0 \qquad \text{at } x = L/2. \tag{3.13}$$

This ensures that the resulting mathematical problem does not allow for infinitely many solutions. This point is explained in detail after the full mathematical problem has been derived. Since the pressure is known on the free surface at $x = L/2$, ϕ can be stepped forward in time according to equation (3.10) at this point. For the remaining part of the free surface $-L/2 \leq x < L/2$ the pressure in the air is unknown and must be found from the air equations as explained in the following. The governing equations of the air domain is the quasi-one-dimensional equations. The mass conservation equation for incompressible quasi-one-dimensional flow can according to Anderson [19] be written as:

$$\frac{\partial h}{\partial t} + \frac{\partial}{\partial x}\left[h\left(\frac{\partial \phi_g}{\partial x}\right)\right] = 0. \tag{3.14}$$

Here ϕ_g is the velocity potential of the air, and the velocity in the air can be written as $u_g = \partial \phi_g/\partial x$. h denotes the vertical distance between the free surface and the roof as defined in figure 3.1. At $x = -L/2$ the wall condition is enforced:

$$\frac{\partial \phi_g}{\partial x} = 0 \qquad (x = \pm L/2). \tag{3.15}$$

This condition is enforced in the numerical procedure at $x = -L/2$. Due to global mass conservation the condition also holds for $x = L/2$ without enforcing it explicitly in the numerical procedure.

Anderson [19] showed that the quasi-one-dimensional momentum equation neglecting viscosity is identical to the one-dimensional Euler's equation. This means that the pressure can be found from Bernoulli's equation. Bernoulli's equation for an accelerated coordinate system is seen in equation (3.8). When this equation is applied to the air it reads:

$$\rho_g \frac{\partial \phi_g}{\partial t} = -\rho_g a_f x + \frac{\rho_g}{2} u_f^2 - \frac{\rho_g}{2}\left(\frac{\partial \phi_g}{\partial x}\right)^2 + p_0 - \bar{p}. \tag{3.16}$$

From the definition of $d()/dt$ in (3.9), it follows that $\partial \phi_g/\partial t = d\phi_g/dt$ since ϕ_g is a function of x only. This equation is combined with the dynamic free surface condition for the water (3.10). The combined dynamic free surface condition for incompressible quasi-one-dimensional air and potential water is then written as:

$$\begin{aligned}
\frac{d\beta}{dt} = &-g\zeta - \mu\phi - a_f x + \frac{1}{2}u_f^2 - \frac{1}{2}\left(\frac{\partial \phi}{\partial x}\right)^2 + \frac{1}{2}\left(\frac{\partial \phi}{\partial y}\right)^2 - \frac{\partial \phi}{\partial y}\frac{\partial \phi}{\partial x}\frac{\partial \zeta}{\partial x} \\
&+ \frac{\rho_g}{\rho}\left[a_f x - \frac{1}{2}u_f^2 + \frac{1}{2}\left(\frac{\partial \phi_g}{\partial x}\right)^2\right].
\end{aligned} \tag{3.17}$$

Here $\beta = \phi - (\rho_g/\rho)\phi_g$. The quantity β can be stepped forward if the fluid velocities $\nabla\phi$, $\partial \phi_g/\partial x$, $\zeta(x,t)$, ζ_x and tank motion x_f, u_f, a_f are known at a time instant. The air domain is connected to the water domain through the term $\partial h/\partial t$ in equation (3.14). Here the goal is to express this term as a function of $\partial \phi/\partial n$ and the known variable β on the free surface. In the following $\partial \phi/\partial n$ is denoted σ for simplicity. Then the resulting mass conservation

equation for the air (3.14), can be inserted into the mass conservation equation for the water (3.1) to form a fully coupled mass conservation equation where ϕ_g is the unknown on the free surface. Next, $h = h_1 - \zeta$ is inserted in equation (3.4). Here h_1 is the vertical distance between the still water level and the roof. This yields:

$$\frac{\partial h}{\partial t} = -\frac{\partial \phi}{\partial y} - \frac{\partial \phi}{\partial x}\frac{\partial h}{\partial x}. \qquad (3.18)$$

Here the velocity components ϕ_x and ϕ_y are expressed through the velocity component normal to the free surface ϕ_n, which is denoted σ, and the velocity component in the tangential direction ϕ_τ. When the subscript τ and n are used it means $\boldsymbol{\tau} \cdot \nabla()$ and $\boldsymbol{n} \cdot \nabla()$. Using the relation $\phi_y = \tau_2\phi_\tau + n_2\phi_n$ and $\phi_x = \tau_1\phi_\tau + n_1\phi_n$ the result is:

$$\frac{\partial h}{\partial t} = -\sigma\left(n_2 + n_1\frac{\partial h}{\partial x}\right) - \phi_\tau\left(\tau_2 + \tau_1\frac{\partial h}{\partial x}\right). \qquad (3.19)$$

Here ϕ_τ is unknown, but by inserting $\phi = \beta + (\rho_g/\rho)\phi_g$ into the equation it reads:

$$\frac{\partial h}{\partial t} = -\sigma\left(n_2 + n_1\frac{\partial h}{\partial x}\right) - \left(\beta_\tau + \frac{\rho_g}{\rho}\phi_{gs}\right)\left(\tau_2 + \tau_1\frac{\partial h}{\partial x}\right). \qquad (3.20)$$

Inserted in the mass conservation equation (3.14), it yields:

$$\sigma\left(n_2 + n_1\frac{\partial h}{\partial x}\right) + \left(\beta_\tau + \frac{\rho_g}{\rho}\phi_{gs}\right)\left(\tau_2 + \tau_1\frac{\partial h}{\partial x}\right) - \frac{\partial}{\partial x}\left[h\left(\frac{\partial \phi_g}{\partial x}\right)\right] = 0. \qquad (3.21)$$

This is the mass conservation equation for the air written in a form convenient when the equations are discretized. This equation takes a simpler form at the right and left end of the air domain. The derivation is similar to the derivation leading to (3.21) with the following two modifications. At the right and left edge of the free surface $\phi_x = 0$. This is inserted in equation (3.18). The other modification is that $\phi_{g\tau} = 0$ at the edges. This is due to the boundary conditions in (3.15) and the quasi-one-dimensional assumption $\phi_{gy} = 0$. The resulting mass conservation equation at the right and left side of the air domain then reads:

$$\sigma n_2 + \tau_2\beta_\tau - \frac{\partial}{\partial x}\left[h\left(\frac{\partial \phi_g}{\partial x}\right)\right] = 0. \qquad (3.22)$$

Choosing proper boundary conditions for a mathematical problem is not trivial. As commented after deriving the dynamic boundary condition, the pressure is set equal to the atmospheric pressure at $x = L/2$. This is done for a particular reason. Imagine if this condition was not enforced. Then the dynamic condition (3.17) is valid for all points on the free surface, while the rest of the mathematical problem is similar. Then if ϕ, ϕ_g solves this mathematical problem at one time instant, then also $\phi - \rho_g/\rho c, \phi_g + c$ solves the same problem. The resulting numerically discretized equation system should reflect this fact by allowing for infinitely many solutions. The solution of the equation system can only be found up to a constant. This problem does not exist if the pressure is fixed on one side, because

then $\phi_g + c$ is no longer a valid solution at this point in the domain. This is why the pressure is set equal to the ullage pressure at $x = L/2$ and it is as if a hole where present in the tank at this position. There was no hole at $x = L/2$ in the tank used in the experiments, however there was a hole in the tank roof at $x \approx 0.15[m]$. However, this difference is not believed to be important, since the pressure in the air domain outside the pocket area is believed to be close to atmospheric pressure.

3.3   The numerical method

The numerical solution of the mathematical problem in figure 3.2 has similarities with the mixed Eulerian-Lagrangian method frequently used for free surface problems. This method was originally proposed by Ogilvie [20] and has later been used by, for instance, Longuet-Higgins and Cokelet [21], Faltinsen [18], Dommermuth and Yue [22] and Tanizawa [23]. The method solves the mathematical problem by dividing it into an Eulerian and a Lagrangian stage. During the Eulerian stage the equation representing mass conservation is solved. During the Lagrangian stage the location of the nodes on the free surface and the velocity potential is stepped forward using the boundary conditions. The word Lagrangian is however not correct for the present method since the nodes on the free surface are only stepped in the vertical direction and do not follow the fluid particles.

In the same way the new numerical procedure, solves an equation system representing mass conservation during the Eulerian stage. This mass conservation equation system expresses mass conservation in the air and water. This equation system is constructed as follows. The differential equations expressing mass conservation in the air domain are the equations (3.22) and (3.21). The finite-difference method (FDM) is used to discretize these equations and yields an equation system for the air. This equation system is inserted in the equation system which represents mass conservation in the water domain. This is the equation system which is obtained by applying the boundary element method (BEM) to the boundary integral equation (3.1). The new numerical procedure is named the boundary-element-finite-difference method (BEFDM).

The stage equivalent to the Lagrangian stage of the mixed Eulerian-Lagrangian method consists of integrating the boundary conditions in time. The dynamic and the kinematic boundary conditions (3.4) and (3.17) are used to step the variable β and the free surface elevation ζ forward in time. The time integration method chosen here is the explicit Runge-Kutta method of fourth order as defined by Kreyszig [24]. Using this integration method the equation system needs to be solved four times during one time step.

3.3.1   The coupled mass conservation equation

In the water domain the mass conservation is satisfied through the boundary integral equation (3.1). This equation is discretized using the linear boundary element method (BEM). The discretization method of the water domain is similar to the method applied by Lu et al. [25] and Kristiansen [26]. In figure 3.3 the boundary of the water domain is divided into linear segments. These segments are called boundary elements and the end points of the
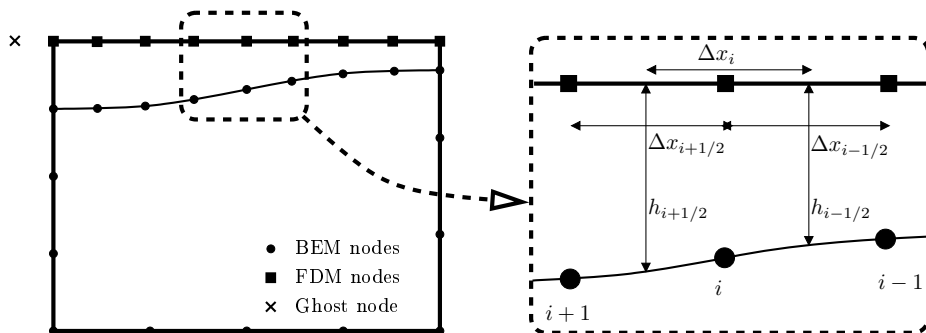
Figure 3.3: The numerical discretization of the mathematical problem. The water is discretized using the boundary element method where the collocation points are seen as ● and the air is discretized using the finite-difference method (■). The nodes on the free surface (●) only moves vertically. The nodes of the air domain (■) share the same horizontal coordinate as the free surface nodes.

elements are called collocation points (nodes) where the boundary conditions are satisfied. The collocation points are indicated as black circles (●) in figure 3.3. The linear boundary element method assumes linear variation of the source and dipole strengths over each element. For element j, the variation of ϕ is written as

$$\phi = \begin{bmatrix} 1 - \frac{\xi - \xi_j}{\xi_{j+1} - \xi_j} & \frac{\xi - \xi_j}{\xi_{j+1} - \xi_j} \end{bmatrix} \begin{Bmatrix} \phi_1 \\ \phi_2 \end{Bmatrix}_j = \lfloor \boldsymbol{N} \rfloor \{\boldsymbol{\phi}\}. \tag{3.23}$$

Here ξ is coordinates in the local coordinate system in figure B.1. Here the subscript 1 and 2 on ϕ refer to the value of ϕ on the ends of the element. Similar representation is used for $d\phi/dn$, that is,

$$\frac{d\phi}{dn} = \lfloor \boldsymbol{N} \rfloor \{\boldsymbol{\sigma}\}. \tag{3.24}$$

When these expressions are inserted into equation (3.1), then

$$\theta_i \phi_i - \sum_{j=1}^{N_e} \int_{s_j} \lfloor \boldsymbol{N} \rfloor \frac{\partial \log(r)}{\partial n} ds \begin{Bmatrix} \phi_1 \\ \phi_2 \end{Bmatrix}_j = -\sum_{j=1}^{N_e} \int_{s_j} \lfloor \boldsymbol{N} \rfloor \log(r) ds \begin{Bmatrix} \sigma_1 \\ \sigma_2 \end{Bmatrix}_j. \tag{3.25}$$

These integrals can be rewritten and expressed through four basic integrals $I_{i,j}^1$, $I_{i,j}^2$, $I_{i,j}^3$ and $I_{i,j}^4$ as follows:

$$\int_{s_j} \lfloor \boldsymbol{N} \rfloor \log(r) ds = \begin{bmatrix} I_{i,j}^1 - \frac{1}{\xi_{j+1} - \xi_j} \left(I_{i,j}^3 - \xi_j I_{i,j}^1 \right) & \frac{1}{\xi_{j+1} - \xi_j} \left(I_{i,j}^3 - \xi_j I_{i,j}^1 \right) \end{bmatrix} \tag{3.26}$$

$$= \frac{1}{\xi_{j+1} - \xi_j} \begin{bmatrix} \xi_{j+1} I_{i,j}^1 - I_{i,j}^3 & I_{i,j}^3 - \xi_j I_{i,j}^1 \end{bmatrix} = -[c_{ij}, d_{ij}]. \tag{3.27}$$

Similarly we get,

$$\int_{s_j} \lfloor \boldsymbol{N} \rfloor \frac{\partial \log(r)}{\partial n} ds = \left[I_{i,j}^2 - \frac{1}{\xi_{j+1}-\xi_j}\left(I_{i,j}^4 - \xi I_{i,j}^2 \right) \quad \frac{1}{\xi_{j+1}-\xi_j}\left(I_{i,j}^4 - \xi_j I_{i,j}^2 \right) \right] \tag{3.28}$$

$$= \frac{1}{\xi_{j+1}-\xi_j}\left[\xi_{j+1}I_{i,j}^2 - I_{i,j}^4 \quad I_{i,j}^4 - \xi_j I_{i,j}^2 \right] = -[a_{ij}, b_{ij}]. \tag{3.29}$$

Here the integrals are given as

$$I_{i,j}^1 = \int_{s_j} \log r \, dS \tag{3.30}$$

$$I_{i,j}^2 = \int_{s_j} \frac{d \log r}{dn} dS \tag{3.31}$$

$$I_{i,j}^3 = \int_{s_j} \xi \log r \, ds \tag{3.32}$$

$$I_{i,j}^4 = \int_{s_j} \xi \frac{\log r}{dn} ds. \tag{3.33}$$

The analytical solution to these integrals are presented in appendix B. Equation number i can now be written as:

$$\theta_i \phi_i + \sum_{j=1}^{N_e} (a_{ij}\phi_{1j} + b_{ij}\phi_{2j}) = \sum_{j=1}^{N_e} (c_{ij}\sigma_{1j} + d_{ij}\sigma_{2j}). \tag{3.34}$$

The boundary element equations are now written in matrix notation,

$$[\boldsymbol{G}]\{\boldsymbol{\phi}\} = [\boldsymbol{H}]\{\boldsymbol{\sigma}\}. \tag{3.35}$$

Here $[\boldsymbol{G}]$ and $[\boldsymbol{H}]$ are coefficient matrices and $\{\boldsymbol{\phi}\}$ and $\{\boldsymbol{\sigma}\}$ are column vectors containing nodal values of ϕ and σ. This equation system, which represents mass conservation of the water domain, is also used in the numerical method for the air pocket oscillation stage of the air pocket experiment which is presented in detail in chapter 4. To ease the presentation of the numerical method in this chapter the equation system (3.35) is conveniently rewritten as:

$$\begin{bmatrix} \boldsymbol{G}_1 & \boldsymbol{G}_f & \boldsymbol{G}_s \end{bmatrix} \begin{Bmatrix} \phi_1 \\ \phi_f \\ \phi_s \end{Bmatrix} = \begin{bmatrix} \boldsymbol{H}_1 & \boldsymbol{H}_f & \boldsymbol{H}_s \end{bmatrix} \begin{Bmatrix} \sigma_1 \\ \sigma_f \\ \sigma_s \end{Bmatrix}. \tag{3.36}$$

The numbering of the unknowns starts at the free surface node located at $(x = L/2)$ and continues in the counter-clockwise direction. The subscript 1 in for instance ϕ_1 and σ_1 denotes this start point. The subscript f denotes all the other nodes on the free surface while the subscript s denotes nodes on the structure. Next the equation system expressing mass conservation in the air domain is derived.

The equations (3.21) and (3.22) express mass conservation for the air. These equations are discretized using the finite difference method (FDM). The black squares (■) seen in

figure 3.3 are the nodes of the air domain and are used to discretize the equations. The free surface contains N_f nodes, hence the leftmost node on the free surface is node number N_f. The numerical discretization of the different terms in (3.21) follows starting with the second order derivative of ϕ_g. The discretization is done on a general node number $2 \leq i \leq N_f$ shown in figure 3.3:

$$
\begin{aligned}
&\frac{\partial}{\partial x}\left[h\left(\frac{\partial \phi_g}{\partial x}\right)\right] \\
&\approx \frac{\left[(\phi_{gx}^{i-1/2} h_{i-1/2}) - \phi_{gx}^{i+1/2}(h_{i+1/2})\right]}{\Delta x_i} \\
&\approx \frac{h_{i-1/2}}{\Delta x_i \Delta x_{i-1/2}}\phi_g^{i-1} - \frac{1}{\Delta x_i}\left[\frac{h_{i-1/2}}{\Delta x_{i-1/2}} + \frac{h_{i+1/2}}{\Delta x_{i+1/2}}\right]\phi_g^i + \frac{h_{i+1/2}}{\Delta x_i \Delta x_{i+1/2}}\phi_g^{i+1} \\
&= a_i \phi_g^{i-1} + b_i \phi_g^i + c_i \phi_g^{i+1}.
\end{aligned}
\tag{3.37}
$$

Here the $\Delta x_{i-1/2}, \Delta x_i, \Delta x_{i+1/2}$ and $h_{i-1/2}, h_{i+1/2}$ are geometrical parameters of equation (3.37) which are defined in figure 3.3. The local truncation error of equation (3.37) is of first order in Δx_i. To further discretize equation (3.21) the normal and tangential vectors $\boldsymbol{n}$ and $\boldsymbol{\tau}$ on the free surface are needed. For the nodes $2 \leq i < N_f$, the normal and tangential vectors are defined as the normal and tangential vector of a quadratic function fitted through the nodes located at $\boldsymbol{x}_{i-1}, \boldsymbol{x}_i, \boldsymbol{x}_{i+1}$. The quadratic function for node i can be seen in figure (3.4) together with the normal and tangential vector.
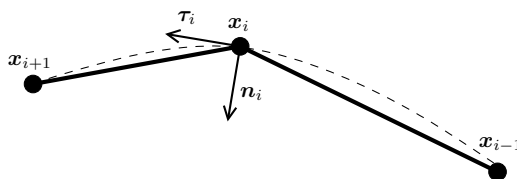
Figure 3.4: Two boundary elements on the free surface. A second order polynomial is fitted to the three node positions $\boldsymbol{x}_{i-1}, \boldsymbol{x}_i, \boldsymbol{x}_{i+1}$. This is used to calculate the normal vector $\boldsymbol{n}_i$ and the tangential vector $\boldsymbol{\tau}_i$.

To find the derivatives $h_x, \phi_{g\tau}$ and β_τ in (3.21), the value of h, ϕ_g and β is fitted to a quadratic polynomial. Then the derivative of this quadratic polynomial is found. The formula for $\phi_{g\tau}$ is then given as:

$$
\begin{aligned}
\frac{\partial \phi_g}{\partial \tau} &= \left(\frac{\Delta s_{i-1}}{\Delta s_i(\Delta s_i + \Delta s_{i-1})}\right)\phi_g^{i+1} - \left(\frac{\Delta s_{i-1} - \Delta s_i}{\Delta s_i \Delta s_{i-1}}\right)\phi_g^i - \left(\frac{\Delta s_i}{\Delta s_{i-1}(\Delta s_i + \Delta s_{i-1})}\right)\phi_g^{i-1} \\
&= o_i \phi_g^{i-1} + m_i \phi_g^i + q_i \phi_g^{i+1}.
\end{aligned}
\tag{3.38}
$$

The same formula is used for h_x and β_τ. This scheme reduces to the central difference scheme when $\Delta s_i = \Delta s_{i-1}$. The approximations of the terms $n_2 + n_1\frac{\partial h}{\partial x}$ and $\tau_2 + \tau_1\frac{\partial h}{\partial x}$ in equation

(3.21) are named d_i and e_i. That is:

$$n_2 + n_1 \frac{\partial h}{\partial x} \approx d_i \qquad (3.39)$$

$$\tau_2 + \tau_1 \frac{\partial h}{\partial x} \approx e_i. \qquad (3.40)$$

Then a discretized form of equation (3.21) at node i reads,

$$\sigma_i = \left[\frac{a_i}{d_i} - \frac{\rho_g}{\rho} \frac{e_i o_i}{d_i} \right] \phi_g^{i-1} + \left[\frac{b_i}{d_i} - \frac{\rho_g}{\rho} \frac{e_i m_i}{d_i} \right] \phi_g^{i} + \left[\frac{c_i}{d_i} - \frac{\rho_g}{\rho} \frac{e_i q_i}{d_i} \right] \phi_g^{i+1}$$
$$- \frac{e_i o_i}{d_i} \beta^{i-1} - \frac{e_i m_i}{d_i} \beta^{i} - \frac{e_i q_i}{d_i} \beta^{i+1} \qquad (3.41)$$

$$= \hat{a}_i \phi_g^{i-1} + \hat{b}_i \phi_g^{i} + \hat{c}_i \phi_g^{i+1} + \hat{w}_i.$$

For node $i = 1$ the pressure is known and hence ϕ_g can be stepped forward in time using equation (3.16). Then ϕ_g is known at node 1 and can hence be inserted in the equation (3.37) when $i = 2$. At node $i = N_f$, the combined mass conservation equation for the air is simpler and given by equation (3.22). In this equation $(h\phi_{gx})_x$ is discretized using equation (3.37). This is possible since a ghost node to the left of node N_f is introduced. This ghost node is referred to as node number $N_f + 1$ and is seen in figure 3.3. The boundary condition of the air domain at $x = -L/2$, that is, $\phi_{gx} = 0$ is discretized using a central difference stencil. This leads to $\phi_g^{N_f-1} = \phi_g^{N_f+1}$ which is inserted into equation (3.37) when $i = N_f$. The normal and tangential vector components in equation (3.22) are set equal to the normal and the tangential vector of the closest free surface element. β_τ in equation (3.22) is discretized using a first order difference stencil using information on node N_f and $N_f - 1$. The discretized version of equation (3.22) is then given as,

$$\sigma_{N_f} = -\frac{\tau_2}{n_2} \left(\frac{\beta_{N_f} - \beta_{N_f-1}}{\Delta s_{N_f-1}} \right) + \frac{(a_{N_f} + c_{N_f})}{n_2} \phi_g^{N_f-1} + \frac{b_{N_f}}{n_2} \phi_g^{N_f}. \qquad (3.42)$$

Based on (3.41) and (3.42) the relation between σ and ϕ_g is expressed in matrix notation as follows:

$$\{\boldsymbol{\sigma}_f\} = [\boldsymbol{A}_g]\{\boldsymbol{\phi}_g\} - \{\boldsymbol{b}_g\}. \qquad (3.43)$$

In addition the relation $\beta = \phi - (\rho_g/\rho)\phi_g$ is known from the dynamic free surface condition (3.17). Written in matrix notation it reads:

$$\{\boldsymbol{\phi}_f\} = \{\boldsymbol{\beta}_f\} + \frac{\rho_g}{\rho}\{\boldsymbol{\phi}_g\}. \qquad (3.44)$$

The equation system (3.43) represents mass conservation in the air domain. Inserting this equation system and the relation (3.44) into the equation representing mass conservation for the water (3.36) and sorting unknowns variables to the left and known variables to the right the following equation system is obtained:

$$[\boldsymbol{A}]\{\boldsymbol{\chi}\} = \{\boldsymbol{b}\}. \qquad (3.45)$$

Where:

$$[\boldsymbol{A}] = \left[\ \{\boldsymbol{H_1}\} \ \vdots \ [\boldsymbol{H_f}][\boldsymbol{A_g}] - \frac{\rho_g}{\rho}[\boldsymbol{G_f}] \ \vdots \ -[\boldsymbol{G_s}] \ \right] \quad , \quad \{\boldsymbol{\chi}\} = \left\{ \begin{array}{c} \sigma_1 \\ \phi_g \\ \phi_s \end{array} \right\}$$

$$\{\boldsymbol{b}\} = \left\{ \ [\boldsymbol{H_f}]\{\boldsymbol{b_g}\} - [\boldsymbol{H_s}]\{\boldsymbol{\sigma_s}\} + [\boldsymbol{G_f}]\{\boldsymbol{\beta_f}\} + \{\boldsymbol{G_1}\}\phi_1 \ \right\}.$$

This is the coupled mass conservation equation system for the air and the water and is in this work solved by using a direct method.

3.3.2   The time integration procedure

The time integration is performed using the explicit fourth order Runge-Kutta method as specified by Kreyszig [24]. The equations containing a time derivative in the mathematical problem (figure 3.2) are the equations (3.17), (3.10), (3.16) and (3.4). The time derivative in these equations are collected in the vector $\psi = \{\beta_f, \phi_1, \phi_{g1}, \zeta\}$. The right hand side of these equations are collected in the vector f accordingly. So that $\psi' = f(t, \psi, \chi)$, where the apostrophe denotes time derivative. If ψ and χ are known then all the variables ϕ, ϕ_g, ϕ_x,ϕ_y, ζ_x can be found and hence f can be evaluated. The procedures for obtaining ϕ, σ, ϕ_x,ϕ_y, ζ_x from ψ and χ are explained next. Along the free surface, ϕ is found by using relation (3.44) while σ on the free surface is obtained from (3.43). The velocity components ϕ_x and ϕ_y are found by decomposing σ and the tangential velocity component ϕ_τ. To do this the normal vector $\boldsymbol{n}$ and the tangential vector $\boldsymbol{\tau}$ is needed. These parameters are calculated in the same way as in connection with the equations (3.21) and (3.22).
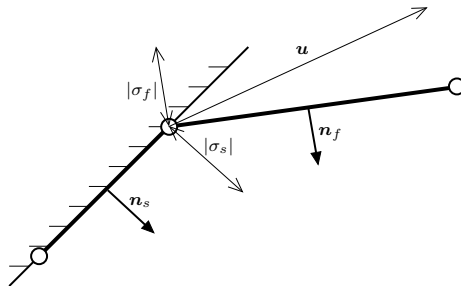
Figure 3.5:   Illustration of the two boundary elements connecting the free surface and the structure.

However, when finding ϕ_x and ϕ_y at the nodes in the ends of the free surface the knowledge of the boundary condition on the walls is exploited in the manner explained by Tanizawa [27]. This method solves a 2×2 equation system for $\boldsymbol{u} = [u, v]$ given as:

$$\left\{ \begin{array}{c} \sigma_s \\ \sigma_f \end{array} \right\} = \left\{ \begin{array}{c} \boldsymbol{u} \cdot \boldsymbol{n_s} \\ \boldsymbol{u} \cdot \boldsymbol{n_f} \end{array} \right\} \tag{3.46}$$

The terms in this equation are illustrated in figure 3.5. Here σ_s is the fluid velocity component normal to the wall element and σ_f is the fluid velocity component normal to the free surface element. Further, $\boldsymbol{u}$ is the fluid velocity vector with components in the x- and y-direction. Finally, $\boldsymbol{n}_s$ and $\boldsymbol{n}_f$ is the corresponding normal vector on the wall and on the fluid element. Equation (3.46) is two equations which can be solved to obtain $\boldsymbol{u} = [u, v]$ for the nodes on the free surface intersecting the walls. ϕ_τ is calculated using the same method as for $\phi_{g\tau}$ in (3.38). At the end nodes one sided finite-differences are used. ζ_x is obtained by the same method as $\phi_{g\tau}$ in equation (3.38) just exchanging Δs with Δx. At the end nodes one sided finite-differences are used.

Now, the evaluation of f based on the knowledge of ψ and χ has been explained. The fourth order Runge-Kutta method applied to the current problem is written in figure 3.6. The

---

Time integration procedure:

For $n = 1..N$

$$k_1 = \Delta t f(t_n, \psi_n, \chi_n)$$

$$k_2 = \Delta t f(t_n + \tfrac{1}{2}\Delta t, \psi_n + \tfrac{1}{2}k_1, [A]^{-1}b(\psi_n + \tfrac{1}{2}k_1))$$

$$k_3 = \Delta t f(t_n + \tfrac{1}{2}\Delta t, \psi_n + \tfrac{1}{2}k_2, [A]^{-1}b(\psi_n + \tfrac{1}{2}k_2))$$

$$k_4 = \Delta t f(t_n + \Delta t, \psi_n + k_3, [A]^{-1}b(\psi_n + k_3))$$

$$t^{n+1} = t^n + \Delta t$$

$$\psi^{n+1} = \psi^n + \tfrac{1}{6}(k_1 + 2k_2 + 2k_3 + k_4)$$

Regridding

$$\chi^{n+1} = [A]^{-1}b(\psi^{n+1})$$

End

Figure 3.6: The 4 th order Runge-Kutta time integration procedure as defined by Kreyszig [24] applied to the boundary-element-finite-difference method.

procedure is explicit in time and evaluates f four times to obtain the variables k_1, k_2, k_3, k_4. This implies solving the equation system (3.45) four times per time step. The regridding is performed before obtaining χ^{n+1}.

3.3.3   Regridding of the free surface

In the time integration procedure in figure 3.6 regridding is performed. This is necessary when solving a problem in the fully nonlinear case, where the free surface is subjected to large deformations. In this work regridding is performed in the same way as presented by Sun [28]. Figure 3.7 shows a segment of the free surface before and after regridding. New
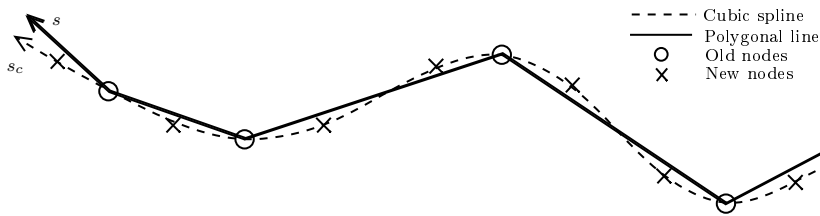
Figure 3.7: A cubic spline is fitted to the old nodal locations (O) in order to obtain new nodal locations (X) during regridding.

nodal locations (X) are obtained by fitting a cubic spline function to the old nodes (O). In the same way values of the variable β at the new nodes are also found. Here this procedure is summarized in three steps:

1. First a cubic spline representation of the free surface geometry is made based on the old nodal locations $(x_{\mathrm{old}}, y_{\mathrm{old}})$. In this way a general point on the free surface (x, y) is expressed as a function of the cubic arc length along the free surface s_c. That is $(x(s_c), y(s_c))$. In the same way the velocity potential at the old nodal locations $\phi(x_{\mathrm{old}}, y_{\mathrm{old}})$ is expressed as a cubic spline function in terms of the cubic arc length s_c. This means that ϕ at a certain location s_c along the free surface can be found by evaluating the cubic spline at this location. That is $\phi(s_c)$.

2. Then new nodal locations are found based on the concept of mesh density functions. The result is an array of new nodal locations s_{cnew}.

3. The cubic spline representation is used to find new nodal locations $x_{\mathrm{new}}(s_{\mathrm{cnew}}), y_{\mathrm{new}}(s_{\mathrm{cnew}})$ and values of the velocity potential at the new nodal positions $\phi(s_{\mathrm{cnew}})$.

New nodal positions s_c are needed in point 2 above. In the present work the concept of mesh density functions are used as explained by Tanizawa [27]. For the sloshing stage the grid used was uniform along all borders of the domain. The procedure of making the array of new nodal locations s_{cnew} is simple in this case. As the wave approaches the roof it is necessary to resolve the interaction effect between the water and the roof. The grid is then refined at the wave crest. Element density functions is used to create a grid which is refined towards the wave crest. An element density function $f(s_c)$ is defined to be the number of elements per unit length of the boundary. The element length function $g(s_c)$ is the inverse of that and is the element length function. Both these functions are continuous. A smooth transition of the element size can be achieved by choosing a linear function for the element length function $g(s_c) = a s_c + b$. The location of the nodal points can be found as the integral of the corresponding element density function as follows,

$$\int_0^{s_{ci}} \frac{1}{a s_c + b} ds_c = i \qquad i = 1 ... N. \tag{3.47}$$

Here

$$a = \frac{g(l) - g(0)}{l}, \qquad b = g(0). \tag{3.48}$$

N denotes the number of elements along the segment. The integral is solved which yields:

$$s_{ci} = \frac{(e^{ai} - 1)b}{a} \tag{3.49}$$

This expression cannot be used when $a = 0$ which is not a problem since a grid with constant element density along the length is easy to create. In figure 3.8 two examples of element refinement based on equation (3.49) are shown. The left plot shows a linear element length
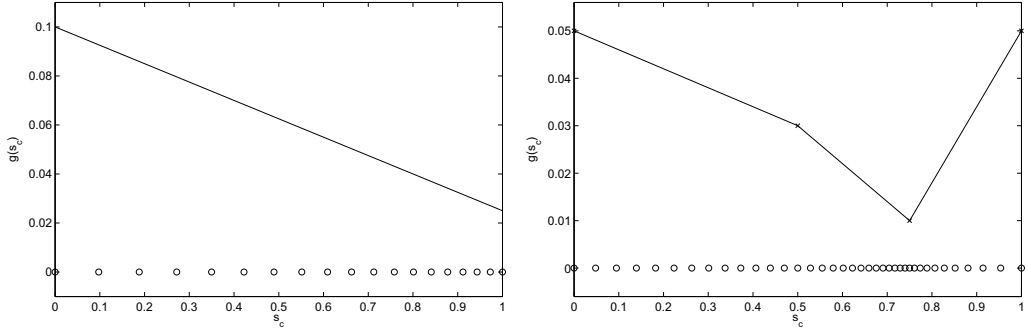
Figure 3.8: An element distribution corresponding to a linear element length function $g(s_c)$ (left) and piecewise linear element length function (right).

function, while the right plot shows a piecewise linear mesh function. The latter method is later used when modelling the air-escape stage of air pocket 6 in section 3.5 to refine the wave peak as it approaches the roof.

3.4   Test cases

The boundary-element-finite-difference method was applied to a test case consisting of a linear standing wave. The analytical solution for this wave is given in appendix C. The analytical solution is found for both the water and the air, where the air can interact with the water. This is hence a two-phase problem. The standing wave consists of the first mode of sloshing. To obtain the natural modes a linearised mathematical problem is solved for. The wave elevation is then written as $\zeta(t, x) = -\zeta_a \sin(\omega_1 t) \cos(\pi(x + L/2)/L)$. Then the analytical solution for ϕ_g is given as

$$\phi_g = \frac{\zeta_a \omega_1}{h_1} \left(\frac{L}{\pi} \right)^2 \cos\left(\pi(x + L/2)/L \right) \cos\left(\omega_1 t \right). \tag{3.50}$$

Here ω_1 is the first natural frequency of the sloshing motion. This is

$$\omega_1^2 = \frac{\rho g h_1}{(\rho_g - \rho C_1)} \left(\frac{\pi}{L} \right)^2 \quad \text{where} \quad C_1 = -\frac{\pi h_1}{L \tanh\left(\frac{\pi H}{L} \right)}. \tag{3.51}$$

Figure 3.9: *Left:* Comparison of the velocity potential in the air ϕ_g for the boundary-element-finite-difference method (BEFDM) and the analytical solution of the two-phase standing wave. *Right:* Spatial convergence study of the unknowns on the free surface intersecting the walls in the BEFDM.

The wave amplitude ζ_a, the water density ρ and the air density ρ_g were set equal to $0.01[\mathrm{m}]$, $1000[\mathrm{kg/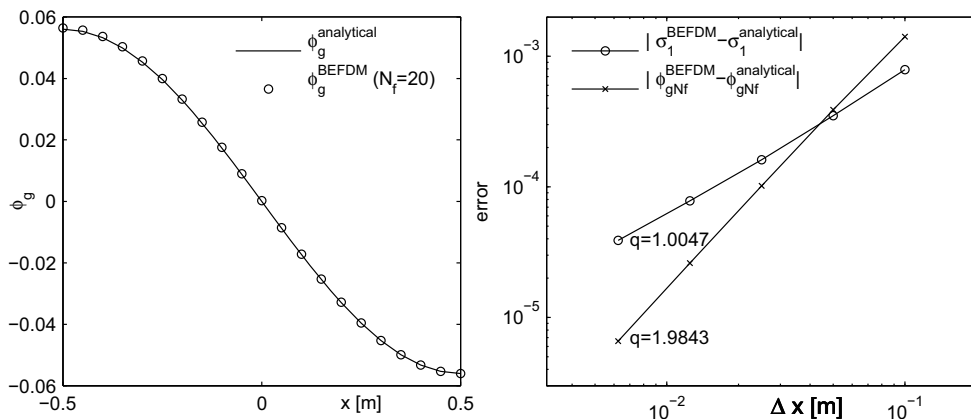m}^3]$ and $1.2[\mathrm{kg/m}^3]$, respectively. The tank dimensions were chosen as $L = 1.0[\mathrm{m}]$, $H = 1.0[\mathrm{m}]$ and $h_1 = 0.1[\mathrm{m}]$. The time integration procedure in figure 3.6 was used with the following modifications. The free surface conditions in the numerical procedure were linearised in the same way as the analytical solution. Also the boundary elements were put on the mean free surface and hence no regridding was required.

A convergence test of the spatial problem in equation (3.45) was then performed using the analytical solution for $t = 0$. Then $\{\boldsymbol{\beta}_f\}$ ϕ_1, ϕ and $\{\boldsymbol{\sigma}_s\}$ from the analytical solution were inserted into the right hand side of the equation system (3.45). Then this equation system was solved to obtain σ_1, $\{\boldsymbol{\phi}_g\}$ and $\{\boldsymbol{\phi}_s\}$. Five different uniform grids with 10, 20, 40, 80 and 120 elements along each side were used to investigate the convergence speed of the solution. Here the corner nodes are investigated in detail because the boundary element method often shows lower order convergence here compared to other areas of the domain. The results of the convergence test are seen in figure 3.9. On the left plot the air velocity potential ϕ_g is plotted for $N_f = 20$. On the right hand side of figure 3.9 a convergence study of the unknowns in the upper corners of the water domain, σ_1 and ϕ_{gN_f} is seen. The error in normal velocity, defined as $|\sigma_1^{\mathrm{BEFDM}} - \sigma_1^{\mathrm{analytical}}|$, goes to zero with linear convergence speed, while the error of ϕ_{gN_f}, defined as $|\phi_{gN_f}^{\mathrm{BEFDM}} - \phi_{gN_f}^{\mathrm{analytical}}|$, goes to zero with nearly quadratic speed. The numerical method described in chapter 4, that is the Mixed Eulerian-Lagrangian (MEL) method, was used to solve a similar type of problem for comparison. Again the wave consisted of the first mode of sloshing but this time the air flow was neglected. This method also uses linear boundary elements. This method solves for σ on the free surface. The results from this method shows first order convergence of σ at $x = \pm L/2$, while the internal nodes on the free surface shows second order convergence. The new method hence shows similar
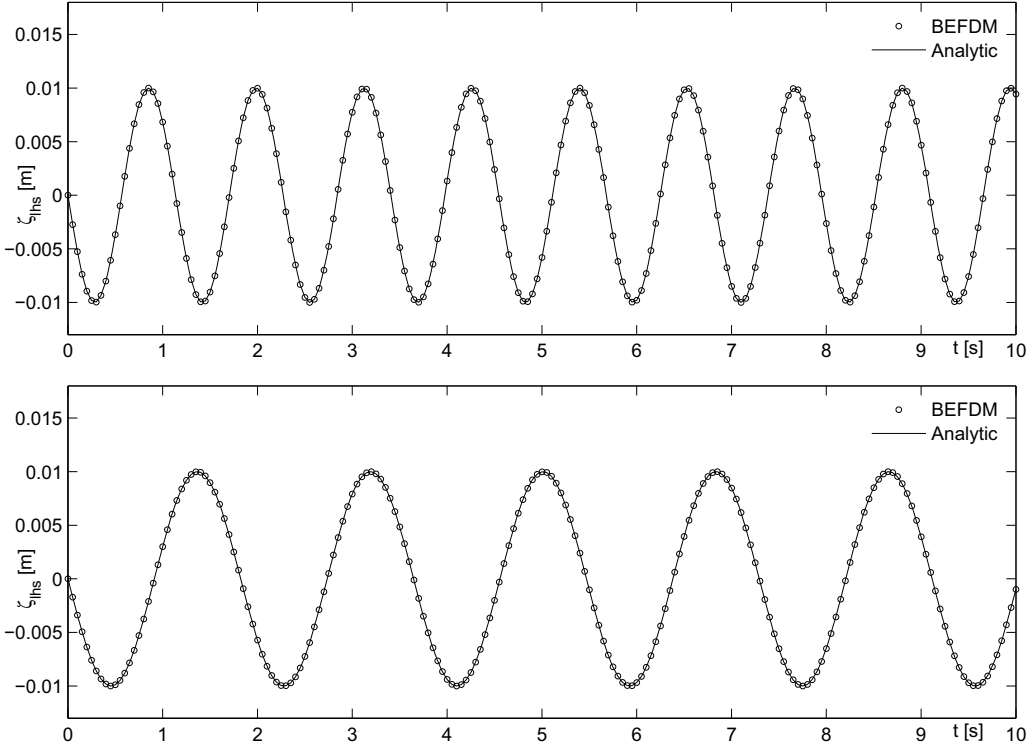
Figure 3.10: Comparison of the boundary-element-finite-difference method (BEFDM), with analytical solution of the two phase linear standing wave. *Top:* $\rho_g = 1.2[\text{kg/m}^3]$. *Bottom:* $\rho_g = 500[\text{kg/m}^3]$.

type of convergence as the mixed Eulerian-Lagrangian method on this test case.

The time integration was tested on the linear two-phase standing wave test case. Then the spatial problem, solved for previously, were used as initial condition. The time integration is made by 20 time steps per second, and 50 elements along each side of the tank. A comparison of the resulting wave elevation on the left hand side ζ_{lhs} is shown in figure 3.10 for two different values of the air density, ρ_g equal to $1.2[\text{kg/m}^3]$ and $500[\text{kg/m}^3]$. The comparison shows good agreement.

Next, the nonlinear implementation of the boundary-element-finite-difference method (BEFDM) including regridding is tested. A good choice for comparison is the single-dominant nonlinear multimodal theory (SDNM) as described by Faltinsen and Timokha [8] for single-phase flow. The tank dimensions were chosen similar to the experiments, that is $L = 1[\text{m}]$ and filling height $H = 0.833[\text{m}]$. The water was fresh water, that is $\rho = 1000[\text{kg/m}^3]$ and acceleration of gravity was set to $g = 9.81[\text{m/s}^2]$. The excitation signal used was:

$$\eta_1(t) = \eta_{a1}(1 - \cos(\sigma t))). \tag{3.52}$$
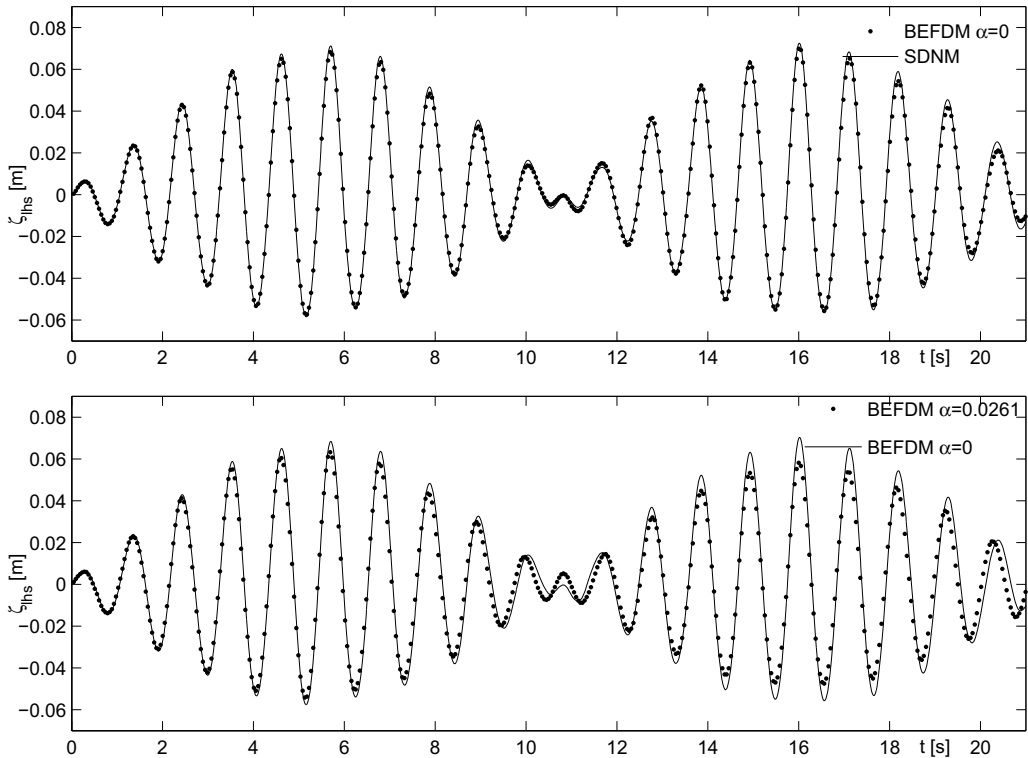
Figure 3.11: *Top:* Comparison of the boundary-element-finite-difference method (BEFDM) and the single-dominant nonlinear multimodal method (SDNM). *Bottom:* The effect of varying the modulus of decay α in the Rayleigh damping model in the BEFDM.

Here $\eta_{a1} = 0.00465$[m], and $\sigma = 6.075$[m/s]. Since the first mode of sloshing dominates the response in this case a uniform grid with 40 elements along the free surface was found to be sufficient. For the time integration 150 time steps per second were found to be enough through a convergence study. For the single-dominant nonlinear multimodal method 20 modes and 150 time steps per second were sufficient. Comparison of the elevation ζ on the left side of the tank is shown in the upper plot in figure 3.11. The new numerical procedure (BEFDM) agrees well with the single-dominant nonlinear multimodal method. However, the wave amplitude of the new numerical procedure is seen to be somewhat lower than the wave amplitude of the single-dominant nonlinear multimodal method. In the lower plot the new numerical procedure is compared when the damping due to viscous boundary layers and meniscus is taken into account and not. Based on the experimental decay tests reported in figure 2.15, the average of the estimated α from the maxima and the minima are used. This results in $\alpha = 0.0261$. This is then inserted in equation (3.11) to obtain the Rayleigh damping parameter μ. The results show that the damping reduces the wave amplitude of
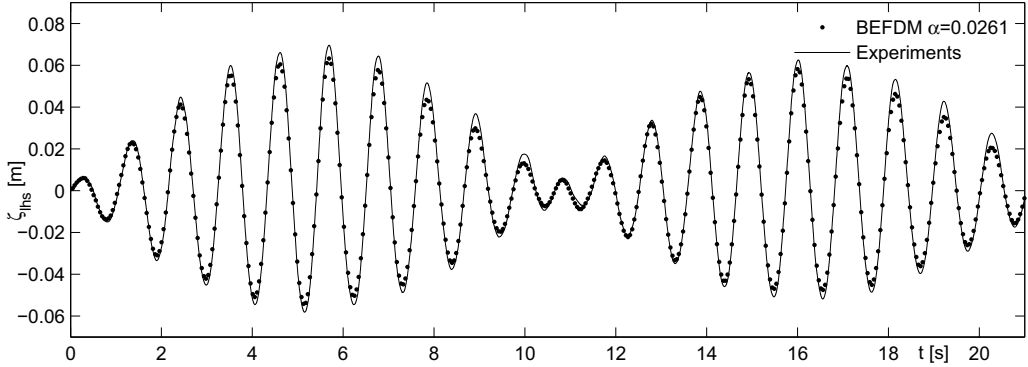
Figure 3.12: Comparison of the experiments and the boundary-element-finite-difference method (BEFDM) including Rayleigh damping.

the sloshing motion as expected.

Also the new numerical procedure was compared with the experimental results for the same case. The experimental excitation signal was used directly in the new numerical procedure and not the analytical signal used previously. A comparison of the wave elevation on the left hand side of the tank is seen in figure 3.12. The numerical procedure agrees well with the experiments but the wave amplitude of the numerical procedure is seen to be a little lower than for the experiments.

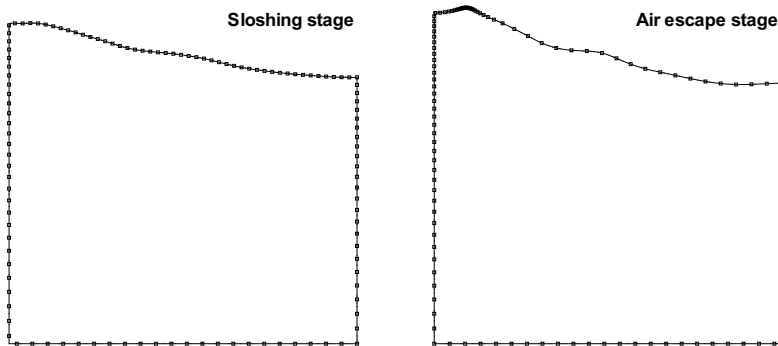## 3.5   Numerical solution of the sloshing and air-escape stages

Figure 3.13: The grid used for the boundary-element-finite-difference method (BEFDM) during the sloshing and air-escape stages. The dots indicate every 4 th grid point for the grid denoted grid 1 (G1).
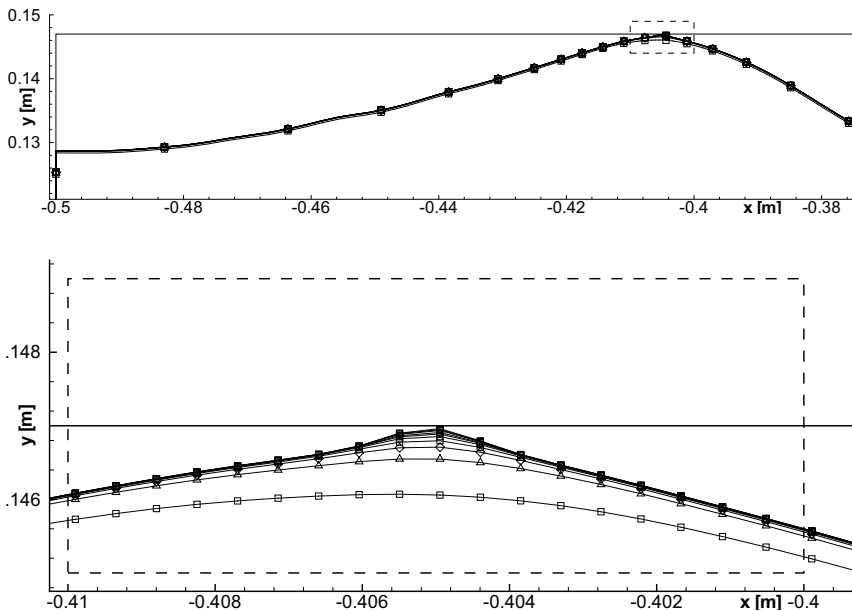
Figure 3.14: The free surface at the time instances when the Mach number $M = u_g^{\max}/c_0$ varies from 0.1 to 1 in steps of 0.1.

Now, the boundary-element-finite-difference method is used to solve for the sloshing and air-escape stages of air pocket 6. The size of the tank and the filling level is set equal to the values of the experimental tank in chapter 2. The density of the water is set to $\rho = 1000[\text{kg/m}^3]$, the density of the air is set set to $\rho_g = 1.2[\text{kg/m}^3]$ and the modulus of decay is set to $\alpha = 0.0261$. To simulate the sloshing and the air-escape stages of air pocket 6, numerical settings which resolve the important physics of the problem needs to be specified. Here the spatial and temporal discretization is discussed. The air pocket experiment is made up of stages containing different spatial and temporal scales. The time-scale of the sloshing motion is the period of the gravity waves. While the air-escape stage occurs on the time scale of the rapidly escaping air just before closure. This means that the time step and the grid must be adjusted during the simulation to resolve these different spatial and temporal scales. The numerical settings are based on physical reasoning, and these settings are denoted grid 1 or G1. Then convergence studies are carried out in order to see the sensitivity of element and time step size on the solution. Characteristic element sizes are introduced for the sloshing and air-escape stages and are named $\Delta s_s, \Delta s_{ae}$, where the subscripts s and ae denote the sloshing and air-escape stages. In the same way characteristic time step sizes $\Delta t_s, \Delta t_{ae}$ are introduced. These numerical parameters are chosen based on physical reasoning. The G1 grid is then refined to see the sensitivity of the grid size on the solution.

For the sloshing stage the element and time step size Δs_s and Δt_s should resolve the shortest important wave component of the problem. From Dommermuth and Yue [22] 40 elements were used per wave length and 40 time steps were used per wave period. The
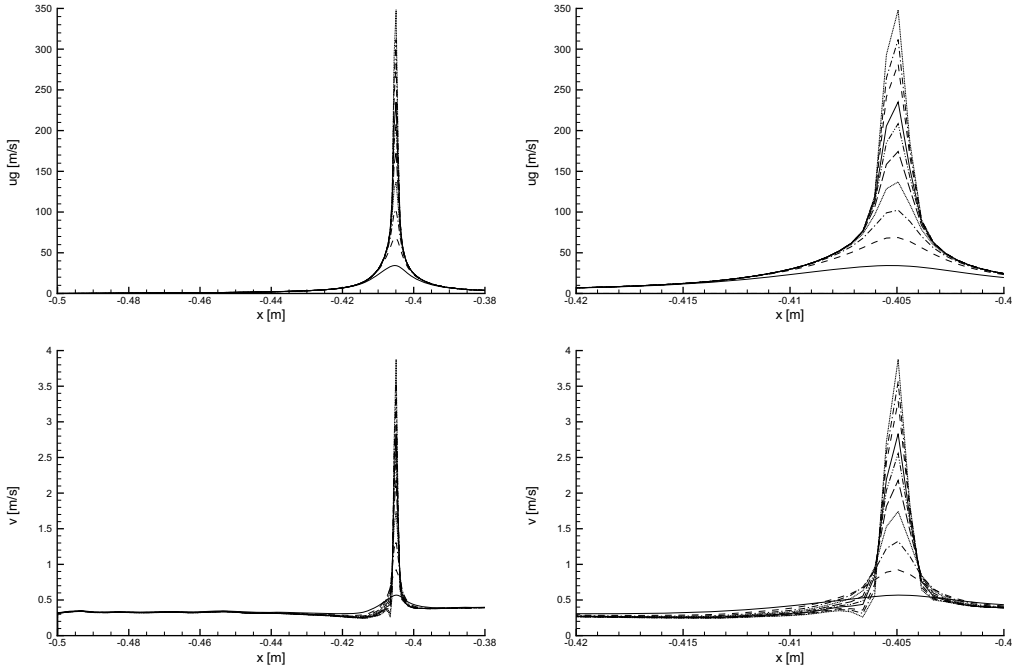
Figure 3.15: *Top:* The air velocity u_g relative to the tank in the area of the air pocket. *Bottom:* The vertical component of the velocity at the free surface in the air pocket area. The right images show close up plots of the peak in the left images.

spatial discretization method and the time integration method are comparable to the methods applied herein. Other researchers like Greco [29] also report the same number of elements to be satisfactory. Therefore 40 elements are used to resolve the shortest wave length of the problem during the sloshing stage. For air pocket 6 the smallest wave length of importance is the 9 th natural mode of sloshing. Its wavelength is $\lambda_9 = 2L/9 = 0.222$[m]. Choosing 40 elements per wave length yield approximately 180 elements along the free surface, which yields a characteristic element size of $\Delta s_s = 5.56$[mm]. This is used as the grid size along the free surface for the grid G1 seen in figure 3.13. Since the velocities of deep water waves are negligible at a depth larger than the wave length, fewer elements are used along the bottom than on the free surface. The ratio between the number of elements on the free surface and the number of elements on the bottom is set to 2. The element density function is chosen as linear along both vertical walls. The natural period for the different sloshing modes can be used to obtain information about the smallest important time scale of the sloshing stage. Utilizing equation 2.2 on page 27 yields $T_9 = 0.3772$[s]. Using 40 time steps per period results in approximately 110 time steps per second or $\Delta t_s = 9.09$[ms].

For the air-escape stage sufficient spatial and temporal refinements of the escaping air are important. Smaller grid size is then required around the wave crest while the grid size
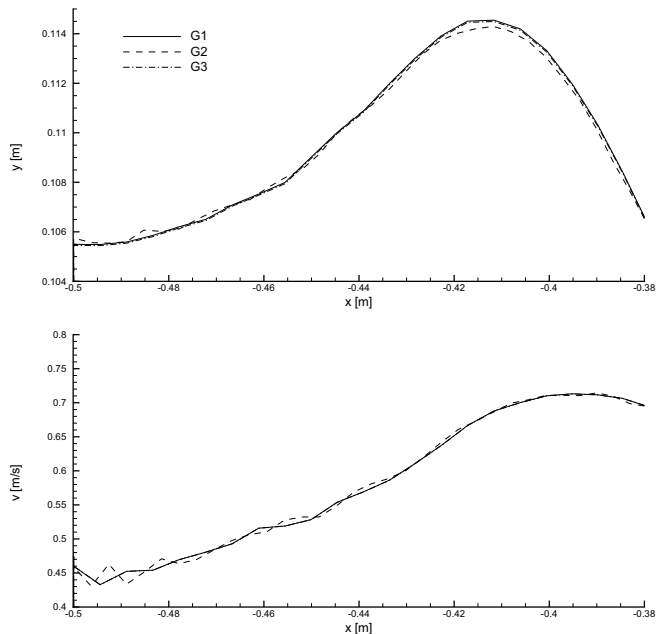
Grid	n_{top}	n_{bot}	$f_{\Delta t}$ [Hz]	$\Delta s_{ae}[mm]$	Description:
G1	180	90	110	0.556	basic grid
G2	270	180	110	-	spatial refined grid
G3	180	90	165	-	temporal refined grid

Figure 3.16: *Top*: The free surface elevation for the air pocket during the air-escape stage. *Middle*: The vertical velocity of the free surface. The results show small dependence on relatively large variations of time step and grid size.

outside the air pocket region can be increased. As the wave reaches the roof, air escapes the air pocket shape at increasing speed and the air starts to affect the free surface. The characteristic time-scale of this process is very small compared to the time-scale of the gravity waves. This means that a smaller time step must be applied. Here the time step size is set smaller than $\Delta x_i/u_{gi}$, where u_{gi} is the air velocity at node i. The time step criteria is changed when the wave crest crosses 0.11 [m] which is defined as the start of the air-escape stage. The time step criteria for the sloshing and air-escape stages are then written as:

$$\Delta t \leq \begin{cases} \Delta t_s & \text{for the sloshing stage,} \\ \min\left(\Delta t_s, \min(\frac{C\Delta x_i}{|u_{gi}|})\right) & \text{for } 1 \leq i \leq N_f \text{ in the air-escape stage.} \end{cases} \quad (3.53)$$

Here Δx_i is the grid spacing of the finite-difference method used to discretize the air and is defined in figure 3.3. C is a parameter which for the grid G1 is assumed to be 1.

Grid	Δs_a [mm]	C	Description:
G1	0.55	1	basic grid
G1b	0.55/2	1	spatial refined grid 1
G1c	0.55/4	1	spatial refined grid 2
G1d	0.55	.5	temporal refined grid 1
G1e	0.55	.25	temporal refined grid 2
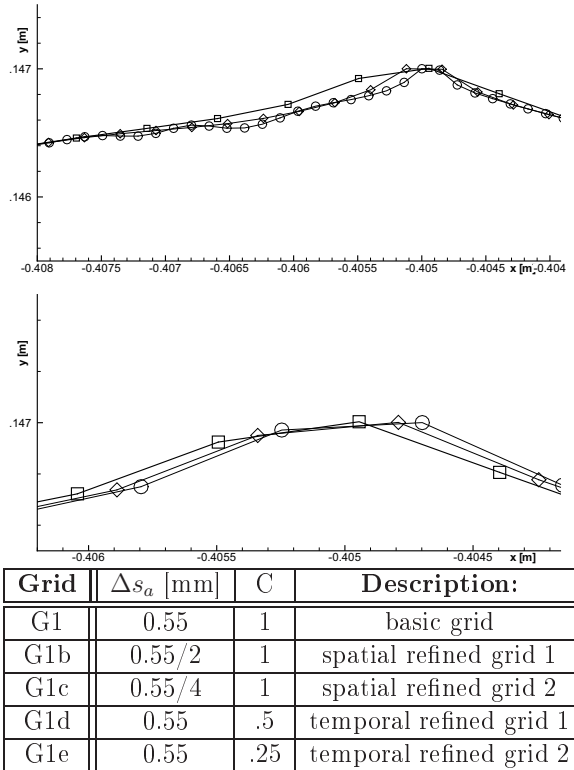
Figure 3.17: *Top:* Spatial convergence study of the air-escape stage, that is the grids G1, G1b and G1c. The plots show the free surface close to the wave peak at the time of closure of the air pocket. *Middle:* Temporal convergence study of the air-escape stage, that is the grids G1, G1d and G1e

In the experiments of chapter 2 the escaping air was seen to affect the wave peak as the wave approached the roof. The spatial scale of this interaction is seen from the upper left image of figure 2.22 to be approximately 2[mm]. To capture this spatial scale a grid size of the wave crest is set to $\Delta s_{ae} = 0.55$[mm]. To resolve the inside of the air pocket, the grid was also refined at the wall at $x = -L/2$, where the element size was set to 3.3[mm]. To avoid too many elements the grid had to be coarsened at other areas of the domain. The resulting G1 grid in the air-escape stage is seen in figure 3.13. The grid and time step sizes are seen in figure 3.16. Here n_{top} and n_{bot} refer to the number of elements along the free surface and the tank bottom at the time $t = 0$. The time step frequency is $f_{\Delta t} = 1/\Delta t_s$.

The results using the G1 grid is presented in the following. As the wave approaches the roof air escapes at increasing speed. In figure 3.14, The air pocket is shown at different time instances when the wave peak is very close to the roof. These are the time instants corresponding to Mach numbers, defined as $M = u_g^{\max}/c_0$, from 0.1 to 1 in steps of 0.1. Here
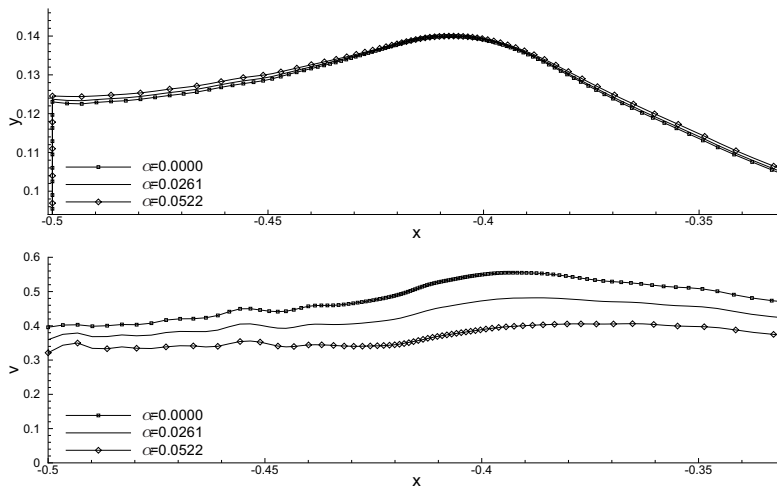
Figure 3.18: The effect of varying the modulus of decay α in the Rayleigh damping model on the free surface geometry and the impact velocity. *Top:* The shape of the free surface just prior to impact. *Bottom:* The vertical velocity on the free surface just prior to impact.

$u_g^{\max}$ is the maximum speed of the air, and c_0 is the speed of sound for the air. The numerical solution shows interaction between the water and the air when the distance between the wave peak and the roof is less than 0.5 [mm]. In the experiments a sharpened peak is also formed as seen in the images in figure 2.18. For the experiments the air pocket did not close instantaneously across the width of the tank, which is the case in the numerical model.

The air velocity and vertical component of the free surface velocity is plotted for the air pocket region in figure 3.15. The solution for both the air velocity and the vertical velocity of the free surface is dominated by a peak at the wave crest.

A grid convergence study was performed in order to identify if the solution was sensitive to spatial and temporal refinement as the wave approached the roof. These grids denoted G2 and G3 are defined in the table in figure 3.16. The effect of this variation on the free surface $\zeta(x, t)$ and vertical velocity $v(x, \zeta, t)$ on the free surface in the impact region can be seen in figure 3.16. The spatial refinement results in small vertical oscillations close to both ends of the free surface. Similar type of oscillations have been identified for other numerical methods where the water domain is discretized using the boundary element method (BEM). For instance it Tanizawa [27] reported that intersection points between the free surface and the structure can contain stability problems when a numerical wave tank is modelled in time domain using the BEM method. This is due to the inaccuracy in the calculated velocities at these points. This suggests that the oscillations seen in the present method originates from the BEM discretization of the water. The spatial refinement yields some change of the free surface elevation and suggests that the solution contains some sensitivity to further spatial refinement. The temporal refinement (grid G3) is seen not to deviate from the basic grid (G1), which indicates that the G1 solution is not sensitive to further temporal refinement.
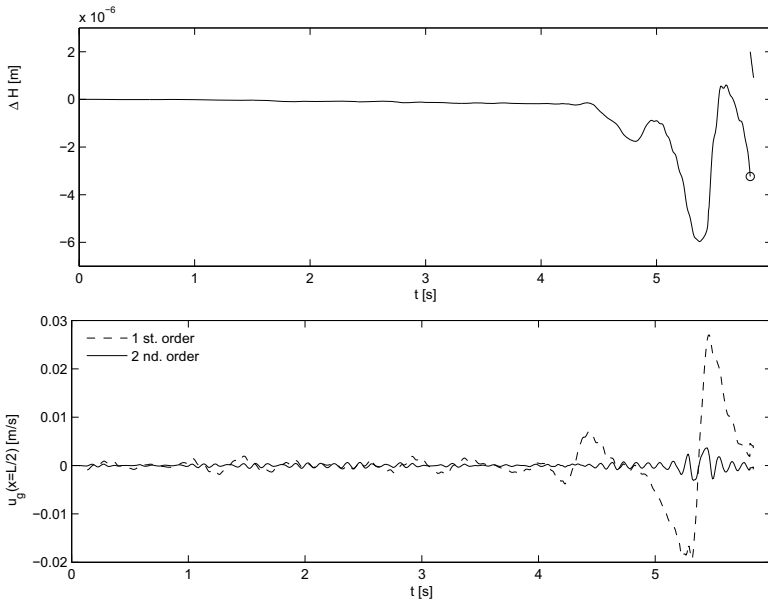
Figure 3.19: Test of global mass conservation of the water and the air.
Top: Change of mean water level $\Delta H(t)$. The ∘ denotes the time instant
when the grid at the wave crest is refined. *Bottom:* The air velocity at the
right hand side of the tank $u_g(x = L/2)$ estimated using first order and
second order backward differences in space.

A grid convergence study was also performed in order to enlight the sensitivity of grid and
time step size on the resulting free surface geometry at the time instant of closure. Sensitivity
to the wave crest grid resolution Δs_{ae} and the time step parameter C on the solution was
studied. The other parameters were set similar to the G1 grid defined previously. The grid
parameters for these grids can be seen in the table presented alongside the results in figure
3.17. A comparison of the free surface geometry at the wave crest at the time of closure is
also seen in the figure. In the upper plot the effect of grid refinement is seen and the lower
plot shows the effect of time step refinement. From this investigation it is concluded that the
solution is grid sensitive, especially to spatial refinement.

A Rayleigh damping term $-\mu\phi$ was added to Bernoulli's equation (3.10), to model the
damping effect of viscous boundary layers and meniscus effects. The Rayleigh damping
parameter μ can be estimated from equation (3.11) using a modulus of decay α from experi-
ments. The Rayleigh damping term has no physical meaning in the air pocket region during
the air-escape stage. It was tested to set this damping term to zero when the wave crest was
less than 10[mm] from the roof. The solution was seen not to be sensitive to whether the
Rayleigh damping term was active during the air-escape stage or not.

The effect of changing the value of the modulus of decay in the Rayleigh damping model
in the sloshing stage on the solution was also investigated. The free surface geometry and

the vertical velocity of the free surface is compared before impact in figure 3.18. The effect of increasing the modulus of decay α in the Rayleigh damping term from zero to 0.0522 is seen to be smaller initial volume and lower impact velocity.

Global mass conservation of the water was investigated. In order to have no mass loss or gain in the code, the integral of the free surface elevation along the tank length should be zero. This means that the mean water level ΔH should remain zero during the simulation. This is defined as:

$$\Delta H = \frac{1}{L} \int_{-L/2}^{L/2} \zeta(x,t)dx \tag{3.54}$$

This quantity is calculated every time step and is shown in the topmost plot in figure 3.19. The change of mean water level due to mass gain or loss is very small compared to the gap between the mean water level and the roof, h_1. The change of the first natural period of the sloshing motion due to the changed mean water level is also very small, that is about 10^{-6}[s]. From this the mass loss or gain is believed not to affect the wave motions. Further, mass conservation of the air is checked. From global mass conservation it is found that the air velocity u_g at $x = L/2$ should be zero. This is not enforced in the numerical method. This condition is checked by numerically differentiating ϕ_g using first and second order backward differences in space. For the second order finite difference the horizontal distance between the first and second node is assumed to be equal. The result is shown in the lower plot in figure 3.19. The air velocity at the right hand side is seen to be small, which indicates that mass is close to be conserved.

3.6 Compressible effects of the escaping air flow
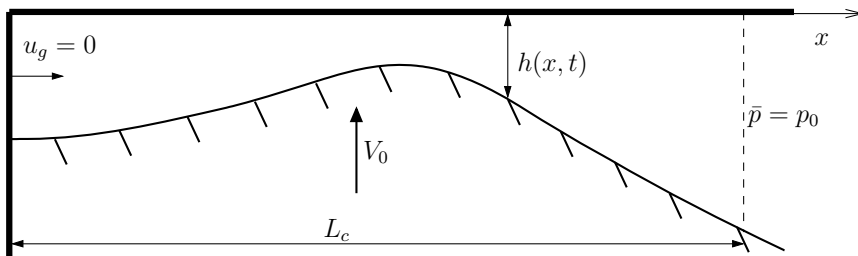
Figure 3.20: The domain of the compressible numerical model of the air-escape stage. The free surface is assumed rigid and approaching the roof at constant speed.

In this section a detailed study of the air escaping the air pocket prior to closure is made. The air flow is assumed compressible while the wave profile approaching the roof is assumed rigid. Ideally, the fact that the air flow affects the water flow should have been taken into account in the compressible calculations. However, this is a challenging problem and is not solved in this work.
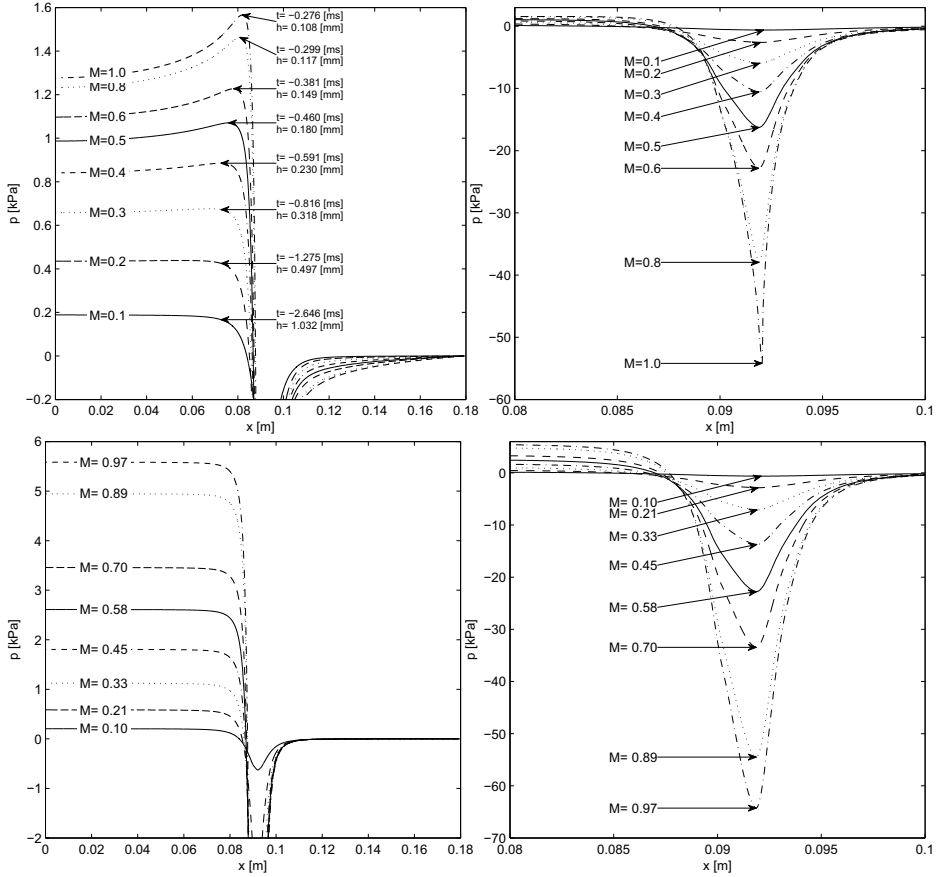
Figure 3.21: The pressure from the solution of the quasi-one-dimensional calculations before closure. The Mach number $M = u_g^{\max}/c_0$. *Top:* Compressible solution. *Bottom:* Incompressible solution.

The domain solved for can be seen in figure 3.20. Quasi-one-dimensional flow is assumed for the air since the variation of the cross section dimension h in the x-direction is small. The approaching free surface profile is rigid and hence does not deform due to the air flow. The shape of the entering free surface is taken from the boundary element solver and is shown in figure 3.20. Only the part from $x = 0$ to $x = L_c$ of the free surface is modelled. At the truncated end of the domain, at $x = L_c$, an outlet is modelled by requiring that the absolute pressure is equal to the atmospheric pressure $\bar{p} = p_0$. On the left hand side the wall condition $u_g = 0$ is applied. The rigid free surface profile approaches the wall with the speed V_0=0.39[m/s]. The ullage pressure is set to p_0=1.01$\cdot$10^5[Pa]. The density of air at this pressure is set to $\rho_{g0} = 1.204$[kg/m^3]. The length of the domain L_c is set equal to 0.18 [m].

The computer code used to solve the problem is named CLAWPACK and is described in Leveque [30]. The computer code solves the compressible quasi-one-dimensional equations
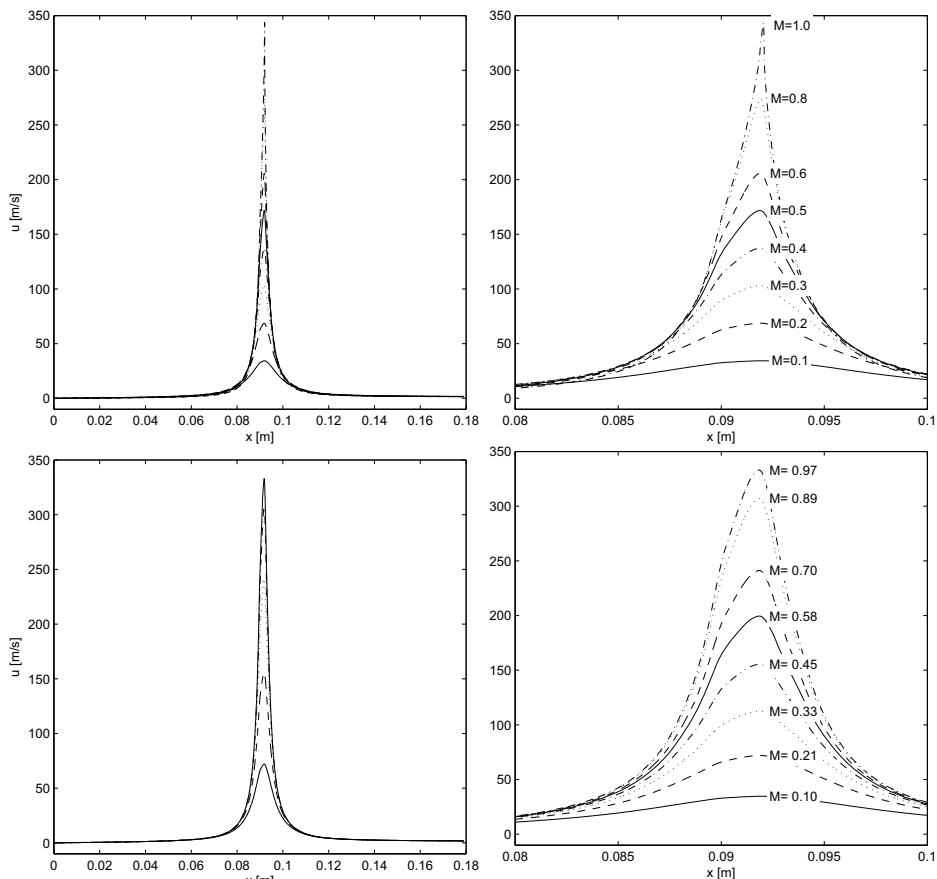
Figure 3.22: The velocity of the air from the solution of the quasi-one-dimensional calculations before closure. The Mach number $M = u_g^{\max}/c_0$.
Top: Compressible solution. *Bottom:* Incompressible solution.

using a fractional-step method. The method is further described in appendix E. The initial conditions of the problem are taken from the incompressible solution which can be found analytically. The analytical solution of the incompressible problem is given in appendix D. The maximum velocity of the air must be much smaller than the speed of sound in order for the incompressible solution to be valid. The ratio between a maximum air velocity and the speed of sound at atmospheric conditions is the Mach number defined as $M = u_g^{\max}/c_0$. If the Mach number is larger than approximately 0.1, compressibility effects start to matter. Based on this it is reasonable to start the calculation when the gap distance $h_{\min} = 4$[mm], which yields an initial Mach number of 0.04. This means that the flow is close to incompressible at the start of the simulation $(t = 0)$.

A convergence study of the solution of the compressible solver is presented in appendix E. This convergence study shows that a uniform grid of 12000 cells is satisfactory to obtain an
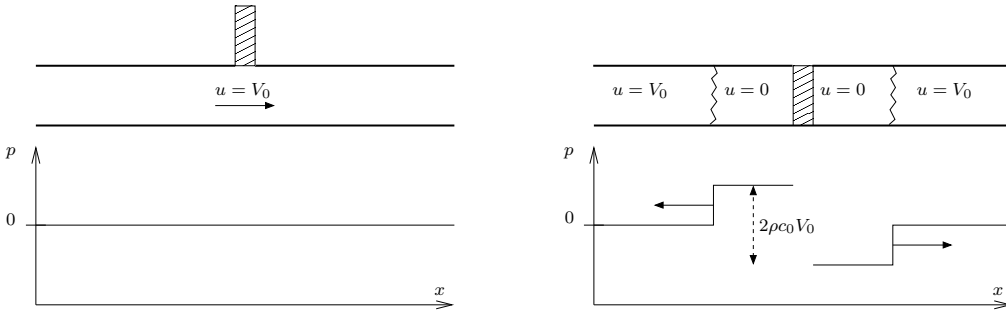
Figure 3.23: The solution of the water hammer problem. *Left:* The initial conditions of the water hammer problem. *Right:* The velocity and the pressure inside the pipe a time t after closing the valve. The valve experiences a pressure difference of $2\rho c_0 V_0$.

accurate solution for Mach numbers less than unity. Hence, the present results are not valid for Mach numbers larger than unity. At the time instant when the Mach number was equal to unity, the vertical distance between the wave crest and the roof was $h_{\min} = 0.108[\text{mm}]$. Since the air velocity is subsonic for Mach number less than unity, there are no shock waves in the presented solutions.

The solution for 12000 grid cells was then compared with the solution obtained from incompressible theory. This is seen in figure 3.21 and 3.22. The pressure from the compressible and the incompressible model are seen in the top and bottom plot of figure 3.21. The pressure from the compressible model agrees well with the incompressible results up to about $M=0.2$. This is in accordance with White [15] who writes that the incompressible theory is invalid if the Mach number is larger than about $M=0.3$. For Mach numbers higher than 0.6 the compressible calculations show a rising pressure peak just to the left of the narrowest point at $x=0.092[\text{m}]$. The corresponding air velocities are plotted in figure 3.22. The velocity profiles are quite similar for both the compressible and the incompressible model. The velocity is rapidly increasing at the narrowest point.

At some point the quasi-one-dimensional inviscid model does not resemble the physical problem anymore. The singular-like behaviour is an indication of that. At some time instant there will be important viscous effects slowing down the air at the narrowest point. There will also be important interaction effects between the water and the air which produces a distorted free surface prior to closure. This can be seen in the experiments reported in chapter 2. From the experimental images in figure 2.18 it is seen that there is a rise-up of water at the narrowest point just prior to closure. The present calculations suggests that this is a consequence of the low pressure in this region. The rise-up causes the air pocket to close rapidly and hence it serves as a valve mechanism. This is also supported by the results from the boundary-element-finite-difference method presented in the previous section. This closing mechanism suggests that the compressible effects after closure can be investigated in a simplistic way.

The rise-up of water at the wave crest resembles the boundary condition of a closing valve
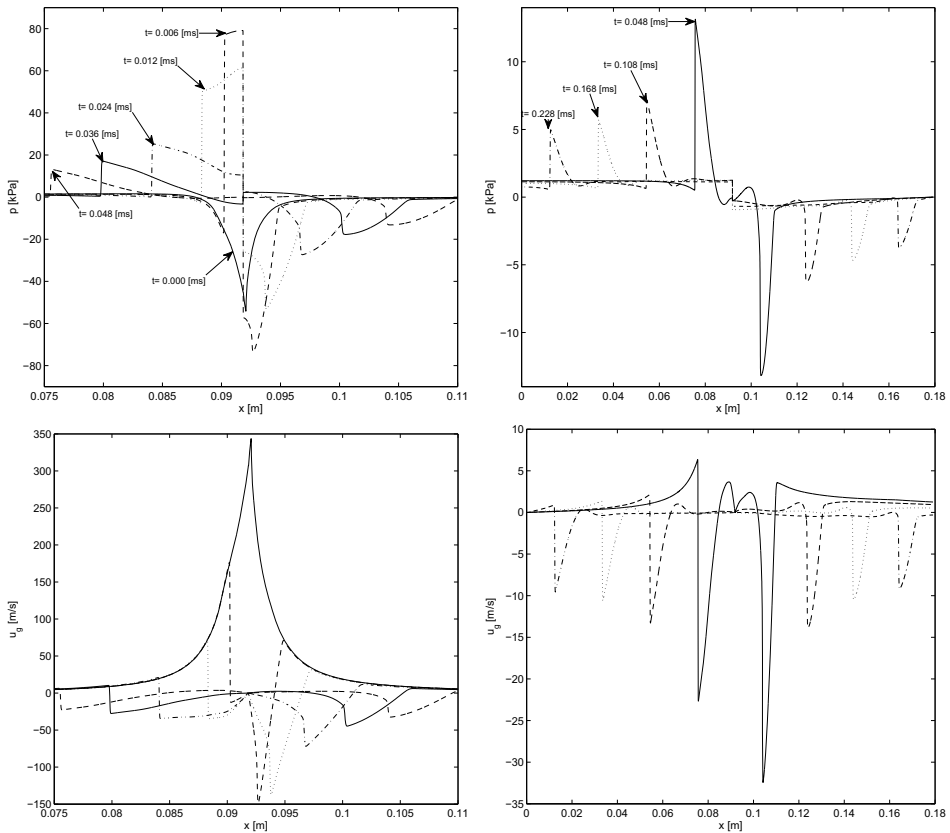
Figure 3.24: After closure of the air pocket two travelling pressure pulses are seen to travel in opposite directions away from the closure point. *Top:* The initial pressure peak just after closure. *Bottom:* The corresponding gas velocity.

in a pipeline. If the flow inside a pipeline is suddenly closed the compressible phenomenon called a "water hammer" can occur. The phenomenon called water hammer is described thoroughly by Wylie and Streeter [31]. A brief description is presented here in connection with figure 3.23. On the upper left drawing an infinitely long horizontal pipe is seen where a fluid is seen to flow at constant speed for all times $t < 0$. The velocity of the fluid V_0 is assumed to be small compared to the sound velocity. At $t = 0$ the pipe is suddenly closed. This is the situation at the right hand side drawing. The information about the blockage is transferred upstream and downstream at a speed equal to the speed of sound. The amplitude of the pressure pulse is given by the formula:

$$p = 2\rho_g c_0 V_0. \tag{3.55}$$

However, the formula is not useful for our problem since the velocity before blockage is
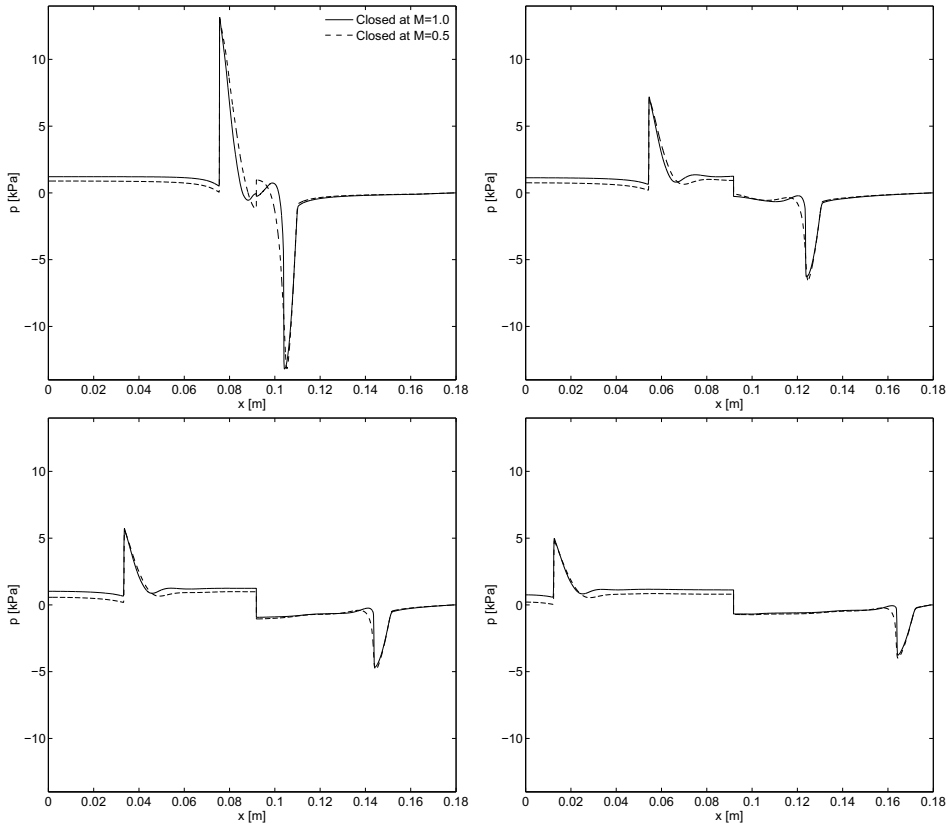
Figure 3.25:   The pressure is plotted for sudden closure at M=1.0 and
M=0.5. The time instances are the same as investigated at the upper right
plot of figure 3.24.

time dependent, and rapidly changing during closure. To investigate the role of compress-
ibility just after closure of the air pocket, the flow in the case studied previously was stopped
instantly at the time when $h_{\min}=-0.108$[mm] and $M = 1.00$. At this time instant the con-
dition of zero air velocity is set at the narrowest point and the vertical motion of the rigid
free surface V_0 is set to zero.

The results are seen in figure 3.24. The left hand side of the plot shows the pressure and
the velocity close to the narrowest point just after closing the air pocket. The right hand side
shows the pressure and velocity at later times as the information of the closure travels up-
and downstream. The pressure peaks decay as they leave the narrow region. This is due to
the expansion of the domains on both sides of the closure point. The pressure and velocity
have similarities with the "fluid hammer" model. Neglecting the travelling pressure peaks the
solution is seen to form a step function at the closing point. From the velocity it is seen that
the air is nearly stopped in the area between the peak pressure and the closing point.

The air pocket was suddenly closed when the Mach number was equal to unity. The convergence study presented in appendix E shows that the grid resolution of 12000 cells is not sufficient to continue simulation after a Mach number of unity is reached. The sensitivity of the time of closure was investigated by closing the air pocket when the Mach number was 0.5. A comparison of the resulting pressure in the air pocket for the time instances shown in the upper right plot of figure 3.24 are seen in figure 3.25. The results show some dependence of when the pocket is suddenly closed. The most important deviation is that the pressure at $x = 0$ is lower when the pocket is closed at $M = 0.5$ than when the pocket is closed at $M = 1.0$. This pressure difference is comparable to the pressure difference at $x = 0$ before closure, seen in figure 3.21.

The present investigation shows a clear effect of compressibility for $h_{\min} < 0.5$[mm] which corresponds to Mach numbers $M > 0.2$. Based on the compressible model it is possible to estimate the average pressure inside the air pocket at the time of closure. The mean pressure is of importance because it is used as a parameter in the lumped air pocket model used in the numerical model of the air pocket oscillation stage which is presented in the next chapter.

Chapter 4

Numerical solution of air pocket 6

In the previous chapter a two-dimensional numerical model called the boundary-element-finite-difference method was established to model the sloshing and air-escape stages of the air pocket experiment. In this chapter a numerical model of the air pocket oscillation stage is presented. First the mathematical problem is posed and then it is solved numerically. This numerical solution uses many of the ingredients already presented in the previous chapter. After this the numerical procedure is applied to a test case before it is applied to the simulation of the air pocket oscillation stage of air pocket 6. The numerical solution of the sloshing and air-escape stages presented in the previous chapter, using the boundary-element-finite-difference method, is used as initial conditions for the numerical simulation of the air pocket oscillation stage. The numerical method used for the air pocket oscillation stage is called the mixed Eulerian-Lagrangian method (MEL). This way of solving the mathematical problem was originally proposed by Ogilvie [20].

4.1 Mathematical problem of the oscillation stage

The boundary-element-finite-difference method presented in the previous chapter is used to solve for air pocket 6 until the wave hits the roof. As the wave crest hits the roof, the assumptions of a quasi-one-dimensional flow is invalid. Here the air pocket is closed in an ad-hoc manner which makes it possible to simulate the air pocket oscillation stage. The mathematical problem for the numerical model of the air pocket oscillation stage is presented here alongside the physical assumptions behind it.

Based on the time scale of the pressure oscillations it is reasonable to assume that the water is incompressible. The model of the water is further simplified by assuming inviscid, irrotational flow. This means that potential flow theory can be used for the water. The water is therefore treated in the same way as for the sloshing stage, by solving the boundary integral equation (3.1). This equation is hence given in the mathematical problem of the air pocket oscillation stage posed in figure 4.1. Boundary conditions on all boundaries are required to solve this equation. On the walls and the wetted part of the roof the same boundary condition as for the sloshing stage applies, that is (3.12). From the experiments presented in chapter 2, the wave elevation is seen not to be a single-valued function of the
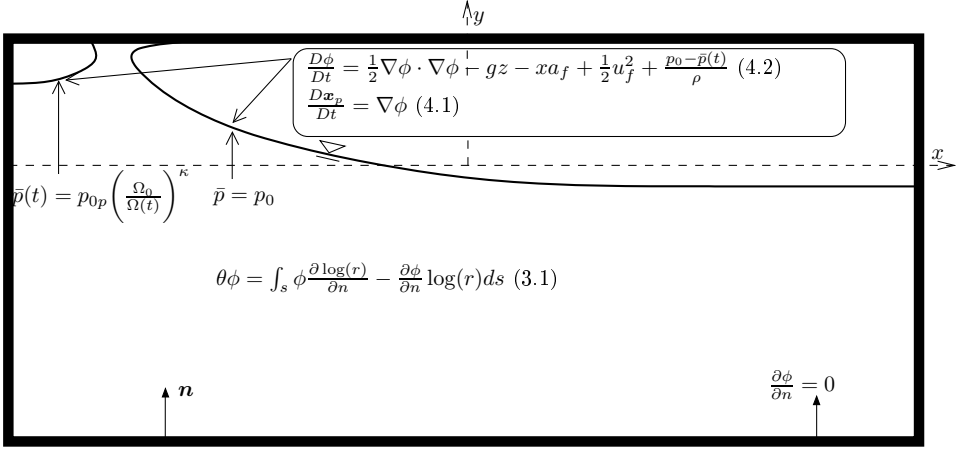
Figure 4.1: The mathematical problem of the air pocket oscillation stage solved for by the mixed Eulerian-Lagrangian method (MEL). The equations inside the box are used for the time integration.

horizontal coordinate in the jet areas. Hence the nodes on the free surface is set to follow the free surface particles in both the vertical and the horizontal direction. The kinematic free surface condition is then given as:

$$\frac{D\boldsymbol{x}_p(t)}{Dt} = \nabla\phi. \tag{4.1}$$

Here $\boldsymbol{x}_p(t)$ is the position of a fluid particle on the free surface. The notation $D()/Dt = \partial()/\partial t + \nabla\phi \cdot \nabla()$ has been used. Evaluating Bernoulli's equation (3.8) on the free surface and inserting the pressure in the air, the dynamic boundary condition appears as:

$$\frac{D\phi}{Dt} = \frac{1}{2}\nabla\phi \cdot \nabla\phi - gz - xa_f + \frac{1}{2}u_f^2 + \frac{p_0 - \bar{p}(t)}{\rho}. \tag{4.2}$$

Here p_0 is the ullage pressure inside the tank defined as the uniform pressure when there is no liquid motion. In this work the ullage pressure is set equal to the atmospheric pressure, that is $p_0 = 1.01 \cdot 10^5$[Pa]. $\bar{p}(t)$ is here equal to the absolute gas pocket pressure at the free surface inside the air pocket or equal to the ullage pressure at the free surface outside the air pocket. As seen from the experiments the pressure was seen to be spatially uniform inside the air pocket for the sample frequency used. Hence the pressure is assumed to be uniform in space for the mathematical model of the air pocket. The air pocket can then be modelled using only one unknown. This model is denoted the "lumped" air pocket model and is explained as follows. Before the air pocket is closed it is assumed that the absolute pressure is equal to the unknown initial pressure denoted p_{0p}. If the compression is assumed adiabatic or isothermal, then there is a simple relation between the density and the pressure given by,

$$\bar{p}(t) = p_{0p}\left(\frac{\rho_g}{\rho_{gp}}\right)^{\kappa}. \tag{4.3}$$

Here ρ_{gp} is the gas density inside the air pocket at the time when the air pocket is closing. If the gas is air and the compression is adiabatic then $\kappa = 1.4$. However, if the compression is isothermal $\kappa = 1$. Mass conservation of the air pocket assuming no air leakage, is written as $\rho_g \Omega = \rho_{gp} \Omega_0$. Here $\Omega(t)$ is the volume of the air pocket and Ω_0 is the volume of the air pocket at the time of closure. A relation between the absolute pressure inside the air pocket and the volume of the air pocket can then be written as

$$\bar{p}(t) = p_{0p} \left(\frac{\Omega_0}{\Omega(t)} \right)^{\kappa}. \tag{4.4}$$

It is not easy to state whether the compression is adiabatic or isothermal. This depends on the heat flow between the air pocket and the surrounding water. Verhagen [7] and Koehler and Kettleborough [32] studied the impact of a flat plate onto an undisturbed free surface. Verhagen assumed the compression to be adiabatic while Koehler and Kettleborough assumed it to be isothermal. For their problem the air pocket was thin which increases the heat exchange between the air and the water. In addition, experimental observations by Verhagen [7] suggests that mixing of water and air occur during the compression. This phenomena also increases the heat exchange between the air and the water. In reality the heat flow between the air pocket and the liquid needs to be modelled in order to find the correct pressure-volume relationship. This is done in chapter 5 under the assumption of linear theory, one-dimensional heat flow and uniform pressure inside the air pocket. It should be noted that equation (4.3) does not model the effect of the air pocket correctly under dynamic conditions, even with an optimally fitted value for the polytropic index. The reason is that the damping due to exchange flow is not included. The thermodynamic aspects of the air pocket is studied in detail in chapter 5. The results from the thermodynamic analysis show that an adiabatic assumption is more appropriate than an isothermal assumption. When using equation 4.4 in the mixed Eulerian-Lagrangian method (MEL) adiabatic conditions are assumed. Adiabatic conditions yield $\kappa = \gamma$, where γ is the ratio of specific heats $\gamma = c_p/c_v$.

In addition, the polytropic gas model also does not account for the acoustic effects present just after closure of the air pocket. These effect was denoted the "fluid hammer" effect in section 3.6. In the following the initial pressure inside the air pocket is set equal to the ullage pressure, that is, $p_{0p} = p_0$. This means that the increased pressure inside the air pocket, which is caused by the escaping air prior to closure, is neglected. From the compressible model of the escaping air prior to closure, in section 3.6, the increased air pressure inside the air pocket due to the escaping air was found to be about 1 [kPa]. The sensitivity of the initial pressure p_{0p} inside the air pocket on the resulting pressure oscillations is later investigated in section 4.2.

4.2 Numerical solution of the air pocket oscillation stage

The numerical method used for the oscillation stage has similarities with the numerical method used by Zhang et. al. [6] to investigate the plunging wave impact on a vertical wall. This means that it is based on the Mixed Eulerian-Lagrangian method pioneered by Ogilvie [20] and later developed by Longuet-Higgins and Cokelet [21] and Faltinsen [18]. Using the

same boundary element description for the liquid as for the boundary-element-finite-difference method, equation (3.35) is expressed as:

$$\begin{bmatrix} \boldsymbol{G}_f & \boldsymbol{G}_s \end{bmatrix} \begin{Bmatrix} \boldsymbol{\phi}_f \\ \boldsymbol{\phi}_s \end{Bmatrix} = \begin{bmatrix} \boldsymbol{H}_f & \boldsymbol{H}_s \end{bmatrix} \begin{Bmatrix} \boldsymbol{\sigma}_f \\ \boldsymbol{\sigma}_s \end{Bmatrix}. \tag{4.5}$$

The unknown variables of this equation system are moved to the left hand side and the known variables to the right. From the dynamic free surface condition (4.2) the velocity potential on the free surface ϕ can be integrated in time in an explicit fashion, and is hence known when the equation system (4.5) is solved. From the boundary condition on the wall (3.12) $\boldsymbol{\sigma}_s$ is known. The unknowns of (4.5) are then $\boldsymbol{\sigma}_f$ and $\boldsymbol{\phi}_s$. The following equation system is then obtained:

$$\begin{bmatrix} \boldsymbol{H}_f & -\boldsymbol{G}_s \end{bmatrix} \begin{Bmatrix} \boldsymbol{\sigma}_f \\ \boldsymbol{\phi}_s \end{Bmatrix} = \begin{bmatrix} -\boldsymbol{H}_s & \boldsymbol{G}_f \end{bmatrix} \begin{Bmatrix} \boldsymbol{\sigma}_s \\ \boldsymbol{\phi}_f \end{Bmatrix}. \tag{4.6}$$

Here ϕ_f is stepped forward using the same integration method as used for the boundary-element-finite-difference method in chapter 3, that is the explicit Runge-Kutta method of fourth order as defined by Kreyszig [24]. The position of the free surface is updated using (4.1) for each of the four sub-steps in the Runge-Kutta time integration procedure. This numerical method is denoted the mixed Eulerian-Lagrangian method (MEL).

4.3   Test case
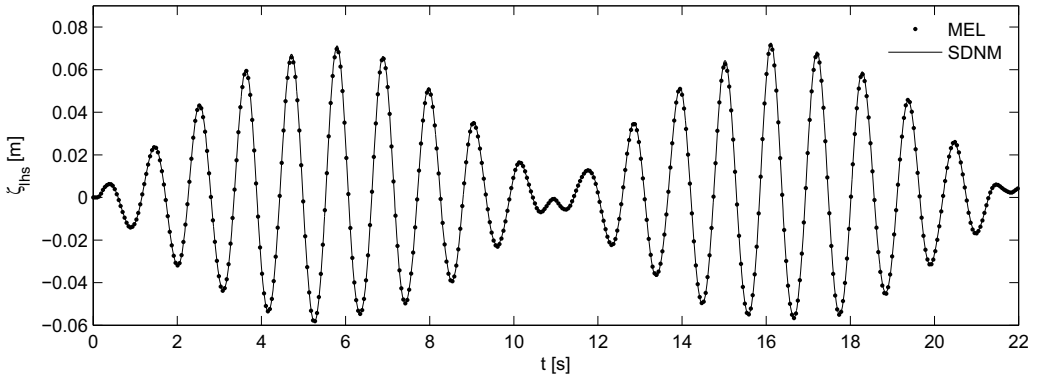
Figure 4.2: Comparison of the water elevation $\xi(t)$ on the left hand side tank wall of a sloshing tank for the mixed Eulerian-Lagrangian method (MEL) and the single-dominant nonlinear multimodal method (SDNM).

The numerical implementation of the mixed Eulerian-Lagrangian method (MEL) was compared with the single-dominant nonlinear multimodal method (SDNM) as described by Faltinsen and Timokha [8]. This is the same nonlinear sloshing test case as used for the boundary-element-finite-difference method (BEFDM) in section 3.4. The tank dimensions
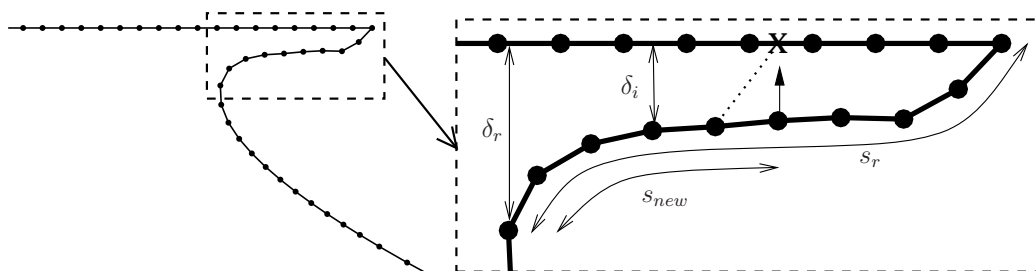
Figure 4.3: *Left:* The right going jet formed during the air pocket oscillation stage. *Right:* A close view of the jet. The jet is cut by moving the indicated node onto the roof.

were set equal to the size of the tank used in the experiments, that is $L = 1$[m] and filling height $H = 0.833$[m]. The water density was set to $\rho = 1000$[kg/m^3] and acceleration of gravity $g = 9.81$[m/s^2]. Since the first mode is dominating the response, 40 element over the free surface and 150 time steps per second were found to be enough through a convergence study. The excitation signal defined in connection with equation (3.52) was used, and the same solution of the single-dominant nonlinear multimodal method was used for comparison. Comparison of the wave elevation on the left side of the tank ξ_{lhs} is shown in figure 4.2. The two methods are in good agreement.

4.4 Numerical trick: Jet cutting

Just after the initial contact between the free surface and the roof, very thin jets are formed. These very thin initial jets are not believed to be important for the behaviour of the air pocket. However, as observed by Zhao and Faltinsen [33], they need to be discretized using small elements in order to avoid numerical instability. Regridding is hence required and is performed using the same procedure as Sun [28]. The regridding is performed every time step to avoid distortion of the grid. The jets also need to be cut to avoid breakdown of the numerical procedure. Zhao and Faltinsen [33] cut the jet when the angle between free surface and the structure at the jet tip was less than a certain value. Here the jet is cut based on two geometric properties defined in figure 4.3. Here δ_r is the shortest distance between the leftmost node on the free surface and the roof and is called the root thickness. s_r is the length of the free surface between the root node and the tip. δ_i is the distance between the node and the roof, for all nodes in the region defined by s_r. Based on this set of parameters two geometrical jet cutting criteria are defined:

1. The jet is cut if it is too thin. If one node on the free surface of the jet is closer to the roof than a certain fraction of the characteristic element length Δs of the jet then that node is moved to the roof and all elements on the right of this node is deleted. This means that for all nodes i between the jet root node and the jet tip node it is checked if $\delta_i < \Delta s/n_f$. If this condition is satisfied, then all nodes to the right of this node are

deleted and the first node satisfying the criteria is moved to the roof. (The value used for n_f in this work was 40.)

2. The jet is cut if the jet is too long compared to the root thickness. If $s_r > \delta_r C_1$, then the jet is cut at the node which is closest to $s_{new} = \delta_r C_2$ from the jet root. See figure 4.3 for dimensions. (The values of $C_1 = 2.7$ and $C_2 = 1.5$ were seen to work fine for the simulation of air pocket 6 presented here.)

After moving the node vertically onto the roof, the same value of ϕ as before the transfer is used. This can be justified by the fact that the flow is horizontal in the jet and hence that the velocity potential does not vary significantly through the thickness of the jet.
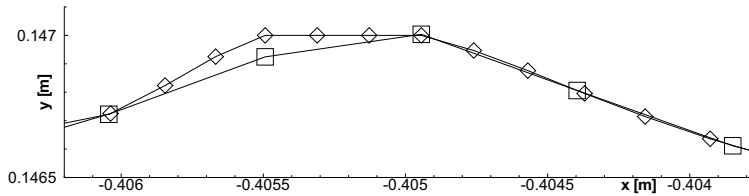
Figure 4.4: The ad-hoc procedure for closing the air pocket at the end of the air-escape stage. The grid G1 before closure is seen as squares (□) and after closure is seen as diamonds (◇).

4.5 Numerical solution of the air pocket oscillation stage

Figure 4.5: The grid used by the mixed Eulerian-Lagrangian method for the air pocket oscillation stage. The grid is refined in the area of the jet roots. The dots indicate every fourth node of the grid G1.
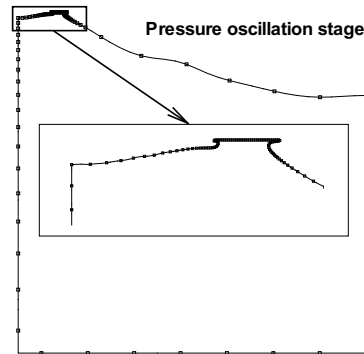
To start the numerical simulation using the mixed Eulerian-Lagrangian method a finite length of the roof needs to be wet. This can be achieved in many ways. Greco and Faltinsen [12] used an analytical solution to step the solution onto a very large floating structure (VLFS). However, the experiments in chapter 2 show that for the present problem there

are interaction effects with the air which complicates the work of finding such an analytical solution. A pragmatic ad-hoc procedure is hence used to step the solution onto the roof before the oscillation stage. At the end of the air-escape stage, when the peak node has just crossed the roof, the two highest nodes (largest y-value) are moved to the roof.
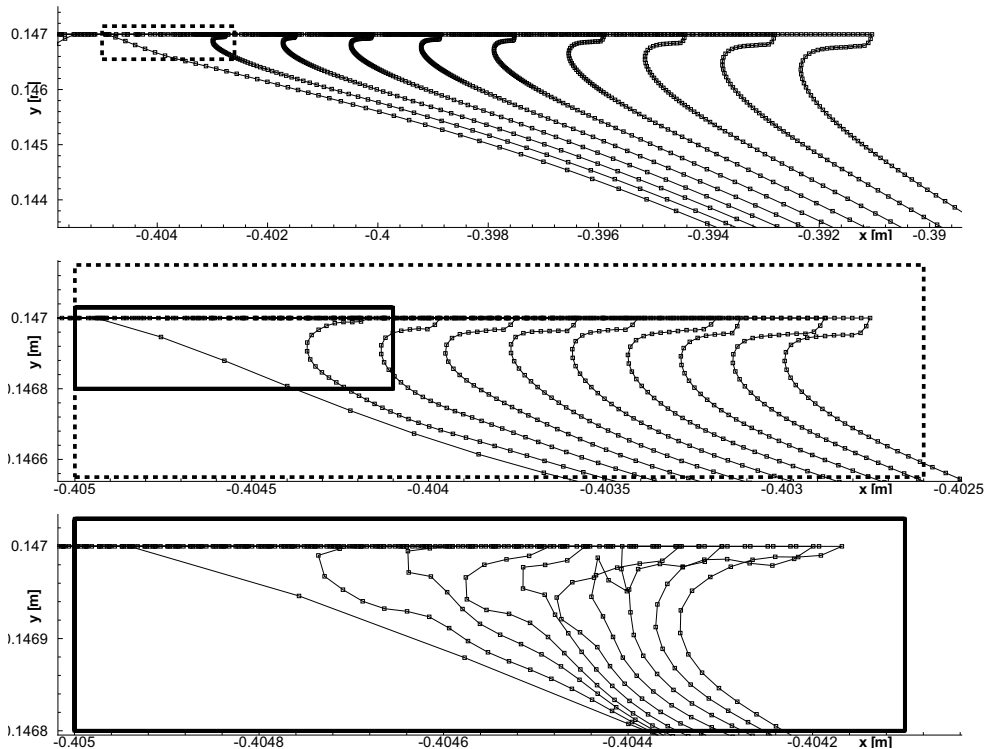
Figure 4.6: *Top:* Results from the mixed Eulerian-Lagrangian method using grid 1 (G1) showing the right going jet during the time from initial contact until the time of maximum pressure. *Middle:* A closer view of the jet during the time it is inside the dashed box in the upper image. *Bottom:* A closer view of the initial jet during the time the jet is inside the solid box of the middle image.

This procedure is seen in figure 4.4 where the area close to the wave crest touching the roof is seen. The squares (□) are the solution from the boundary-element-finite-difference method using the G1 grid settings. The peak node has crossed the roof marginally. This makes the boundary-element-finite-difference method invalid since it requires a finite height of the air domain h. However, to start the mixed Eulerian-Lagrangian solver, a finite wetted section of the roof needs to be defined. The vertical velocity of the free surface was seen to be larger at the top of the wave crest, both in the experiments and in the numerical solution for the air-escape stage. This suggests that fictitiously moving the closest neighbouring node

onto the roof and continue the simulation might be accurate enough to capture the later air pocket oscillations. The grid used as initial conditions for the mixed Eulerian-Lagrangian method (MEL) is seen as diamonds (⋄) in figure 4.4. On the roof the grid is resolved using three boundary elements to roughly capture the solution which contains a right and a left going jet. These jets are formed in each direction and are cut as described in section 4.4.
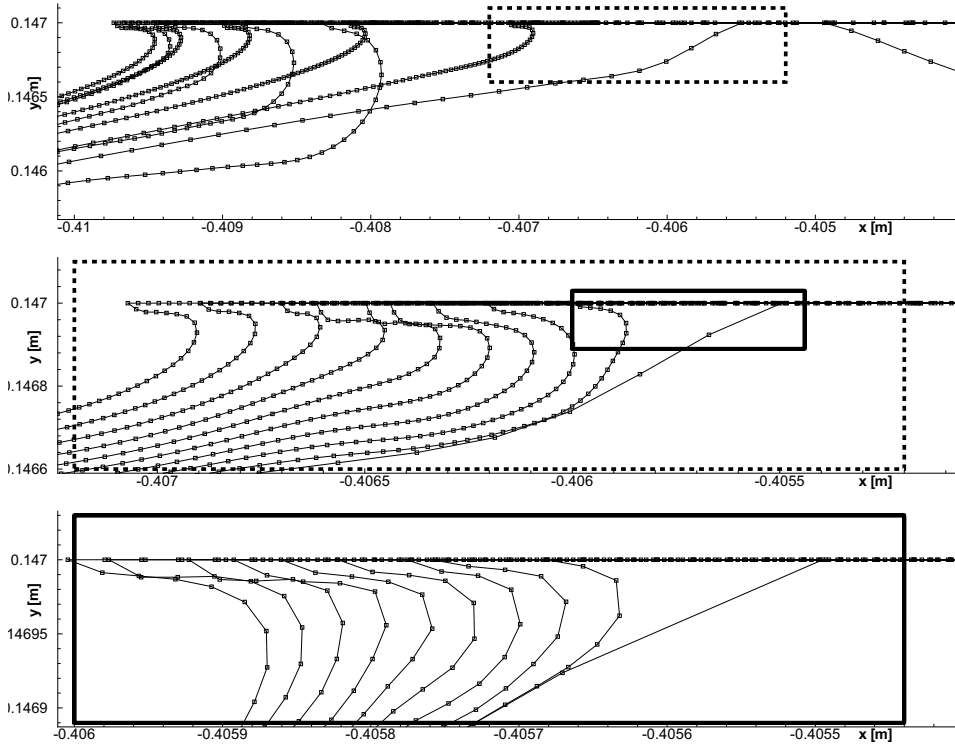
Figure 4.7: *Top:* Results from the mixed Eulerian-Lagrangian method using grid 1 (G1) showing the left going jet between the time of closure and the time of maximum pressure. *Middle:* A closer view of the jet during the time it is inside the dashed box in the upper image. *Bottom:* A closer view of the initial jet during the time the jet is inside the solid box of the middle image.

In section 3.5 the sloshing and air-escape stages were simulated using the boundary-element-finite-difference method. The time step size and grid resolution was argued on a physical basis and a standard setting of the numerical parameters was defined and was denoted G1. Here the spatial and temporal discretization of the air pocket oscillation stage are defined. This means that the characteristic element and time step size Δs_o and Δt_o of the air pocket oscillation stage will be defined.

During the air pocket oscillation stage, thin jets are formed. As previously mentioned
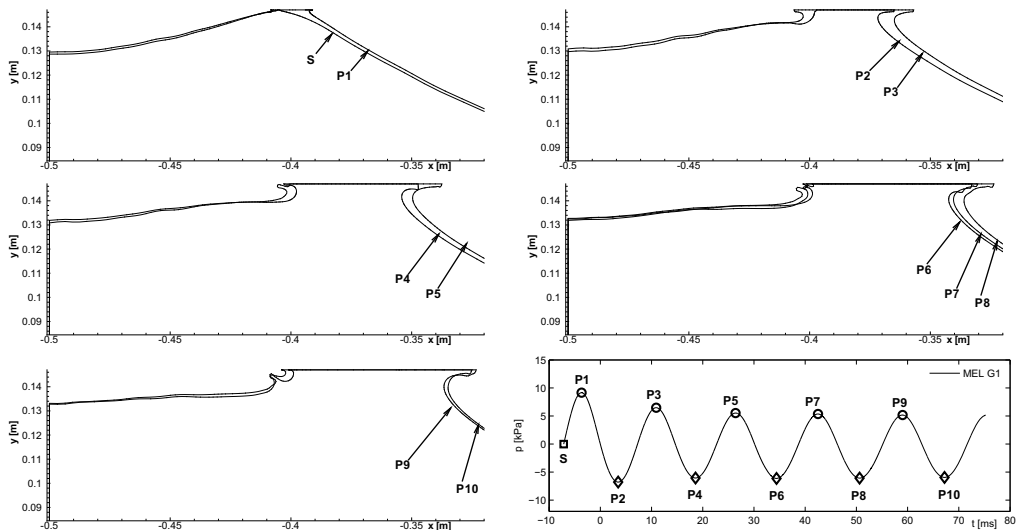
Figure 4.8: Results from the mixed Eulerian-Lagrangian method using grid 1 (G1) showing the free surface geometry during the air pocket oscillation stage. The time instances of the pressure oscillations are seen on the lower right plot.

these jets must be resolved in order for the numerical method not to break down. In order to have a stable jet it requires that the jet root is resolved with enough elements. If this is not the case the angle between neighbouring elements become too large and the mixed Eulerian-Lagrangian method breaks down. The G1 grid is shown in figure 4.5. Here the characteristic element size of the jet is $\Delta s_o = \Delta s_{ae}/21$ resulted in a numerical solution that did not break down. The velocities of the jets and the corresponding time scale $\Delta s_o/u$ must be resolved in order to avoid numerical instability problems. The time step criteria for the air pocket oscillation stage is hence written as:

$$\Delta t_o \leq \min\left(\Delta t_{os}, \min(\frac{\Delta s_o}{|u|})\right) \qquad \text{For both jet tips.} \qquad (4.7)$$

Here Δt_{os} is the time scale of the air pocket oscillation, that is 15 [ms], divided by 100.

The evolution of the right and left going jets are seen in the figures 4.6 and 4.7, respectively. The topmost images in the two figures show the jet geometry during the time from the moment when the mixed Eulerian-Lagrangian method (MEL) simulation starts ($t = t_0$) and until the pressure reaches its peak value $p = P_1$ at the time $t = t_0 + T$. The duration of this period T is denoted the rise time. The time between the different jets are $T/9$. The topmost images of the two figures contain a rectangle (dashed). This rectangle contains the area where the jet is during the time $t_0 \leq t \leq t_0 + T/9$. This area is shown in full size in the second images. Here the time between the different jets are $T/81$. The second images again contain a smaller rectangle showing the jets during the time $t_0 \leq t \leq t_0 + T/81$. A full size image of this region is shown in the third (bottom) image where the time between each jet is

$T/729$. From the bottom image of figure 4.6 it is seen that the free surface develops a wrin-
kled pattern on the jet. These wrinkles can lead to breakdown of the numerical simulation.
These wrinkles are sensitive to both the grid size and the time step, which makes it difficult
to do a proper convergence study of the air pocket oscillation stage. However, it is believed
that these wrinkles of the jet do not affect the global behaviour of the air pocket oscillations
significantly.
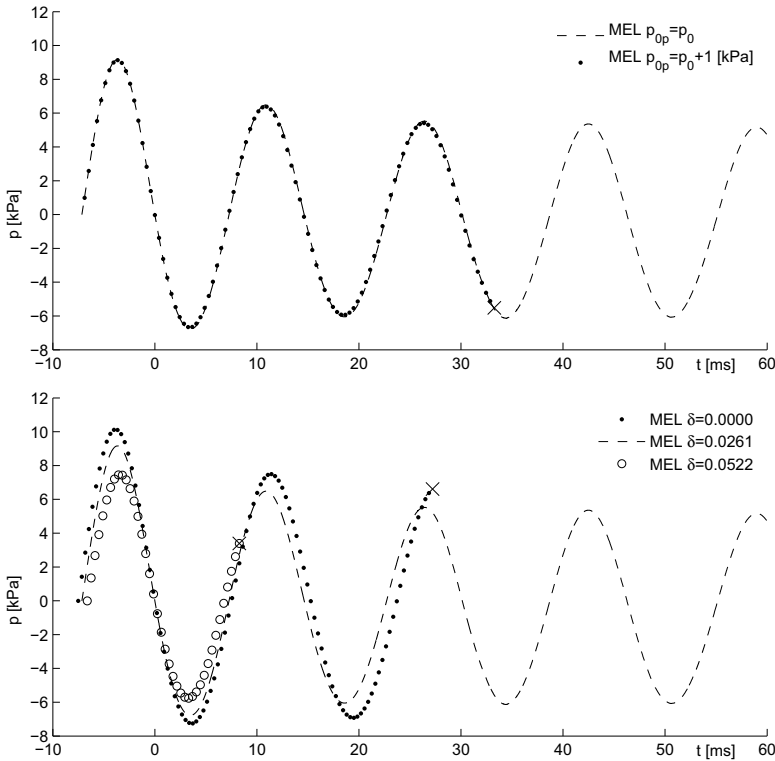
Figure 4.9: *Top:* The effect of changing the initial pressure p_{0p} on the
pressure time history. *Bottom:* The effect of changing the Rayleigh damp-
ing parameter δ on the pressure time history. The solution breaks down at
the time instant denoted X.

The pressure inside the air pocket is found from the volume of the air pocket as seen from
equation 4.4. However, when the left going jet is cut the volume is increased which results
in a fictitious pressure drop inside the air pocket. This means that the volume of the jet
which is removed should be subtracted from the later calculated volume in order to obtain
the correct pressure.

The air pocket geometry during the air pocket oscillation stage from the MEL results
using the grid settings G1 is seen in figure 4.8. The lower right plot shows the pressure
time history and the time instants where the air pocket geometry is shown. The free surface

geometry is changing during the air pocket oscillations. An instability is seen to grow inside
the air pocket next to the left going jet. This instability grows and causes the simulation to
break down at $t = 76$[ms].

The initial pressure inside the air pocket p_{0p} in equation (4.4) is set to atmospheric pressure
p_0 for the calculations using the G1 grid. In section 3.6 the air flow out of the air pocket
prior to closure was modelled assuming that the free surface profile was rigid. The resulting
pressure inside the air pocket can be seen in figure 3.21. It is seen that the pressure increases
inside the air pocket as the wave profile approaches the roof. Based on these pressure curves
the effect of increasing the initial pressure inside the air pocket with 1[kPa] was investigated.
This is presented in the upper plot of figure 4.9. The effect on the resulting pressure time
history is seen to be small.

In section 3.5 the effect of varying the Rayleigh damping coefficient on the inflow con-
ditions was investigated. Here the effect of varying the Rayleigh damping coefficient on the
resulting pressure oscillations is investigated. The results are seen in the lower plot in figure
4.9. From the inflow conditions seen in figure 3.18 it is seen that an increased δ value reduces
the impact speed and the volume of the air pocket. The effect of increased δ on the pressure
oscillations is seen to be decreased pressure amplitude and increased oscillation frequency.
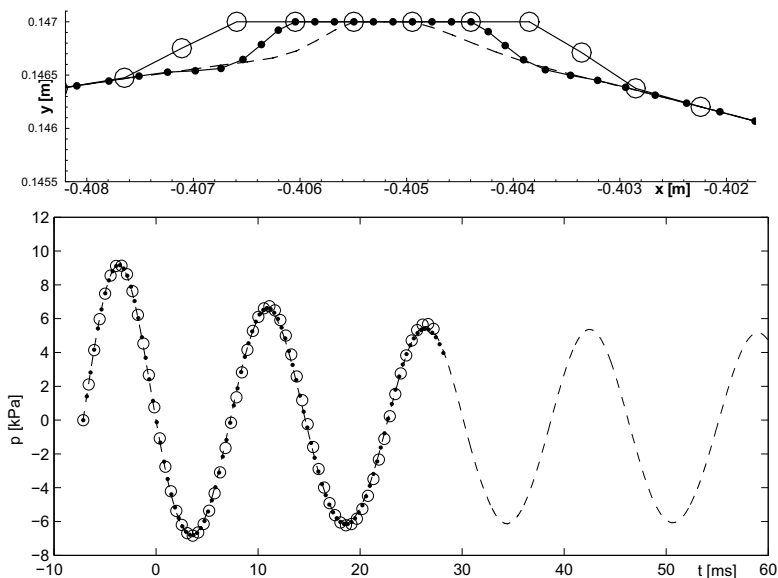
Figure 4.10: The initial conditions for the mixed Eulerian-Lagrangian
method using grid 1 (G1) is varied to check the sensitivity to the ad-hoc
closing procedure. *Top:* The grids used as initial condition for the MEL
simulation. *Bottom:* Pressure time history resulting from the calculations.

To investigate how sensitive the pressure time history was to the ad-hoc closing procedure
seen in figure 4.4, the initial wetted length of the roof was varied. In the topmost plot in
figure 4.10 the nodes of the new grids are seen as ● and ○, while the previous results from

grid G1 is seen as ——. The resulting pressure time history can be seen in the lower plot in the same figure. The pressure time history is seen not to be sensitive to the perturbations.

Chapter 5

Semi-analytical model of the air pocket oscillation stage

In the previous chapter it was shown that the mixed Eulerian-Lagrangian method (MEL) broke down after about four periods of the air pocket oscillation stage. In the present chapter the whole air pocket oscillation stage is solved for using the semi-analytical method (SAM) of Faltinsen and Timokha [8]. This method is extended to include the damping effect of heat transfer to and from the air pocket and the damping effect due to viscous boundary layers in the liquid at the tank walls.

5.1   Background of the semi-analytical model (SAM)

A brief background of the original semi-analytical air pocket model (SAM) is given next. For a more thorough description of the method see Faltinsen and Timokha [8]. The semi-analytical method (SAM) uses potential flow theory to describe the liquid motion. The velocity potential is written as $\phi + V_0 y$. The solution domain and the coordinate system used are seen in figure 5.1. The free surface conditions are enforced at the line $y = 0$. The free surface condition for $x < -a$ is $\phi = 0$, which is commonly used in slamming analysis and for high-frequency oscillation problems. Along the wetted section of the roof $-a < x < -b$ the boundary condition is $\partial \phi / \partial y = -V_0$. The hydrodynamic pressure is linearised and is given as $p = -\rho \partial \phi / \partial t$. Since the pressure is assumed uniform inside the air pocket, the velocity potential is constant along the projected free surface on $y = 0$ for $-b < x < 0$. The velocity
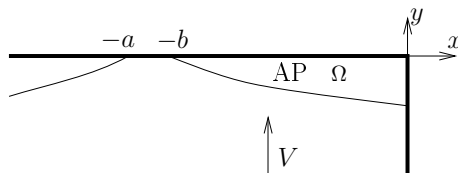
Figure 5.1:   Drawing of the air pocket and coordinate system used for the semi-analytical method (SAM).

potential is then found analytically. The dynamic pressure, in the liquid on the free surface inside the air pocket, must be set equal to the dynamic pressure inside the air pocket. This yields the following equation:

$$\frac{\partial \phi}{\partial t} = -\frac{p}{\rho}. \tag{5.1}$$

Here p is the dynamic pressure and ρ is the density of the liquid. The time derivative of the volume of the air pocket is equal to the integral of the vertical velocity component from x equal to $-b$ to x equal to zero. This yields the following equation:

$$\frac{d\Omega}{dt} = V(t)a[K(b/a) - E(b/a)] - \left(\phi_{ap} + aV(t)E(\sqrt{(1-(b/a)^2)})\right)\frac{K(b/a)}{K(\sqrt{(1-(b/a)^2)})}. \tag{5.2}$$

Here $K(k)$ and $E(k)$ are the complete elliptic integrals of the first and second kind, respectively. The definition of these integrals are given in Gradshteyn and Ryzhik [34] as:

$$\begin{aligned}
K(k) &= \int_0^1 \frac{1}{\sqrt{(1-x^2)(1-k^2x^2)}}dx \\
E(k) &= \int_0^1 \frac{\sqrt{1-k^2t^2}}{\sqrt{1-t^2}}dt.
\end{aligned} \tag{5.3}$$

Air leakage is included in the mass conservation equation for the air pocket and results in the following equation:

$$\frac{d\Omega\rho_g}{dt} = \rho_{g0}(Q_{in} - Q_{out}) = -0.61\rho_{g0}A_L\text{sign}(p)\sqrt{\frac{2|p|}{\rho_{g0}}}. \tag{5.4}$$

The last equality relates the mass flux out of the air pocket to the dynamic pressure inside the air pocket. The air leakage model is a quasi-steady model and the hole must be small compared to the length and the height of the air pocket. A relation between the density and the pressure inside the air pocket is needed. Here the polytropic relation given by equation (4.3) is applied assuming adiabatic conditions for the compressed air which yields $\kappa = \gamma = 1.4$.

   Linearising these equation further yields the natural frequency of the air pocket oscillations ω_0. Assuming that the impacting velocity V and the wetted length parameters a and b are constant in time and in addition linearising the pressure-volume relationship (4.4) assuming $p_{0p} = p_0$, then according to Faltinsen and Timokha [8], the natural frequency of the air pocket can be written as:

$$\omega_0 = \sqrt{\left(\frac{\kappa p_0}{\Omega_0\rho}\right)\frac{K(b/a)}{K(\sqrt{1-(b/a)^2})}}. \tag{5.5}$$

   In the nonlinear case the equations (5.1), (5.2) and (5.4) are integrated in time using a numerical time integration procedure. Initial conditions are needed to solve the problem. These are:
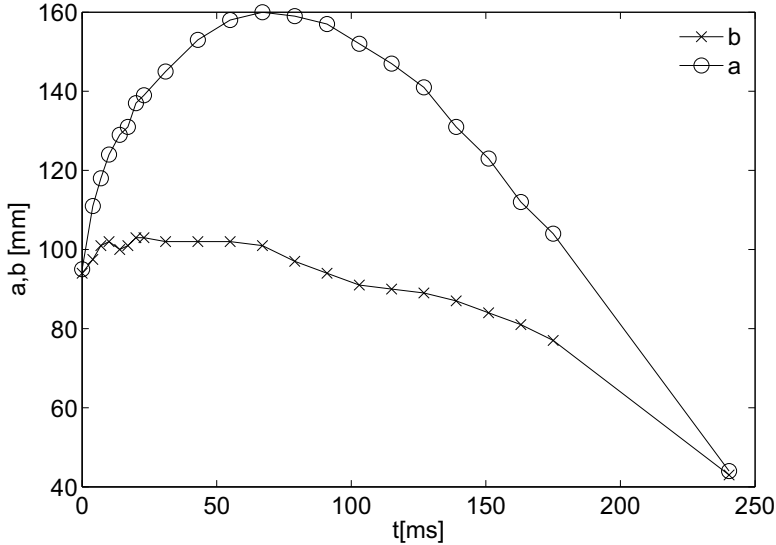
Figure 5.2: The measured wetted length parameters a and b from the experimental results of air pocket 6.

$$\begin{aligned}
\phi_{ap} &= 0 && \text{at} \quad t = 0 \\
\Omega &= \Omega_0 && \text{at} \quad t = 0 \\
\Omega \rho_g &= \Omega_0 \rho_{g0} && \text{at} \quad t = 0.
\end{aligned} \tag{5.6}$$

A fourth order Runge-Kutta method is used for time integration of the equations. Some parameters of the model are found from experiments in order to apply it to the air pocket oscillation stage. These parameters are the wetted length parameters $a(t), b(t)$, the initial volume of the air pocket Ω_0 and the impact velocity $V(t)$. a and b are estimated from the experimental pictures of air pocket 6 taken from above (CA 2) and are plotted as a function of time in figure 5.2. The wetted section of the roof vary in the z-direction due to three-dimensional effects. From the experimental pictures in figure 2.22, the wetted length is varying substantially before the first pressure maximum. Because of this the wetted length parameters a and b are estimated at the first pressure peak. It is assumed to vary linearly with time before this time instant. The initial values $b(t = 0), a(t = 0)$, are uncertain due to the three-dimensional closure of the air pocket. Here $a(t = 0) - b(t = 0)$ is set to 1 [mm]. After the first pressure peak, the wetted length parameters are well defined. The wetted length parameters a and b are plotted in figure 5.2. The water exit stage is three-dimensional leading to large variation of a and b in the z-direction of the tank. Hence it is hard to estimate the wetted length. Again a linear variation of a and b with time is assumed in the areas where the wetted length is varying a lot in the z-direction. The initial volume of air pocket 6 was in the experimental chapter estimated to be $\Omega_0 = 810[\text{mm}^2]$, and the initial flow velocity was estimated to be $V_0 = 0.395[\text{m/s}]$. The semi-analytical method (SAM) assumes a time varying
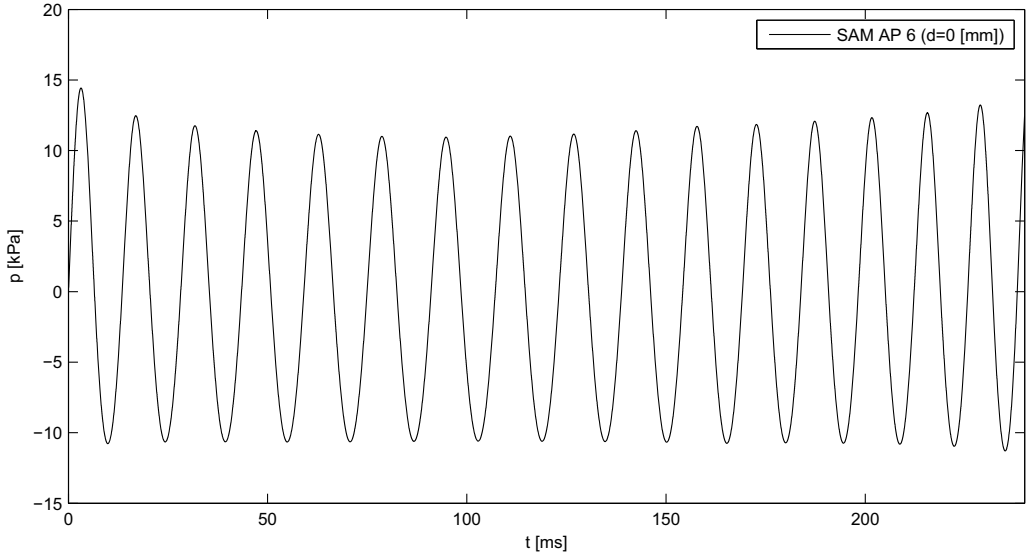
Figure 5.3: The semi-analytical method (SAM) for air pocket 6 when the hole in the roof is closed $d = 0$[mm]. The SAM does not capture the overall decay trend after the first pressure minimum observed in the experiments.

entering velocity. The temporal variation is uncertain in this case. Faltinsen and Timokha [8] assumed that the time variation of the velocity was linear that is $V = V_0 + V_1 t$. Here it is assumed that the vertical position of the fluid particles far down in the fluid should return to the initial position at the end of the slamming event then: $\int_0^{t_{ap}} V(t)dt = 0$. Using that the duration of the impact is $t_{ap} = 240$ [ms], then $V_1 = -3.29$[m/s^2]. All the parameters in the semi-analytical method are then established.

The results of the semi-analytical method is presented in figure 5.3. The pressure amplitudes are seen to be overestimated compared to the experimental results for air pocket 6 seen in figure 2.8 and 2.12. Also a period of the pressure oscillations are slightly overestimated. Further discussion of the reasons for these deviations are found in chapter 6. In figure 5.3 an initial decay is seen during the time from the first pressure peak to the first pressure minimum. The reason for this is reported by Faltinsen and Timokha [8] to be nonlinear effects connected with the temporal variation of the wetted length parameters a and b. However, the results from semi-analytical method in figure 5.3 do not show an overall decay trend after the first pressure minimum as seen for the experiments in figure 2.12. Hence, there are physical effects causing decay, which are not included in the mathematical model. Physical mechanisms explaining the decay trend after the first pressure minimum is the topic in the remaining of this chapter. The investigated damping mechanisms are the damping effect from viscous boundary layers in the liquid and the damping effect of heat exchange between the air inside the air pocket and the liquid. Finally, the damping effect of air leakage from the air pocket is investigated.

5.2 Effect of heat exchange on the pressure oscillations

So far the compression of the air pocket was assumed to follow an adiabatic gas law. This gives a simple relationship between pressure and density given by equation (4.3). By assuming that the air is compressed adiabatically or isothermally the polytropic exponent κ for air is given as 1.4 or 1.0. At these limits there are no heat exchange between the water and the air. However, when the air inside the air pocket is compressed the temperature increases. The temperature difference between the air inside the air pocket and the surrounding water and tank wall leads to heat exchange to and from the air pocket. This heat exchange affects both the stiffness and the damping properties of the pressure oscillations. In this section a steady state thermodynamic analysis in one dimension of an oscillating air pocket is presented. A similar type of analysis was made by Devin [10] in the case of an oscillating spherical air bubble in infinite water.

5.2.1 Linear steady state thermodynamic analysis

In the following a linear steady state thermodynamical analysis assuming assuming that the pressure p inside the air pocket is uniform in space and that the velocity of the air inside the air pocket is neglected. Since the vertical dimension of the air pocket is much smaller than its horizontal dimension the vertical temperature gradients are assumed to be much bigger than the horizontal temperature gradients. This suggests that a one-dimensional model in the vertical direction (y-direction) can be applied. To analyse the problem analytically the height of the air pocket h is assumed constant in the x-direction and equal to h_0. The linearised energy equation can then according to White [35] be written as:

$$\rho_{g0}c_p\frac{\partial\theta}{\partial t} = K_1\frac{\partial^2\theta}{\partial y^2} + \frac{dp}{dt}. \tag{5.7}$$
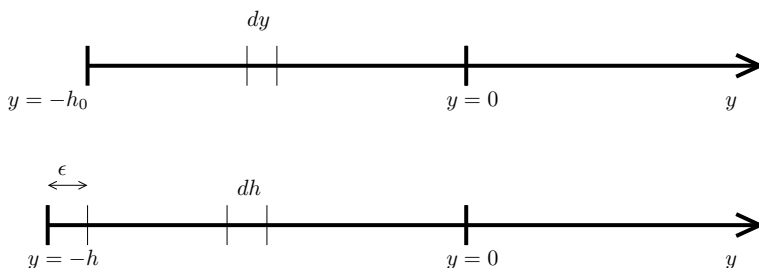
Figure 5.4: The coordinate system used for the one-dimensional heat problem assuming spatially uniform pressure.

Here ρ_{g0} is the density of the gas at atmospheric conditions, c_p is the specific heat coefficient at constant pressure and K_1 is the thermal conductivity of air. θ is the relative temperature $\theta = T_{abs} - T_0$, where T_{abs} is the absolute temperature and T_0 is the temperature at atmospheric conditions in degrees Kelvin. This equation is solved for in the area between

$y = -h_0$ and $y = 0$ illustrated in figure 5.4. The energy equation (5.7) is analysed assuming harmonic pressure oscillations. Then the pressure can be written as $p = Pe^{i\omega_0 t}$ and the equation can be solved by writing the solution as a product of one time and one space varying function as follows:

$$\theta = F(y)e^{i\omega_0 t}. \tag{5.8}$$

Inserted in equation (5.7) it reads:

$$D_1 \frac{\partial^2 F}{\partial y^2} - i\omega_0 F = -\frac{Pi\omega_0}{c_p \rho_{g0}}. \tag{5.9}$$

Here $D_1 = K_1/(c_p \rho_{g0})$ is the thermal diffusivity of the air. Equation (5.9) has the general solution:

$$F(y) = \frac{P}{c_p \rho_{g0}} \left(1 + A_1 e^{\alpha y} + A_2 e^{-\alpha y} \right). \tag{5.10}$$

Here:

$$\alpha = \sqrt{\frac{i\omega_0}{D_1}} = (1+i)\sqrt{\frac{\omega_0}{2D_1}}. \tag{5.11}$$

Here the first term is a particular solution and the two other terms are homogeneous solutions. To find the constants A_1 and A_2, boundary conditions are required. Since water and acrylic have much larger heat capacity and thermal conductivity compared to air, the relative temperature θ will be nearly zero at $y = -h$ and $y = 0$. This means that the constants A_1, A_2 are found as:

$$A_1 = -A_2 - 1 \tag{5.12}$$

$$A_2 = \frac{1 - e^{-\alpha h_0}}{e^{-\alpha h_0} - e^{\alpha h_0}}. \tag{5.13}$$

Now that the temperature inside the air pocket is known, the density inside the air pocket can be found as a function of time through the ideal gas law. The ideal gas law is expressed as:

$$\bar{p} = \rho_g R T_{abs}. \tag{5.14}$$

Here R is the gas constant whos value is dependent on the specific gas. The goal is to express a relation between the displacement ϵ and the pressure inside the air pocket. To obtain this relation the principle of mass conservation is applied to a differential element dy which after the deformation is denoted dh. The change of length of this element is denoted $d\epsilon$, so that $d\epsilon = dh - dy$. Mass conservation for this element yields $\rho_{g0} dy = \rho_g dh = \rho_g (dy + d\epsilon)$. This leads to $\rho_g d\epsilon = (\rho_{g0} - \rho_g) dy$. The displacement ϵ can then be written as:

$$\epsilon = \int_{-h_0}^{0} d\epsilon \tag{5.15}$$

The ideal gas law (5.14) is then expressed in therms of density $\rho_g(p, \theta)$ and linearised. The displacement ϵ can then be written as

$$\epsilon = \int_{-h_0}^{0} \left[\frac{\theta}{T_0} - \frac{P}{P_0} e^{i\omega_0 t} \right] dy. \tag{5.16}$$

The solution is written as:

$$\Psi\epsilon = p. \tag{5.17}$$

Where Ψ is a complex quantity:

$$\Psi = \rho_{g0}c_p\left[\frac{1}{T_0}\left(h_0 + \frac{A_1}{\alpha}(1-e^{-\alpha h_0}) - \frac{A_2}{\alpha}(1-e^{\alpha h_0})\right) - \frac{\rho_{g0}c_p h_0}{p_0}\right]^{-1} \tag{5.18}$$

$$\Psi = \frac{p_0}{h_0}\left[\frac{(\gamma-1)}{\gamma}\left(1 + \frac{A_1}{\alpha h_0}(1-e^{-\alpha h_0}) - \frac{A_2}{\alpha h_0}(1-e^{\alpha h_0})\right) - 1\right]^{-1}. \tag{5.19}$$

This is the linear steady state pressure-volume relationship when heat flow is taken into account and pressure is assumed uniform in space. Now the pressure in (5.17) is related to the hydrodynamic problem. The hydrodynamical problem is two-dimensional, that is the thickness of the air pocket h vary in the x-direction. Here h_0 as a characteristic thickness when the air pocket is assumed rectangular $h_0 b = \Omega_0$. Where b is the length of the air pocket at the time of maximum pressure $p = P$. Since the thermodynamical model is a steady-state type of model, the mathematical model for the semi-analytical method is simplified in the following fashion. Firstly the entering liquid velocity V_0 and the wetted length parameters a and b are assumed to have no time dependence. Introducing these two assumptions into equation (5.2) and using the relation (5.1) it results in:

$$p = \rho I_1 b \frac{\partial^2 \epsilon}{\partial t^2}. \tag{5.20}$$

Here I_1 is given by

$$I_1 = \frac{K[\sqrt{1-(b/a)^2}]}{K[b/a]}. \tag{5.21}$$

Then introducing the thermodynamic relation (5.17) results in:

$$\rho I_1 b \frac{d^2\epsilon}{dt^2} - \Psi\epsilon = 0. \tag{5.22}$$

This equation is then compared with a general freely oscillating, damped mass-spring system:

$$M\frac{d^2\epsilon}{dt^2} + B\frac{d\epsilon}{dt} + K\epsilon = 0. \tag{5.23}$$

Now, assuming that the response is given as $\epsilon = \epsilon_0 e^{iwt}$ a comparison of the different terms yield:

$$M = \rho I_1 b$$
$$B = -\frac{1}{\omega_0}\Im(\Psi) \tag{5.24}$$
$$K = -\Re(\Psi).$$

The mass of this system is a property of the hydrodynamical problem and is proportional to the density of the liquid. The stiffness and damping terms are a function of the thickness of the air pocket, the atmospheric pressure p_0, the ratio of specific heats γ and the diffusion coefficient D_1. In the following the stiffness and damping terms of this equation system are discussed in detail.

5.2.2   Calculating the effective polytropic exponent

A linearised relation between dynamic pressure p and displacement ϵ based on the polytropic gas model (4.4) is derived in the following. In one dimension (4.4) yield:

$$p + p_0 = p_0 \left(\frac{h_0}{h} \right)^\kappa. \tag{5.25}$$

Linearising this relation around $p = 0$ and introducing the displacement $\epsilon = h - h_0$ the result is:

$$p = -\frac{p_0 \kappa}{h_0} \epsilon \tag{5.26}$$

The model has no pressure term proportional to the time derivative of the displacement, that is $\dot{\epsilon}$, and hence the model does not include any source of damping. By comparison with the thermodynamic mass-spring system it is evident that:

$$\kappa = -\frac{h_0}{p_0} \Re(\Psi). \tag{5.27}$$

Now, Ψ is rewritten introducing the thermal boundary layer thickness δ_T. The thermal boundary layer thickness δ_T is defined by Leighton [36] as $\delta_T = \sqrt{D_1/(2\omega_0)}$. This means that Ψ can be written as:

$$\Psi = \frac{p_0}{h_0} \left[\frac{(\gamma - 1)}{\gamma} \left(1 + \frac{2A_1}{(1+i)\frac{h}{\delta_T}} (1 - e^{-\frac{(1+i)}{2}\frac{h}{\delta_T}}) - \frac{2A_2}{(1+i)\frac{h}{\delta_T}} (1 - e^{\frac{(1+i)}{2}\frac{h}{\delta_T}}) \right) - 1 \right]^{-1}. \tag{5.28}$$

The resulting polytropic exponent is given as:

$$\kappa = -\Re \left\{ \left[\frac{(\gamma - 1)}{\gamma} \left(1 + \frac{2A_1}{(1+i)\frac{h}{\delta_T}} (1 - e^{-\frac{(1+i)}{2}\frac{h}{\delta_T}}) - \frac{2A_2}{(1+i)\frac{h}{\delta_T}} (1 - e^{\frac{(1+i)}{2}\frac{h}{\delta_T}}) \right) - 1 \right]^{-1} \right\}. \tag{5.29}$$

This is the polytropic exponent predicted by linear theory assuming one dimension, uniform pressure and conduction heat flow only. The polytropic exponent is plotted as a function of h/δ_T for air, that is $\gamma = 1.4$, in figure 5.5. It is seen that the polytropic exponent is between $1 \leq \kappa \leq \gamma$.

In figure 5.5 the values of h_0/δ_T are indicated for the different air pockets from the experiments in section 2.3. From this a volume equivalent air pocket thickness denoted $h_0 = \Omega_0/b$ is obtained from the experimental results. The thermal diffusivity is set to $D_1 = 2.2160 \cdot 10^{-5} [\mathrm{m^2/s}]$. The period T_n is estimated as the average of the first five periods taken from the right plot in figure 2.13. When using a polytropic air pocket model (4.4) the heat flow of the air pocket does not need to be solved for. However, the compression of the air pocket must be assumed to be either adiabatic or isothermal. From figure 5.5 it is seen that the adiabatic value of the polytropic exponent is most appropriate for the air pockets studied here. However, the polytropic model suffers from a deficiency in the case of a time dependent problem like the oscillating air pocket. This is the case when the compression of the air is not close to adiabatic or isothermal. This is because the imaginary part of Ψ is
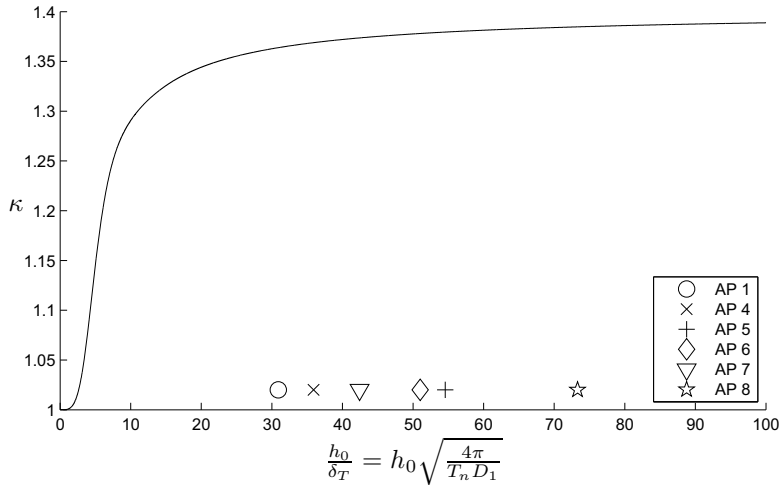
Figure 5.5: The polytropic exponent as a function of the ratio between the thickness of the air pocket and the thermal boundary layer thickness h_0/δ_T. The values of h_0/δ_T for the air pockets investigated experimentally are indicated by symbols.
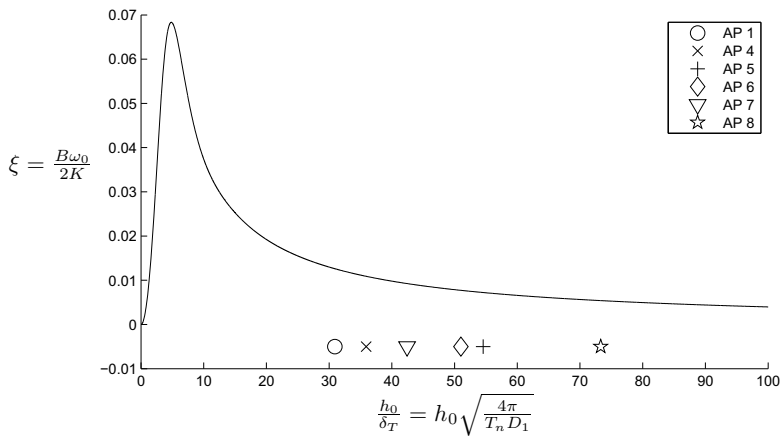
Figure 5.6: The damping ratio as a function of the ratio between the thickness of the air pocket and the thickness of the thermal boundary layer h_0/δ_T. The value of h_0/δ_T for the air pockets investigated experimentally are indicated by symbols.

non-zero, and hence there is a damping mechanism related to the heat flow. This damping effect cannot be captured by the polytropic gas model (4.4). The damping ratio resulting from the present one-dimensional, linear, steady state and uniform pressure model is written as $\xi = B\omega_0/(2K)$. The damping ratio is plotted in figure 5.6 as a function of h_0/δ_T. The plot shows that the damping of air pocket oscillations due to heat flow can be as high as 7% of the critical damping and also that it is significant thermal damping for the air pockets studied in this work.

It is possible to plot the temperature variation from equation (5.8) since the parameter h_0/δ_T for the experimentally investigated air pockets are known. Here the temperature is made non-dimensional in the following way; $\theta = T_0\bar{\theta}$ and $y = h_0\bar{y}$. The results show that the temperature is spatially varying towards the water and the roof, while the temperature is fairly constant in space in the middle of the air pocket.
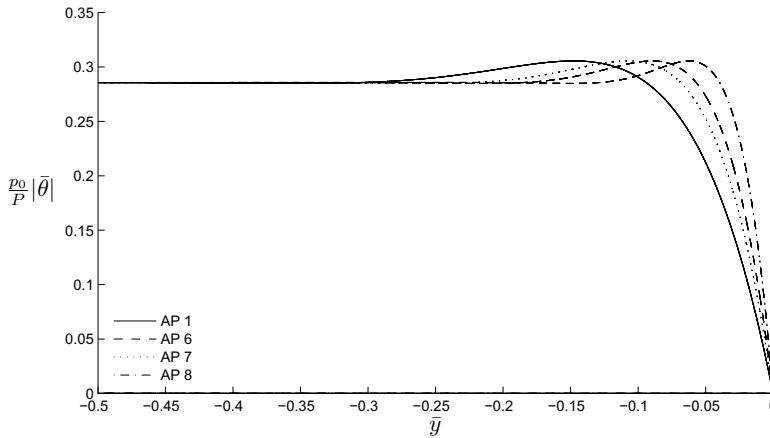
Figure 5.7: The non-dimensional temperature plotted as a function of the non-dimensional thickness of the air pocket $\bar{y}$. The solution is symmetric about $\bar{y} = -0.5$.

The energy equation (5.7) is now written in non-dimensional form to investigate which non-dimensional numbers it contains. Introducing the following non-dimensional parameters $\theta = T_0\hat{\theta}$, $p = \rho_{g0}\omega_0^2 h_0^2\hat{p}$ and $t = \hat{t}/\omega_0$, and rewriting the equation using the ideal gas law (5.14), and the thermodynamical relations $R = c_p - c_v$ and $\gamma = c_p/c_v$ the energy equation (5.7) yields:

$$\frac{\partial\hat{\theta}}{\partial\hat{t}} = Pe\frac{\partial^2\hat{\theta}}{\partial\hat{y}^2} + M^2(\gamma - 1)\frac{\partial\hat{p}}{\partial\hat{t}}. \tag{5.30}$$

Here Pe is the Péclet number defined as:

$$Pe = \frac{D_1}{h_0^2\omega_0}, \tag{5.31}$$

and M is the Mach number written in terms of the natural frequency, the thickness of the

air pocket h_0 and the speed of sound c_0, that is:

$$M = \frac{\omega_0 h_0}{c_0}. \tag{5.32}$$

The polytropic exponent and the damping ratio in figure 5.5 and 5.6 is only dependent on one parameter h_0/δ_T which again is only dependent on the Péclet number:

$$\frac{h_0}{\delta_T} = \sqrt{\frac{2}{Pe}}. \tag{5.33}$$

This means that the Mach number does not affect the polytropic exponent and the damping ratio. From appendix F it is seen that assuming constant pressure is the first order asymptotic solution of the linear problem in the small parameter C. Here C is proportional to the Mach number M squared.

5.3 Effect of viscous boundary layers

The damping effect of the viscous boundary layers in the liquid at the tank walls is estimated by using laminar boundary layer theory. The mathematical problem solved for in the semi-analytical method contains two temporal scales. One time scale is slow and due to the entering water. The other time scale is fast and due to the flow field of the pulsating air pocket. In reality there will be an interaction effect between these two flow fields which will affect the damping caused by the viscous boundary layers. This effect could have been modelled by coupling a three-dimensional boundary element method with a two-dimensional boundary layer model as described by Faltinsen and Timokha [8].

Here a simplified approach is followed by assuming free oscillations of the air pocket oscillations, hence, the interaction effect between the slowly varying flow field of the entering water and the oscillatory flow field due to the air pocket oscillations are neglected. The calculation is performed in a similar fashion as Keulegan's [17] derivation of viscous damping of the lowest mode of sloshing in a rectangular tank.

If the mathematical problem of the semi-analytical method is linearised, by assuming constant inflow velocity V and wetted length parameters a and b, the solution represents free oscillations of a linear mass-spring system. Here Stokes' 2 nd. problem is used to estimate the energy dissipated by laminar boundary layers during one oscillation period. The energy loss is then associated with a damping term of a linear damped mass-spring system assuming a small damping ratio.

Potential energy due to gravity is not present since the semi-analytical model neglects the effect of gravity. During compression, work is made to compress the air pocket. The velocity field of the semi-analytical method due to the free oscillations of an air pocket is given by Faltinsen and Timokha [8] as:

$$u - iv = \frac{iA\cos\left(\omega_0 t + \epsilon\right)}{\sqrt{(z^2 - a^2)(z^2 - b^2)}} \tag{5.34}$$

In this expression $i = \sqrt{-1}$, $z = x + iy$ and A is a constant. The coordinate system used is the same as in figure 5.1. The velocity obtained from (5.34) is used as the velocity outside the boundary layers. To illustrate the boundary layers on the different walls the coordinate system and the tank is drawn in figure 5.8. To obtain the velocity field at a point (x, y) from

Figure 5.8: A drawing of the tank including the coordinate system used in the semi-analytical method. The tank has internal dimensions L=1000[mm], D=100[mm] and H_{tot}=980[mm].
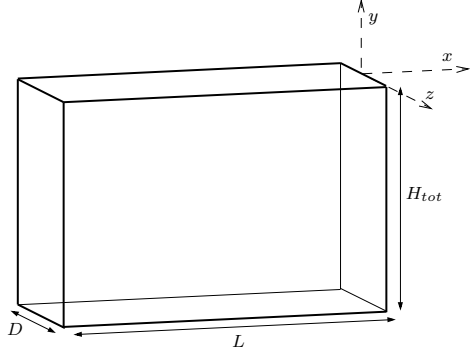
equation (5.34) it needs to be evaluated as explained by Faltinsen and Timokha [8]. The energy content of the air pocket oscillations is equal to the amplitude of the kinetic energy of the liquid, which can be found to be:

$$
\begin{aligned}
\frac{\rho}{2} \int_Q \nabla\phi \cdot \nabla\phi \, dQ &= \frac{\rho}{2} \int_Q \nabla \cdot (\phi\nabla\phi) \, dQ \\
&= \frac{\rho}{2} \int_{S_{ap}} \boldsymbol{n} \cdot (\phi\nabla\phi) \, dS \\
&= \frac{\rho D}{2} \phi_{ap} \int_{-b}^{0} v \, dx.
\end{aligned}
\tag{5.35}
$$

Here S_{ap} is the area of the free surface towards the air pocket. The generalized Gauss theorem as given by Faltinsen and Timokha [8] is used to transform the volume integral of the first line to a surface integral in the second line. Because of the boundary conditions of the problem only the surface integral inside the air pocket contributes. The velocity potential ϕ_{ap} and the vertical component of the velocity v at the surface S_{ap} can according to Faltinsen and Timokha [8] be written as:

$$
\phi_{ap} = \frac{A \cos{(\omega_0 t + \epsilon)}}{a} K(\sqrt{1 - (b/a)^2})
\tag{5.36}
$$

and

$$
v = \frac{A \cos{(\omega_0 t + \epsilon)}}{\sqrt{(a^2 - x^2)(b^2 - x^2)}}.
\tag{5.37}
$$

The amplitude of the kinetic energy is equal to the total amount of energy in the system and can hence be written as:

$$
E_k = \frac{\rho}{2} \frac{A^2}{a} K[\sqrt{1 - (b/a)^2}] I_1 D.
\tag{5.38}
$$

Here I_1 is the integral

$$I_1 = \int_{-b}^{0} \left[\frac{1}{\sqrt{(a^2 - x^2)(b^2 - x^2)}} \right] dx. \tag{5.39}$$

The dissipation from the boundary layers of the different wetted tank surfaces are considered next. The tank and the coordinate system used is illustrated in figure 5.8. Since the semi-analytical method does not satisfy the boundary conditions on the tank bottom and the $y - z$ parallel wall at $x = -L$, the viscous boundary layers there are neglected. The walls included are the closest $y - z$ parallel wall at $x = 0$, the large front and back walls parallel to the $x - y$ plane and the roof of the tank. From Stokes 2 nd. problem, the following equation represents the average viscous energy dissipation for one period of oscillation per unit area:

$$\dot{E}_{vd} = -\frac{\mu}{2} \sqrt{\frac{\omega_0}{2\nu}} V_0^2(x). \tag{5.40}$$

Here μ and ν are the dynamic and kinematic viscosity coefficients, respectively. $V_0(x)$ is the velocity of the fluid outside the boundary layer and can be found from (5.34) if evaluated as by Faltinsen and Timokha [8] on the different walls. First the $y - z$ parallel side wall at $x = 0$ is analysed. The the rate of energy dissipation from this wall is:

$$\dot{E}_{vd1} = -\frac{DA^2 \mu}{2} \sqrt{\frac{\omega_0}{2\nu}} I_2. \tag{5.41}$$

Here

$$I_2 = \int_{-H_{tot}}^{0} \left[\frac{1}{(a^2 + y^2)(b^2 + y^2)} \right] dy. \tag{5.42}$$

For one of the plates parallel to the $x - y$ plane the energy dissipation can be written as:

$$\dot{E}_{vd2} = -\frac{A^2 \mu}{2} \sqrt{\frac{\omega_0}{2\nu}} I_3. \tag{5.43}$$

Here:

$$I_3 = \int_{-L}^{0} \int_{-H_{tot}}^{0} \left[\frac{1}{\sqrt{[(x-a)^2 + y^2][(x+a)^2 + y^2][(x-b)^2 + y^2][(x+b)^2 + y^2]}} \right] dx dy. \tag{5.44}$$

The energy dissipation from the wetted part of the roof for $-a \leq x \leq -b$ is given as:

$$\dot{E}_{vd3} = -\frac{DA^2 \mu}{2} \sqrt{\frac{\omega_0}{2\nu}} I_4. \tag{5.45}$$

Here

$$I_4 = \int_{-a+\delta}^{-b-\delta} \left[\frac{1}{(a^2 - x^2)(x^2 - b^2)} \right] dx. \tag{5.46}$$

If the integration is performed from $x = -a$ to $x = -b$, the integral is singular and yields infinitely large damping ratio. This is non-physical and is related to the fact that the mathematical model does not represent the real flow around $x = -a$ and $x = -b$. To avoid this

problem the area close to a and b are not included in the integration by introducing the δ in the integration. There is ambiguity related to the distance δ. Here the boundary layer thickness as defined by Faltinsen and Timokha [8] is used. This is defined as

$$\delta = 4.6\sqrt{\frac{2\nu}{\omega_0}}.$$ (5.47)

In the previous derivation the amplitude of the oscillations was assumed constant in time since no damping was present in the mathematical problem. From here on a slight amplitude change is allowed, based on the assumption that the amplitude reduction per period is small. From the experiments in chapter 2 this is not entirely correct since the observed decay of the oscillations is large during the time from the first pressure maximum to the first pressure minimum. From the results of the present mixed Eulerian-Lagrangian method and results from the semi-analytical method given by Faltinsen and Timokha [8] it was seen that the source of this decay was of nonlinear origin. The nonlinearity is mainly due to the geometrical change of the air pocket. After the first period of oscillation the change of amplitude over one period can be assumed small. The amplitude of a freely oscillating, under-damped mass-spring system decays exponentially. Assuming that the pressure amplitude $P(t)$ behaves in this manner then

$$\frac{P}{P_1} = e^{-\alpha t/T_0}.$$ (5.48)

Here the pressure amplitude P can be related to the velocity potential since $p = -\rho\partial\phi_{ap}/\partial t$. Using equation (5.36) it is evident that $P/P_1 = A/A_1$. From the expressions for the damping it follows that:

$$\frac{E_k}{E_{k1}} = \left(\frac{A}{A_1}\right)^2 = e^{-2\alpha t/T_0}.$$ (5.49)

Taking the time derivative of this equation results in an equation for α based on the derived energy expressions, then:

$$\alpha = -\frac{1}{2}\frac{T_0\sum\dot{E}_{vd}}{E_{k1}}.$$ (5.50)

From the known solution of a damped mass-spring system, α can be related to the damping ratio ξ_{vd} as:

$$\xi_{vd} = \frac{\alpha}{2\pi}.$$ (5.51)

The damping ratio ξ_{vd} is written as a sum of the contributions from the different walls in the following way

$$\xi_{vd} = \xi_{vd1} + \xi_{vd2} + \xi_{vd3}.$$ (5.52)

Here ξ_{vd1}, ξ_{vd2} and ξ_{vd3} are the contributions to the damping ratio from the side wall ($y - z$ parallel), the front and back wall ($x - y$ parallel) and of the roof. They are given as:

$$\xi_{vd1} = B_1DI_2, \qquad \xi_{vd2} = 2B_1I_3, \qquad \xi_{vd3} = B_1DI_4.$$ (5.53)

Where

$$B_1 = \sqrt{\frac{\nu}{2\omega_0}}\left(\frac{a}{2DI_1K[\sqrt{1-(b/a)^2}]}\right).$$

To evaluate the damping ratio the kinematic viscosity ν is set equal to $0.89 \cdot 10^{-6} [\mathrm{m}^2/\mathrm{s}]$ and the density is set equal to $\rho = 997 [\mathrm{kg/m}^3]$ corresponding to a temperature of $T_0 = 25°\mathrm{C}$. The initial volume of the air pocket is set to $\Omega_0 = 810 [\mathrm{mm}^2]$ according to the experiments reported in chapter 2. The damping ratio is varying in time during the air pocket oscillation stage, this is due to the temporal variation of a and b according to figure 5.2. Hence, the damping ratio is plotted as a function of time. The contributions to the damping ratio from the different walls ξ_{vd1}, ξ_{vd2} and ξ_{vd3} are seen in the left plot in figure 5.9. The damping
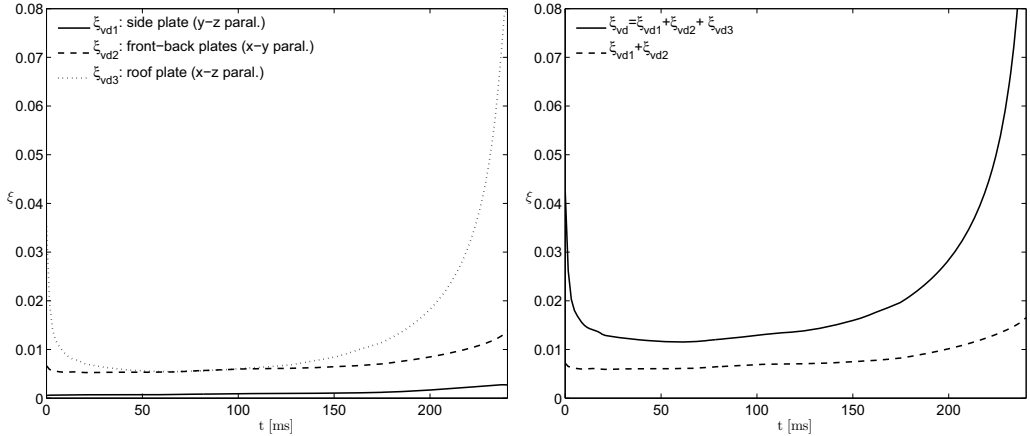
Figure 5.9: The damping ratio as a function of time illustrating the damping ratio dependence on the wetted length parameters a and b.

contributions from the front and back wall and the roof, that is ξ_{vd2} and ξ_{vd3}, are seen to dominate. There is uncertainty related to ξ_{vd3}, this is due to the singular integral. If the damping contribution due to the roof is neglected, an estimate of the lower bound of the damping ratio can be obtained as $\xi_{vd} > \min(\xi_{vd1} + \xi_{vd2}) = 0.0059$. If the roof is included, the damping can amount to $\xi_{vd} \approx \min(\xi_{vd1} + \xi_{vd2} + \xi_{vd3}) = 0.012$.

5.4 Damping included in the semi-analytical method

The damping effect of viscous boundary layers and heat flow is now included in the semi-analytical method. Here this is done by adding a term denoted $F(\Omega_1)$, where Ω_1 is the volume fluctuation $\Omega_1 = \Omega - \Omega_0$, on the right hand side of equation (5.2). This term is then chosen so that it damps the air pocket oscillations. Now equation (5.2) including the not yet determined linear term $F(\Omega_1)$ is linearised by assuming that a, b and V are constant in time. Then the following equation is arrived at:

$$\frac{d\Omega_1}{dt} = -\phi_{ap} \frac{K(b/a)}{K(\sqrt{1-(b/a)^2})} + F(\Omega_1) \tag{5.54}$$
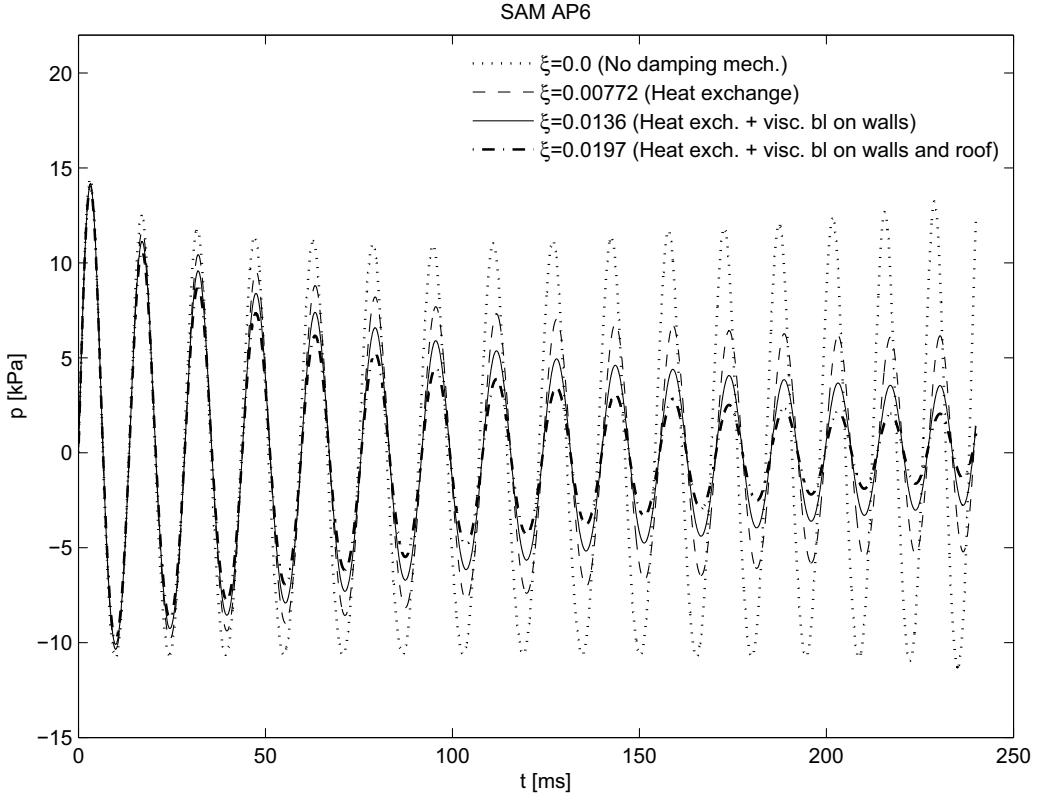
Figure 5.10: Results from the semi-analytical method for air pocket 6, showing the damping effect due to heat exchange and viscous boundary layers on the air pocket oscillations.

The pressure-volume relationship (4.4) is linearised assuming that the initial pressure inside the air pocket is atmospheric $p_{0p} = p_0$ and that there is no air leakage. Then:

$$p = -\frac{p_0 \kappa}{\Omega_0} \Omega_1. \tag{5.55}$$

The linearised hydrodynamical pressure is connected to the velocity potential through $p = -\rho \phi_t$. Then the following mass-spring like system follows:

$$\frac{d^2 \Omega_1}{dt^2} - \frac{dF(\Omega_1)}{dt} + \frac{p_0 \kappa}{\rho \Omega_0} \frac{K(b/a)}{K(\sqrt{1 - (b/a)^2})} \Omega_1 = 0. \tag{5.56}$$

For $F(\Omega_1)$ to represent a damping term in a linearised sense, then

$$-\frac{dF}{dt} = \mu \frac{d\Omega_1}{dt} \tag{5.57}$$

Integration of this equation leaves a constant which needs to be quantified. The initial conditions of the oscillations should not change because of the damping term. The initial condition $\dot{\Omega}_1 = 0$ then forces this constant to be zero. Then $F = -\mu d\Omega_1/dt$. It still remains to relate μ to the damping ratio ξ. This is done through the well known formula:

$$\xi = \frac{\mu}{2\sqrt{KM}} \tag{5.58}$$

Here the mass M and stiffness K can be identified in equation (5.56) as the term in front of $\ddot{\Omega}_1$ and Ω_1 respectively. μ can then be written as:

$$\mu = 2\xi\sqrt{\frac{p_0\kappa}{\Omega_0\rho}}\sqrt{\frac{K(b/a)}{K(\sqrt{1-(b/a)^2})}} \tag{5.59}$$

This way of modelling is only valid to the extent that the solution of the nonlinear model is close to the solution of a linear under-damped mass-spring system. In the following the nonlinear semi-analytical method, including the damping effect of heat exchange and viscous boundary layers, is applied to air pocket 6. To calculate the damping ratio due to heat exchange the ratio h_0/δ_T needs to be determined. This means that the period of oscillations needs to be estimated. This is calculated using equation (5.5) where the experimental value of the initial volume Ω_0, and a and b in figure 5.2 is inserted. The ullage pressure is set to $p_0 = 1.01 \cdot 10^5 [\text{Pa}]$ and the density of the water is set to $\rho = 997 [\text{kg/m}^3]$. Since a and b vary throughout the time series the period T_n used to establish h_0/δ_T is the average natural period of the impact given as 14.9 [ms]. To estimate the average thickness of the air pocket then the average value of b during the time series is used, that is 0.0847 [m]. This leads to a value of $h_0/\delta_T = 51.0$ which from figure 5.6 and 5.5 lead to a thermal damping ratio of $\xi_{th} = 0.00772$ and a polytropic exponent of $\kappa = 1.378$. The resulting pressure time histories are compared in figure 5.10. The first is when no damping mechanisms are modelled. The second, $\xi = 0.00772$, is due to heat exchange only. The third, $\xi = 0.01362$, is due to heat exchange and viscous boundary layer damping from all walls except the roof. The fourth, $\xi = 0.01972$, is the damping effect of heat exchange and viscous boundary layers from all walls including the roof.

The results show that both heat exchange and viscous boundary layers contribute to the damping of the air pocket oscillations. From equation (5.5) it is seen that a reduction of the polytropic index yields a reduced natural frequency of the air pocket oscillations. However, the reduction of the polytropic exponent is small, and does not modify the pressure oscillation frequency significantly.

5.5   The effect of air leakage

In the experiments the effect of air leakage was investigated by drilling holes in the roof above the air pocket. The air pockets studied were air pocket 6 and 7, which were both seen to close before the first pressure peak. The experiments show that when air was allowed to flow through a circular hole in the roof the resulting pressure oscillations show increased
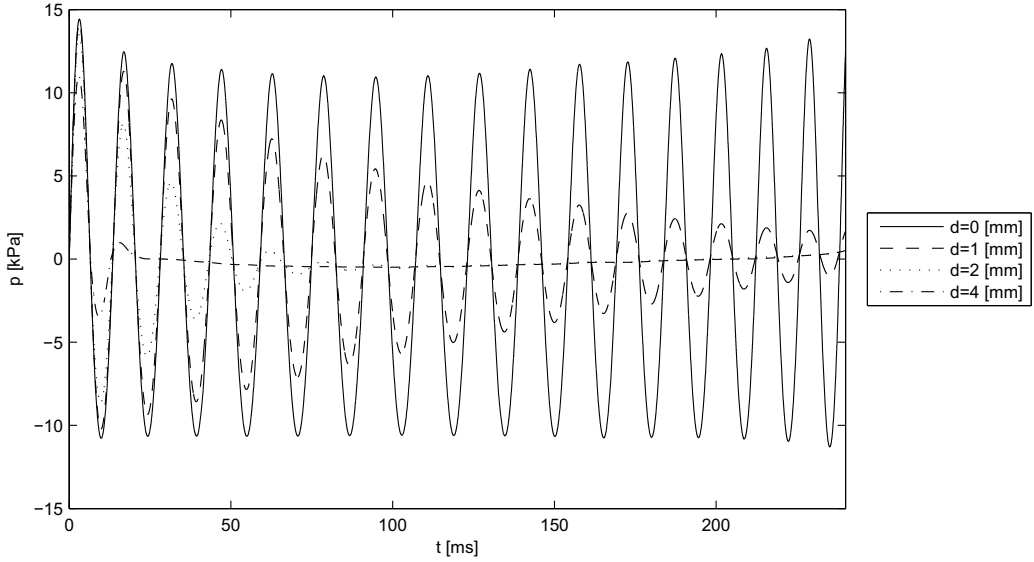
Figure 5.11: The semi-analytical method (SAM) when solving for air pocket 6. The model shows the effect of a small leakage through a hole in the roof over the air pocket with diameter d.

decay. For air pocket 6, this is plotted in figure 2.21. The role of air leakage through a hole in the air pocket was then investigated using the original semi-analytical method as proposed by Faltinsen and Timokha [8]. The diameter of the holes have equal size as for the experiments, that is $d = 0, 1, 2, 4$[mm]. The results are plotted in figure 5.11. The results from the original SAM confirm the experimental findings that air leakage cause decay of the air pocket oscillations.

5.6   Findings from the semi-analytical method

Under the assumption of heat flow due to conduction the damping due to heat exchange between the water and the air was seen to contribute to the decay of the air pocket oscillations. Also the heat exchange modified the polytropic exponent compared to its adiabatic value. The one-dimensional heat exchange model shows that the damping ratio due to heat exchange can be as high as 6.8%. But a question is if this damping can be observed in reality. Here the thickness is modified for air pocket 6 in order to obtain this damping ratio. Using the formula for h_0/δ_T in figure 5.6 and inserting the natural frequency from equation (5.5) and assuming that a and b for the modified air pocket is equal to a and b for air pocket 6, then it yields a thickness for the modified air pocket of 0.44 [mm]. This is a very thin air pocket. Carrying out the same procedure for air pocket 1, yields a characteristic air pocket thickness of 0.29 [mm].

   The mathematical model of the damping effect due to laminar viscous boundary layers assumed no interaction between the flow field of the entering water and the flow field of the air pocket oscillations. There is uncertainty related to the damping effect of the roof, due to a singular integral. A lower bound of the damping ratio was estimated by excluding the contribution from the roof. Even when this lower bound was used in the calculations the viscous boundary layer contributed to the damping of the pressure oscillations.

   The viscous boundary layers and the heat exchange between the air pocket and the liquid were seen to cause damping of the pressure time history. This means that if the damping mechanisms should be similar in model and full scale, then the non-dimensional parameters governing the damping must be equal in model and prototype. The thermodynamical analysis then shows that the Péclet number and the ratio of specific heats γ needs to be equal in model and prototype. The viscous calculations show that the Reynolds number Re needs to be equal in model and full scale in order to have the same viscous boundary layer damping. However, maintaining the same Reynolds number in model and full scale is hard in marine problems when the Froude number is similar in model and full scale and the liquid is water. This is due to the required viscosity of the liquid in model scale.

Chapter 6

Comparison of experiments and mathematical models

In this section the results from the mathematical models are compared to the experiments. First the results from the boundary-element-finite-difference method (BEFDM), which was used to model the sloshing and air escape stages in section 3.5, is compared to the experiments. The emphasis is on the inflow conditions just before the wave crest hits the roof. After this the pressure time histories inside the air pocket are compared and reasons for the deviations are discussed. The characteristic period of the oscillations and the amplitude of the pressure is emphasised. A discussion of the reasons for the decay of the air pocket oscillations is added at the end of the chapter.

6.1   Comparison of the free surface geometry
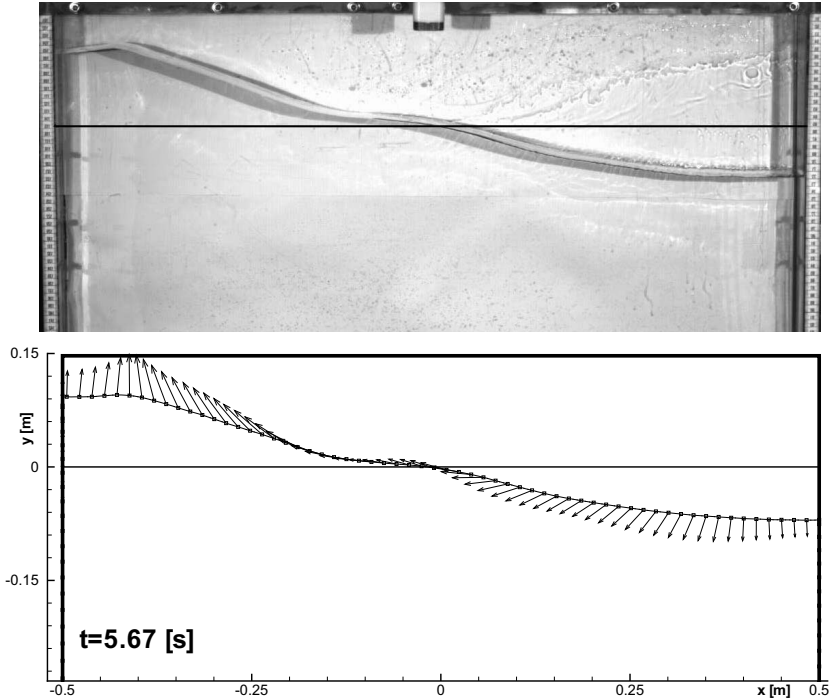
Figure 6.1: Comparison of the wave elevation from experiments and the boundary-element-finite-difference method (BEFDM) using the grid settings G1. *Top:* Experiments. *Bottom:* The BEFDM where the arrows show the velocity of the particles on the free surface relative to the tank.

A comparison of the free surface during the sloshing stage of air pocket 6 from the experiments and the boundary-element-finite-difference method (BEFDM) using the grid settings G1 is seen in figure 6.1. The grid settings G1 uses a Rayleigh damping parameter $\delta = 0.0261$. The free surface geometry is seen to be in reasonable agreement. In the two images on the left in figure 6.2, the air pocket geometry for the boundary-element-finite-difference method is compared with the experiments when the wave first touches the roof. In the experimental images in figure 6.2 both the intersection lines between the free surface and the front glass (FSF) and the intersection line between the free surface and the rear glass (FSR) is indicated. When comparing the geometry of the experimental air pocket with the results from the numerical model the free surface at the front glass (FSF) should be considered. In the experiments a period of closure lasting about 2 [ms] was observed where the air pocket was partially open and closed along the width of the tank. The top left image in figure 6.2 is the same image as image one in figure 2.18 and is taken approximately in the middle of this closure period. This experimental picture show a sharpening of the wave crest

as it approaches the roof. The boundary-element-finite-difference method (BEFDM) shows similar type of behaviour, although not as pronounced as in the experiments. The driving mechanism for this sharpening can be the low pressure generated from the escaping air which was investigated in section 3.6. This effect should be present in the results from the boundary-element-finite-difference method (BEFDM) since the air flow is modelled. However, the free surface geometry at closure is seen not to be similar. Reasons for this deviation could be one or more of the physical effects neglected in the mathematical problem of the boundary-element-finite-difference method (BEFDM). Those are viscous- ,compressible-, surface tension- and 3D effects. The two images on the right in figure 6.2 show the air pocket geometry when the pressure inside the air pocket is maximum. The wetted length is seen to be overestimated in the mixed Eulerian-Lagrangian method (MEL). Reasons for this deviation can be incomplete modelling of the air-water interaction during closure. The velocity
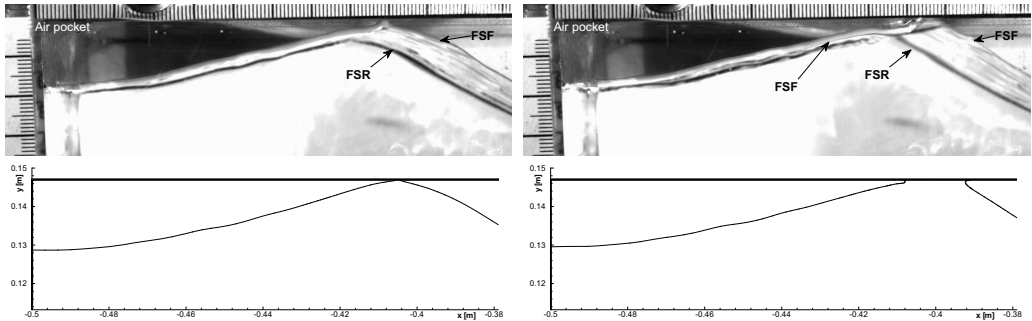
Figure 6.2: A comparison of the shape of the air pocket. Upper image row is of the air pocket 6 from experiments, compared to the lower image row taken from the boundary-element-finite-difference method (BEFDM) using the G1 grid setting. The intersection line between the free surface and the front glass (FSF) should be used when comparing the air pocket geometry. *Left:* The time instant when the wave crest is first touching the roof. *Right:* The time instant when pressure is maximum.

of the entering wave was $V_1 = 0.352$[m/s] along the wall and $V_2 = 0.446$ [m/s] at the wave crest for the boundary-element-finite-difference method (BEFDM) using the grid settings G1. The velocities are evaluated when the wave crest is 6[mm] from the roof. In the experimental results reported in figure 2.7 these velocities are given as $V_1 = 0.41$[m/s] and $V_2 = 0.38$[m/s]. The boundary-element-finite-difference method (BEFDM) is seen to overestimate the vertical velocity at the wave peak, while underestimating it at the left wall. The average of V_1 and V_2 are seen to be of similar magnitude for the boundary-element-finite-difference method (BEFDM) and the experiments. The mixed Eulerian-Lagrangian method (MEL) using the grid settings G1, overestimates the initial volume, which is 1076 [mm^2] compared to 810[mm^2] in the experiments. An explanation of this deviation can be the Rayleigh damping model which is a simplified treatment of damping.

6.2 Comparison of the pressure-time history

The pressure time histories from the numerical methods and the experiments are compared in figure 6.3. The upper plot shows a comparison between the mixed Eulerian-Lagrangian method (MEL), the semi-analytical method (SAM) and the average of 13 runs of the experiments.

The results from the mixed Eulerian-Lagrangian method (MEL) overestimate the period of the pressure time history. The period of the pressure time history for the different numerical methods and the experiments are plotted separately in figure 6.4. The natural period T_n is seen to decrease with the square root of the volume according to equation (5.5). Assuming that the wetted length parameters in the experiments and in the results from the mixed Eulerian-Lagrangian method (MEL) is equal, the difference in volume suggests a ratio between the experimental period and numerical period of $T_n^{mel}/T_n^{exp} = 1.15$. This is in fair agreement with figure 6.4. The natural periods obtained from equation (5.5) using the experimentally measured air pocket volume Ω_0 and wetted length parameters a and b are also plotted in figure 6.4. The period is seen to be overestimated. One reason for this deviation can be the simplified geometry of the air pocket used in the semi-analytical method (SAM), where the boundary conditions of the free surface was applied to a straight line intersecting the roof. The free surface in the experiments is not close to horizontal outside the air pocket. The deviation is an error source in the semi-analytical method (SAM).

Both numerical methods overestimate the maximum pressure P. When the semi-analytical method (SAM) is linearised the peak pressure is proportional to the impact velocity. The average of the velocity at the wall V_1 and the velocity at the crest V_2 from the experiments was used as input to the semi-analytical method (SAM). For the mixed Eulerian-Lagrangian method (MEL) the average impact velocity was taken from the end of the simulation using the boundary-element-finite-difference method (BEFDM). The average impact velocity $(V_1 + V_2)/2$ from the BEFDM was seen to be close to the experimental value. However, the velocity at the crest was seen to be larger, and the velocity at the wall smaller. This might be the reason for the over-prediction by the mixed Eulerian-Lagrangian method (MEL). However, one should keep in mind that the experiments show air leakage after the wave first touches the roof and until the whole width of the roof is wetted. This can in a two-dimensional sense be seen as air leakage and air leakage was shown both experimentally and mathematically, through the semi-analytical method (SAM), to cause damping. The overestimation of the maximum pressure for the semi-analytical method (SAM) compared to the mixed Eulerian-Lagrangian method (MEL) is believed to be the simplified geometry of the semi-analytical method (SAM) on which the boundary conditions are satisfied. The decay of the air pocket oscillations is discussed next.

6.3 Damping of the pressure time history?

For the air pocket oscillations to behave as the free decay of a linear under-damped mass-spring system the decay of the oscillations should be exponential and the frequency of oscillations should be constant and equal to the natural frequency during the whole impact. The
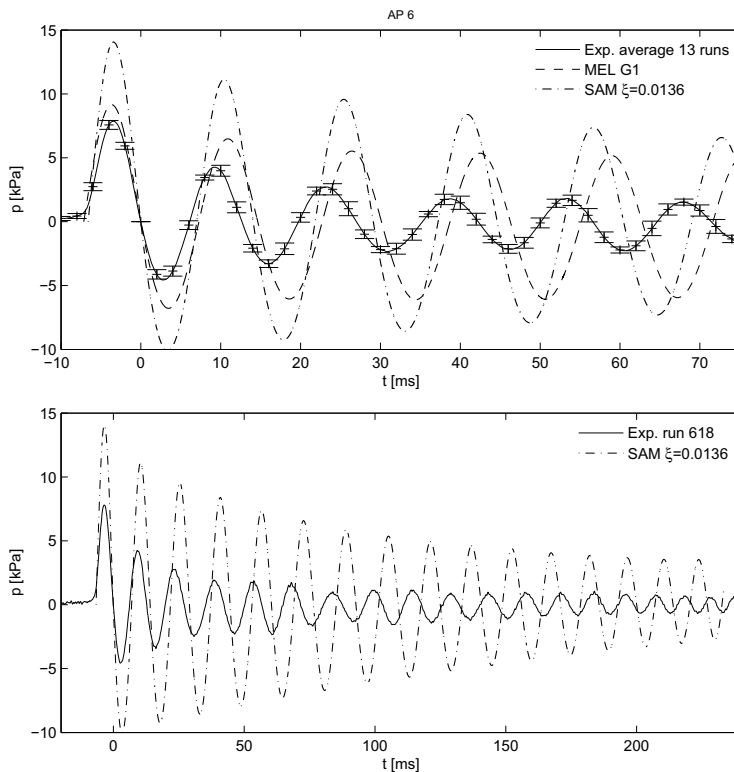
Figure 6.3: *Top:* Comparison of the initial part of the pressure time history for air pocket 6 from experiments (average of 13 runs), the mixed Eulerian-Lagrangian method (MEL) using grid setting G1 and the semi-analytical method (SAM) including damping. *Bottom:* Comparison of the pressure time history for air pocket 6 for run 18 of the experiment, and the SAM method including damping.

experiments reported in chapter 2 show to what extent the air pocket at the upper corner deviates from the free decay of an under-damped mass-spring system. This is seen as non-exponential decay of the pressure amplitudes in figure 2.11 and 2.12 and non-constant period T_i in the figure 6.4, of the pressure time history. A general trend is that the decay is especially large during the time from the first pressure maximum to the first pressure minimum. The ratio of the first two pressure amplitudes, P_2/P_1 is 0.73 for the semi-analytical method (SAM) including damping from heat exchange, and viscous boundary layers from the walls not including the roof. The same ratio is 0.74 for the mixed Eulerian-Lagrangian method (MEL), while the average line of 13 experimental runs give 0.58. The reason for the decay of the semi-analytical method (SAM) during the first period is the change of the wetted length parameters a and b, which changes the natural frequency. The change of the natural period during the initial stage is evident from figure 6.4. The change of a and b during the time of

Figure 6.4: Comparison of the time between pressure peaks T_i for air pocket 6, from the analytical expression (5.5) using experimental values for a,b and Ω_0, the mixed Eulerian-Lagrangian method (MEL) using the G1 settings and the experiments. $T_i = t_{i+1} - t_i$, where t_i denotes the time of pressure peak i.
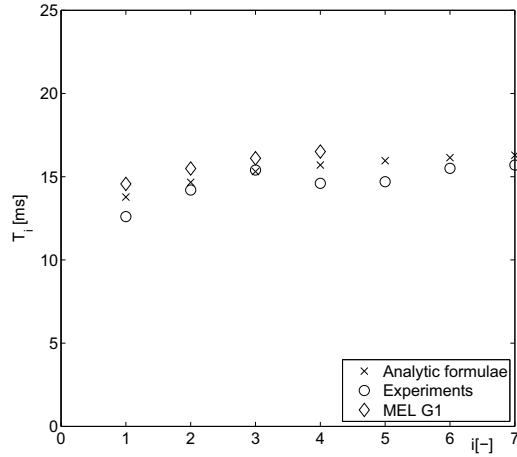
oscillations is a nonlinear effect, and this nonlinear effect is seen to cause substantial decay during the initial stage of the impact. From the undamped semi-analytical method (SAM) it is also evident that this nonlinear effect increases the amplitude at the end of the impact (see figure 5.10). This effect is not seen in the experiments where an overall decay trend of the pressure oscillations are observed. From the results of the semi-analytical method it is seen that the overall decay trend of the experimental pressure time histories can be explained by thermal and boundary layer damping.

Jets are formed just after impact. The kinetic energy which enters these jets follow the roof for some time before it falls down on the underlying water as "rain". This energy can be considered lost or destroyed. The jets in the mixed Eulerian-Lagrangian method (MEL) are cut, and hence the kinetic energy assosiated with the jets are lost. The jet cutting is however not seen to cause any significant decay of the pressure time history. This suggests that the jets does not serve as a damping mechanism of significance for air pocket 6 during the time before the mixed Eulerian-Lagrangian method (MEL) breaks down. To summarize the present study, the decay of the air pocket oscillations are found to be affected by nonlinear effects, heat conduction, viscous dissipation and if present; air leakage.

Chapter 7

Scaling of air pocket impacts

The scaling of pressure time histories of air pocket slamming events is investigated. The experiments carried out in chapter 2 consisted of air and freshwater under atmospheric conditions. This experimental set-up is often used to represent full scale problems consisting of air and seawater at atmospheric conditions. The presence of waves requires that the Froude number Fn must be similar in model and full scale. However, since nearly the same fluids are used in model and full scale and the same atmospheric pressure is maintained, the model has a different Euler number Eu. Since the Euler number is important for air pocket slamming events, the air pocket behaviour will not be similar in model and full scale, and hence the pressure measured in model experiments cannot be scaled to full scale using Froude scaling. So what kind of scaling procedure can be applied for this problem?

Lundgren [11] established a scaling procedure for the maximum pressure of air pocket impacts based on Bagnold's piston model [1]. The input to this scaling procedure is the peak pressure in model scale and the result is the peak pressure in prototype scale. Hence, the procedure does not give any information about the temporal variation of the pressure, which from a structural response point of view is important. A new scaling procedure called the pressure-amplitude and rise-time scaling procedure (PARTS) is proposed which also yields information about the temporal variation of the pressure. This means that information about the rise time T can be found. In the new procedure a simplified nonlinear mathematical problem for the air pocket is established. This mathematical problem is a nonlinear ordinary differential equation (ODE) in terms of the absolute pressure $\bar{p}$. The input to the present method is the pressure time history from the model. No other information is required like the air pocket geometry or impact speed. The mathematical problem of the air pocket contains two parameters. The values of these two parameters are obtained from the measured pressure-amplitude and the rise-time in experiments. Then the mathematical problem is scaled to prototype scale and solved to obtain the pressure time history in prototype scale. From this pressure time history the peak pressure and rise time for the prototype can be found. The pressure amplitudes obtained from this scaling procedure is equal to the pressure amplitudes obtained using Lundgren's scaling procedure based on Bagnold's piston model. The validity of the new scaling procedure is investigated by comparison with the mixed Eulerian-Lagrangian method (MEL) for air pocket 6.
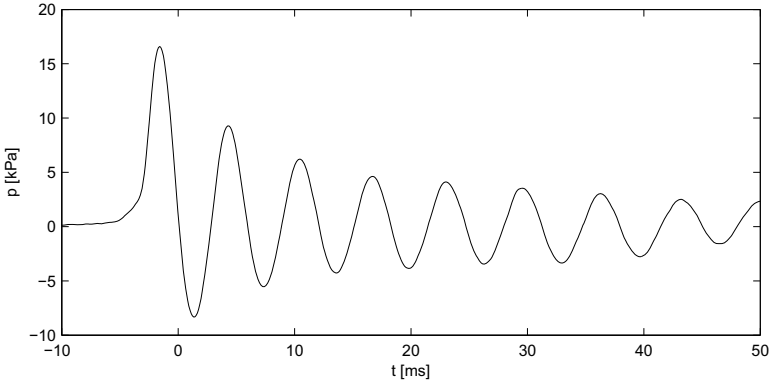
Figure 7.1:   Pressure measurements in model scale from air pocket 1 run 10. The rise time $T_e = 2$[ms] and peak dynamic pressure is $P_e = 16.630$[kPa].

7.1   A mathematical model of an air pocket

In the following the mathematical problem is posed. Here the semi-analytic air pocket model (SAM) by Faltinsen and Timokha [8] is used as presented in chapter 5. To arrive at a scaling procedure for the pressure, simplifications to this mathematical problem is introduced in the following way. The first simplification is that air leakage must be neglected. The second simplification is that the entering liquid velocity V has no time dependence. This can be justified by the fact that the origin of the entering velocity is often the first mode of sloshing which varies slowly in time compared to the pressure oscillations. The third requirement imposed is that the geometry parameters a and b of the air pocket seen in figure 5.1 do not vary during the oscillations. Introducing these two conditions into Faltinsen and Timokha's equations result in

$$\rho I_1 \frac{\partial^2 \Omega}{\partial t^2} = p_0 \left[\left(\frac{\Omega_0}{\Omega(t)} \right)^\kappa - 1 \right]. \tag{7.1}$$

Here I_1 is given by

$$I_1 = \frac{K[\sqrt{1 - (b/a)^2}]}{K[b/a]}. \tag{7.2}$$

The function $K(k)$ is defined in equation (5.3). The initial conditions for the equation are:

$$\begin{aligned} \Omega &= \Omega_0 & t &= 0 \\ \frac{d\Omega}{dt} &= -V_0 I_2 & t &= 0. \end{aligned} \tag{7.3}$$

Here I_2 is given by

$$I_2 = a[E(b/a) - K(b/a)]. \tag{7.4}$$

The function $E(k)$ is defined in equation (5.3). The polytropic gas law is used in the present method. There are several assumptions that need to be valid in order to use this mathematical

model to scale the pressure time history to prototype scale. These assumptions are listed next for clarity.

- The compression of the air pocket must be assumed either adiabatic or isothermal. In general the heat exchange between the air inside the air pocket and the surroundings may matter as described in chapter 5.

- There cannot be any boiling or condensation phenomena associated with the air pocket oscillations.

- There cannot be any significant air leakage to and from the air pocket during the air pocket impact.

- The hydrodynamic problem must be well described through a linearised model, and this linearised hydrodynamic problem must be geometrically similar in model and in prototype scale.

- The oscillation needs to be free. This is true if the problem of the entering water varies slowly in time corresponding to the time scale of the air pocket oscillations.

- At the time instant when the air pocket is closing, the pressure inside the air pocket needs to be close to the ullage pressure.

- The pressure inside the air pocket is uniform in space. The time scale of the pressure oscillations must be longer than the acoustic time scale of the air pocket.

The assumptions only need to be valid during the time from $t = 0$ to $t = T$ in order for the scaling procedure to give information about the pressure amplitude P and the rise time T. The proposed procedure can be generalized to, for instance, entrapped air pocket impacts due to breaking waves on vertical walls.

7.2   Procedure for scaling

The proposed method, the pressure-amplitude and rise-time scaling procedure (PARTS), does not make use of energy considerations as Lundgren's procedure based on Bagnold's piston model [11], but instead solves the ordinary differential equation (7.1) and the initial conditions (7.3). Since the procedure aims to scale pressure measurements this problem is rewritten so that the primary unknown is the absolute pressure $\bar{p}$ and not the volume Ω. Equation (4.4) is then expressed as:

$$\Omega = \Omega_0 \left(\frac{p_0}{\bar{p}(t)} \right)^{\frac{1}{\kappa}}. \tag{7.5}$$

Which means that

$$\frac{d\Omega}{dt} = -\frac{\Omega_0 p_0 \bar{p}^{-2}}{\kappa} \left(\frac{p_0}{\bar{p}(t)} \right)^{\frac{1}{\kappa}-1} \frac{d\bar{p}}{dt} \tag{7.6}$$
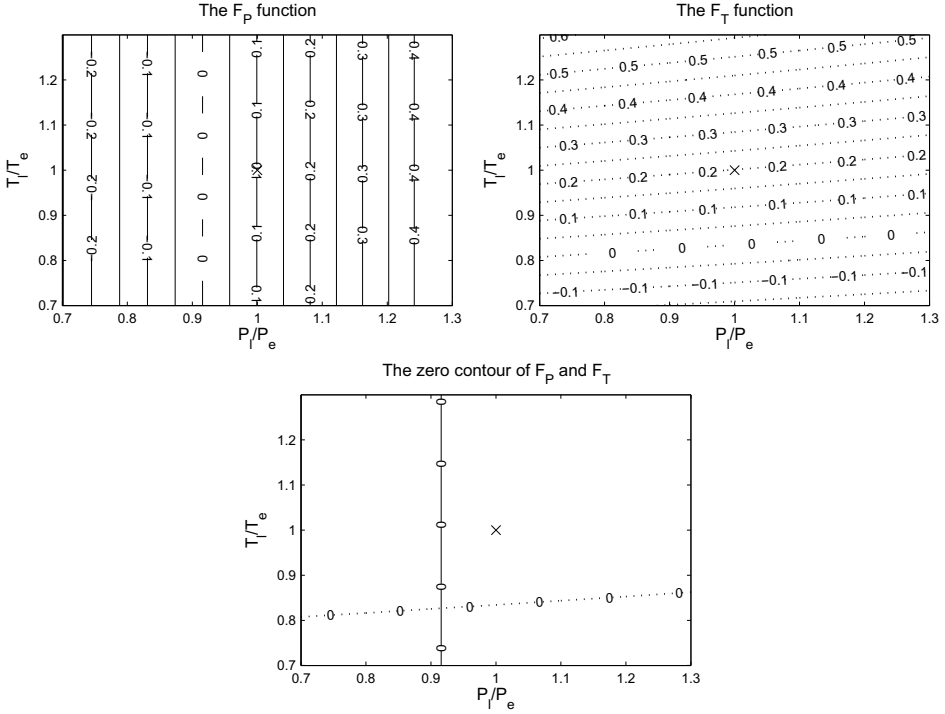
Figure 7.2: The graphical procedure which fits the nonlinear problem to experimental measurements. The upper left and upper right plots show the isocontours of the functions $F_P(P_l, T_l)$ and $F_P(P_l, T_l)$. The intersection between the zero contours of these two functions is plotted on the lowermost plot. The intersection point of these lines is the optimal values of $P_l = P_o, T_l = T_o$

and

$$
\frac{d^2\Omega}{dt^2} = -\frac{\Omega_0 p_0}{\kappa}
$$
$$
\left[\left\{ -2\bar{p}^{-3} \left(\frac{p_0}{\bar{p}} \right)^{\frac{1}{\kappa}-1} - (\frac{1}{\kappa} - 1) \left(\frac{p_0}{\bar{p}} \right)^{\frac{1}{\kappa}-2} p_0 \bar{p}^{-4} \right\} \right. \tag{7.7}
$$
$$
\left. \left(\frac{d\bar{p}}{dt} \right)^2 + \left(\frac{p_0}{\bar{p}} \right)^{\frac{1}{\kappa}-1} \bar{p}^{-2} \frac{d^2\bar{p}}{dt^2} \right].
$$

In this way the pressure can be used as the primary unknown in the differential equation:

$$
\frac{d^2\bar{p}}{dt^2} = \left\{ \frac{1}{\kappa} + 1 \right\} \left(\frac{1}{\bar{p}} \right) \left(\frac{d\bar{p}}{dt} \right)^2 + \left[\frac{1}{I_1 \Omega_0} \right] \left(\frac{\kappa \bar{p}}{\rho} \right) \left(\frac{\bar{p}}{p_0} \right)^{\frac{1}{\kappa}} \left(p_0 - \bar{p} \right). \tag{7.8}
$$

Now, initial conditions for $\bar{p}$ and $d\bar{p}/dt$ are needed. The initial pressure is set equal to the ullage pressure p_0 and the initial condition for $d\bar{p}/dt$ is found from (7.6). The initial conditions

are then given as:

$$\begin{aligned}
\bar{p} &= p_0 & t &= 0 \\
\frac{d\bar{p}}{dt} &= p_0 \kappa \left(\frac{V_0 I_2}{\Omega_0} \right) & t &= 0
\end{aligned} \tag{7.9}$$
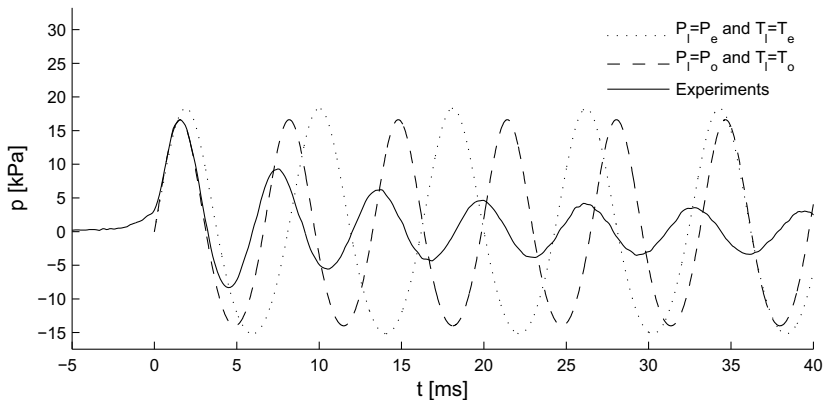
Figure 7.3: The nonlinear mathematical problem fitted to experiments using parameters from experiments ($T_l = T_e$, $P_l = P_e$) and the optimal parameters from the graphical procedure ($T_l = T_o$, $P_l = P_o$).

In order to obtain the same pressure time history when solving (7.8) using (7.9), then the parameters $I_1\Omega_0$, V_0I_2/Ω_0, p_0, κ and ρ needs to be equal. The two first parameters, $I_1\Omega_0$, V_0I_2/Ω_0, are kinematic parameters originating from the geometry and the velocity field of the air pocket. These two parameters can be fitted to one particular air pocket. The other three parameters p_0, κ and ρ are in this work assumed to be equal at all scales. However, in general they can be different and the present procedure can be generalized to include this fact. The nonlinear mathematical problem can be solved numerically using a standard numerical procedure. Here an explicit Runge-Kutta method is used for this purpose.

The solution of the nonlinear problem (7.8), (7.9) is now fitted to experiments. This is done by finding values for the two kinematic parameters which produces the same maximum dynamic pressure and rise time. The maximum dynamic pressure and rise time obtained when solving (7.8), (7.9) is denoted P and T. Since no analytical solution exists for the nonlinear problem, no analytical relation between (P, T) and $(I_1\Omega_0$, $V_0I_2/\Omega_0)$ can be found. However, if the problem is linearised, analytical relations can be found. Introducing $\Omega = \Omega_0 + \Delta\Omega$ and linearising equation (7.1) leads to the following linear differential equation for the dynamic pressure p:

$$\frac{d^2 p}{dt^2} + \frac{p_0 \kappa}{I_1 \rho \Omega_0} p = 0 \tag{7.10}$$

The solution to this equation is $p(t) = P_l sin(\omega_0 t)$. Here P_l is the pressure amplitude for the

solution of the linear problem and ω_0 is the natural frequency given by:

$$\omega_0 = \sqrt{\frac{p_0\kappa}{I_1\Omega_0\rho}} = \frac{\pi}{2T_l}. \tag{7.11}$$

Where T_l is the rise time of the linear problem. Now we have a linear estimate of the parameter $I_1\Omega_0$ from equation (7.11):

$$I_1\Omega_0 = \frac{4T_l^2 p_0\kappa}{\pi^2\rho}. \tag{7.12}$$

By taking the time derivative of the solution of the linear problem (7.10) and inserting ω_0 through equation (7.11), a value for the second parameter is found as:

$$\frac{V_0 I_2}{\Omega_0} = \frac{\pi}{2p_0\kappa}\frac{P_l}{T_l} \tag{7.13}$$

Now, linear estimates of the parameters for the nonlinear problem are established. If experimental values of the maximum dynamic pressure P_e and rise time T_e is inserted in equation (7.12) and (7.13), then the value of these parameters can be inserted in the nonlinear problem (7.8) and (7.9). The solution to this problem will have a dynamic pressure amplitude P and rise time T, which will be different from P_e, T_e. However, P, T will be close to P_e, T_e if the compression of the air pocket is close to linear.

Figure 7.4: The pressure time history after the pressure-amplitude and rise-time scaling procedure (PARTS) has been applied to air pocket 1 run 10. The results are made non-dimensional assuming Froude scaling. λ is the geometric scaling factor $\lambda = L_p/L_m$ where L_m and L_p are the same characteristic dimension for the model and prototype, respectively.
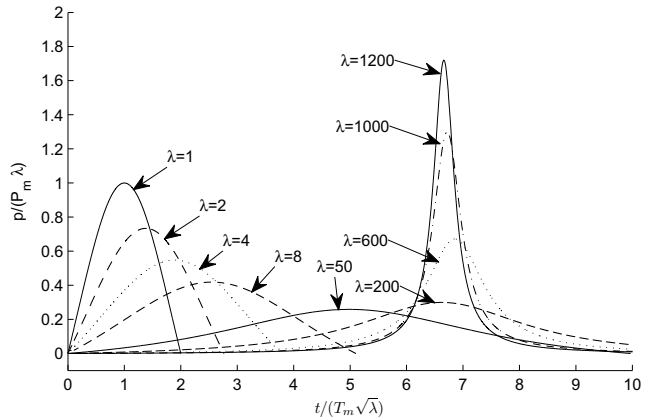
The procedure of inserting linear estimates of the maximum dynamic pressure P_l and rise time T_l and solving the nonlinear problem (7.8) and (7.9), obtaining nonlinear maximum dynamic pressure P and rise time T, can be seen as evaluating the functions $P(P_l, T_l)$ and $T(P_l, T_l)$. Different values of P_l, T_l are then solved for around the experimental values P_e, T_e in order to find the optimal values of the input parameters P_l, T_l which produces $P = P_e$ and $T = T_e$. These optimal values of P_l, T_l are denoted P_o, T_o.

The maximum dynamic pressure P_e and rise time T_e is taken from the pressure measurements in figure 7.1. The rise time is estimated as two times the time between $p = P_e/2$ and
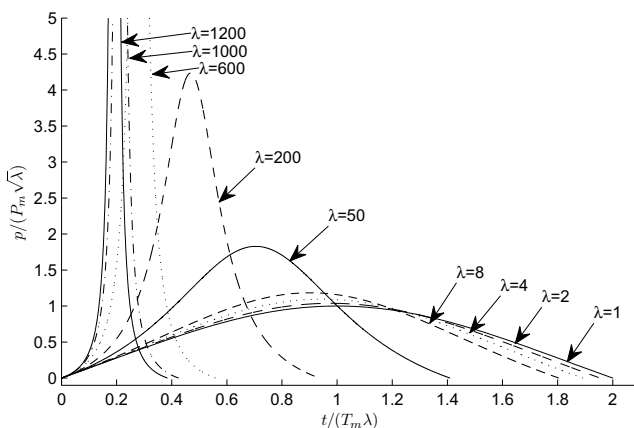
Figure 7.5: The pressure time history after the pressure-amplitude and rise-time scaling procedure (PARTS) has been applied to air pocket 1 run 10. The results are made non-dimensional based on the analytical scaling resulting from a linearised polytropic air pocket model. λ is the geometric scaling factor $\lambda = L_p/L_m$ where L_m and L_p are the same characteristic dimension for the model and prototype, respectively.

$p = P_e$. This results in $T_e = 2.0$[ms] and maximum dynamic pressure $P_e = 16.630$[kPa]. The ullage pressure is set to $p_0 = 101$[kPa], $\kappa = 1.4$ and $\rho = 1000$[kg/m^3]. Two functions are then defined as

$$F_P(T_l, P_l) = \frac{P(P_l, T_l) - P_e}{P_e} \tag{7.14}$$

and

$$F_T(T_l, P_l) = \frac{T(P_l, T_l) - T_e}{T_e}. \tag{7.15}$$

The nonlinear problem is then solved using values for P_l, T_l ranging from $0.7P_e \leq P_l \leq 1.3P_e$ and $0.7T_e \leq T_l \leq 1.3T_e$. In the upper left and right plot in figure 7.2 the functions F_P and F_T are seen. On the lower most plot the optimal values P_o, T_o is seen as the intersection between the zero contour of the function F_P and the zero contour of F_T. This point is $P_o/P_e = 0.9158$ and $T_o/T_e = 1.0569$.

The numerical solution of the nonlinear mathematical problem using $P_l = P_e$ and $T_l = T_e$ and optimal values $P_l = P_0$ and $T_l = T_o$ can be seen in figure 7.3. It is seen that the optimal values fit the experiments well during the initial compression of the air pocket. Later there are deviations related to changing natural period and decay of the pressure amplitudes. In the plot the solution of the nonlinear problem using $P_l = P_e$ and $T_l = T_e$ is also seen. This results in too long rise time and too large maximum pressure.

Now, having fitted the mathematical model to the experiments, the model can be scaled to prototype scale and then solved. Assuming that the air pocket can be well represented by a linearised hydrodynamic problem which is geometrically similar at all relevant scales then I_2 should be scaled with λ, where λ is defined as the geometric scale factor $\lambda = L_p/L_m$. L_m and L_p being the same characteristic length for the model and prototype, respectively. When using the expression "the linearized hydrodynamic problem" it concerns the parameters a and b. It is emphasized that the nonlinear polytropic gas law is used and that it is the only source of nonlinearity present in the nonlinear problem. I_1 is equal in all scales since a and b scales geometrically. V_0 is the impact velocity and is connected to the gravity waves, hence

this velocity follows Froude scaling. Then the two parameters of the nonlinear problem can be scaled. $I_1\Omega_0$ then scales like λ^2 and $V_0 I_2/\Omega_0$ scales like $\lambda^{-1/2}$.
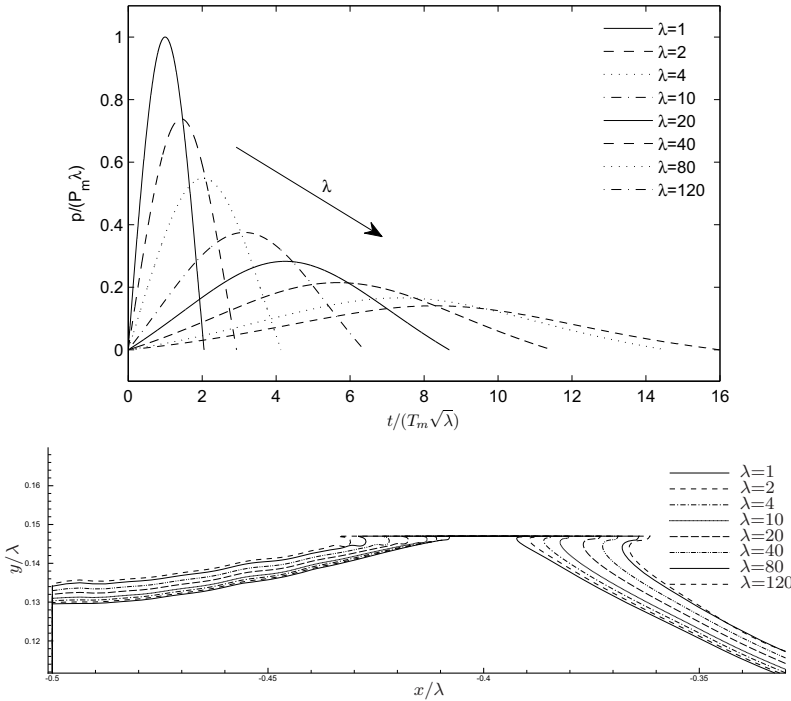
Figure 7.6: *Top:* Dynamic pressure inside the air pocket from the mixed Eulerian-Lagrangian method (MEL) using the G1 grid setting applied to air pocket 6. The curves are made non-dimensional using the Froude scaled maximum pressure: $P_m\lambda$ and the Froude scaled value of the rise time $T_m\sqrt{\lambda}$. *Bottom:* The free surface profiles for the mixed Eulerian-Lagrangian method (MEL) at different scales for the time instant of maximum pressure $p = P$. The geometry has been scaled to model scale.

The result can be seen in figure 7.4. Here the pressure is made non-dimensional based on the Froude scaled maximum pressure $P_m\lambda$. Here P_m denotes the maximum dynamic pressure in model scale. If Froude scaling was applicable, all curves would lie on top of the curve for $\lambda = 1$. For this air pocket it is seen that Froude scaling is conservative, in terms of maximum pressure, for a scaling parameter less than 600. The rise time measured in terms of the mentioned definition, is seen to be longer than the Froude estimate for the range of scales $\lambda = 1 - 600$. At larger scales the rise time is shorter than the Froude scale estimate.

In the pressure-amplitude and rise-time scaling procedure nonlinearity with respect to the polytropic air pocket model is maintained. If this relation is linearised, scaling of the pressure and time can be made analytically. From (7.12) it is evident that the time in prototype scale t_p is related to the time in model scale t_m as $t_p = t_m\lambda$. Then equation (7.13) yields that the

pressure is scaled according to the formula $p_p = p_m\sqrt{\lambda}$. Scaling according to these formulas is denoted linear scaling in the following. Making the results non-dimensional assuming this scaling is shown in figure 7.5. For air pocket 1 it is seen that the linear scaling law works for small scaling ratios $\lambda < 8$ and that it is inaccurate for scaling ratios larger than this. However, this conclusion is dependent on the maximum pressure in model scale and is not general.

The horizontal tank dimension (L) was one meter, so interesting prototype tanks inside ships are less than $\lambda = 50$. The range of scales investigated exceeds this. However, if a larger peak pressure was observed for the model scale air pocket, then the critical scale where Froude scaling is no longer conservative would be reduced. The validity of this kind of scaling is based on the validity of the assumptions listed in the previous section.
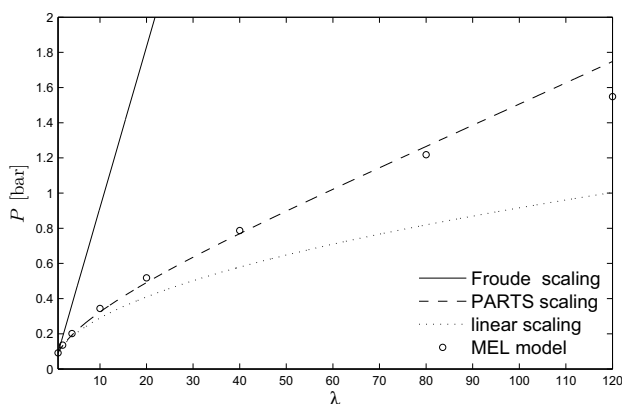
Figure 7.7: Dynamic pressure maxima from the mixed Eulerian-Lagrangian method (MEL) compared with the Froude scaling law, the pressure-amplitude and rise-time scaling procedure and the linear scaling law.

7.3 Comparison with the MEL method

To verify the new scaling procedure, the mixed Eulerian-Lagrangian method (MEL) presented and applied to air pocket 6 in chapter 4 is now used to solve the problem at different scales. The results are then used to test the new scaling procedure. The input parameters of air pocket 6 were scaled to different prototype scales assuming Froude scaling only. That is $\lambda = 1, 2, 4, 10, 20, 40, 80, 120$. The ullage pressure was kept equal to the atmospheric pressure in all scales. This means different Euler numbers for all scales. For the smallest scale the code runs for many oscillations of the air pocket. For the other scales the model breaks down after the first half period of oscillation. Therefore only the first half period is included in the following plots. The different non-dimensional dynamic pressure time histories are shown in figure 7.6. In this plot the dynamic pressure time history is made non-dimensional by dividing the pressure by $P_m\lambda$. $P_m\lambda$ is the maximum dynamic pressure assuming Froude scaling. The time is made non-dimensional by the time scale $T_m\sqrt{\lambda}$, which is the Froude scaled rise time. The pressure maximum is lower and the rise time is longer than the corresponding Froude scaled values.

Figure 7.8: Compar-
ison of the pressure-
amplitude and rise-time
scaling procedure
(PARTS) and the results
from mixed Eulerian-
Lagrangian method
using the grid setting
G1.
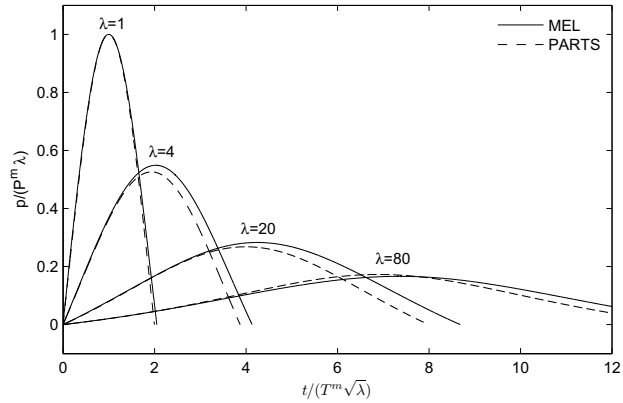
The free surface geometry is compared for the different scales in the lower plot of figure 7.6 at the time instant of maximum pressure $p = P$. The geometry of the free surface is scaled down a factor λ. The flow field and the geometry of the air pocket is not similar due to the different Euler numbers at the different scales. One of the assumptions of the pressure-amplitude and rise-time scaling procedure is that the same linearised hydrodynamic problem should be valid for both the model and the prototype scale.

Figure 7.9: The im-
pulse of the pressure
time history from
the mixed Eulerian-
Lagrangian method
using grid setting G1
is compared to Froude
scaling.
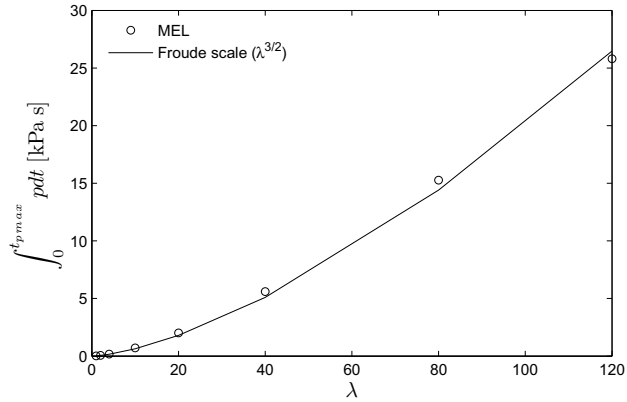
In figure 7.7 the pressure amplitude from the mixed Eulerian-Lagrangian method is compared with Froude scaling, the pressure-amplitude and rise-time scaling procedure (PARTS) and the linear scaling law. The linear scaling law is the scaling law if the pressure-volume relationship is linearised. When applying the pressure-amplitude and rise-time scaling procedure (PARTS) the parameters of the mathematical problem was fitted to the pressure time history in model scale. Then the parameters of the problem were scaled to prototype scale and the mathematical problem was solved numerically. The rise time was easier to estimate for the pressure time history than for the experiments in figure 7.1 so the rise time was defined to be the time from $p = 0$ to $p = P$. The results in figure 7.7 show that the

mixed Eulerian-Lagrangian method is close to the results from the pressure-amplitude and rise-time scaling procedure. Further, the pressure-amplitude and rise-time scaling procedure was compared to the mixed Eulerian-Lagrangian method in time domain in figure 7.8. It is seen that the rise time is fairly well captured by the pressure-amplitude and rise-time scaling procedure.

Bagnold's piston model of the air pocket suggests that the impulse of the pressure time curve from the time when the compression starts to the time when the pressure is maximum, should Froude scale. This means that the quantity $\int_0^T p(t)dt$ should scale like $\lambda^{3/2}$. In figure 7.9 the mixed Eulerian-Lagrangian method is compared with Froude scaling. The figure shows that the impulse follows closely the scaling $\lambda^{3/2}$ derived based on Froude scaling.

Chapter 8

Conclusions

An extensive investigation of the physical behaviour of an air pocket slamming event in the upper corner of a two-dimensional sloshing tank has been carried out. In this study experimental, numerical and semi-analytical methods have been applied. In the following the work carried out in connection with the three objectives listed in the introduction is summarized and concluded upon.

The first objective of this work was to design experiments of idealized air pocket slamming events in the upper corner of a liquid-filled tank during sloshing at high filling which are as repeatable as possible. To achieve this objective a new experimental set up was established in order to create more repeatable, idealized air pocket impact events still showing the same physical behaviour as air pockets occurring during regular sloshing. The key ingredient was the derivation of a new excitation signal based on linear multi-modal theory. The excitation signal was then inserted as forced motion of a tank. Six different air pockets were produced based on variation of the excitation signal. The pressure time history from the experimental impacts show varying degree of repeatability.

Conclusion 1: The air pocket which was most repeatable, which is referred to as air pocket 6, had generally the same physical characteristics as the other air pocket slamming events. Air pocket 6 had also the same characteristics as the air pocket reported by Faltinsen and Timokha [8] which was obtained during regular sloshing after multiple contacts with the roof. It is concluded that the experiments made in this work were sufficiently repeatable for reliable comparison with two dimensional mathematical models. However, air pocket 6 did not close instantly across the width of the tank. This three-dimensional effect must be considered when comparing the results with two-dimensional mathematical models.

Based on the experiments the air pocket impact was divided into a sloshing stage, an air-escape stage and an air pocket oscillation stage. The experiments were also used to motivate the assumptions behind the mathematical problem of the boundary-element-finite-difference method applied for the sloshing and air-escape stages and the mixed Eulerian-Lagrangian method applied to the air pocket oscillation stage. In order to describe the physical effects

governing the air pocket impact, mathematical models were used in combination with experiments. A summary of the mathematical models applied follows. In chapter 3 a new numerical procedure the boundary-element-finite-difference method (BEFDM) for the sloshing and air-escape stage was derived, tested and applied to model the sloshing and air-escape stage of air pocket 6. In chapter 4, a version of the classical mixed Eulerian-Lagrangian method, was applied to the air pocket oscillation stage. The initial conditions were found from the results from the boundary-element-finite-difference method (BEFDM) applied to the sloshing and air-escape stages. At the end of the air-escape stage, one node of the boundary-element-finite-difference method crosses the roof. In order to continue the simulation using the mixed Eulerian-Lagrangian method (MEL) the roof needs to have an initial wetted length. Due to the complexity of the physical effects governing the closure of the air pocket, a pragmatic ad-hoc approach is used to close the air pocket, so that initial conditions for the mixed Eulerian-Lagrangian method can be obtained and the simulation continued. Based on a sensitivity analysis the results are seen to be insensitive to this ad-hoc procedure. The mixed Eulerian-Lagrangian method broke down after some oscillations of the air pocket, due to a growing instability inside the air pocket. The results from the mixed Eulerian-Lagrangian method show that the peak pressure can be reasonable well predicted. Due to the breakdown of the mixed Eulerian-Lagrangian method, the semi-analytical method (SAM) of Faltinsen and Timokha [8] was applied to model the whole air pocket oscillation stage. The initial volume, the parameters describing the wetted length and the impact velocity used in the semi-analytical method were found from experiments. The SAM method was extended to include the damping effect of heat exchange to and from the air pocket. The method describing the air pocket assumed one dimension, steady state, linear, uniform pressure and heat flow through conduction. The SAM method was also extended to include the damping effect of laminar boundary layers in the water at the tank walls. The mathematical model of the damping effect due to viscous boundary layers assumed no interaction between the flow field of the entering water and the flow field of the air pocket oscillations. There is uncertainty related to the contribution from the boundary layers at the roof, due to a singular integral. However, a lower bound of the damping ratio was estimated by excluding the contribution from the roof.

The following conclusions are reached in connection to the second objective of this work which was to obtain new knowledge regarding the physical effects governing air pocket slamming events. In the following the results from the experiments and mathematical models are compared for the different stages of the air pocket slamming event.

Conclusion 2: The air pocket slamming event starts when the wave crest approaches the roof and air escapes at increasing speed. For all the air pockets studied in the experiments, interaction between the escaping air and the water was observed just before the wave crest touched the roof. For air pocket 6 this was seen as a sharpened wave crest just prior to closure of the air pocket. The closure of the air pocket 6 was also seen not to be instantaneous perpendicular to the two-dimensional plane of the assumed theoretical flow. The sloshing and air-escape stages were solved by using the boundary-element-finite-difference method. The results show interaction between the air and the water, however not as pronounced as

seen in the experiments. This might suggests that there are physical effects missing in the mathematical model. The compressibility effects of the escaping air were then investigated in a separate model where the free surface was assumed to be rigid and approaching the roof at constant speed. The problem was solved using an existing numerical code called CLAWPACK. The results show that compressibility effects are important when the distance between the wave crest and the roof is less than 0.5[mm]. For comparison the maximum thickness of the air pocket is 18 [mm], while the initial length of the air pocket is 89 [mm]. The simulation was stopped when the Mach number, defined as $M = u_g^{\max}/c_o$ was equal to unity. Here $u_g^{\max}$ is the maximum gas velocity and c_0 is the speed of sound. The air pocket was closed instantaneously at a Mach number equal to one, and two shock waves were seen to travel in opposite directions horizontally out from the area of the wave crest. The closure of the air pocket resembles the "water hammer" effect which is a known problem in connection to sudden blockage of pipe flows. This physical effect can be of importance for the closure of the air pocket, however other physical effects can also matter, like viscosity of the air and water. The time of closure is the time instant when air can no longer escape the air pocket through any opening. This means that the roof is continously wetted. From the experiments it was found that the time of closure varied dependent on which type of air pocket which was studied. Air pocket 1 and 6 closed just after the first contact with the roof. Air pocket 4 closed at the time instant of maximum pressure and air pocket 5 and 8 closed just after the first zero down crossing. The leakage of air out of air pocket 5 and 8 took place through the later wetted section of the roof. This means that the tank roof was not continuously wet across the thickness (z-direction) during the time of leakage. When the wave crest touches the roof the pressure inside the air pocket increases and starts to oscillate. The pressure time history of the oscillating air pocket does to some extent resemble the free oscillations of a linear under-damped mass-spring system. However, the response of such a system should have a constant period of oscillation and exponential decay. Here a remark is made on the difference between decay and damping. Decay refer to general reduction of the pressure amplitude and does not suggest anything about the physical or mathematical reason for the amplitude reduction. Damping refer to the reduction of the amplitudes due to dissipation of kinetic and potential energy of the system. For the free oscillations of an under-damped linear mass-spring system, then the only sources of amplitude reduction is energy leaving the system or what is denoted damping sources. Examples of damping sources, which remove energy from the system, are heat exchange and viscous boundary layers. However, for an air pocket impact the reasons for the decay does not need to be damping sources. The semi-analytical method by Faltinsen and Timokha [8] shows that the reason for decay can be nonlinear potential flow effects connected to the change of the wetted length of the roof or forcing terms. In general, the decay of the air pocket pressure amplitude can be due to exchange of combined kinetic and potential energy between the air and the water and can not in general be denoted damping sources. The characteristics of the air pocket oscillations are the period, maximum amplitude and the decay. In the following these characteristics are commented.

The following experimental observations related to the decay of the air pocket oscillations were made. All the experimentally investigated air pockets show large initial decay compared

to the later decay trend. Here initial decay refers to the decay during the time from the first pressure maximum to the first pressure minimum and the later decay trend refers to the the decay after the first pressure minimum. The word trend is used to indicate that the air pockets generally looses amplitude as a function of time, however irregularities related to this has been observed, like air pocket 4, where the amplitude increases after about 4 periods of oscillation. However, also for air pocket 4 the overall trend is decay of the pressure amplitude. The fact that the decay is not strictly exponential suggests that there are physical effects which cannot be explained as free oscillations of a one degree of freedom under-damped mass-spring system. The mechanical system is more complex than this and the reason is nonlinear effects, as seen in the semi-analytic method. The results from the mixed Eulerian-Lagrangian method support the conclusions from the original semi-analytical method by Faltinsen and Timokha [8] where it was concluded that there are nonlinear effects related to the changing geometry of the air pocket which cause significant decay of the pressure time history during the first period of oscillation. This nonlinearity also causes the period of oscillation to change, particularly during the first period of oscillation. After the first period of oscillation, the mixed Eulerian-Lagrangian method and the original semi-analytical method, based on a polytropic air pocket model assuming adiabatic conditions, do not show decay. This indicates that there are physical effects not included in the mathematical problem which add to the overall decay trend in the experiments. To find effects that could explain the overall decay of the experimental air pockets the role of heat exchange between the air pocket and the water, viscous boundary layers in the water at the tank walls and air leakage were investigated.

From the linear, one-dimensional, steady state and constant pressure heat conduction model it is seen that the polytropic gas model fail to model the damping effect of heat flow on the air pocket oscillations. The heat exchange was found to contribute to the decay of the pressure oscillations. The damping ratio ξ for all the investigated air pockets was between $0.540\% \leq \xi \leq 1.26\%$ and for air pocket 6 it was found to be $\xi = 0.772\%$. The heat exchange model also shows that the polytropic index κ for all the investigated air pockets was between $1.36 \leq \kappa \leq 1.39$ and that the polytropic index for air pocket 6 was $\kappa = 1.38$. This is close to the adiabatic value of $\kappa = \gamma = 1.4$. The heat exchange is in general seen to modify the stiffness of the air pocket and to damp the air pocket oscillations. This fact is believed to be important also for other air pocket slamming events discussed in the introduction like the impact of a horizontal flat plate on an initially calm free surface, the breaking wave entrapping an air pocket at a vertical wall and the wave entrapping an air pocket underneath a marine structure.

The mathematical model of the damping effect due to linear, laminar and viscous boundary-layers assumed no interaction between the flow field of the entering water and the flow field of the air pocket oscillations. There is uncertainty related to the contribution from the boundary layers at the roof, due to a singular integral. However, a lower bound of the damping ratio was estimated by excluding the contribution from the roof. Even when this lower bound was used in the calculations the viscous boundary layers contributed with similar magnitude as the heat conduction to the damping of the pressure oscillations.

A main finding of the present experiments was that no air was leaking into or out from

the air pocket after the first pressure minimum for any of the investigated air pockets. This means that air leakage cannot explain the overall decay trend of the air pocket oscillations after the first pressure minimum. A separate set of experiments were carried out to investigate the role of air leakage in general. This was done by varying the diameter of a circular hole in the tank roof. Air pockets 6 and 7, which were seen to close before the first pressure maximum, were investigated. This means that air was only leaking through the hole in the roof during the air pocket oscillation stage for these air pockets. The experiments show that the air pocket oscillations have larger decay if air is allowed to leak into or out from the air pocket during the air pocket oscillation stage relative to if such air leakage does not occur. Air leakage cannot explain the initial and later decay of the air pockets oscillations of air pocket 1, 4, 6 and 7 when the hole in the roof is closed. This is because these air pockets are totally closed during the pressure oscillation stage. However, air leakage can explain the larger initial decay experienced for air pocket 5 and 8 compared to the closed air pockets 1, 4, 6 and 7. This because air pocket 5 and 8 show air leakage almost until the first pressure minimum. The experiments show that air leakage, if present, can very well be the largest cause of decay of air pocket pressure oscillation amplitudes.

Conclusion 3: The third objective of the present work was to investigate the scaling of air pocket impact events, and to describe the errors made by model experiments where the Euler number Eu is different in model and prototype. In addition the objective was to investigate if there are other non-dimensional numbers which are important related to slamming including air pockets. To achieve this objective a scaling procedure for pressure measurements of air pocket impacts is proposed. The new scaling procedure is denoted the pressure-amplitude and rise-time scaling procedure (PARTS). This scaling procedure is applicable for air pocket slamming events where the inflow conditions originate from gravity waves and hence follow Froude scaling. The model is assumed to be geometrically similar to the prototype. The Euler number is often different for model and prototype because the reference pressure in model and prototype is the atmospheric pressure. The method fits two parameters in a mathematical problem to model experiments using a graphical method. Then these parameters are scaled and the mathematical problem solved on different scales using numerical time integration. The polytropic gas model is applied for the air pocket assuming adiabatic conditions. The method produces the same peak pressures as Lundgren's scaling procedure [11] based on Bagnold's piston model. Contrary to Lundgren's procedure, the present scaling procedure also estimates the time variation of the pressure. This is useful for dynamic structural analysis where the rise time is an important parameter. The proposed pressure-amplitude and rise-time scaling procedure assumes that the hydrodynamic part of the air pocket problem can be linearized, and that the air pocket at larger scales can be represented by a geometrically similar problem. The procedure is validated using the mixed Eulerian-Lagrangian method. The rise time and peak pressure obtained from the scaling procedure agrees with the numerical model.

In order to do model tests of air pocket impact events, the governing physical effects of the air pocket impact and corresponding non-dimensional numbers need to be identified. These non-dimensional numbers can be identified by a non-dimensional version of the mathematical

problem, which reproduce the real air pocket slamming event. For the mixed Eulerian-Lagrangian method (MEL) and the original semi-analytic method (SAM) used in this work this yields the following non-dimensional numbers. That is the Froude number Fn, the Euler number Eu and the polytropic exponent κ. The polytropic index corresponding to adiabatic conditions is used in the present work. However, in general the polytropic index is dependent on the heat exchange between the air inside the air pocket and the water as stated in the second conclusion of this work. The non-dimensional number connected to heat exchange was in this work seen to be the Péclet number Pe, and the ratio of specific heats γ.

Chapter 9

Suggestions for future work

A list of suggestions are made for further work on this topic:

- Development of numerical tools that can handle the physical effects during closure of the air pocket.

- To carry out model experiments maintaining the same Euler number as in prototype scale, to verify the pressure-amplitude and rise-time scaling procedure (PARTS).

- To create a mathematical model where structural deflections are accounted for. This would allow to investigate hydroelastic effects, which is not investigated in the present work.

Bibliography

[1] R. A. Bagnold. Interim report on wave pressure research. *Journal of the Institution of Civil Engineers*, 12:201–226, 1939.

[2] M. Hattori and A. Arami. Impact breaking wave pressures on vertical walls. In *Ocean Engineering, Proceedings of the twenty-third international conference, vol 2*, 1992.

[3] H. Mitsuyasu. Shock pressure of breaking wave. In *Proceedings of the 10th International Conference on Coastal Engineering, Tokyo*, 1966.

[4] C. Lugni, M. Brocchini, and O. M. Faltinsen. Evolution of the air cavity during a depressurized wave impact I. The kinematic flow field. *Physics of Fluids*, 22:1–13, 2010.

[5] C. Lugni, M. Brocchini, and O. M. Faltinsen. Evolution of the air cavity during a depressurized wave impact II. The dynamic field. *Physics of Fluids*, 22:1–13, 2010.

[6] S. Zhang, D. K. P. Yue, and K. Tanizawa. Simulation of plunging wave impact on a vertical wall. *Journal of Fluid Mechanics*, 327:221–254, 1996.

[7] J. H. G. Verhagen. The impact of a flat plate on a water surface. *Journal of Ship Research*, pages 211–223, 1967.

[8] O. M. Faltinsen and A. N. Timokha. *Sloshing*. Cambridge University Press, 2009.

[9] J. M. Allers. Experimental investigation of high filling sloshing induced impacts for two-dimensional flow conditions. Master's thesis, Norwegian University of Science and Technology, 2004.

[10] C. Devin. Survey of thermal, radiation, and viscous damping of pulsating air bubbles in water. *The Journal of the Acoustic Society of America*, 31:12, 1959.

[11] H. Lundgren. Wave shock forces: An analysis of deformations and forces in the wave and in the foundation. In *In Proc. Symp. Res. Wave Action, vol 2, paper 4, Delft*, 1969.

[12] M. Greco, M. Landrini, and O.M. Faltinsen. Local hydroelastic analysis of a VLFS with shallow draft. In *Hydroelasticity in Marine Technology, 2003 Oxford*, 2003.

[13] R. J. H. Stive. Wave impact on uniform steep slopes at approximate prototype scale. In *Symposium on scale effects in modelling hydraulic structures, sept 3-6*, 1984.

[14] S. Maillard and L. Brosset. Influence of density ratio between liquid and gas on sloshing model test results. In *ISOPE*, 2009.

[15] F. M. White. *Fluid Mechanics*. McGraw-Hill, 1999.

[16] G. N. Bullock, A. R. Crawford, P. J. Hewson, M. J. A. Walkden, and P. A. D. Bird. The influence of air and scale on wave impact pressures. *Coastal Engineering*, 42:291–312, 2001.

[17] G. H. Keulegan. Energy dissipation in standing waves in rectangular basins. *Journal of Fluid Mechanics*, 6:33–49, 1959.

[18] O. M. Faltinsen. A numerical nonlinear method of sloshing in tanks with two-dimensional flow. *Journal of Ship Research*, 22:193–202, 1978.

[19] J. D. Anderson. *Computational fluid dynamics*. McGraw-Hill, 1995.

[20] T.F. Ogilvie. Nonlinear high-Froude-number free surface problems. *Journal of Engineering Mathematics*, 1(3):215–235, 1967.

[21] M. S. Longuet-Higgins and E. D. Cokelet. The deformation of steep surface waves on water I. A numerical method of computation. *Proceedings of the Royal Society of London*, 350:1–26, 1976.

[22] D. G. Dommermuth and D. K. P. Yue. Numerical simulations of nonlinear axisymetric flows with a free surface. *Journal of Fluid Mechanics*, 178:195–219, 1987.

[23] K. Tanizawa. A numerical simulation method of hydroelastic water surface impact based on acceleration potential. In *FEDSM99 3rd ASME/JSME Joint Fluids Engineering Conference, San Fransisco*, 1999.

[24] E. Kreyzsig. *Advanced Engineering Mathematics 8th*. John Wiley & Sons, 1999.

[25] C. H. Lu, Y. S. He, and G. X. Wu. Coupled analysis of nonlinear interaction between fluid and structure during impact. *Journal of Fluids and Structures*, 14:127–146, 2000.

[26] T. Kristiansen. *Two-dimensional numerical and experimental studies of piston mode resonance*. PhD thesis, Norwegian University of Science and Technology (NTNU), 2009.

[27] K. Tanizawa. The state of the art on numerical wave tank. In *Proceeding of the 4th Osaka Colloquium on Seakeeping Performance of Ships*, 2000.

[28] H. Sun. *A boundary element method applied to strongly nonlinear wave-body interaction problems*. PhD thesis, NTNU (Norwegian University of Science and Technology), 2007.

[29] M. Greco. *A two-dimensional study of green-water loading*. PhD thesis, Norwegian University of Science and Technology, NTNU, 2001.

[30] R. J. Leveque. *Finite volume methods for hyperbolic problems.* Cambridge University Press, 2002.

[31] E. B. Wylie and V. L. Streeter. *Fluid Transients.* FEB Press, 1983.

[32] B. Koehler and C. F. Kettleborough. Hydrodynamic impact of a falling body upon a viscous incompressible fluid. *Journal of Ship Research*, 21:165–181, 1977.

[33] R. Zhao and O. M. Faltinsen. Water entry of two-dimensional bodies. *Journal of Fluid Mechanics*, 246:593–612, 1993.

[34] I. S. Gradshteyn and I. M. Ryzhik. *Tables of integrals, series and products.* Academic press, 2000.

[35] F. M. White. *Viscous fluid flow.* McGraw-Hill, 2006.

[36] T. G. Leighton. *The acoustic bubble.* Academic Press, 1994.

[37] E. F. Toro. *Riemann solvers and numerical methods for fluid dynamics.* Springer, 1999.

Appendix A

Does the flexibility of the tank roof influence the results?
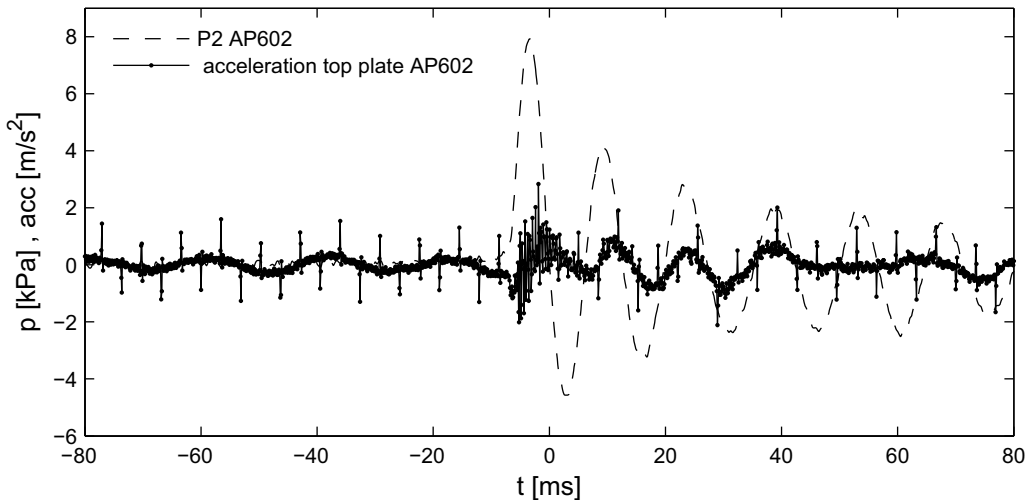
Figure A.1: Acceleration measurement of the top plate. The accelerations are seen not to create large enough displacements of the roof to considerably change the air pocket volume and hence affect the pressure oscillations.

When slamming experiments are performed the structure might deform, and cause important hydroelastic effects. The latter effect may be important for a real tank in full scale. However, our objective in the model tests was to consider a rigid tank. Because the elastic response of the tank interferes with the physical mechanism of the impact event, the corresponding bias error must be minimized in the model tests. The physics of the oscillating air pocket is governed by the spatially uniform pressure inside the air pocket which is directly related to the volume of the air pocket. Since the roof is the tank surface with the

largest exposed area towards the air pocket, the acceleration of the roof was monitored by an accelerometer mounted in the air pocket area. This accelerometer was attached beside the pressure sensors (see figure 2.3) and the measurements are shown in figure A.1. There is a tendency that the roof is oscillating with the same frequency as the air pocket. Assuming that the acceleration fits a sine or cosine function with an amplitude of $1[\text{m/s}^2]$ and a period of $10[\text{ms}]$ the amplitude of the plate oscillations would be approximately $0.0025[\text{mm}]$. Assuming that the displacement is uniform for the whole roof plate this causes a volume change of $\Delta\Omega = 25.1[\text{mm}^3]$. In the following the polytropic gas law (4.4) assuming adiabatic compression $\kappa = 1.4$ is used. In this equation the initial pressure is set equal to the atmospheric pressure $p_{0p} = 1.01 \cdot 10^5[\text{Pa}]$, the initial volume is set to $\Omega_0 = 810 \cdot 100[\text{mm}^3]$. From equation (4.4) the volume change induces a pressure variation of 44 [Pa] which is very small compared to the amplitude of the pressure oscillations and hence the roof can be considered as rigid in the experiments. The flexibility of the $x - y$-parallel side plates were also investigated by stiffening the tank by adding a clamp over the side plates of the tank. This stiffening did not alter the pressure signal and hence bias errors related to unwanted fluid-structure interaction seem negligible.

Appendix B

Analytic solution of the BEM integrals

Here the integrals $I^1_{i,j}$, $I^2_{i,j}$, $I^3_{i,j}$, $I^4_{i,j}$ in section 3.3.1 are solved analytically. To solve the integrals
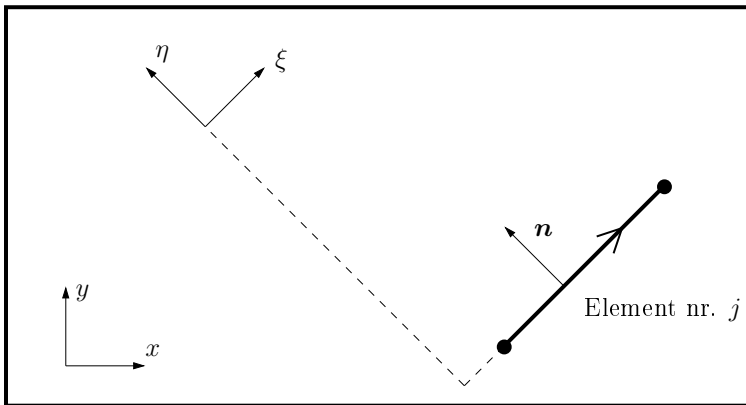
Figure B.1: The local coordinate system used to derive the integrals.

it is convenient to introduce a rotated and translated coordinate system. This coordinate system (ξ, η) is chosen so that the ξ-axis is parallel to the element. and the η-axis is in the direction of the normal vector. The normal vector is defined to be on the left side, when one walk in the counter clockwise direction. This coordinate system is shown in figure B.1. The rotation of the coordinates in the global (x, y) system to the local system is performed using the following transformation which can be derived by geometric considerations, that is,

$$\begin{Bmatrix} \xi \\ \eta \end{Bmatrix} = \begin{bmatrix} \cos\theta & \sin\theta \\ -\sin\theta & \cos\theta \end{bmatrix} \begin{Bmatrix} x \\ y \end{Bmatrix}. \tag{B.1}$$

After that a translation of the coordinates is performed. Now the integration is handled. $I_{i,j}^2$ is given by

$$
\begin{aligned}
I^2 &= \int \frac{d\log r}{dn} d\xi = \int \frac{d\log r}{d\eta} d\xi \\
&= \int \frac{d\log r}{dr} \frac{dr}{d\eta} d\xi = \eta \int \frac{1}{\xi^2 + \eta^2} d\xi \\
&= \arctan \frac{\xi}{\eta} + C.
\end{aligned}
$$

Here we know that

$$
r = \sqrt{\xi^2 + \eta^2}. \tag{B.2}
$$

The I^1 integral is solved as follows,

$$
\begin{aligned}
I^1 &= \int \log r \, d\xi = \int 1 \cdot \log r \, d\xi \\
&= \xi \log r - \int \xi \frac{\partial \log r}{\partial \xi} d\xi \qquad \text{partial integration} \\
&= \xi \log r - \int \frac{\xi^2}{\xi^2 + \eta^2} d\xi \\
&= \xi \log r - \xi + \eta \arctan \frac{\xi}{\eta}.
\end{aligned}
$$

The I^3 integral is solved as follows,

$$
\begin{aligned}
I^3 &= \int \xi \log r \, d\xi \\
&= \xi \int \log r \, d\xi - \int \int \log r \, d\xi d\xi \qquad \text{partial integration} \\
&= \xi \left[\xi \log r - \xi + \eta \arctan \frac{\xi}{\eta} \right] - \int \left[\xi \log r - \xi + \eta \arctan \frac{\xi}{\eta} \right] d\xi \\
&= \frac{r^2}{4} \log r^2 - \frac{\xi^2}{4}.
\end{aligned}
$$

The I^4 integral is solved as follows,

$$
I^4 = \int \xi \frac{\partial \log r}{\partial \eta} d\xi = \eta \int \frac{\xi}{\xi^2 + \eta^2} = \frac{\eta}{2} \log r^2.
$$

When the the limits are taken, the integrals can be written as,

$$
I_{i,j}^2 = \arctan \frac{\xi_2}{\eta} - \arctan \frac{\xi_1}{\eta} \tag{B.3}
$$

$$
I_{i,j}^1 = \frac{1}{2} [\xi_2 \log r_2^2 - \xi_1 \log r_1^2] - (\xi_2 - \xi_1) + \eta I_{i,j}^2 \tag{B.4}
$$

$$I_{i,j}^3 = \frac{1}{4}[r_2^2 \log r_2^2 - r_1^2 \log r_1^2 - \xi_2^2 + \xi_1^2] \tag{B.5}$$

$$I_{i,j}^4 = \frac{\eta}{2}\left[\log r_2^2 - \log r_1^2\right]. \tag{B.6}$$

Appendix C

Derivation of an analytical two-phase standing wave

Here the analytical solution for a linear two-phase standing wave inside a rectangular tank is derived in the case where the liquid is assumed two-dimensional, assuming that potential flow theory is valid and where the gas is assumed quasi-one-dimensional, inviscid and incompressible. In the following the velocity potential in the liquid is denoted ϕ and the velocity potential in the air is denoted ϕ_g. The analytical solution of a standing wave is based on knowing the natural modes and frequencies. The linearised mathematical problem reads:

$$\frac{\partial^2 \phi}{\partial x^2} + \frac{\partial^2 \phi}{\partial y^2} = 0 \qquad \text{in the liquid,} \qquad (C.1)$$

$$\frac{\partial^2 (\rho\phi - \rho_g\phi_g)}{\partial t^2} = -\rho g \phi_y \qquad \text{on the free surface,} \qquad (C.2)$$

$$\frac{d\phi}{dn} = 0 \qquad \text{on the walls,} \qquad (C.3)$$

$$h_0 \frac{\partial^2 \phi_g}{\partial x^2} = \phi_y \qquad \text{in the gas,} \qquad (C.4)$$

$$\frac{\partial \phi_g}{\partial x} = 0 \qquad \text{on } x = \pm\frac{L}{2}. \qquad (C.5)$$

The second equation results from the dynamic free surface condition, requiring that the pressure is equal on the two sides of the free surface. The fourth equation is the linearised mass conservation equation in the air. The boundary conditions for the gas at $x = \pm L/2$ is the wall condition at both sides. Note that using this boundary condition and not the boundary condition $\bar{p} = p_0$ at the right hand side does not change the velocities or the wave elevation inside the tank, however the velocity potentials will be different. In the following it is assumed harmonic time dependence with frequency ω, then $\phi = i\omega e^{i\omega t}\varphi(x, y)$

and $\phi_g = i\omega e^{i\omega t}\varphi_g(x, y)$. This results in a problem for φ, φ_g which is given as:

$$\frac{\partial^2 \varphi}{\partial x^2} + \frac{\partial^2 \varphi}{\partial y^2} = 0 \qquad \text{in the liquid,} \qquad (C.6)$$

$$(\rho_g \varphi_g - \rho \varphi)\omega^2 = -\rho g \varphi_y \qquad \text{on the free surface,} \qquad (C.7)$$

$$\frac{d\varphi}{dn} = 0 \qquad \text{on the walls,} \qquad (C.8)$$

$$h_0 \frac{\partial^2 \varphi_g}{\partial x^2} = \varphi_y \qquad \text{in the gas,} \qquad (C.9)$$

$$\frac{\partial \varphi_g}{\partial x} = 0 \qquad \text{on } x = \pm \frac{L}{2}. \qquad (C.10)$$

Then the solution is assumed to be:

$$\varphi = C_m \cos\left(\pi m(x + L/2)/L\right) \frac{\cosh\left(\pi m(y + H)1/L\right)}{\cosh\left(\pi m H/L\right)} \qquad (C.11)$$

$$\varphi_g = \cos\left(\pi m(x + L/2)/L\right). \qquad (C.12)$$

These solutions satisfies the differential equations inside the liquid and the gas, and the boundary conditions on the free surface, and at $x = \pm L/2$ for the gas. Then condition C.9 gives

$$C_m = -\frac{\pi m h_0}{L \tanh\left(\frac{\pi m H}{L}\right)}. \qquad (C.13)$$

Equation C.7 gives the natural frequencies as:

$$\omega_m^2 = \frac{\rho g h_0}{(\rho_g - \rho C_m)} \left(\frac{\pi m}{L}\right)^2. \qquad (C.14)$$

An analytical solution can be found for a standing wave with free surface profile given as $\zeta(t, x) = -\zeta_a \sin(\omega_1 t)\cos\left(\pi(x + L/2)/L\right)$. Since only the elevation is compared and not the value of the velocity potentials, the normal modes in equation C.11 and C.12 can be used. We assume $\phi = R(t)\varphi$ and $\phi_g = R_g(t)\varphi_g$. Then equation C.9 results in $R_g(t) = R(t)$ and equation C.7 results in:

$$R(t) = \frac{\zeta_a \omega_1}{h_0} \left(\frac{L}{\pi}\right)^2 \cos(\omega_1 t). \qquad (C.15)$$

Appendix D

Incompressible solution for the escaping air

Here the incompressible, quasi-one-dimensional gas flow over a rigid free surface is solved analytically. This means that the effect of the air flow on the water is neglected. The rigid free surface motion is given as $h(x,t) = h_0(x) - V_0 t$. Here $h_0(x) = h(x, t = 0)$. Further V_0 is constant and not a function of space or time. From the 1D mass conservation equation (3.14), the horizontal velocity can be found as:

$$u_g(x,t) = -\frac{1}{h(x,t)} \int_0^x \frac{\partial h}{\partial t} dx = \frac{V_0 x}{h}. \tag{D.1}$$

Using the fact that $\partial h / \partial t = -V_0$. Anderson [19] showed that the quasi-one-dimensional momentum equation neglecting viscosity is identical to the one-dimensional Euler's equation. Then the dynamic pressure can be found as:

$$p(x,t) = \rho_g \int_x^L \frac{\partial u_g(x',t)}{\partial t} + u_g(x',t)\frac{\partial u_g(x',t)}{\partial x'} \partial x'. \tag{D.2}$$

The derivatives of u_g are given as:

$$\frac{\partial u_g}{\partial t} = \frac{V_0^2 x}{h^2}$$

$$\frac{\partial u_g}{\partial x} = \frac{V_0}{h} - \frac{V_0 x}{h^2}\frac{\partial h}{\partial x}.$$

The following integrals are then solved:

$$I_1 = \rho_g \int_x^L \frac{\partial u_g(x',t)}{\partial t} = \rho_g V_0^2 \int_x^L \frac{x'}{h^2} dx' \tag{D.3}$$

and

$$I_2 = \frac{\rho_g}{2} \int_x^L \frac{\partial u_g^2}{\partial x} dx' = \frac{\rho_g U_0^2}{2}\left[\left(\frac{L}{h_L}\right)^2 - \left(\frac{x}{h}\right)^2\right], \tag{D.4}$$

157

by realizing that $u_g u_{gx} = .5 \partial (u_g^2)/\partial x$. The pressure can then be written as:

$$p(x,t) = I_1 + \frac{\rho_g V_0^2}{2} \left(\frac{L^2}{h_L^2} - \frac{x^2}{h^2} \right). \tag{D.5}$$

Appendix E

Background of the compressible gas solver

The problem of a compressible, quasi-one-dimensional gas escaping a rigid surface approaching the upper corner of a sloshing tank was investigated using the CLAWPACK software described in the book by Leveque [30]. The equations solved for is the compressible and quasi-one-dimensional equations as written by Toro[37]:

$$\frac{\partial \rho_g}{\partial t} + \frac{\partial (\rho_g u_g)}{\partial x} = -\frac{1}{h}\left(\frac{\partial h}{\partial t} + u_g \frac{\partial h}{\partial x}\right)\rho_g \tag{E.1}$$

$$\frac{\partial \rho_g u_g}{\partial t} + \frac{\partial (\rho_g u_g^2 + p)}{\partial x} = -\frac{1}{h}\left(\frac{\partial h}{\partial t} + u_g \frac{\partial h}{\partial x}\right)\rho_g u_g \tag{E.2}$$

$$\frac{\partial E}{\partial t} + \frac{\partial u_g(E+p)}{\partial x} = -\frac{1}{h}\left(\frac{\partial h}{\partial t} + u_g \frac{\partial h}{\partial x}\right)(E+p) \tag{E.3}$$

Here $E = \rho_g(\frac{1}{2}u_g^2 + e)$, where e is the specific internal energy. This equation system is written in a non-accelerated coordinate system and is on the form:

$$\frac{\partial \boldsymbol{U}}{\partial t} + \frac{\partial \boldsymbol{F}(\boldsymbol{U})}{\partial x} = \boldsymbol{S}(\boldsymbol{U}) \tag{E.4}$$

CLAWPACK uses a fractional-step method (Leveque [30]) to solve these equations. This method first finds a solution of the homogeneous equation system, that means $\boldsymbol{S} = 0$ in equation (E.4). The problem solved for is then:

$$\frac{\partial \boldsymbol{U}}{\partial t} + \frac{\partial \boldsymbol{F}(\boldsymbol{U})}{\partial x} = 0 \tag{E.5}$$

The solution of this equation system is used as input in the next sub-step, the source step, which neglects the spatial variation, that is $\boldsymbol{F}_x = 0$:

$$\frac{\partial \boldsymbol{U}}{\partial t} = \boldsymbol{S}(\boldsymbol{U}) \tag{E.6}$$

This is a set of ordinary differential equations. The splitting is approximate, but yields the important benefit that specialized solution methods can be applied for the two steps. Since $h(x,t)$ does not appear on the left hand side of the equations (E.1) - (E.3), it means that a specialized solver can be applied to the homogeneous problem. The details of this solver can be found in Leveque [30]. To solve the source step a second order Runge-Kutta method is applied. The specific splitting method used is called Strang splitting. Further details about this method can be found in Leveque [30].
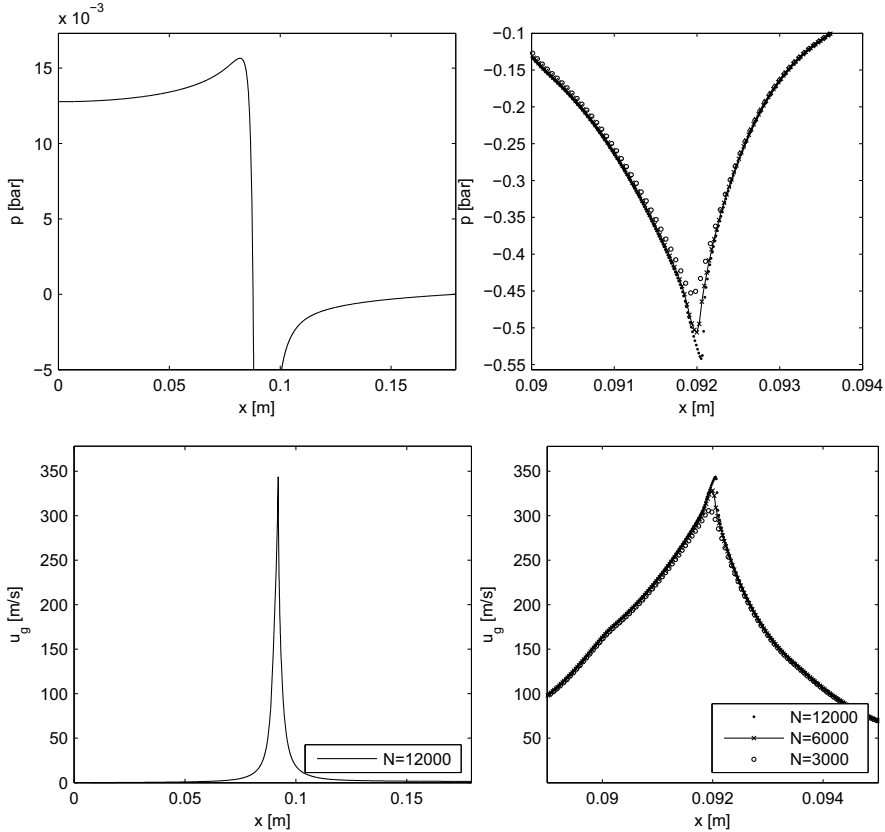
Figure E.1: Convergence study of the escaping air over an approaching rigid surface. The Mach number $M = 1.0$ and the minimum height $h_{\min} = 0.108[mm]$. The Mach number is here defined as $M = u_g^{\max}/c_0$. The topmost plots show the pressure while the lowermost plots show the horizontal gas velocity. The left hand side plot is a close up view of the singularity. Some grid dependence is seen on peak values.

A convergence study of the case specified in section 3.6 follows. The solution for the compressible flow model shows singular-type behaviour at the narrowest point when the gap between the free surface and the roof approaches zero. The air velocity as a function of

the x-coordinate then forms a spike with increasing amplitude. Hence a convergence study was carried out in order to see the cell size dependence at different stages of the simulation. Three different uniform grids using $N = [3000, 6000, 12000]$ cells along the length of the domain are used in the investigation. The Courant-Friedrich-Lewy (CFL) number in the simulation was set to $C_{\mathrm{CFL}} = 0.9$. The CFL stability criteria then limits the time step size to $\Delta t = C_{\mathrm{CFL}} \Delta x / u_g^{\max}$. The resulting pressure and velocity is seen in figure E.1 for Mach number equal to 1.0. The Mach number is here defined as $M = u_g^{\max} / c_0$. The results are seen to be grid dependent at the the narrowest point, however 12000 grid cells where found to be satisfactory for M=1.0. If the simulation should be continued further than $M = 1.0$ then more grid cells are required.

Appendix F

Complete 1D linear heat analysis

In the one-dimensional, linear, steady-state thermodynamic analysis in section 5.2 the pressure was assumed to be uniform inside the air pocket. Here this assumption is investigated by performing a complete linear analysis where the pressure is not restricted to be uniform inside the air pocket. Assuming steady state, equation 5.7 can be written as:

$$\rho_{g0} c_p i \omega_0 \theta = i \omega_0 p + K_1 \frac{\partial^2 \theta}{\partial y^2}. \tag{F.1}$$

Linearising the ideal gas law yields:

$$\rho_1 = \frac{p}{R T_0} - \frac{\rho_{g0}}{T_0} \theta. \tag{F.2}$$

Here $\rho_1 = \rho_g - \rho_{g0}$. The linear equation expressing conservation of mass is:

$$i \omega_0 \rho_1 + \rho_{g0} \frac{\partial v}{\partial y} = 0 \tag{F.3}$$

Now the velocity potential is introduced, that is $p = -\rho_{g0} \partial \phi / \partial t$, and $v = \partial \phi / \partial y$, into (F.3) and (F.2). These two equations combined then yield:

$$\frac{\omega_0^2}{R T_0} \phi + \frac{\partial^2 \phi}{\partial y^2} - \frac{i \omega_0}{T_0} \theta = 0 \tag{F.4}$$

Introducing the velocity potential into (F.1), yields:

$$\rho_{g0} c_p i \omega_0 \theta = \rho_{g0} \omega_0^2 \phi + K_1 \frac{\partial^2 \theta}{\partial y^2} \tag{F.5}$$

The boundary conditions are given as:

$$
\begin{aligned}
\frac{\partial \phi}{\partial y} &= 0 & \text{on} && y &= 0 \\
-\rho_{g0} i \omega_0 \phi &= p_{liq} & \text{on} && y &= -h_0 \\
\theta &= 0 & \text{on} && y &= -h_0 \\
\theta &= 0 & \text{on} && y &= 0
\end{aligned}
\tag{F.6}
$$

Next, non-dimensional variables $\theta = T_0\hat{\theta}$, $y = h_0\hat{y}$, $\phi = \omega_0 h_0^2\hat{\phi}$ and $p = \rho_{g0}\omega_0^2 h_0^2\hat{p}$ are introduced. Using the known relations from section 5.2, that is $D_1 = K_1/(\rho_{g0}c_p)$, and $\delta_T = \sqrt{D_1/(2\omega_0)}$ equation (F.4) and (F.5) can be written as:

$$\frac{\rho_{g0}\omega_0^2 h_0^2}{p_0}\hat{\phi} + \frac{\partial^2\hat{\phi}}{\partial\hat{y}^2} - i\hat{\theta} = 0 \tag{F.7}$$

$$i\hat{\theta} = \left(\frac{\gamma-1}{\gamma}\right)\left(\frac{\rho_{g0}\omega_0^2 h_0^2}{p_0}\right)\hat{\phi} + 2\left(\frac{\delta_T}{h_0}\right)^2\frac{\partial^2\hat{\theta}}{\partial\hat{y}^2} \tag{F.8}$$

Boundary conditions in non-dimensional form are given as:

$$\frac{\partial\hat{\phi}}{\partial\hat{y}} = 0 \qquad \text{on} \qquad \hat{y} = 0$$

$$-i\hat{\phi} = \hat{p}_{liq} \qquad \text{on} \qquad \hat{y} = -1$$

$$\hat{\theta} = 0 \qquad \text{on} \qquad \hat{y} = -1 \tag{F.9}$$

$$\hat{\theta} = 0 \qquad \text{on} \qquad \hat{y} = 0.$$

Assuming that the solutions have the forms $\hat{\phi} = Ae^{\alpha\hat{y}}$ and $\hat{\theta} = Be^{\alpha\hat{y}}$ the following equation system is obtained:

$$(C + \alpha^2)A - iB = 0 \tag{F.10}$$

$$\beta CA + \left(\frac{2\alpha^2}{E^2} - i\right)B = 0. \tag{F.11}$$

Here the following non-dimensional parameters are introduced:

$$C = \frac{\rho_{g0}\omega_0^2 h_0^2}{p_0} \tag{F.12}$$

$$E = \frac{h_0}{\delta_T} \tag{F.13}$$

$$\beta = \frac{(\gamma-1)}{\gamma}. \tag{F.14}$$

For solutions to exist the determinant of the coefficient matrix has to be zero. This leads to the following equation:

$$\frac{2\alpha^4}{E^2} + \left(\frac{2C}{E^2} - i\right)\alpha^2 + (\beta-1)iC = 0. \tag{F.15}$$

This has potentially four solutions $\alpha_i (i = 1...4)$. The solution can then be written as:

$$\hat{\phi} = \sum_{j=1}^{4} A_j e^{\alpha_j\hat{y}} \tag{F.16}$$

$$\hat{\theta} = \sum_{j=1}^{4} B_j e^{\alpha_j\hat{y}}. \tag{F.17}$$

A_j and B_j are related through (F.10) as

$$B_j = -i(C + \alpha_j^2)A_j. \tag{F.18}$$

The boundary conditions can be used to establish a four by four equation system for A_j. This is:

$$\sum_{j=1}^{4} A_j \alpha_j = 0 \tag{F.19}$$

$$\sum_{j=1}^{4} A_j e^{-\alpha_j} = i\hat{p}_{liq} \tag{F.20}$$

$$\sum_{j=1}^{4} (C + \alpha_j^2)e^{-\alpha_j} A_j = 0 \tag{F.21}$$

$$\sum_{j=1}^{4} (C + \alpha_j^2) A_j = 0. \tag{F.22}$$

Now a relation between the non-dimensional pressure $\hat{p}(\hat{z} = -1)$ and the displacement of the boundary ϵ needs to be established. ϵ is specified to be positive when the volume of the piston is increasing (see figure 5.4). The non-dimensional displacement of the piston is $\hat{\epsilon}$ is defined as $\hat{\epsilon} = h_0 \epsilon$. The boundary condition at $y = -h_0$ is then $\epsilon_t = -\phi_y$ and $p_{liq} = -\rho_{g0}\phi_t$. The non-dimensional ratio between pressure and displacement is then:

$$G = \frac{\hat{p}}{\hat{\epsilon}} = -\frac{\hat{\phi}}{\hat{\phi}_{\hat{y}}} = -\frac{\sum_{j=1}^{4} A_j e^{-\alpha_j}}{\sum_{j=1}^{4} A_j \alpha_j e^{-\alpha_j}}. \tag{F.23}$$

Then the polytropic exponent κ follows from (5.27) as:

$$\kappa = -\frac{h_0^2 \rho_{g0} \omega_0^2}{p_0} \Re(G). \tag{F.24}$$

The resulting polytropic index $\kappa(h_0/\delta_T)$ is plotted in figure F.1 and is seen to fit the previous calculated polytropic index from the model in section 5.2 assuming uniform pressure. But how does the pressure vary inside the air pocket? To investigate this the ratio of the absolute value of the relative pressure divided by the pressure on the liquid surface $|p|/p_{liq}$, given as

$$\frac{p}{p_{liq}} = \frac{-\rho_{g0}i\omega_0\phi}{p_{liq}} = \frac{-i}{\hat{p}_{liq}} \sum_{i=1}^{4} A_j e^{\alpha_j \hat{y}}, \tag{F.25}$$

is plotted. This means that E needs to be specified which for air pocket 6 is $E = 51.01$. The ratio of specific heats for air is $\gamma = 1.4$. The resulting spatial pressure variation is
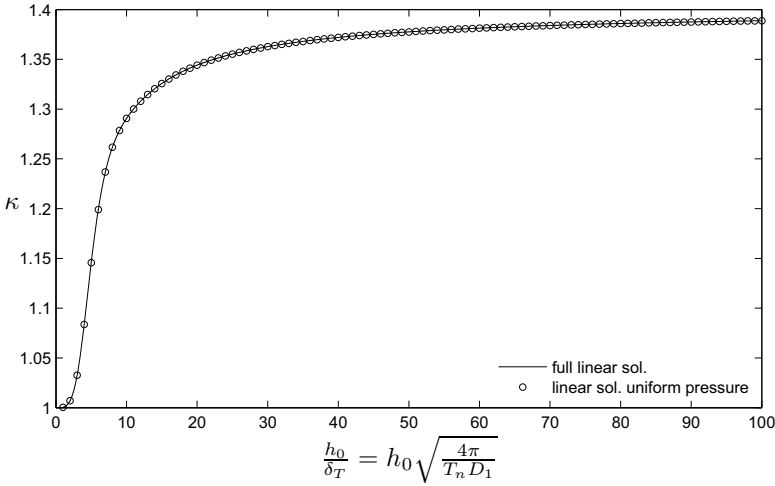
Figure F.1: The polytropic index based for the spatially varying pressure for the value for C from AP 6 compared with the results from the uniform pressure model.

seen in figure F.2. The pressure variation is seen to be very small. In the following the non-dimensional parameter C is rewritten in different ways to see its physical origin:

$$c_0^2 = \frac{\partial p}{\partial \rho}_{ad.} = \gamma R T_0. \tag{F.26}$$

Acoustic resonance of the one-dimensional gas chamber will occur at different frequencies the lowest frequency is connected to a standing first mode inside the chamber which occurs at the frequency ω_{ac}. This is given by Faltinsen and Timokha [8] as:

$$\omega_{\mathrm{ac}} = \frac{\pi c_0}{h_0}. \tag{F.27}$$

Using these formulas C can be given in the following alternative forms:

$$C = \frac{\gamma \omega_0^2 h_0^2}{c_0^2} = \pi^2 \gamma \left(\frac{\omega_0}{\omega_{\mathrm{ac}}} \right)^2 = \gamma M^2 \tag{F.28}$$

C is seen to be a small parameter in the air pockets studied in chapter 2. For air pocket 6 its value is $C = 0.148e - 3$. The last equality of equation F.28 relates the value of C to the Mach number expressed in terms of air pocket thickness and oscillation frequency, that is $M = h_o \omega_0 / c_0$. If this Mach number is high it means that acoustic effects are of importance. The fact that M and hence C is small for the air pockets studied herein is used as a basis in the next asymptotic analysis.

In the following an asymptotic analysis of the linear problem is performed. In section 5.2 the pressure was assumed uniform inside the air pocket, this was not proved to be a valid

assumption. The question is under what conditions this is true. In the following C is assumed to be a small parameter. From equation F.8 it is for the two limiting cases of isothermal and adiabatic conditions, true that the term related to heat (the right most term) is negligible. Therefore it is assumed that the first and the second term are of the same size, which yields that $\mathcal{O}(\hat{\theta}) = \mathcal{O}(C\hat{\phi})$. $\hat{\phi}$ and $\hat{\theta}$ are then written as $\hat{\phi} = \hat{\phi}_1 + \hat{\phi}_2 + ...$ and $\hat{\theta} = \hat{\theta}_1 + \hat{\theta}_2 + ...$ Here $\mathcal{O}(\hat{\phi}_1) = 1$, $\mathcal{O}(\hat{\phi}_2) = C$ $\mathcal{O}(\hat{\theta}_1) = C$ $\mathcal{O}(\hat{\theta}_2) = C^2$. We then keep leading order terms in the mathematical problem posed by the equations (F.7), (F.8) and (F.9). This leads to $\hat{\phi}_1 = i\hat{p}_{\text{liq}}$, which in fact is equivalent to assuming that the pressure is uniform. This leads to a temperature solution $\hat{\theta}_1$ which is identical to the solution already calculated in section 5.2. Then keeping terms to second order in the mathematical problem equation (F.7) yields:

$$\frac{\partial \hat{\phi}_2}{\partial \hat{y}^2} = -C\hat{\phi}_1 + i\hat{\theta}_1 \tag{F.29}$$

Using equation (F.8) leads to the following equation:

$$\frac{\partial \hat{\phi}_2}{\partial \hat{y}^2} - 2\left(\frac{\delta_T}{h_0}\right)^2 \frac{\partial^2 \hat{\theta}_1}{\partial \hat{y}^2} = -\frac{C}{\gamma}\hat{\phi}_1 \tag{F.30}$$

Integration of this equation leads to:

$$\hat{\phi}_2 = 2\left(\frac{\delta_T}{h_0}\right)^2 \hat{\theta}_1 - \frac{C}{2\gamma}i\hat{p}_{\text{liq}}\hat{y}^2 + A_1\hat{y} + A_2. \tag{F.31}$$

The solution of $\hat{\theta}_1$ is given as:

$$\hat{\theta}_1 = -iB_2\left[1 + C_1 e^{\alpha \hat{y}} + C_2 e^{-\alpha \hat{y}}\right] \tag{F.32}$$

Where $\alpha = (1+i)\sqrt{1/(2B_1)}$. The constants are:

$$B_1 \quad = 2\left(\frac{\delta_T}{h_0}\right)^2 \tag{F.33}$$

$$B_2 \quad = -\frac{\gamma-1}{\gamma}C\hat{\phi}_1 \tag{F.34}$$

$$C_2 \quad = \frac{1-e^{-\alpha}}{e^{-\alpha}-e^{\alpha}} \tag{F.35}$$

$$C_1 \quad = -C_2 - 1. \tag{F.36}$$

The constants A_1 and A_2 are determined by satisfying the boundary conditions. The boundary condition at the tank roof $\hat{y} = 0$, leads to:

$$A_1 = 2\left(\frac{\delta_T}{h_0}\right)^2 iB_2\alpha(C_1 - C_2) \tag{F.37}$$

The boundary condition at $\hat{y} = -1$ leads to:

$$A_2 = \frac{C}{2\gamma}i\hat{p}_{\text{liq}} + A_1. \tag{F.38}$$

The constants in equation (F.31) are now determined. A comparison of the pressure from the complete linear solution and the asymptotic solution is seen in figure F.2. Here the ratio between the amplitude of the pressure inside the air pocket divided by the amplitude of the pressure at the boundary is plotted. Based on the present findings it is concluded that
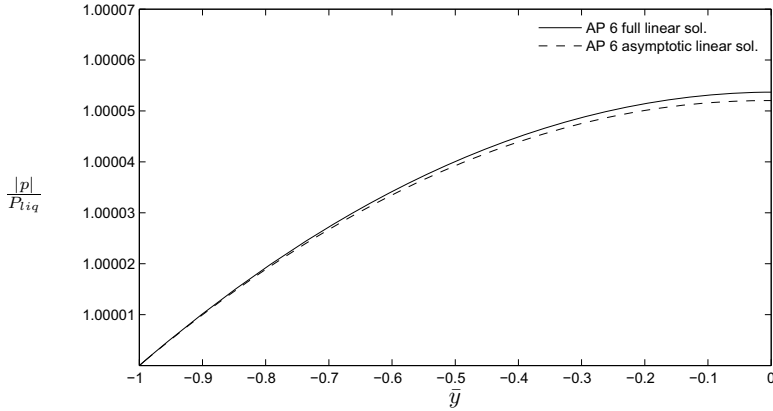
Figure F.2: The spatial variation of the pressure inside the air pocket for AP 6.

assuming constant pressure is the first order asymptotic solution of the linear problem in the small parameter C which is proportional to the Mach number squared, expressed through the oscillation frequency ω_0 and the characteristic thickness of the air pocket h_0.

R A P P O R T E R
UTGITT VED
INSTITUTT FOR MARIN TEKNIKK
(tidligere: FAKULTET FOR MARIN TEKNIKK)
NORGES TEKNISK-NATURVITENSKAPELIGE UNIVERSITET

Report No.	Author	Title
	Kavlie, Dag	Optimization of Plane Elastic Grillages, 1967
	Hansen, Hans R.	Man-Machine Communication and Data-Storage Methods in Ship Structural Design, 1971
	Gisvold, Kaare M.	A Method for non-linear mixed -integer programming and its Application to Design Problems, 1971
	Lund, Sverre	Tanker Frame Optimalization by means of SUMT-Transformation and Behaviour Models, 1971
	Vinje, Tor	On Vibration of Spherical Shells Interacting with Fluid, 1972
	Lorentz, Jan D.	Tank Arrangement for Crude Oil Carriers in Accordance with the new Anti-Pollution Regulations, 1975
	Carlsen, Carl A.	Computer-Aided Design of Tanker Structures, 1975
	Larsen, Carl M.	Static and Dynamic Analysis of Offshore Pipelines during Installation, 1976
UR-79-01	Brigt Hatlestad, MK	The finite element method used in a fatigue evaluation of fixed offshore platforms. (Dr.Ing. Thesis)
UR-79-02	Erik Pettersen, MK	Analysis and design of cellular structures. (Dr.Ing. Thesis)
UR-79-03	Sverre Valsgård, MK	Finite difference and finite element methods applied to nonlinear analysis of plated structures. (Dr.Ing. Thesis)
UR-79-04	Nils T. Nordsve, MK	Finite element collapse analysis of structural members considering imperfections and stresses due to fabrication. (Dr.Ing. Thesis)
UR-79-05	Ivar J. Fylling, MK	Analysis of towline forces in ocean towing systems. (Dr.Ing. Thesis)
UR-80-06	Nils Sandsmark, MM	Analysis of Stationary and Transient Heat Conduction by the Use of the Finite Element Method. (Dr.Ing. Thesis)
UR-80-09	Sverre Haver, MK	Analysis of uncertainties related to the stochastic modeling of ocean waves. (Dr.Ing. Thesis)
UR-81-15	Odland, Jonas	On the Strength of welded Ring stiffened cylindrical Shells primarily subjected to axial Compression

UR-82-17	Engesvik, Knut	Analysis of Uncertainties in the fatigue Capacity of Welded Joints
UR-82-18	Rye, Henrik	Ocean wave groups
UR-83-30	Eide, Oddvar Inge	On Cumulative Fatigue Damage in Steel Welded Joints
UR-83-33	Mo, Olav	Stochastic Time Domain Analysis of Slender Offshore Structures
UR-83-34	Amdahl, Jørgen	Energy absorption in Ship-platform impacts
UR-84-37	Mørch, Morten	Motions and mooring forces of semi submersibles as determined by full-scale measurements and theoretical analysis
UR-84-38	Soares, C. Guedes	Probabilistic models for load effects in ship structures
UR-84-39	Aarsnes, Jan V.	Current forces on ships
UR-84-40	Czujko, Jerzy	Collapse Analysis of Plates subjected to Biaxial Compression and Lateral Load
UR-85-46	Alf G. Engseth, MK	Finite element collapse analysis of tubular steel offshore structures. (Dr.Ing. Thesis)
UR-86-47	Dengody Sheshappa, MP	A Computer Design Model for Optimizing Fishing Vessel Designs Based on Techno-Economic Analysis. (Dr.Ing. Thesis)
UR-86-48	Vidar Aanesland, MH	A Theoretical and Numerical Study of Ship Wave Resistance. (Dr.Ing. Thesis)
UR-86-49	Heinz-Joachim Wessel, MK	Fracture Mechanics Analysis of Crack Growth in Plate Girders. (Dr.Ing. Thesis)
UR-86-50	Jon Taby, MK	Ultimate and Post-ultimate Strength of Dented Tubular Members. (Dr.Ing. Thesis)
UR-86-51	Walter Lian, MH	A Numerical Study of Two-Dimensional Separated Flow Past Bluff Bodies at Moderate KC-Numbers. (Dr.Ing. Thesis)
UR-86-52	Bjørn Sortland, MH	Force Measurements in Oscillating Flow on Ship Sections and Circular Cylinders in a U-Tube Water Tank. (Dr.Ing. Thesis)
UR-86-53	Kurt Strand, MM	A System Dynamic Approach to One-dimensional Fluid Flow. (Dr.Ing. Thesis)
UR-86-54	Arne Edvin Løken, MH	Three Dimensional Second Order Hydrodynamic Effects on Ocean Structures in Waves. (Dr.Ing. Thesis)
UR-86-55	Sigurd Falch, MH	A Numerical Study of Slamming of Two-Dimensional Bodies. (Dr.Ing. Thesis)
UR-87-56	Arne Braathen, MH	Application of a Vortex Tracking Method to the Prediction of Roll Damping of a Two-Dimension

Floating Body. (Dr.Ing. Thesis)

UR-87-57	Bernt Leira, MK	Gaussian Vector Processes for Reliability Analysis involving Wave-Induced Load Effects. (Dr.Ing. Thesis)
UR-87-58	Magnus Småvik, MM	Thermal Load and Process Characteristics in a Two-Stroke Diesel Engine with Thermal Barriers (in Norwegian). (Dr.Ing. Thesis)
MTA-88-59	Bernt Arild Bremdal, MP	An Investigation of Marine Installation Processes – A Knowledge - Based Planning Approach. (Dr.Ing. Thesis)
MTA-88-60	Xu Jun, MK	Non-linear Dynamic Analysis of Space-framed Offshore Structures. (Dr.Ing. Thesis)
MTA-89-61	Gang Miao, MH	Hydrodynamic Forces and Dynamic Responses of Circular Cylinders in Wave Zones. (Dr.Ing. Thesis)
MTA-89-62	Martin Greenhow, MH	Linear and Non-Linear Studies of Waves and Floating Bodies. Part I and Part II. (Dr.Techn. Thesis)
MTA-89-63	Chang Li, MH	Force Coefficients of Spheres and Cubes in Oscillatory Flow with and without Current. (Dr.Ing. Thesis
MTA-89-64	Hu Ying, MP	A Study of Marketing and Design in Development of Marine Transport Systems. (Dr.Ing. Thesis)
MTA-89-65	Arild Jæger, MH	Seakeeping, Dynamic Stability and Performance of a Wedge Shaped Planing Hull. (Dr.Ing. Thesis)
MTA-89-66	Chan Siu Hung, MM	The dynamic characteristics of tilting-pad bearings
MTA-89-67	Kim Wikstrøm, MP	Analysis av projekteringen for ett offshore projekt. (Licenciat-avhandling)
MTA-89-68	Jiao Guoyang, MK	Reliability Analysis of Crack Growth under Random Loading, considering Model Updating. (Dr.Ing. Thesis)
MTA-89-69	Arnt Olufsen, MK	Uncertainty and Reliability Analysis of Fixed Offshore Structures. (Dr.Ing. Thesis)
MTA-89-70	Wu Yu-Lin, MR	System Reliability Analyses of Offshore Structures using improved Truss and Beam Models. (Dr.Ing. Thesis)
MTA-90-71	Jan Roger Hoff, MH	Three-dimensional Green function of a vessel with forward speed in waves. (Dr.Ing. Thesis)
MTA-90-72	Rong Zhao, MH	Slow-Drift Motions of a Moored Two-Dimensional Body in Irregular Waves. (Dr.Ing. Thesis)
MTA-90-73	Atle Minsaas, MP	Economical Risk Analysis. (Dr.Ing. Thesis)
MTA-90-74	Knut-Aril Farnes, MK	Long-term Statistics of Response in Non-linear Marine Structures. (Dr.Ing. Thesis)
MTA-90-	Torbjørn Sotberg, MK	Application of Reliability Methods for Safety

75		Assessment of Submarine Pipelines. (Dr.Ing. Thesis)
MTA-90-76	Zeuthen, Steffen, MP	SEAMAID. A computational model of the design process in a constraint-based logic programming environment. An example from the offshore domain. (Dr.Ing. Thesis)
MTA-91-77	Haagensen, Sven, MM	Fuel Dependant Cyclic Variability in a Spark Ignition Engine - An Optical Approach. (Dr.Ing. Thesis)
MTA-91-78	Løland, Geir, MH	Current forces on and flow through fish farms. (Dr.Ing. Thesis)
MTA-91-79	Hoen, Christopher, MK	System Identification of Structures Excited by Stochastic Load Processes. (Dr.Ing. Thesis)
MTA-91-80	Haugen, Stein, MK	Probabilistic Evaluation of Frequency of Collision between Ships and Offshore Platforms. (Dr.Ing. Thesis)
MTA-91-81	Sødahl, Nils, MK	Methods for Design and Analysis of Flexible Risers. (Dr.Ing. Thesis)
MTA-91-82	Ormberg, Harald, MK	Non-linear Response Analysis of Floating Fish Farm Systems. (Dr.Ing. Thesis)
MTA-91-83	Marley, Mark J., MK	Time Variant Reliability under Fatigue Degradation. (Dr.Ing. Thesis)
MTA-91-84	Krokstad, Jørgen R., MH	Second-order Loads in Multidirectional Seas. (Dr.Ing. Thesis)
MTA-91-85	Molteberg, Gunnar A., MM	The Application of System Identification Techniques to Performance Monitoring of Four Stroke Turbocharged Diesel Engines. (Dr.Ing. Thesis)
MTA-92-86	Mørch, Hans Jørgen Bjelke, MH	Aspects of Hydrofoil Design: with Emphasis on Hydrofoil Interaction in Calm Water. (Dr.Ing. Thesis)
MTA-92-87	Chan Siu Hung, MM	Nonlinear Analysis of Rotordynamic Instabilities in Highspeed Turbomachinery. (Dr.Ing. Thesis)
MTA-92-88	Bessason, Bjarni, MK	Assessment of Earthquake Loading and Response of Seismically Isolated Bridges. (Dr.Ing. Thesis)
MTA-92-89	Langli, Geir, MP	Improving Operational Safety through exploitation of Design Knowledge - an investigation of offshore platform safety. (Dr.Ing. Thesis)
MTA-92-90	Sævik, Svein, MK	On Stresses and Fatigue in Flexible Pipes. (Dr.Ing. Thesis)
MTA-92-91	Ask, Tor Ø., MM	Ignition and Flame Growth in Lean Gas-Air Mixtures. An Experimental Study with a Schlieren System. (Dr.Ing. Thesis)
MTA-86-92	Hessen, Gunnar, MK	Fracture Mechanics Analysis of Stiffened Tubular

Members. (Dr.Ing. Thesis)

MTA-93-93	Steinebach, Christian, MM	Knowledge Based Systems for Diagnosis of Rotating Machinery. (Dr.Ing. Thesis)
MTA-93-94	Dalane, Jan Inge, MK	System Reliability in Design and Maintenance of Fixed Offshore Structures. (Dr.Ing. Thesis)
MTA-93-95	Steen, Sverre, MH	Cobblestone Effect on SES. (Dr.Ing. Thesis)
MTA-93-96	Karunakaran, Daniel, MK	Nonlinear Dynamic Response and Reliability Analysis of Drag-dominated Offshore Platforms. (Dr.Ing. Thesis)
MTA-93-97	Hagen, Arnulf, MP	The Framework of a Design Process Language. (Dr.Ing. Thesis)
MTA-93-98	Nordrik, Rune, MM	Investigation of Spark Ignition and Autoignition in Methane and Air Using Computational Fluid Dynamics and Chemical Reaction Kinetics. A Numerical Study of Ignition Processes in Internal Combustion Engines. (Dr.Ing. Thesis)
MTA-94-99	Passano, Elizabeth, MK	Efficient Analysis of Nonlinear Slender Marine Structures. (Dr.Ing. Thesis)
MTA-94-100	Kvålsvold, Jan, MH	Hydroelastic Modelling of Wetdeck Slamming on Multihull Vessels. (Dr.Ing. Thesis)
MTA-94-102	Bech, Sidsel M., MK	Experimental and Numerical Determination of Stiffness and Strength of GRP/PVC Sandwich Structures. (Dr.Ing. Thesis)
MTA-95-103	Paulsen, Hallvard, MM	A Study of Transient Jet and Spray using a Schlieren Method and Digital Image Processing. (Dr.Ing. Thesis)
MTA-95-104	Hovde, Geir Olav, MK	Fatigue and Overload Reliability of Offshore Structural Systems, Considering the Effect of Inspection and Repair. (Dr.Ing. Thesis)
MTA-95-105	Wang, Xiaozhi, MK	Reliability Analysis of Production Ships with Emphasis on Load Combination and Ultimate Strength. (Dr.Ing. Thesis)
MTA-95-106	Ulstein, Tore, MH	Nonlinear Effects of a Flexible Stern Seal Bag on Cobblestone Oscillations of an SES. (Dr.Ing. Thesis)
MTA-95-107	Solaas, Frøydis, MH	Analytical and Numerical Studies of Sloshing in Tanks. (Dr.Ing. Thesis)
MTA-95-108	Hellan, Øyvind, MK	Nonlinear Pushover and Cyclic Analyses in Ultimate Limit State Design and Reassessment of Tubular Steel Offshore Structures. (Dr.Ing. Thesis)
MTA-95-109	Hermundstad, Ole A., MK	Theoretical and Experimental Hydroelastic Analysis of High Speed Vessels. (Dr.Ing. Thesis)
MTA-96-110	Bratland, Anne K., MH	Wave-Current Interaction Effects on Large-Volume Bodies in Water of Finite Depth. (Dr.Ing. Thesis)

MTA-96-111	Herfjord, Kjell, MH	A Study of Two-dimensional Separated Flow by a Combination of the Finite Element Method and Navier-Stokes Equations. (Dr.Ing. Thesis)
MTA-96-112	Æsøy, Vilmar, MM	Hot Surface Assisted Compression Ignition in a Direct Injection Natural Gas Engine. (Dr.Ing. Thesis)
MTA-96-113	Eknes, Monika L., MK	Escalation Scenarios Initiated by Gas Explosions on Offshore Installations. (Dr.Ing. Thesis)
MTA-96-114	Erikstad, Stein O., MP	A Decision Support Model for Preliminary Ship Design. (Dr.Ing. Thesis)
MTA-96-115	Pedersen, Egil, MH	A Nautical Study of Towed Marine Seismic Streamer Cable Configurations. (Dr.Ing. Thesis)
MTA-97-116	Moksnes, Paul O., MM	Modelling Two-Phase Thermo-Fluid Systems Using Bond Graphs. (Dr.Ing. Thesis)
MTA-97-117	Halse, Karl H., MK	On Vortex Shedding and Prediction of Vortex-Induced Vibrations of Circular Cylinders. (Dr.Ing. Thesis)
MTA-97-118	Igland, Ragnar T., MK	Reliability Analysis of Pipelines during Laying, considering Ultimate Strength under Combined Loads. (Dr.Ing. Thesis)
MTA-97-119	Pedersen, Hans-P., MP	Levendefiskteknologi for fiskefartøy. (Dr.Ing. Thesis)
MTA-98-120	Vikestad, Kyrre, MK	Multi-Frequency Response of a Cylinder Subjected to Vortex Shedding and Support Motions. (Dr.Ing. Thesis)
MTA-98-121	Azadi, Mohammad R. E., MK	Analysis of Static and Dynamic Pile-Soil-Jacket Behaviour. (Dr.Ing. Thesis)
MTA-98-122	Ulltang, Terje, MP	A Communication Model for Product Information. (Dr.Ing. Thesis)
MTA-98-123	Torbergsen, Erik, MM	Impeller/Diffuser Interaction Forces in Centrifugal Pumps. (Dr.Ing. Thesis)
MTA-98-124	Hansen, Edmond, MH	A Discrete Element Model to Study Marginal Ice Zone Dynamics and the Behaviour of Vessels Moored in Broken Ice. (Dr.Ing. Thesis)
MTA-98-125	Videiro, Paulo M., MK	Reliability Based Design of Marine Structures. (Dr.Ing. Thesis)
MTA-99-126	Mainçon, Philippe, MK	Fatigue Reliability of Long Welds Application to Titanium Risers. (Dr.Ing. Thesis)
MTA-99-127	Haugen, Elin M., MH	Hydroelastic Analysis of Slamming on Stiffened Plates with Application to Catamaran Wetdecks. (Dr.Ing. Thesis)
MTA-99-128	Langhelle, Nina K., MK	Experimental Validation and Calibration of Nonlinear Finite Element Models for Use in Design of Aluminium Structures Exposed to Fire. (Dr.Ing.

		Thesis)
MTA-99-129	Berstad, Are J., MK	Calculation of Fatigue Damage in Ship Structures. (Dr.Ing. Thesis)
MTA-99-130	Andersen, Trond M., MM	Short Term Maintenance Planning. (Dr.Ing. Thesis)
MTA-99-131	Tveiten, Bård Wathne, MK	Fatigue Assessment of Welded Aluminium Ship Details. (Dr.Ing. Thesis)
MTA-99-132	Søreide, Fredrik, MP	Applications of underwater technology in deep water archaeology. Principles and practice. (Dr.Ing. Thesis)
MTA-99-133	Tønnessen, Rune, MH	A Finite Element Method Applied to Unsteady Viscous Flow Around 2D Blunt Bodies With Sharp Corners. (Dr.Ing. Thesis)
MTA-99-134	Elvekrok, Dag R., MP	Engineering Integration in Field Development Projects in the Norwegian Oil and Gas Industry. The Supplier Management of Norne. (Dr.Ing. Thesis)
MTA-99-135	Fagerholt, Kjetil, MP	Optimeringsbaserte Metoder for Ruteplanlegging innen skipsfart. (Dr.Ing. Thesis)
MTA-99-136	Bysveen, Marie, MM	Visualization in Two Directions on a Dynamic Combustion Rig for Studies of Fuel Quality. (Dr.Ing. Thesis)
MTA-2000-137	Storteig, Eskild, MM	Dynamic characteristics and leakage performance of liquid annular seals in centrifugal pumps. (Dr.Ing. Thesis)
MTA-2000-138	Sagli, Gro, MK	Model uncertainty and simplified estimates of long term extremes of hull girder loads in ships. (Dr.Ing. Thesis)
MTA-2000-139	Tronstad, Harald, MK	Nonlinear analysis and design of cable net structures like fishing gear based on the finite element method. (Dr.Ing. Thesis)
MTA-2000-140	Kroneberg, André, MP	Innovation in shipping by using scenarios. (Dr.Ing. Thesis)
MTA-2000-141	Haslum, Herbjørn Alf, MH	Simplified methods applied to nonlinear motion of spar platforms. (Dr.Ing. Thesis)
MTA-2001-142	Samdal, Ole Johan, MM	Modelling of Degradation Mechanisms and Stressor Interaction on Static Mechanical Equipment Residual Lifetime. (Dr.Ing. Thesis)
MTA-2001-143	Baarholm, Rolf Jarle, MH	Theoretical and experimental studies of wave impact underneath decks of offshore platforms. (Dr.Ing. Thesis)
MTA-2001-144	Wang, Lihua, MK	Probabilistic Analysis of Nonlinear Wave-induced Loads on Ships. (Dr.Ing. Thesis)
MTA-2001-145	Kristensen, Odd H. Holt, MK	Ultimate Capacity of Aluminium Plates under Multiple Loads, Considering HAZ Properties. (Dr.Ing. Thesis)

MTA-2001-146	Greco, Marilena, MH	A Two-Dimensional Study of Green-Water Loading. (Dr.Ing. Thesis)
MTA-2001-147	Heggelund, Svein E., MK	Calculation of Global Design Loads and Load Effects in Large High Speed Catamarans. (Dr.Ing. Thesis)
MTA-2001-148	Babalola, Olusegun T., MK	Fatigue Strength of Titanium Risers – Defect Sensitivity. (Dr.Ing. Thesis)
MTA-2001-149	Mohammed, Abuu K., MK	Nonlinear Shell Finite Elements for Ultimate Strength and Collapse Analysis of Ship Structures. (Dr.Ing. Thesis)
MTA-2002-150	Holmedal, Lars E., MH	Wave-current interactions in the vicinity of the sea bed. (Dr.Ing. Thesis)
MTA-2002-151	Rognebakke, Olav F., MH	Sloshing in rectangular tanks and interaction with ship motions. (Dr.Ing. Thesis)
MTA-2002-152	Lader, Pål Furset, MH	Geometry and Kinematics of Breaking Waves. (Dr.Ing. Thesis)
MTA-2002-153	Yang, Qinzheng, MH	Wash and wave resistance of ships in finite water depth. (Dr.Ing. Thesis)
MTA-2002-154	Melhus, Øyvin, MM	Utilization of VOC in Diesel Engines. Ignition and combustion of VOC released by crude oil tankers. (Dr.Ing. Thesis)
MTA-2002-155	Ronæss, Marit, MH	Wave Induced Motions of Two Ships Advancing on Parallel Course. (Dr.Ing. Thesis)
MTA-2002-156	Økland, Ole D., MK	Numerical and experimental investigation of whipping in twin hull vessels exposed to severe wet deck slamming. (Dr.Ing. Thesis)
MTA-2002-157	Ge, Chunhua, MK	Global Hydroelastic Response of Catamarans due to Wet Deck Slamming. (Dr.Ing. Thesis)
MTA-2002-158	Byklum, Eirik, MK	Nonlinear Shell Finite Elements for Ultimate Strength and Collapse Analysis of Ship Structures. (Dr.Ing. Thesis)
IMT-2003-1	Chen, Haibo, MK	Probabilistic Evaluation of FPSO-Tanker Collision in Tandem Offloading Operation. (Dr.Ing. Thesis)
IMT-2003-2	Skaugset, Kjetil Bjørn, MK	On the Suppression of Vortex Induced Vibrations of Circular Cylinders by Radial Water Jets. (Dr.Ing. Thesis)
IMT-2003-3	Chezhian, Muthu	Three-Dimensional Analysis of Slamming. (Dr.Ing. Thesis)
IMT-2003-4	Buhaug, Øyvind	Deposit Formation on Cylinder Liner Surfaces in Medium Speed Engines. (Dr.Ing. Thesis)
IMT-2003-5	Tregde, Vidar	Aspects of Ship Design: Optimization of Aft Hull with Inverse Geometry Design. (Dr.Ing. Thesis)

IMT-2003-6	Wist, Hanne Therese	Statistical Properties of Successive Ocean Wave Parameters. (Dr.Ing. Thesis)
IMT-2004-7	Ransau, Samuel	Numerical Methods for Flows with Evolving Interfaces. (Dr.Ing. Thesis)
IMT-2004-8	Soma, Torkel	Blue-Chip or Sub-Standard. A data interrogation approach of identity safety characteristics of shipping organization. (Dr.Ing. Thesis)
IMT-2004-9	Ersdal, Svein	An experimental study of hydrodynamic forces on cylinders and cables in near axial flow. (Dr.Ing. Thesis)
IMT-2005-10	Brodtkorb, Per Andreas	The Probability of Occurrence of Dangerous Wave Situations at Sea. (Dr.Ing. Thesis)
IMT-2005-11	Yttervik, Rune	Ocean current variability in relation to offshore engineering. (Dr.Ing. Thesis)
IMT-2005-12	Fredheim, Arne	Current Forces on Net-Structures. (Dr.Ing. Thesis)
IMT-2005-13	Heggernes, Kjetil	Flow around marine structures. (Dr.Ing. Thesis
IMT-2005-14	Fouques, Sebastien	Lagrangian Modelling of Ocean Surface Waves and Synthetic Aperture Radar Wave Measurements. (Dr.Ing. Thesis)
IMT-2006-15	Holm, Håvard	Numerical calculation of viscous free surface flow around marine structures. (Dr.Ing. Thesis)
IMT-2006-16	Bjørheim, Lars G.	Failure Assessment of Long Through Thickness Fatigue Cracks in Ship Hulls. (Dr.Ing. Thesis)
IMT-2006-17	Hansson, Lisbeth	Safety Management for Prevention of Occupational Accidents. (Dr.Ing. Thesis)
IMT-2006-18	Zhu, Xinying	Application of the CIP Method to Strongly Nonlinear Wave-Body Interaction Problems. (Dr.Ing. Thesis)
IMT-2006-19	Reite, Karl Johan	Modelling and Control of Trawl Systems. (Dr.Ing. Thesis)
IMT-2006-20	Smogeli, Øyvind Notland	Control of Marine Propellers. From Normal to Extreme Conditions. (Dr.Ing. Thesis)
IMT-2007-21	Storhaug, Gaute	Experimental Investigation of Wave Induced Vibrations and Their Effect on the Fatigue Loading of Ships. (Dr.Ing. Thesis)
IMT-2007-22	Sun, Hui	A Boundary Element Method Applied to Strongly Nonlinear Wave-Body Interaction Problems. (PhD Thesis, CeSOS)
IMT-2007-23	Rustad, Anne Marthine	Modelling and Control of Top Tensioned Risers. (PhD Thesis, CeSOS)
IMT-2007-24	Johansen, Vegar	Modelling flexible slender system for real-time simulations and control applications
IMT-	Wroldsen, Anders Sunde	Modelling and control of tensegrity structures. (PhD

2007-25		Thesis, CeSOS)
IMT-2007-26	Aronsen, Kristoffer Høye	An experimental investigation of in-line and combined inline and cross flow vortex induced vibrations. (Dr. avhandling, IMT)
IMT-2007-27	Gao, Zhen	Stochastic Response Analysis of Mooring Systems with Emphasis on Frequency-domain Analysis of Fatigue due to Wide-band Response Processes (PhD Thesis, CeSOS)
IMT-2007-28	Thorstensen, Tom Anders	Lifetime Profit Modelling of Ageing Systems Utilizing Information about Technical Condition. (Dr.ing. thesis, IMT)
IMT-2008-29	Berntsen, Per Ivar B.	Structural Reliability Based Position Mooring. (PhD-Thesis, IMT)
IMT-2008-30	Ye, Naiquan	Fatigue Assessment of Aluminium Welded Box-stiffener Joints in Ships (Dr.ing. thesis, IMT)
IMT-2008-31	Radan, Damir	Integrated Control of Marine Electrical Power Systems. (PhD-Thesis, IMT)
IMT-2008-32	Thomassen, Paul	Methods for Dynamic Response Analysis and Fatigue Life Estimation of Floating Fish Cages. (Dr.ing. thesis, IMT)
IMT-2008-33	Pákozdi, Csaba	A Smoothed Particle Hydrodynamics Study of Two-dimensional Nonlinear Sloshing in Rectangular Tanks. (Dr.ing.thesis, IMT)
IMT-2007-34	Grytøyr, Guttorm	A Higher-Order Boundary Element Method and Applications to Marine Hydrodynamics. (Dr.ing.thesis, IMT)
IMT-2008-35	Drummen, Ingo	Experimental and Numerical Investigation of Nonlinear Wave-Induced Load Effects in Containerships considering Hydroelasticity. (PhD thesis, CeSOS)
IMT-2008-36	Skejic, Renato	Maneuvering and Seakeeping of a Singel Ship and of Two Ships in Interaction. (PhD-Thesis, CeSOS)
IMT-2008-37	Harlem, Alf	An Age-Based Replacement Model for Repairable Systems with Attention to High-Speed Marine Diesel Engines. (PhD-Thesis, IMT)
IMT-2008-38	Alsos, Hagbart S.	Ship Grounding. Analysis of Ductile Fracture, Bottom Damage and Hull Girder Response. (PhD-thesis, IMT)
IMT-2008-39	Graczyk, Mateusz	Experimental Investigation of Sloshing Loading and Load Effects in Membrane LNG Tanks Subjected to Random Excitation. (PhD-thesis, CeSOS)
IMT-2008-40	Taghipour, Reza	Efficient Prediction of Dynamic Response for Flexible amd Multi-body Marine Structures. (PhD-thesis, CeSOS)
IMT-2008-41	Ruth, Eivind	Propulsion control and thrust allocation on marine vessels. (PhD thesis, CeSOS)

IMT- 2008-42	Nystad, Bent Helge	Technical Condition Indexes and Remaining Useful Life of Aggregated Systems. PhD thesis, IMT
IMT- 2008-43	Soni, Prashant Kumar	Hydrodynamic Coefficients for Vortex Induced Vibrations of Flexible Beams, PhD thesis, CeSOS
IMT- 2009-43	Amlashi, Hadi K.K.	Ultimate Strength and Reliability-based Design of Ship Hulls with Emphasis on Combined Global and Local Loads. PhD Thesis, IMT
IMT- 2009-44	Pedersen, Tom Arne	Bond Graph Modelling of Marine Power Systems. PhD Thesis, IMT
IMT- 2009-45	Kristiansen, Trygve	Two-Dimensional Numerical and Experimental Studies of Piston-Mode Resonance. PhD-Thesis, CeSOS
IMT- 2009-46	Ong, Muk Chen	Applications of a Standard High Reynolds Number Model and a Stochastic Scour Prediction Model for Marine Structures. PhD-thesis, IMT
IMT- 2009-47	Hong, Lin	Simplified Analysis and Design of Ships subjected to Collision and Grounding. PhD-thesis, IMT
IMT- 2009-48	Koushan, Kamran	Vortex Induced Vibrations of Free Span Pipelines, PhD thesis, IMT
IMT- 2009-49	Korsvik, Jarl Eirik	Heuristic Methods for Ship Routing and Scheduling. PhD-thesis, IMT
IMT- 2009-50	Lee, Jihoon	Experimental Investigation and Numerical in Analyzing the Ocean Current Displacement of Longlines. Ph.d.-Thesis, IMT.
IMT- 2009-51	Vestbøstad, Tone Gran	A Numerical Study of Wave-in-Deck Impact usin a Two-Dimensional Constrained Interpolation Profile Method, Ph.d.thesis, CeSOS.
IMT- 2009-52	Bruun, Kristine	Bond Graph Modelling of Fuel Cells for Marine Power Plants. Ph.d.-thesis, IMT
IMT 2009-53	Holstad, Anders	Numerical Investigation of Turbulence in a Sekwed Three-Dimensional Channel Flow, Ph.d.-thesis, IMT.
IMT 2009-54	Ayala-Uraga, Efren	Reliability-Based Assessment of Deteriorating Ship-shaped Offshore Structures, Ph.d.-thesis, IMT
IMT 2009-55	Kong, Xiangjun	A Numerical Study of a Damaged Ship in Beam Sea Waves. Ph.d.-thesis, IMT/CeSOS.
IMT 2010-56	Kristiansen, David	Wave Induced Effects on Floaters of Aquaculture Plants, Ph.d.-thesis, IMT/CeSOS.
IMT 2010-57	Ludvigsen, Martin	An ROV-Toolbox for Optical and Acoustic Scientific Seabed Investigation. Ph.d.-thesis IMT.
IMT 2010-58	Hals, Jørgen	Modelling and Phase Control of Wave-Energy Converters. Ph.d.thesis, CeSOS.

IMT IMT 2010- 59	Shu, Zhi	Uncertainty Assessment of Wave Loads and Ultimate Strength of Tankers and Bulk Carriers in a Reliability Framework. Ph.d. Thesis, IMT.
IMT 2010-60	Shao, Yanlin	Numerical Potential-Flow Studies on Weakly-Nonlinear Wave-Body Interactions with/without Small Forward Speed, Ph.d.thesis, IMT.
IMT 2010-61	Califano, Andrea	Dynamic Loads on Marine Propellers due to Intermittent Ventilation. Ph.d.thesis, IMT.
IMT 2010-62	El Khoury, George	Numerical Simulations of Massively Separated Turbulent Flows, Ph.d.-thesis, IMT
IMT 2010-63	Seim, Knut Sponheim	Mixing Process in Dense Overflows with Emphasis on the Faroe Bank Channel Overflow. Ph.d.thesis, IMT
IMT 2010-64	Jia, Huirong	Structural Reliability Analysis of Intact and Damaged Ships in a Collision Risk Analysis Perspective. Ph.d.-thesis CeSOS.